TISSUE ENGINEERING OF CERVICAL INTERVERTEBRAL DISCS: AN IN VITRO AND IN VIVO PRE-CLINICAL CANINE MODEL OF TOTAL DISC REPLACEMENT

A Dissertation

Presented to the Faculty of the Graduate School

of Cornell University

in Partial Fulfillment of the Requirements for the Degree of

Doctor of Philosophy

by

Jorge Alexis Mojica Santiago

August 2018

TISSUE ENGINEERING OF CERVICAL INTERVERTEBRAL DISCS: AN IN VITRO AND IN VIVO PRE-CLINICAL CANINE MODEL OF TOTAL DISC REPLACEMENT

Jorge Alexis Mojica Santiago, PhD

Cornell University 2018

Degeneration of the intervertebral disc (IVD) is directly associated with the leading causes of disability in the industrialized world, neck and back pain. Current treatments focus on pain relief and mitigating symptoms rather than addressing the underlying source of pain, which in the majority of cases stems from radiculopathy. Strategies from tissue engineering have been introduced for the past 20 years to create biological treatments that can replace the pathologic tissue with a biomimetic implant that possesses regenerative potential. The current state of the field of IVD tissue engineering includes strategies for repair and replacement of individual components of the disc, the nucleus pulposus (NP) and annulus fibrosus (AF), but only a handful of technologies for total disc replacement (TDR) have shown promise for clinical translation *in vitro* and *in vivo*.

Total disc replacement with biological tissue-engineered IVDs (TE-IVDs) has only been tested in small animal models to date. This dissertation sought to address the need for a larger animal model that is clinically relevant to humans by demonstrating the feasibility of the canine cervical spine as a pre-clinical model of TDR with TE-IVDs. In this work, the focus was to investigate the appropriate implantation conditions for TDR in the cervical spine and the ability of TE-IVDs to integrate host tissue, mature, and restore function *in vivo* (Chapter 2). TE-IVDs for the canine cervical spine were developed as composite structures made of cell-seeded alginate NP surrounded by circumferentially aligned cell-seeded collagen AF. This *in vivo* study was the first to demonstrate that stably implanted TE-IVDs produced integrated tissues that resemble native IVD structure with viable cells in a canine pre-clinical model of TDR.

Despite the favorable outcomes in stably implanted TE-IVDs, new challenges were identified in the canine model that had not been encountered in rodents before. Segment instability caused 50% of TE-IVDs to displace out of the disc space upon implantation and scaled-up TE-IVDs had yet to match native-like properties pre-operatively. The instability issue was addressed (chapter 3) by investigating a combined treatment approach of TE-IVD implantation with a resorbable plating system proposed to assist in transferring compressive loads of motion segments along the vertebral bodies and retain TE-IVD implants in the disc space. To improve potential functionality of TE-IVDs, the study described in chapter 4 leverages the tunable AF region of the TE-IVDs to investigate the potential of high-density collagen as AF scaffolds and assess the effects of initial scaffold concentration and cell seeding density with hMSCs on the remodeling of the resultant composite TE-IVD structure. Collectively, these studies offered promising alternatives to promote the success of TDR in a pre-clinical animal model with TE-IVDs.

BIOGRAPHICAL SKETCH

Jorge was born and raised in Mayagüez, Puerto Rico. He attended the magnet high school, specialized in math and sciences, CROEM (Spanish acronym for Residential Center of Educational Opportunities of Mayagüez), where he cultivated inquisitiveness towards art, engineering design, and the life sciences. He then began his college education at the age of 16 attending University of Puerto Rico at Mayagüez (UPRM), from which he graduated *magna cum laude* in 2012 with a BS in Mechanical Engineering. While at UPRM, Jorge was fascinated with tutoring and mentoring underclassmen on engineering coursework; he also discovered his interest in biomechanics and biomaterials under the training of Dr. Paul Sundaram. For two years in this group, he investigated bovine spine motion segments and intervertebral disc biomechanics. Jorge also participated in a Bioengineering REU program at University of California San Diego, mentored by Dr. Andrew McCulloch, where he was encouraged to pursue a doctoral degree.

In 2012, Jorge began pursuing his PhD at Cornell University under the direction of Dr. Lawrence Bonassar. At Cornell, Jorge was awarded the prestigious National Science Foundation Graduate Research Fellowship and received support from the Alfred P. Sloan Foundation to advance his research in tissue engineering of intervertebral discs. In addition to research, Jorge devoted time to serving various leadership roles at the Society for Hispanic Professional Engineers in efforts to help increase the number of Hispanics in STEM fields, and participating in recruitment as a Graduate School Ambassador and with the BME department. Jorge also actively assisted the Office of Diversity Programs in Engineering to help further their mission as a graduate coordinator, while his three terms as a teaching assistant asserted his commitment as an educator.

Jorge will be taking a postdoctoral position in the lab of Dr. Christine Schmidt at University of Florida Gainesville following his completion of all PhD requirements. At the lab of Dr. Schmidt, he will focus on biomaterials design and tissue engineering of electroconductive tissues. After his postdoctoral work, Jorge aspires to begin a career in academia and champion efforts to broaden access to opportunities in scientific experiences and higher education in diverse communities.

Dedicado a mi amada familia y amistades por su incesante apoyo

y brindarme motivación para completar esta travesía.

In loving memory and dedication to Turi Alberto Alcoser.

ACKNOWLEDGMENTS

First, I would like to thank my advisor Dr. Lawrence Bonassar for his unwavering support and mentorship over the past six years. Dr. Bonassar has truly been a role model as a scientist and an educator; I am especially grateful for his advice on balancing an academic career with family interests. Occasionally, factors that could have threatened my continuation in the graduate program were present, but his guidance and encouragement were key to my completion of this degree.

Thanks to Dr. Marjolein van der Meulen for offering me the first opportunity of research experience at Cornell during my initial rotation in the BME PhD program and for your guidance and advice since the NSF application process and through this date as a Special Committee member. I would also like to thank Dr. Rory Todhunter for your guidance and insights as a Special Committee member and for offering your expertise as a veterinary clinician since our first meeting in the Vet School. In addition, thanks are offered to my clinical advisor, Dr. Roger Härtl, whose invaluable input enlightened my perspective on the clinical implications of this work.

Special thanks are due to Belinda Floyd, who has supported my journey through Cornell since day zero, even before I got accepted to the PhD program when I was just another applicant inquiring information over the phone. Thanks are due to Dr. Shivaun Archer as well for her inspiring dedication as an educator, her advice on teaching strategies and career advancement, and for demonstrating compassion and understanding towards me in times of need. Thank you to Jami Joyner, Cindy Mosqueda, Anitra Douglas-McCarthy, and Sara Xayarath Hernandez for your continuous inspiration and encouragement throughout the years in valuing diversity and inclusion in mentoring and in higher education. The time I have spent in roles with events that are associated or conducted by you have been among the most rewarding experiences I had these past few years.

Thank you to my past and present officemates and colleagues, Drs. Nizeet Aguilar, Kirk Samaroo, Mingchee Tan, Darvin Griffin, as well as Dr. Chris DiDomenico, Jill Middendorf, Alex Boys, and Nicole Diamantides. All of you had made me laugh over inside jokes at the office and

supported me on the worst office days, at one point or another. I am grateful to previous and current members of team IVD, Drs. Katie Hudson and Brandon Borde, as well as Stephen Sloan and Marianne Lintz. I would also like to thank all other past and present Bonassar Lab members not already mentioned with whom I spent time these past six years, for their camaraderie and the collegial feedback they provided. I could not have asked for a better working environment inside the lab and outside on conference travels and escapades from ORS or BMES to the Grand Canyon.

I am incredibly grateful to Turi Alcoser, who was the very first friend I made at Cornell during recruitment weekend. Having decided to share an apartment with Turi for our first year as PhD students, we quickly became friends and, although he left us too soon, his excitement about pursuing scientific research and maximum attainable life enjoyment were motivating and will always resonate with me. Thank you to the many graduate students in BME and other departments whose friendships I cherish and who made the graduate school experience far more enjoyable for your support on professional matters as well as in entertainment outside work.

Finally, thank you feels short for the support, persistence, encouragement, and confidence that my mother Mariana, my father Elson, my siblings Adaliz and Gabriel, and my beloved fiancée Perla bestowed on me over the years. Their love and understanding were a safety net, a rock on which to stand, an energy boost, and a shoulder on which to cry, simultaneously, in a number of occasions through my graduate school journey. Similarly, thank you to my friends in Ithaca who have been present in different aspects of my transition from Puerto Rico here. Family and friends, the completion of this degree is a testament to my everlasting gratitude to you, and it would simply not have been possible without you.

Funding for this work was provided by Cornell University's Dean's Excellence Fellowship, the National Science Foundation Graduate Research Fellowship (NSF DGE-1650441), and the Alfred P. Sloan Foundation.

TABLE OF CONTENTS

LIST OF FIGURES

LIST OF TABLES

CHAPTER 1

Introduction

Overview of Intervertebral Disc

1.1.1 Biological structure and function

The intervertebral disc is a fibrocartilaginous joint structure located between the vertebral endplates of the spinal column. The intervertebral disc (IVD) is responsible for allowing spine flexibility and a range of motion with six degrees of freedom, while simultaneously assisting the vertebral bodies (VBs) in protecting the spinal cord and branches of peripheral nerves that stem from the spine (Fig. 1.A). The human spinal column contains 23 IVDs, categorized by their location within the spine and by their adjacent VBs. The 6 IVDs in the neck are known as cervical (e.g. C2/C3 is located between the axis vertebra C2 and the adjacent inferior vertebra C3). The thoracic region follows with 12 IVDs (T1/T2-T12/L1) from below the base of the neck to the middle back; then from the lower back to the sacrum, the lumbar region is extended with 5 IVDs (L1/L2-L5/S1). Due to its characteristic avascular nature, absorption of nutrients in the IVD is limited to the top and bottom interfaces with the cartilaginous endplates (CEPs).[1] Along with the CEPs, the VBs, and the surrounding ligaments and musculature, the IVD constitutes the functional motion segments of the spine.

The range of motion in these functional motion segments is known to vary considerably by level or location in the spine. The upper cervical segments are characterized by flexion-extension and over 80° of axial rotation at the C1/C2 level,[2-3] but the median range of motion of lower cervical segments remains between 5-15° of axial rotation and less than 5° of lateral bending. Flexion-extension bending moments are also predominant in segments C4 to C6, towards the middle of the neck. The thoracolumbar region has been shown to reach a median range of motion of up to 20° in axial rotation at the first thoracic motion segment T1/T2 and decrease to less than 5°

rotation at the lower segment levels from T10 to L5/S1. In flexion-extension the mid-to-lower-thoracic segments T6 to T11 do not exceed 10°, but from T11/T12 to L4/L5 the segments can range between 15 to 20°. Similarly, lateral bending range of motion exceeds 15° in the thoracolumbar region reaching up to 25° in the lower segments below T11.[4] Although the range of motion in spinal segments differs across segment levels, varying geometrical parameters of the adjacent VBs give rise to these major differences, but the structural composition of the IVD is relatively consistent throughout the spine.

The IVD is a composite tissue comprised of three main tissue regions: the nucleus pulposus (NP), the annulus fibrosus (AF), and the CEPs that associate the disc with the adjacent vertebrae (Fig. 1.B). The NP consists of a soft gelatinous mesh of collagen fibrils, predominantly types I and II,[5-6] to which chains of brush-like proteoglycans, mostly aggrecan and biglycan (GAGs) attach. These GAGs contain sulfates and uronic acid groups, to which their distinctive negative charges are attributed, and attract molecules of water to produce osmotic swelling of the NP. The AF consists of an oriented lamellar array of collagen fiber bundles, predominantly types I, II, and VI,[7] that are circumferentially aligned around the NP and attached to the CEP and VB boundaries. The distribution of proteoglycans present in the AF varies radially with decreasing GAG content at the AF layers further away from the NP. The orientation of the collagen fibers at each lamella also varies in an angle-ply laminate fashion with respect to the radial distance from the NP. The laminate structure of the AF contains the swelling of the NP and directs diffusion of metabolites primarily through the CEP, where nutrients exchange occurs with the VBs. The AF also limits the radial bulge, allows distention, and rotation to facilitate mobility of the motion segment. A thin layer of hyaline cartilage ranging between 0.5 to 15 mm thick comprises the top and bottom CEPs.[1] These CEPs provide a graded transition from the fibrocartilaginous

disc, rich in water, proteoglycans and collagen, to the mineralized (calcium-rich) vertebral bodies.

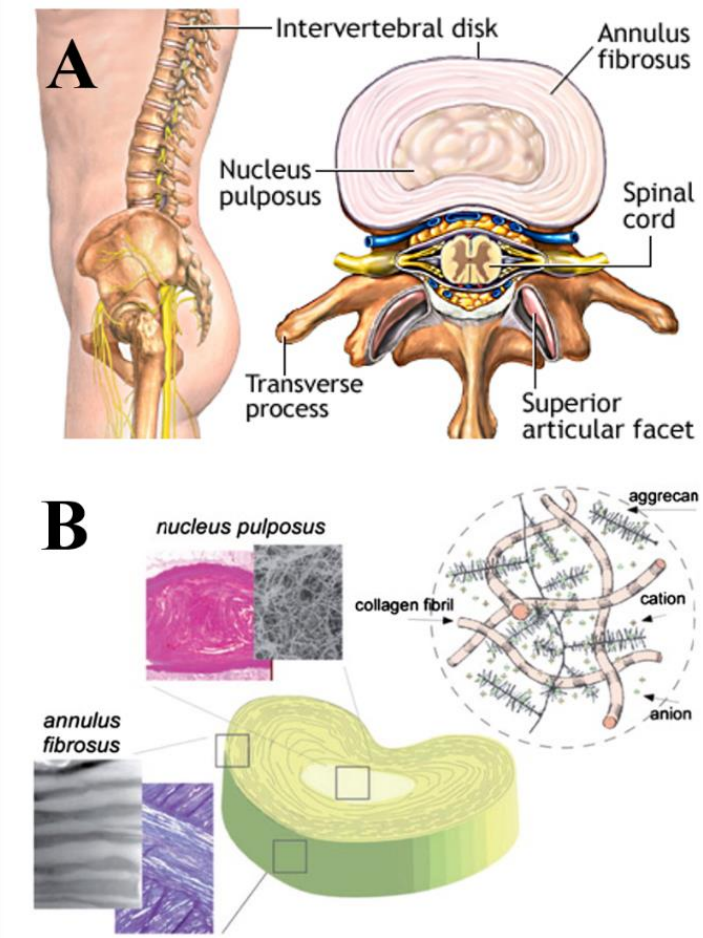

Figure 1.1. A) Schematic of the location of the IVD in the spine with a cross-sectional view of the major structures surrounding the IVD that the motion segments protect. Image adapted from: https://medlineplus.gov/ency/images/ency/fullsize/19469.jpg. B) Representative image depicting the main regions NP and AF that comprise the IVD, and their predominant constituents of collagen and proteoglycans. Image adapted from Whatley et al.[8]

The NP and AF have distinct predominant cell types that guide the turnover and remodeling of the extracellular matrix (ECM), and maintain the overall health of the IVD. The NP contains chondrocyte-like cells that link with the collagen fibrils but remain with a round phenotype. On the other hand, the AF contains fibroblast-like cells

that align preferentially with the orientation of the collagen fibers at each lamella throughout the depth of the tissue. The NP cells are accustomed to a unique hypoxic environment and are scattered at 2 to 5 million cells/mL within the avascular matrix.[9] AF cells are densely distributed throughout the ECM at least at 9 million cells/mL and are mechanosensitive to tensile and compressive loads experienced in the tissue.[8]

1.1.2 Tissue Development and organization

The specialized IVD structure derives from the natural and physiologic environment to which the primitive IVD tissues are exposed during embryonic development and their developmental pathways are dependent on the expression of several genes. Most IVD tissues are derived from mesenchymal origins. During tissue development, musculoskeletal tissues of the spine start out as mesenchyme from the mesoderm with cells embedded in a water-rich soft ECM that allows for free diffusion of metabolites. As the embryo matures, this water-rich soft ECM in the primitive spine region is exposed to a wide range of physical and biochemical cues that activate developmental pathways and promote cells to differentiate from chondrocyte-like phenotype to fibrochondrocyte-like phenotype. The physiological environment near the IVD is unique in that the vertebral bodies undergo ossification and surrounding ligaments develop a preferentially aligned structure, but the IVD tissues become organized in a composite manner. Furthermore, while the CEPs retain a cartilaginous phenotype, the NP and AF develop and mature differently. The NP is originated from the notochordal region of the embryo and its development is driven by the expression of Forkhead box A2, Brachyury, and Notochord homolog genes.[10] The AF, VBs, and CEP stem from the segmented mesodermal layer surrounding the notochord called somites, which give rise to other musculoskeletal tissues such as skeletal muscles and tendons, and help direct peripheral nerve segmentation.[11] A segment of these somites, the sclerotome, is instructed by the Sonic hedgehog factors and transforming growth

factor-beta to control the vertebral ossification process and form VBs, CEP, and AF.[12-13] After vertebrae proliferate from the sclerotome, notochordal cells die by apoptosis, although a varying number of notochordal cells remain in numerous mammalian species.

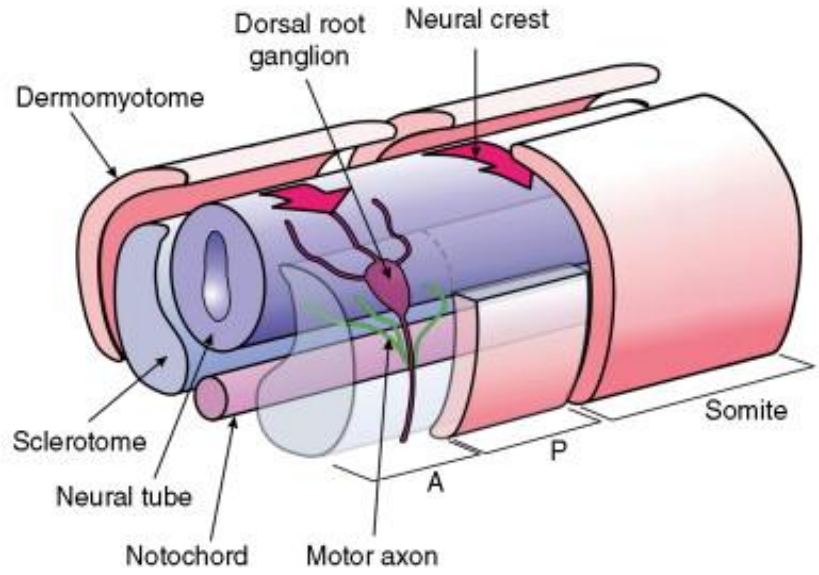

Figure 1.2. The mesodermal axially oriented layer that surrounds the notochord during embryonic development gives rise to several vertebral motion segment tissues including VBs, CEP, and AF, while the NP derives from notochord. Image adapted from Cook et al.[11]

1.1.3 Mechanical and biochemical properties of the IVD

The mechanical behavior of the IVD structure is relevant to assess the degree of health or disease of the disc because it is directly related to its biochemical constituents and composite structure. An estimated 70% of the dry weight of the IVD is comprised of collagen with decreasing concentration from the NP towards the outer region of the AF that ranges between 50-300 μg/mg wet tissue.[5,14] Between 2-45% of the NP dry weight is constituted by non-collagenous proteins (e.g. elastin, fibrillins, adhesive glycoproteins such as fibronectin and laminin), while this ranges between 5-25% of the AF dry weight. These constituents are believed to assist collagen fibers in their

mechanical and ECM remodeling roles; for example, approximately 10% of the human IVD is comprised of elastin, which are believed to assist collagen fibers recover after deformation.[5] Relative dry weight contents of GAGs in the IVD regions are estimated between 50-65% of the NP and 10-20% of the AF,[7,15] with aggrecan as the predominant proteoglycan in the NP. The collagen network and GAGs in the ECM jointly resist compression of the IVD in the NP and provide tensile strength to the concentric fibers in the AF.

The IVD functions as a pressure vessel whereby swelling of the NP caused by the GAG-rich matrix maintains osmotic pressures as high as 2.3 MPa and water content between 70-90%,[16-17] whereas the collagen fiber laminated AF provides the necessary boundary conditions to help distribute up to 80% of the compressive loads in the spine along the CEPs to the VBs.[18-19] The material properties of each constituent region, NP, AF, and CEP have been extensively studied individually and in combination with their adjacent vertebrae as functional motion segments.[20] Due to its biochemical composition, the IVD and, consequently, the spinal motion segments exhibit viscoelastic and biphasic mechanical behavior. The collagen fiber bundles and hydrated mesh that constitute the extracellular matrix are responsible for this time-dependent poroelastic mechanical response. The NP exhibits mostly isotropic behavior with a compressive stiffness of 3-31 kPa, while the AF contains the NP due to its tensile modulus of 0.2-136 MPa and compressive modulus of 0.116-2.3 MPa.[8] The ranges of mechanical properties vary according to testing modalities and condition of the tissues under study; however, the trends are consistent in that fibrous AF contains higher tensile properties than compressive and NP is measured in compression, under osmotic pressure, or in shear. Alterations to the composition and structure of the IVD due to disease or injury often leads to mechanical instability of the spine and further breakdown of the entire motion segment.

Degenerative Disc Disease

1.2.1 Epidemiology and etiology of degenerative disc disease

Chronic pain of the back and neck are among the most prevalent causes of limited activity in people younger than 45 years old, the second most common reason for visits to the physician in the western world, and the third most frequent cause for surgical intervention.[21-22] At least 80% of the population will experience neck or back pain in their lifetime. Nearly two-thirds of the world is affected by neck pain especially. Low back pain is estimated to cost society $100 billion annually and $11-17 billion in the US alone.[23-27] Degenerative disc disease (DDD) has been linked as the leading cause of chronic pain of the spine.[28-30]. Although the specific etiology of DDD is not well known, the risk factors associated with high probabilities of suffering neck and back pain caused by DDD have been well documented. Diseases of the vasculature in which blood flow is compromised, individual habits such as smoking, and pathological metabolism such as in diabetes are highly correlated with affecting the nutrient supply to the already metabolically-challenged IVD.[31-40] Environmental factors such as those affected by work-related activities and genetic predisposition have also been demonstrated to play a role in affecting natural ageing processes of the spine.[31-36]

1.2.2 Mechanisms of disease progression

The progression of DDD has been associated with changes in the composition of its constituents driven by compromised diffusion of nutrients and accumulation of waste products. This, in turn leads to a loss of tissue hydration that results in a cascade of effects exacerbating the precarious disc nutritional state further. During disc degeneration, the ECM in the NP and AF is degraded and the IVD loses its physiological pressurization and swelling. The NP becomes dry and total number of viable cells declines, thereby reducing ECM turnover. Without pressure from the NP, AF fibers lose tension and organization, thus resulting in disc thinning and structural collapse.

Collagen fibrils in the AF are damaged, increasing the risks for tears and accelerating disc degeneration further.[31,37] The CEP undergoes calcification characterized by the appearance of bone spurs and decreased diffusion of nutrients to the IVD. Furthermore, in the most severe cases of degeneration, narrowing of the foraminal canal space leads to impingement of the nerve roots that stem from the spinal cord and symptoms of radiculopathy and myelopathy. Other effects of this cascade of IVD degeneration include neovascularization, where blood vessels gain access to previously avascular regions, and disruption of the neural networks surrounding the outer AF and the CEP, thereby provoking an inflammatory response and excruciating pain.[38-40]

1.2.3 Symptomatic characterization and clinical identification

Clinicians look for certain symptoms associated with radiculopathy, but due to the intermittence of discomfort in patients, the relationship between neck and back pain with radiological (abnormal) observations is relatively inconsistent.[37] Due to these conflicts, factors such as medical history, neurological, and physical exams are used in conjunction with medical imaging. Neurological and physical exams are used to identify problems with limb movements and/or posture, which can help rule out extraspinal diseases. Certain symptoms typically associated with DDD can also be related to other non-degenerative spine problems. Initial diagnostics with radiographs help exclude scoliosis, spondylolisthesis, and fractures, among other spine ailments. The current standard diagnostic procedure is the low-pressure discography, albeit its interpretation remains controversial.[41-42] The discography involves an injection technique by which the suspected pathologic disc is pressurized with an X-ray dye to assess the discomfort levels that the patient is sensitive to. Computed tomography (CT) scanning by itself does not help evaluate discogenic pain, but it can be used to rule out spondylolisthesis and/or osteophyte formation after DDD had long affected the disc space and disrupted the bony endplates.[43] Although a discogram obtained under fluoroscopic guidance and

radiopaque dye is the most direct tool to diagnose disc degeneration,[44] magnetic resonance imaging (MRI) can help determine whether the pain a patient experiences is derived from DDD. Employing MRI can help evaluate the hydration within the IVD by means of T2-weighted images, and observe potential pain inducing factors in the spinal canal and surrounding neural tissues.

T2 mapping with T2-MRI involves measuring the relaxation time decay of IVD tissues, which is related to the biochemical composition of the disc structures.[45-48] A system for grading degeneration in IVD as evaluated via T2 mapping, namely the Pfirrmann grading, has been shown to provide reliable intra- and interobserver results.[45,50] The Pfirrmann scale employs five grades to rank T2 signal intensity and disc morphology (Fig. 1.3): grades I and II are representative of normal discs, grade III discs display reduced T2 signal or dehydrated discs, and grades IV and V are often described by disc height loss and of other normal features. A grade III disc can be treated conservatively, while higher grades may require surgical intervention.

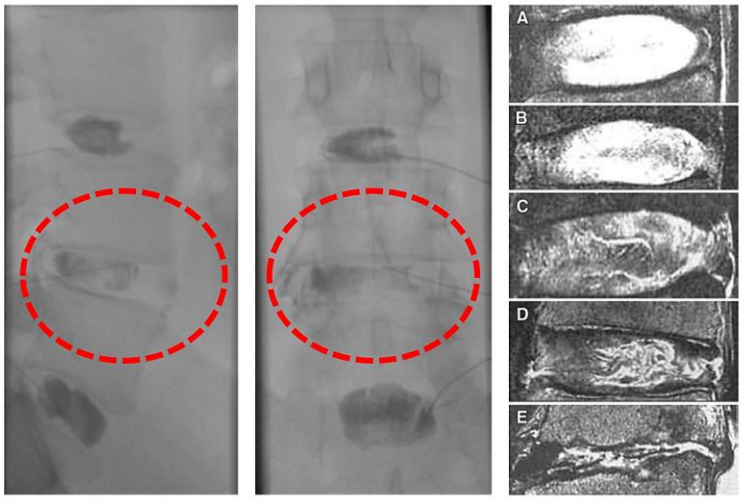

Figure 1.3. Representative discograms of a disrupted L4-L5 disc (encircled in red) that reproduced clinical pain in patient as compared to adjacent healthy discs from a sagittal view (Left) and coronal view (Center); images adapted from Hasz 2012.[44] IVDs representing levels of Pfirrmann's grade (Right): from A to E correspond to grades I through V; image adapted from Lotz et al.[45]

Current and Proposed Treatments for Disc Degeneration

1.3.1 Conservative treatments for neck and back pain

Distress of patients with neck and back pain are initially addressed with conservative treatments to help ameliorate discogenic pain. Non-steroidal anti-inflammatories, opiates, and corticosteroid injections are commonly used to relieve the cascade of pain signals, but they do not influence the radiculopathy and structural source of the pain. Often, physical therapy is recommended to help patients manage pain on their own; however, the risk for further injury without further assisted treatment can increase in these cases. As such, surgical treatment is ultimately the last resort for nearly 4 million patients worldwide.[51]

1.3.2 Surgical treatment alternatives

The current standard of treatment for discogenic pain is based on severity of the condition in which the patient presents and the level of conservative treatments previously attempted. Impingement of nerves can be relieved by spinal decompression via opening of the foramen around the spinal nerve in a vertebral portion with minimally invasive surgery (e.g. laminectomy and foraminotomy). In the most severe cases, decompression of pinched nerve roots is achieved by removal of IVD tissues (i.e. discectomy) in the affected motion segment. The golden standard of surgical intervention involves partial or total discectomy accompanied by fusion of the adjacent vertebrae to relieve effects on soft neural tissues and maintain disc height in the disc space. However, the loss of range of motion resultant of this fusion increases the risks for subsequent surgical revisions, in some cases due to pseudarthrosis and adjacent segment disease.[52-53] Synthetic devices have also been designed as alternatives for spinal fusion to help maintain segment stability and preserve range of motion; but the extent to which these perform better than standard spinal fusion is not clear yet.[53-58] Furthermore, these metallic or ultra-high molecular weight polyethylene prosthetics

have been shown to degrade and wear, thereby elevating the risk of surgical revision and failure of the device.[56-57] While dynamic stabilizing devices designed to provide a controllable range of motion to the functional segments have shown promise, current standard of treatment using spinal fusion holds being the golden standard of care.[59-60]

1.3.3 Biological treatments: molecular, cellular, and tissue alternatives

Attention has been given to biologic-based treatments as alternatives to the standard surgical interventions to address the need for a therapeutic solution that repairs or even replace the pathologic IVD with a long-term regenerative potential. Biological treatments offer promise in that they are designed to accommodate to the diseased environment in a biomimetic way, to integrate with the native tissues, or to follow developmentally inspired behavior that engages the body into repairing its own tissues.[61-62] Discs that present with early signs of degeneration such as those described by grade III on the Pfirmann's scale are suitable for biological therapies at the molecular level, such as recombinant genes and proteins. The mechanism of action with molecular therapies leverages the existing cell population to promote ECM deposition, stimulate cell growth, and/or modify gene expression, as well as to interrupt the degenerative process with appropriate molecular signals and factors. Several *in vivo* studies have reported promising results with increased GAG content following intradiscal injection of exogenous factors or after cell-based gene therapy.[63-65] Once the loss of viable cells ensues in diseased discs, such as in grade IV degeneration, biological therapies require incorporating donor cells. The transplanted cells are meant to reboot the mechanisms of ECM turnover and aid in restoring the function of IVD tissues. Fully differentiated IVD cells and articular chondrocytes have been successful at retarding DDD with *in vivo* canine models.[66-67] Transplantation of mesenchymal stem cells (MSCs), embryonic stem cells (ESCs), and induced pluripotent stem cells (iPSCs) also proved their potential

to differentiate into IVD cells and repair disc tissues *in vivo*, when strategically implanted or stimulated.[68-69]

In the worst cases of disc degeneration as in grade V, most recent efforts have been devoted to engineering whole IVD tissues with biological implants that potentially reconstruct the composition and function of the entire segment. Since the advent of tissue engineering by Langer and Vacanti,[70] the efforts to repair and replace diseased tissues have grown across multiple disciplines and physiological systems. More recently, several groups have attempted to develop tissue-engineered IVD treatments with the objectives of repairing or replacing NP, AF, or whole IVDs.[71]

1.3.4 Tissue engineering of the IVD: NP engineering, AF engineering, and whole disc engineering

Over the years, engineered NP tissues consisted of combinations of natural and synthetic polymers[72] that aimed to mimic the hydrating capabilities of GAGs to relieve the dehydration and disc height loss in a diseased NP,[73] but have recently shifted to combinations of naturally occurring matrix components such as GAGs and hyaluronic acid (HA) with cells that can repopulate a degenerated NP.[74] Although many of these options have been explored pre-clinically and clinically, increasing concern prevails about the consequences of implanting a medical device without fully understanding the extent to which other IVD tissues and local cell populations will be affected. An ideal tissue-engineered strategy for NP repair should not only restore mechanical function but should provide the necessary cues to promote tissue regeneration and cellular activity in the long term. Strategies for AF repair focus primarily on addressing tears caused by injuries where incorrect motion or mechanical loading provokes the propagation of a fissure of the fibrous AF wall. Biomaterials have been widely studied as an alternative to traditional AF sutures to patch small defects in the AF; among which injectable hydrogels and sponges remain the most popular due to their facile delivery during

surgical intervention. Treatments with alginate, agarose, gelatin, collagen, fibrin, silk, HA, polyglycolic acid (PGA), and polycaprolactone (PCL) have been proposed alone and in combination with cells;[74-75] however, most of these approaches fail to produce an aligned matrix with cells of the characteristic elongated phenotype *in situ*. Concerns about the ability of these materials to effectively transfer tensile loads across the defect site and restore mechanical function of the AF have also led to induce crosslinking of the implanted biomaterial as well as to the development of composite biomaterials that reproduce the native tissue fiber architecture.[76-78]

To this end, a combined approach of tissue-engineered whole IVDs was pioneered by Mizuno et al.[79] employing a PGA/PLA AF with an alginate NP composite scaffold seeded with cells. Since then, efforts to create composite implants that mimic the native IVD structure have been advancing over the last two decades. Gelatinous materials such as agarose, hyaluronan, and alginate were often proposed for the NP region, while fibrous synthetic and natural scaffolds like polycaprolactone (PCL), biphasic silk with fibrin, demineralized bone matrix gel, and collagen type I gel, mimicked the AF region of these engineered tissues.[81-87] These innovative alternatives have provided meaningful contributions to the development of a clinically viable engineered IVD; from identifying the surgical challenges associated to location of the implanted segment to understanding the necessary benchmarks to consider in implant design. In addition to recreating the native IVD, recent work pays considerable attention to ensuring retention of the implant and promoting engraftment via external fixation devices or by providing anchorage to the CEP and VBs.[88-89] Certainly, engineering a whole disc that promotes long term integration with the host tissue in a diseased motion segment will require further studies before it can be applicable to humans.

Clinical Translation of Total Disc Replacement with TE-IVDs

To successfully translate engineered IVD constructs for total disc replacement into the clinical stage, studies with several small and large animal models help identify challenges and promising strategies with rising technologies. The first *in vivo* studies for screening biomaterials and whole disc replacement biologics employed the use of rodent and rabbits. These murine and leporine animal models continue to be useful for high-throughput quick screening of early stage technologies developed for clinical translation. However, several differences between the spine of these small animal models and the human spine prevent these models from being considered far enough for clinical translation. For example, in athymic rats, the loading conditions are almost exclusively uniaxially compressive and, in fact, axial loads are significantly higher in the human disc space. Nevertheless, small animal models are certainly valued and relevant as an initial step of *in vivo* assessment.

Building upon previous successes in TE-IVD development and *in vivo* assessment with rodent models, the next logical step in the clinical translation pathway is to test our discs in large animal models. Several groups have employed different large animal models, among which goats, calves, and minipigs remain popular.[90] In addition, chondrodystrophic dog breeds are considered important models to study spine biomechanics and diseases.[91-94] These canine breeds usually consist of small dogs with elongated bodies and short legs; they have been shown to spontaneously develop disc degeneration around 3-7 years of age[95] and the progression of their degenerative processes has been well documented and evaluated with a grading scale used in humans to characterize disc degeneration.[96] The human cervical spine and the canine cervical spine also possesses similar kinematic motion patterns. Although the kinematics of the canine spine remains an area of continuous research, coupled lateral bending and axial rotation has been reported in the cervical spine albeit in larger magnitudes of range of

motion than in humans.[97] Furthermore, the authors in said study found that axial rotation increased in lower levels of the cervical spine (C5/C6), but the flexion-extension decreased from that of levels closer to cranial (C2/C3). Notably, variations between small and large dog breeds have been seen, where the highest range of flexion/extension motion in small dogs is observed in the caudal levels of the cervical spine as in humans.[98] Moreover, medical and surgical treatments for cervical disc degeneration in canines are analogous to those used in human cervical radiculopathy such as the anterior cervical discectomy and fusion technique.[99] Due to the gradual loss of notochord cells upon skeletal maturity in chondrodystrophic breeds such as beagles, the cervical spine of small canines proves an ideal animal model for testing tissue-engineered implants without the natural regenerative mechanisms that could confound a total disc replacement *in vivo* study.[100]

Research Objectives

The focus of this dissertation was to develop canine disc-sized composite TE-IVDs made of cell-seeded alginate and collagen scaffolds that mimic the native IVD structure *in vitro*, evaluate the canine cervical spine as a preclinical *in vivo* model of total disc replacement, and investigate strategies to promote a stable implantation of scaled-up TE-IVD constructs *ex-vivo* and *in vitro*. This work represents the first study to translate whole engineered IVD implants from a small animal model to a large preclinical *in vivo* model, with a long-term goal of providing a biological alternative to the current surgical standard of treatment for fully degenerated IVDs. The overriding hypotheses were that: 1) TE-IVDs will integrate the canine cervical disc space and maintain disc height, physiological hydration, and tissue viability upon implantation *in vivo* (Chapter 2, Appendix A); 2) a combined treatment approach of implanted TE-IVDs with resorbable PLGA plating will improve the stiffness of canine cervical spine motion segments *ex vivo* and prevent the extrusion of TE-IVD constructs from the disc space

(Chapter 3); and 3) interactions in high-density collagen scaffolds seeded with hMSCs will improve baseline AF properties in TE-IVDs in terms of tissue structure and composition (Chapter 4).

Specific Aim 1 (Chapter 2)

Produce canine-sized TE-IVD and examine the efficacy of replacing canine cervical discs by investigating stability of surgical conditions, and tissue integration, disc hydration and height after 4 and 16 weeks of implantation.

This study was focused on two parts: scaling-up the fabrication of TE-IVDs from a rodent-sized disc to an anatomically relevant model of a canine cervical IVD and evaluating the efficacy of the canine cervical spine as a preclinical animal model of total disc replacement with TE-IVDs. TE-IVDs were fabricated following anatomical dimensions of canine cervical NPs in disc spaces between levels 3-4 and 4-5 using newly designed 3D printed molds. Injection-molded alginate NP cores seeded with canine NP cells were surrounded by type I collagen AF laden with canine AF cells to create TE-IVDs. After identifying the appropriate formulation of collagen layers and NP size, TE-IVDs with optimal cell content were cultured for 2 weeks and harvested for *in vivo* implantation in canine cervical spines. Skeletally mature beagles received total discectomy at levels between C3/C4 and C6/C7 and subsequently were either treated with a TE-IVD or left with tissues removed only. Despite some subjects facing displacement of the TE-IVDs, the stably implanted TE-IVDs exhibit greater disc height and NP hydration than untreated disc spaces post-operatively during 4 and 16 weeks. Data also demonstrated that for up to 16 weeks, TE-IVDs integrated to host tissue in the cervical disc space without any signs of immune reaction and retained viable cells with relevant morphological features that produced native-typical ECM. This study was the first to examine the efficacy of total disc replacement of cervical spine with TE-IVDs

in a large preclinical model and provided insights about the challenges to expect when translating into human-sized disc replacement.

Specific Aim 2 (Chapter 3)

Assess the effects of a resorbable plating system on the stiffness of canine cervical motion segments and *ex vivo* stability of implanted TE-IVDs subjected to uniaxial compression under a combined treatment approach.

Stable implantation was favored by composite TE-IVDs in the canine cervical spine model *in vivo* by maintaining promising cell viability and tissue integration into host tissue; however, significant implant displacement occurred at multiple spinal levels. This study was focused on a combined treatment approach for TE-IVD implantation with a stabilizing PLGA plating system, to enhance motion segment compressive stiffness and improve implant retention in the disc space. Canine motion segments were assessed as intact controls, after discectomy, with an implanted TE-IVD only, and with a TE-IVD combined with an attached resorbable plate. Projections of 2D-displacements were measured using digital image correlation techniques on video recordings taken during uniaxial testing. Plated segments with implanted discs partially restored more than 25% of the control motion segment stiffness and outperformed un-plated motion segments. Plating combined with TE-IVDs also fully restored endplate separation and prevented implant extrusion from the disc space at 50% compressive strain. Significant differences were observed between the level of implant retention in levels C3/4 and C5/6. Collectively, these findings demonstrated that resorbable plating assisted in the stabilization of motion segments with implanted TE-IVDs, while allowing shared loads with the implants. This suggested that TE-IVD implantation with assisted resorbable plating could remain stable in the disc space while integration with host tissues, ECM maturation, and optimal restoration of spine mechanics occurs.

Specific Aim 3 (Chapter 4)

Investigate the potential of high-density collagen gels as annulus fibrosus scaffolds for TE-IVDs and study the effects of initial seeding density of hMSCs on disc structure and composition of cell-seeded constructs

The development of whole engineered IVD constructs with *in vitro* stiffness and composition properties that closely resemble those of a native IVD before *in vivo* implantation has proven challenging for composite TE-IVDs. The combined effects of initial high-density collagen AF at 10 and 20 mg/mL and initial human MSCs seeding density between 2 and 20 million cells/mL at the AF were measured mechanically, histologically, and morphologically on composite TE-IVDs. Structural changes in disc morphology and apparent AF densification examined over the culture period revealed that increasing seeding density and apparent AF density, as a measure of structural alignment, were directly correlated with the compressive properties of the TE-IVDs. Furthermore, in 10 mg/mL collagen AF discs, increased seeding density 5-10 times that of the baseline cell content increased their stiffness in a dose-dependent manner. The same effects could not be appreciated in 20 mg/mL collagen AF discs. Also, the phenotype of hMSCs appeared elongated and AF-like in the 10 mg/mL group only with the highest initial cell content. Alterations in collagen AF structure driven by hMSCs remodeling was best identified on moderately-dense collagen scaffolds than either the baseline or the highest density one. Although previous work had achieved native-like structure in composite TE-IVDs, the interplay between cell content and high-density collagen for TE-IVDs had not been studied, despite the comparable thickness of the native AF to other dense fibrous tissues. These data support the potential of employing modulation of hMSCs seeding density in TE-IVDs with dense AF/collagen matrices to achieve a controllable tissue composition and structure of the remodeled AF scaffold.

REFERENCES

1. Pattappa G, Li Z, Peroglio M, Wismer N, Alini M, Grad S. Diversity of intervertebral disc cells: phenotype and function. J Anat. 2012; 221: 480-96.

2. Werne S. Studies in spontaneous atlas dislocation. Acta Orthop Scand. 1957; Suppl 23:1–150.

3. White AA, Panjabi MM (1978) Clinical Biomechanics of the Spine. Lippincott Williams and Wilkins, Philadelphia.

4. Wilke HJ, Krischak ST, Wenger KH, Claes LE. Load-displacement properties of the thoracolumbar calf spine: experimental results and comparison to known human data. 1997. Eur Spine J. 6:129-31.

5. Sivan SS, Hayes AJ, Wachtel E, Caterson B, Merkher Y, Maroudas A, Brown S, Roberts S. Biochemical composition and turnover of the extracellular matrix of the normal and degenerate intervertebral disc. Eur Spine J. 2014; 23 (Suppl 3): S344-S353.

6. Eyre DR, Matsui Y, Wu JJ. Collagen polymorphisms of the intervertebral disc. Biochem Soc Trans. 2002; 30: 844-8.

7. Roughley PJ. Biology of intervertebral disc aging and degeneration: involvement of the extracellular matrix. Spine. 2004; 29(23): 2691-9.

8. Whatley BR, Wen X. Intervertebral disc (IVD): structure, degeneration, repair and regeneration. Mat Sci Eng C. 2012; 32: 61-77.

9. Muller J, Benz K, Ahlers M, Gaissmaier C, Mollenhauer J. Hypoxic conditions during expansion culture prime human mesenchymal stromal precursor cells for chondrogenic differentiation in three-dimensional cultures. Cell Transplantation. 2011; 20: 1589-1602.

10. Colombier P, Clouet J, Hamel O, Lescaudron L, Guicheux J. The lumbar intervertebral disc: from embryonic development to degeneration. Joint Bone Spine. 2014; 81(2): 125-9.

11. Cook GMW, Lewis KE, Keynes RJ. Segmentation: spinal cord segmentation and A-P somite patterning. Encyclop of Neuroscience.

12. Christ B, Huang R, Wilting J. From somites to vertebral column. Ann Anat. 1992; 174: 23-32.

13. Hayes AJ, Isaacs MD, Hughes C, et al. Collagen fibrillogenesis in the development of the annulus fibrosus of the intervertebral disc. Eur Cell Mater. 2011; 22: 226-41.

14. Lyons G, Eisenstein SM, Sweet MB. Biochemical changes in intervertebral disc degeneration. Biochim Biophys Acta. 1981; 673(4): 443-53.

15. Perie D, Maclean JJ, Owen JP, Iatridis JC. Correlating material properties with tissue composition in enzymatically digested bovine annulus fibrosus and nucleus pulposus tissue. Ann Biomed Eng 34: 769-77.

16. Wilke HJ, Neef P, Caimi M, Hoogland T, Claes LE. New in vivo measurements of pressures in the intervertebral disc in daily life. Spine (Phila. Pa. 1976). 1999; 24: 755-62.

17. Antoniou J, Steffen T, Nelson F, Winterbottom N, Hollander AP, Poole RA, Aebi M, Alini M. The human lumbar intervertebral disc: evidence for changes in the biosynthesis and denaturation of the extracellular matrix with growth, maturation, ageing, and degeneration. J Clin Invest. 1996; 98: 996-1003.

18. Oxland, T. A history of spine biomechanics: Focus on 20th century progress. Unfallchirurg. 2015; 118(Suppl 1): 80.

19. Adams MA, Hutton WC. The effect of posture on the role of the apophyseal joints in resisting intervertebral compressive forces. J Bone Joint Surg Br. 1980; 62(3): 358-62.

20. Newell N, Little JP, Christou A, Adams MA, Adam CJ, Masouros SD. Biomechanics of the human intervertebral disc: A review of testing techniques and results. J Mech Behav Biomed Mats. 2017; 69: 420-34.

21. Andersson GBJ. Epidemiological features of chronic low-back pain. Lancet 1999; 354: 581-85.

22. Hart LG, Deyo RA, Cherkin DC. Physician office visits for low back pain. Spine 1995; 20: 11-19.

23. Okada E, Matsumoto M, Ichihara D, Chiba K, Toyama Y, Fujiwara H, et al. Aging of the cervical spine in healthy volunteers: a 10-year longitudinal magnetic resonance imaging study. Spine 2009; 34: 706-12.

24. Arana E, Marti-Bonmatí L, Mollá E, Costa S. Upper thoracic spine disc degeneration in patients with cervical pain. Skeletal Radiol 2004; 33: 29-33.

25. Todd AG. Cervical spine: degenerative conditions. Curr Rev Musculoskelet Med 2011; 4: 168–174.

26. Ehrlich GE. Low back pain. Bull World Health Organ. 2003; 81(9): 671–676.

27. Menezes Costa LC, Maher CG, Hancock MJ, Herbert RD, Refshauge KM, Henschke N. Prognosis for patients with chronic low back pain: inception cohort study. BMJ 2009; 339: b3829.

28. Urban JPG and Roberts S. Degeneration of the intervertebral disc. Arthritis Res Ther 2003; 5(3): 120-130.

29. Luoma K, Riihimaki H, Luukkonen R, Raininko R, Viikari-Juntura E, Lamminen A. Low back pain in relation to lumbar disc degeneration. Spine 2000; 25(4): 487-92.

30. Teraguchi M, Yoshimura N, Hashizume H, Muraki S, Yamada H, Minamide A, Oka H, Ishimoto Y, Nagata K, Kagotani R, Takiguchi N, Akune T, Kawaguchi H, Nakamura K, Yoshida M. Prevalence and distribution of intervertebral disc degeneration over the entire spine in a population-based cohort: the Wakayama Spine Study. Osteoarthritis and Cartilage 2013; 22: 104-110.

31. Guiot BH, Fessler RG. Molecular biology of degenerative disc disease. Neurosurgery. 2000; 47(5): 1034-40.

32. Cowell HR, Hall JN, MacEwen GD. Genetic aspects of idiopathic scoliosis: A Nicholas Andry Award essay, 1970. Clin Orthop. 1972; 86: 121-31.

33. Postacchini F, Lami R, Pugliese O Familial predisposition to discogenic low-back pain: An epidemiologic and immunogenetic study. Spine 13: 1403–1406, 1988.

34. Matsui H, Terahata N, Tsuji H, Hirano N, Naruse Y. Familial predisposition and clustering for juvenile lumbar disc herniation. Spine. 1992; 17: 1323-8.

35. Varlotta GP, Brown MD, Kelsey JL, Golden AL. Familial predisposition for herniation of a lumbar disc in patients who are less than twenty-one years old. J Bone Joint Surg Am. 1991; 73A: 124-8.

36. Natarajan RN, Ke JH, Andersson GB. A model to study the disc degeneration process. Spine. 1994; 19: 259-65.

37. Williams FMK, Sambrook PN. Neck and back pain and intervertebral disc degeneration: Role of occupational factors. Best Practice & Research Clinical Rheumatology. 2011; 25(1): 69-79.

38. Sambrook PN, MacGregor AJ, Spector TD. Genetic influences on cervical and lumbar disc degeneration: a magnetic resonance imaging study in twins. Arthritis Rheum. 1999; 42: 366-72.

39. Kjaer P, Laboeuf-Yde C, Korsholm L, Sorensen JS, Bendix T. Magnetic resonance imaging and low back pain in adults: a diagnostic imaging study of 40-year-old men and women. Spine 2005; 30: 1173-80.

40. Hassett G, Hart D, Manek N, Doyle DV, Spector TD. Risk factors for progression of lumbar spine disc degeneration: the Chingford Study. Arthritis Rheum. 2003; 48: 3112-7.

41. Wolfer LR, Derby R, Lee JE, Lee SH. Systematic review of lumbar provocation discography in asymptomatic subjects with a meta-analysis of false-positive rates. Pain Physician 2008;11(4):513–538.

42. Carragee EJ, Alamin TF. Discography. a review. Spine J 2001;1(5):364–372.

43. M. T. Modic, T. J. Masaryk, J. S. Ross, and J. R. Carter, "Imaging of degenerative disk disease," Radiology, vol. 168, no. 1, pp. 177-86, 1988.

44. Hasz MW. Diagnostic testing for degenerative disc disease. Adv Orthop. 2012; 2012:413913.

45. Lotz JC, Haughton V, Boden SD, An HS, Kang JD, Masuda K, Freemont A, Berven S, Sengupta DK, Tanenbaum L, Maurer P, Ranganathan A, Alavi A, Marinelli NL. New treatments and imaging strategies in degenerative disease of the intervertebral disks. Radiology. 2012; 264(1): 6-19.

46. Lotz JC, Weidenbaum M, Foster RJ, Best BA, et al. Correlating magnetic resonance imaging with the biochemical content of the normal human intervertebral disc. J Orthop Res. 1992; 10(4): 552-61.

47. Tertti M, Paajanen H, Laato M, Aho H, Komu M, Kormano M. Disc degeneration in magnetic resonance imaging. A comparative biochemical, histologic, and radiologic study in cadaver spines. Spine (Phila Pa 1976). 1991; 16(6): 629-34.

48. Marinelli NL, Haughton VM, Muñoz A, Anderson PA. T2 relaxation times of intervertebral disc tissue correlated with water content and proteoglycan content. Spine (Phila Pa 1976). 2009; 34(5): 520-4.

49. Nightingale T, MacKay A, Pearce RH, Whittall KP, Flak B. A model of unloaded human intervertebral disk based on NMR relaxation. Magn Reson Med. 2000; 43(1): 34-44.

50. Pfirrmann CW, Metzdorf A, Zanetti M, Hodler J, Boos N. Magnetic resonance classification of lumbar intervertebral disc degeneration. Spine (Phila Pa 1976). 2001; 26(17): 1873-8.

51. Brodke DS, Ritter SM. Non-surgical management of low back pain and lumbar disk degeneration. Instr Course Lect. 2005; 54: 279-86.

52. Sugawara T, Itoh Y, Hirano Y, Higashiyama N, Mizoi K. Long term outcome and adjacent disc degeneration after anterior cervical discectomy and fusion with titanium cylindrical cages. Acta Neurochir (Wien) 2009; 151(4): 303-9.

53. Maldonado CV, Paz RD, Martin CB. Adjacent-level degeneration after cervical disc arthroplasty versus fusion. Eur Spine J 2011;20 (Suppl 3):403-7.

54. Harrop JS, Youssef JA, Maltenfort M, Vorwald P, Jabbour P, Bono CM, Goldfarb N, Vaccaro AR, Hilibrand AS. Lumbar adjacent segment degeneration and disease after arthrodesis and total disc arthroplasty. Spine (Phila Pa 1976). 2008; 33: 1701.

55. Beaurain J, Bernard P, Dufour T, Fuentes JM, Hovorka I, Huppert J, Steib JP, Vital JM, Aubourg L, Vila T. Intermediate clinical and radiological results of cervical TDR (Mobi-C) with up to 2 years of follow-up. Eur Spine J. 2009; 18: 841.

56. Kurtz, S.M., van Ooij, A., Ross, R., de Waal Malefijt, J., Peloza, J., Ciccarelli, L., and Villarraga, M.L. Polyethylene wear and rim fracture in total disc arthroplasty. Spine J 7, 12, 2007.

57. van Ooij, A., Kurtz, S.M., Stessels, F., Noten, H., and van Rhijn, L. Polyethylene wear debris and long-term clinical failure of the Charite disc prosthesis: a study of 4 patients. Spine (Phila Pa 1976) 32, 223, 2007.

58. Kelly MP, Mok JM, Frisch RF, Tay BK. Adjacent segment motion after anterior cervical discectomy and fusion versus Prodisc-c cervical total disk arthroplasty: analysis from a randomized, controlled trial. Spine (Phila Pa 1976). 2011; 36(15): 1171-1179.

59. Bozkus H, Senoglu M, Baek S, Sawa AG, Ozer AF, Sonntag VK, Crawford NR. Dynamic lumbar pedicle screw-rod stabilization: in vitro biomechanical comparison with standard rigid pedicle screw-rod stabilization. Journal of neurosurgery. 12, 183.

60. Mandigo CE, Sampath P, Kaiser MG. Posterior dynamic stabilization of the lumbar spine: pedicle-based stabilization with the AccuFlex rod system. Neurosurgical focus. 2007; 22, E9.

61. Moriguchi Y, Alimi M, Khair T, Manolarakis G, Berlin C, Bonassar LJ, Hartl R. Biological treatment approaches for degenerative disk disease: A literature review of in vivo animal and clinical data. 2016; 6(5): 497-518.

62. Pennicooke B, Moriguchi Y, Hussain I, Bonassar LJ, Hartl R. Biological treatment approaches for degenerative disc disease: A review of clinical trials and future directions. Cureus. 2016; 8(11): e892.

63. An HS, Takegami K, Kamada H, et al. Intradiscal administration of osteogenic protein-1 increases intervertebral disc height and proteoglycan content in the nucleus pulposus in normal adolescent rabbits. Spine (Phila Pa 1976). 2005; 30(1): 25-31.

64. Miyamoto K, Masuda K, Kim JG, et al. Intradiscal injections of osteogenic protein-1 restore the viscoelastic properties of degenerated intervertebral discs. Spine J. 2006; 6(6): 692-703.

65. Nishida K, Kang JD, Gilbertson LG, et al. Modulation of the biologic activity of the rabbit intervertebral disc by gene therapy: an in vivo study of adenovirus-mediated transfer of the human transforming growth factor beta 1 encoding gene. Spine (Phila Pa 1976). 1999; 24(23): 2419-2425.

66. Ganey T, Libera J, Moos V, et al. Disc chondrocyte transplantation in a canine model: a treatment for degenerated or damaged intervertebral disc. Spine (Phila Pa 1976). 2003; 28(23): 2609-2620.

67. Brittberg M, Lindahl A, Nilsson A, Ohlsson C, Isaksson O, Peterson L. Treatment of deep cartilage defects in the knee with autologous chondrocyte transplantation. N Engl J Med. 1994; 331(14): 889-895.

68. Feng G, Zhao X, Liu H, et al. Transplantation of mesenchymal stem cells and nucleus pulposus cells in a degenerative disc model in rabbits: a comparison of 2 cell types as potential candidates for disc regeneration. J Neurosurg Spine 2011;14(3):322-329.

69. Sheikh H, Zakharian K, De La Torre RP, et al. In vivo intervertebral disc regeneration using stem cell-derived chondroprogenitors. J Neurosurg Spine. 2009; 10(3): 265-272.

70. Langer R, Vacanti JP. Tissue engineering. Science 1993; 260(5110): 920-926.

71. Masuda K and Lotz JC. New challenges for intervertebral disc treatment using regenerative medicine. Tissue Eng Part B Rev. 2010; 16(1): 147-158.

72. Thomas J, Lowman A, Marcolongo M. Novel associated hydrogels for nucleus pulposus replacement. J Biomed Mater Res A. 2003; 67(4):1329-37.

73. Hu J, Chen B, Guo F, Du J, Gu P, Lin X, Yang W, Zhang H, Lu M, Huang Y, Xu G. Injectable silk fibroin/polyurethane composite hydrogel for nucleus pulposus replacement. J Mater Sci Mater Med. 2012;23(3):711–22.

74. Boyd LM, Carter AJ. Injectable biomaterials and vertebral endplate treatment for repair and regeneration of the intervertebral disc. Eur Spine J. 2006 Aug; 15 Suppl 3: S414-21.

75. Chang G, Kim HJ, Kaplan D, Vunjak-Novakovic G, Kandel RA. Porous silk scaffolds can be used for tissue engineering annulus fibrosus. Eur Spine J. 2007; 16(11):1848–57.

76. Nerurkar NL, Baker BM, Sen S, Wible EE, Elliott DM, Mauck RL. Nanofibrous biologic laminates replicate the form and function of the annulus fibrosus. Nature Materials. 2009; 8(12): 986–92.

77. Grunert P, Borde BH, Hudson KD, Macielak MR, Bonassar LJ, Härtl R. Annular repair using high-density collagen gel: a rat-tail in vivo model. Spine (Phila Pa 1976). 2014; 39(3):198-206.

78. Guterl CC, Torre OM, Purmessur D, Dave K, Likhitpanichkul M, Hecht AC, Nicoll SB, Iatridis JC. Characterization of mechanics and cytocompatibility of fibrin-genipin annulus fibrosus sealant with the addition of cell adhesion molecules. Tissue Eng. Part A. 2014;20(17–18):2536–45.

79. Mizuno H, Roy AK, Vacanti CA, Kojima K, Ueda M, Bonassar LJ. 2004. Tissue-engineered composites of anulus fibrosus and nucleus pulposus for intervertebral disc replacement. Spine (Phila Pa 1976). 29(12): 1290-7.

80. Bowles RD, Williams RM, Zipfel WR, Bonassar LJ. Self-assembly of aligned tissue-engineered annulus fibrosus and intervertebral disc composite via collagen gel contraction. Tissue Eng Part A. 2010; 16 (4):1339–48.

81. Nerurkar NL, Sen S, Huang AH, Elliott DM, Mauck RL. Engineered disc-like angle-ply structures for intervertebral disc replacement. Spine. 2010; 35(8):867–73.

82. Nesti LJ, Li WJ, Shanti RM, Jiang YJ, Jackson W, Freedman BA, et al. Intervertebral disc tissue engineering using a novel hyaluronic acid-nanofibrous scaffold (HANFS) amalgam. Tissue Eng Part A. 2008; 14(9):1527–37.

83. Abbushi A, Endres M, Cabraja M, Kroppenstedt SN, Thomale UW, Sittinger M, et al. Regeneration of intervertebral disc tissue by resorbable cell-free polyglycolic acid-based implants in a rabbit model of disc degeneration. Spine. 2008; 33(14):1527–32.

84. Huang B, Zhuang Y, Li CQ, Liu LT, Zhou Y. Regeneration of the intervertebral disc with nucleus pulposus cell-seeded collagen II/hyaluronan/chondroitin-6-sulfate tri-copolymer constructs in a rabbit disc degeneration model. Spine. 2011; 36(26):2252–9.

85. Park SH, Gil ES, Cho H, Mandal BB, Tien LW, Min BH, Kaplan DL. Intervertebral disk tissue engineering using biphasic silk composite scaffolds. Tissue Eng Part A. 2012; 18(5-6): 447-58.

86. Lazebnik M, Singh M, Glatt P, Friis LA, Berkland CJ, Detamore MS. Biomimetic method for combining the nucleus pulposus and annulus fibrosus for intervertebral disc tissue engineering. J Tissue Eng Regen Med. 2011; 5(8): e179-87.

87. Zhuang Y, Huang B, Li CQ, Liu LT, Pan Y, Zheng WJ, Luo G, Zhou Y. Construction of tissue-engineered composite intervertebral disc and preliminary morphological and biochemical evaluation. Biochem Biophys Res Commun. 2011; 407(2): 327-32.

88. Martin JT, Milby AH, Chiaro JA, Kim DH, Hebela NM, Smith LJ, et al. Translation of an engineered nanofibrous disc-like angle-ply structure for intervertebral disc replacement in a small animal model. Acta Biomater. 2014; 10(6):2473–81.

89. Chik TK, Chooi WH, Li YY, Ho FC, Cheng HW, Choy TH, Sze KY, Luk KK, Cheung KM, Chan BP. Bioengineering a multicomponent spinal motion segment construct– a 3D model for complex tissue engineering. Adv Healthc Mater. 2015; 4(1): 99–112.

90. Sheng SR, Xu HZ, Wang YL, Zhu QA, Mao FM, et al. Comparison of cervical spine anatomy in calves, pigs and humans. PLoS One. 2016; 11(2): e0148610.

91. Thompson K, Moore S, Tang S, Wiet M, Purmessur D. The chondrodystrophic dog-A clinically relevant intermediate-sized animal model of the study of intervertebral disc-associated spinal pain. J Orthop Res Spine. 2018; 1: e1011.

92. Frick, S.L., Hanley, E.N., Jr., Meyer, R.A., Jr., Ramp, W.K., and Chapman, T.M. Lumbar intervertebral disc transfer. A canine study. Spine (Phila Pa 1976). 1994; 19: 1826.

93. Katsuura, A., and Hukuda, S. Experimental study of intervertebral disc allografting in the dog. Spine (Phila Pa 1976) 1994; 19: 2426.

94. Matsuzaki, H., Wakabayashi, K., Ishihara, K., Ishikawa, H., and Ohkawa, A. Allografting intervertebral discs in dogs: a possible clinical application. Spine (Phila Pa 1976). 1996; 21: 178.

95. Bergknut N, Rutges JP, Kranenburg HJ, Smolders LA, Hagman R, Smidt HJ, et al. The dog as an animal model for intervertebral disc degeneration? Spine (Phila Pa 1976). 2012; 37(5):351–8.

96. Thompson JP, Pearce RH, Schechter MT, et al. Preliminary evaluation of a scheme for grading the gross morphology of the human intervertebral disc. Spine. 1990; 15: 411 – 5.

97. Johnson JA, da Costa RC, Bhattacharya S, Goel V, and Allen MJ. Kinematic motion patterns of the cranial and caudal canine cervical spine. Vet Surg. 2011; 40: 720-7.

98. Breit S, Kunzel W: Shape and orientation of articular facets of cervical vertebrae (C3–C7) in dogs denoting axial rotational ability: an osteological study. Eur J Morphol 2002; 40:43–51.

99. Cole TC, Burkhardt D, Ghosh P, Ryan M, Taylor T. Effects of spinal fusion on the proteoglycans of the canine intervertebral disc. J Orthop Res. 1985; 3(3):277–91.

100. Hunter CJ, Matyas JR, Duncan NA. Cytomorphology of notochordal and chondrocytic cells from the nucleus pulposus: a species comparison. J Anat. 2004; 205(5):357–62.

CHAPTER 2

Total disc replacement using tissue-engineered intervertebral discs in the canine cervical spine[1]

Abstract

The most common reason that adults in the United States see their physician is lower back or neck pain secondary to degenerative disc disease. To date, approaches to treat degenerative disc disease are confined to purely mechanical devices designed to either eliminate or enable flexibility of the diseased motion segment. Tissue engineered intervertebral discs (TE-IVDs) have been proposed as an alternative approach and have shown promise in replacing native IVD in the rodent tail spine. Here we demonstrate the efficacy of our TE-IVDs in the canine cervical spine. TE-IVD components were constructed using adult canine annulus fibrosus (AF) and nucleus pulposus (NP) cells seeded into collagen and alginate hydrogels, respectively. Seeded gels were formed into a single disc unit using molds designed from the geometry of the canine spine. Skeletally mature beagles underwent discectomy with whole IVD resection at levels between C3/4 and C6/7 and were then divided into two groups that received only discectomy or discectomy followed by implantation of TE-IVD. Stably implanted TE-IVDs demonstrated significant retention of disc height and physiological hydration compared to discectomy control. Both 4-week and 16-week histological assessments demonstrated chondrocytic cells surrounded by proteoglycan-rich matrices in the NP and by fibrocartilaginous matrices in the AF portions of implanted TE-IVDs. Integration into host tissue was confirmed over 16 weeks without any signs of immune reaction. Despite the significant biomechanical demands of the beagle cervical spine, our stably

[1] This chapter has already been published: Moriguchi Y, Mojica-Santiago J, Grunert P, Pennicooke B, Berlin C, Khair T, Navarro-Ramirez R, Ricart Arbona RJ, Nguyen J, Härtl R, Bonassar LJ. (2017) Total disc replacement using tissue-engineered intervertebral discs in the canine cervical spine. PLoS ONE 12(10): e0185716.

implanted TE-IVDs maintained their position, structure and hydration as well as disc height over 16 weeks *in vivo*.

Introduction

Degenerative disc disease (DDD) is a prevalent clinical condition occurring in 40% of individuals younger than 30 and more than 90% of individuals over the age of 50,[1] which can lead to nerve compression and chronic back pain. Though pharmacological and physiotherapeutic treatments relieve early symptoms,[2] surgical intervention is required in over half a million patients in the US annually.[3] The current surgical standard to treat DDD involves the removal of the entire IVD followed by fusion of the adjacent vertebrae or interposition of a mechanical disc prosthesis to preserve motion. However, fusion brings risks of possible pseudarthrosis and adjacent segment disease, resulting in a higher rate of reoperation in these patients.[4,5] Prosthetic total disc replacement devices, developed to maintain segmental mobility, are an alternative to fusion surgery. However, recent studies have shown that total disc replacement also leads to adjacent segment disease.[4,6] The main concern with current treatment options for DDD –conservative or surgical– is that they fail to treat the underlying etiology and the degenerated disc remains unrepaired.

To overcome the limitations of available treatments and enhance patient care outcome, biological approaches to IVD repair or regeneration are of increasing interest. The first attempt to reconstruct a whole disc segment with biological implants now dates back approximately 10 years.[7] The feasibility of allogenic disc transplantation was demonstrated in clinical trials with favorable outcomes over a five-year follow-up. Despite the challenge of widespread deployment of this strategy due to limited implant availability and potential disease transmission, the results obtained were encouraging. Since Langer and Vacanti pioneered the multidisciplinary field of tissue engineering in 1993,[8] much effort has been directed towards the construction of functional substitutes

for damaged disc tissues, especially for advanced stages of disc degeneration with extensive loss of extracellular matrix and functional structure. Numerous studies have assessed tissue-engineered whole disc constructs *in vitro*, but few have looked at these constructs *in vivo*. Mizuno et al. first developed the tissue engineered disc composed of NP cells seeded into an alginate hydrogel surrounded by a polyglycolic acid and polylactic acid scaffold seeded with AF cells. This *de novo* construct was implanted in the subcutaneous space of the dorsum of athymic mice, demonstrating the feasibility of creating a composite IVD with both AF and NP tissues.[9,10] Several other studies have reported the development of composite tissue engineered IVD constructs, using combinations of materials such as demineralized bone matrix gelatin with type II collagen, hyaluronate and chondroitin-6-sulfate (C2/HyA-CS),[11] electrospun polycaprolactone and agarose;[12] and self-assembled NP cells seeded onto calcium polyphosphate.[13] We have shown previously the development of a tissue-engineered IVD composed of an inner NP cell-laden alginate core surrounded by an outer AF cell-laden collagen layer (Fig 1A).[14,15] We demonstrated the *in vivo* efficacy of this model at maintaining disc height and physiological hydration, when implanted in the rat tail for up to nine months.[16-20]

Although these results are promising, there are several differences between the rat tail model and the human cervical spine that pose significant challenges for clinical translation.[21-23] The rat tail spine has a significantly different loading profile, and TE-IVDs will be exposed to higher axial loads when implanted into a human disc space. There are also anatomical differences, as the rat tail vertebrae lack a spinal canal containing nervous tissue as well as posterior bone and joint elements. To bring this innovation toward clinical application, we tested the feasibility of total disc replacement using TE-IVDs in a beagle cervical spine model. We determined surgical conditions

that promote stable implantation and investigated the ability of TE-IVDs to maintain disc height, physiological hydration, and tissue viability in the present study.

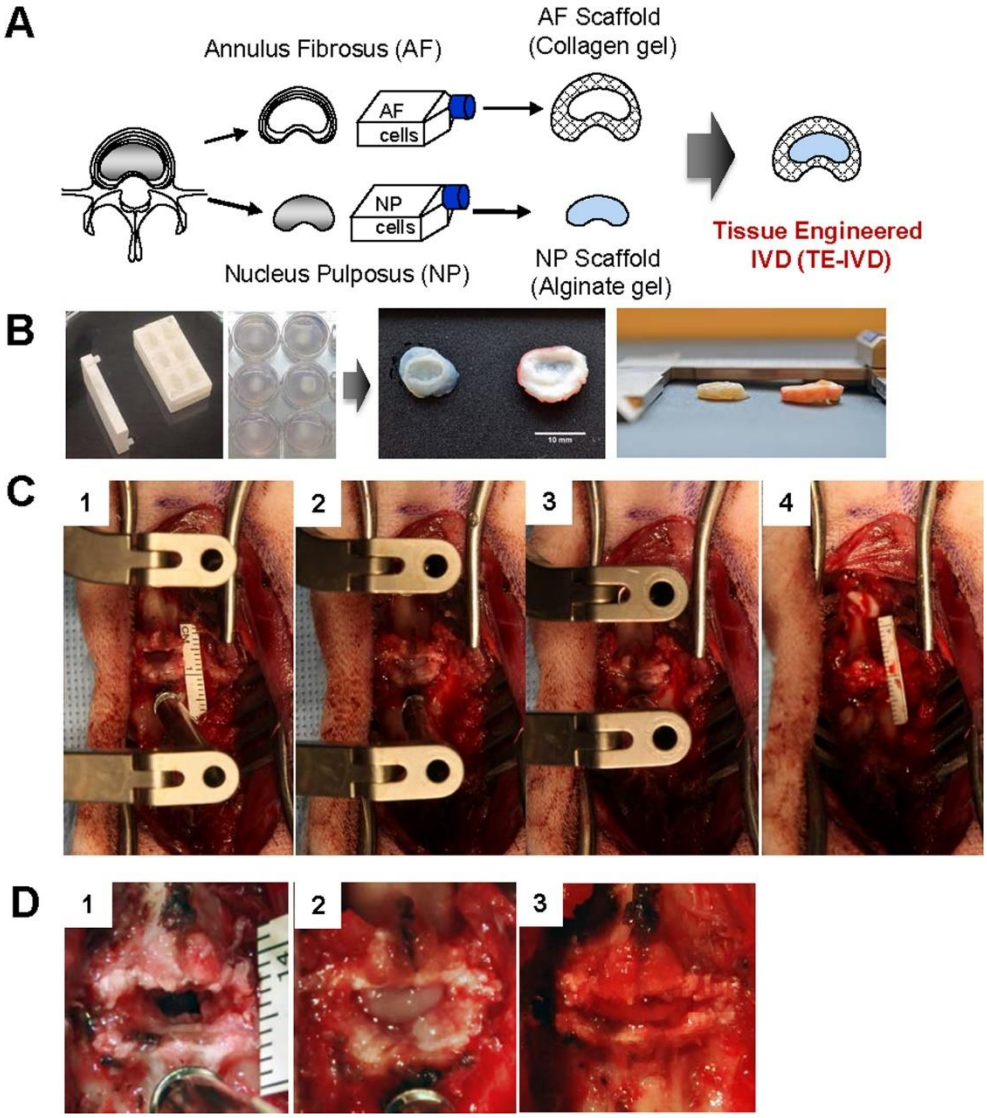

Figure 2.1. A) Schematic picture of disc tissue engineering. NP and AF cells were separately isolated from canine lumbar spine and cultured *in vitro*. Cultured NP and AF cells were seeded in alginate and collagen gels, respectively, and subsequently both composites were combined into a TE-IVD. B) Photographs of TE-IVD fabrication. Cultured NP cells were injected into a predesigned mold and encircled with two layers of AF cell-laden collagen gels. These AF layers circumferentially contract over cultivation time until they reach a size similar to native IVD as observed in top view and side view. C) Total discectomy and TE-IVD implantation were performed anteriorly under segmental distraction. D) Upon distraction release, stably transplanted TE-IVDs remained in place and were secured in the disc space.

Results

In vitro generation of tissue-engineered intervertebral discs (TE-IVDs)

We isolated nucleus pulpous (NP) cells and annulus fibrosus (AF) cells from the intervertebral discs from the cervical spines of skeletally mature beagles. These cells were separately cultured for 2–3 weeks and subsequently seeded in an alginate scaffold for NP and collagen for AF (Fig 2.1A and 2.1B). For TE-IVD construction, NP cell-laden alginate (25×10^6 NP cells/mL) was injected into a predesigned mold and encircled with two layers of AF cell-laden collagen gels (1×10^6 AF cells/mL). This 3D construct of TE-IVD demonstrated the contraction at the AF part during further two-week cultivation.

Implanted TE-IVD maintained its position without neurological complication

Cervical discectomy was performed in vivo anteriorly as in human surgeries. The annulus fibrosus (AF) and nucleus pulposus (NP) were extensively resected under the microscope (Fig 2.1C and 2.1D). To determine a condition that promotes implant stability, we varied the surgical level operated on and presence or absence of ligament resection. With the lateral dimension over 80% of the disc width (most of the AF and all the NP portion), the entire antero-posterior depth of the disc was resected, confirming exposure of the posterior longitudinal ligament at the bottom (PLL). The PLL was resected in four dogs, but not in the others (to help determine favorable implant conditions, as aforementioned). Subsequently, all implants were successfully inserted into the discectomized segment under segmental distraction using a CASPAR distraction system. Upon distraction release, half of the TE-IVDs remained stable (n = 6), while the other half (n = 6) were considered displaced based on the extent of anterior protrusion (The summaries of implant stability immediately after removal of distraction are summarized in Tables 2.1–2.3). PLL resection did not have a significant effect on

implant stability ($p = 0.072$). None of the dogs demonstrated segmental instability of the experimental level and none of the TE-IVDs demonstrated a propensity of posterior displacement intraoperatively. All animals were neurologically normal immediately after surgery and remained so for the duration of the experiments, with neurological assessments for abnormalities in gait, wheelbarrow assessment, limb hopping, and plantar reflex.

All animals were imaged postoperatively using X-ray and MRI to monitor the implanted TE-IVD and screen for any host reaction (Fig 2.2). None of the dogs had neurological symptoms or adverse effects due to TE-IVD implantation, despite being free of external fixation or orthosis immediately after surgery. X-rays demonstrated no significant pathological abnormality observed in the vertebrae or signs of spinal malalignment such as spondylolisthesis among the groups. In MRIs, proximal adjacent discs served as a healthy control. The solely discectomized segments demonstrated a collapsed black disc on postoperative images and paucity of reparative tissues in the disc histology, suggesting that our discectomy procedure induced an incurable lesion by resecting the vast majority of the disc. In the TE-IVD implanted groups, location of the implant was confirmed by sagittal and axial MRIs. Stably implanted TE-IVDs demonstrated hyperintensity in T2-weighed images at 4 weeks and maintained their position in the disc space with relatively decreased T2 intensity at 16 weeks. This loss in T2 signal is likely associated with a decrease in tissue hydration, and these data were consistent with the Safranin-O histology for proteoglycans, which are known to attract water into these tissues. Such histology also indicated a continuous connection between newly developed tissue and the surrounding vertebral body. This indicated that the implanted TE-IVDs engrafted within the disc space despite the biomechanical forces of the beagle cervical spine.

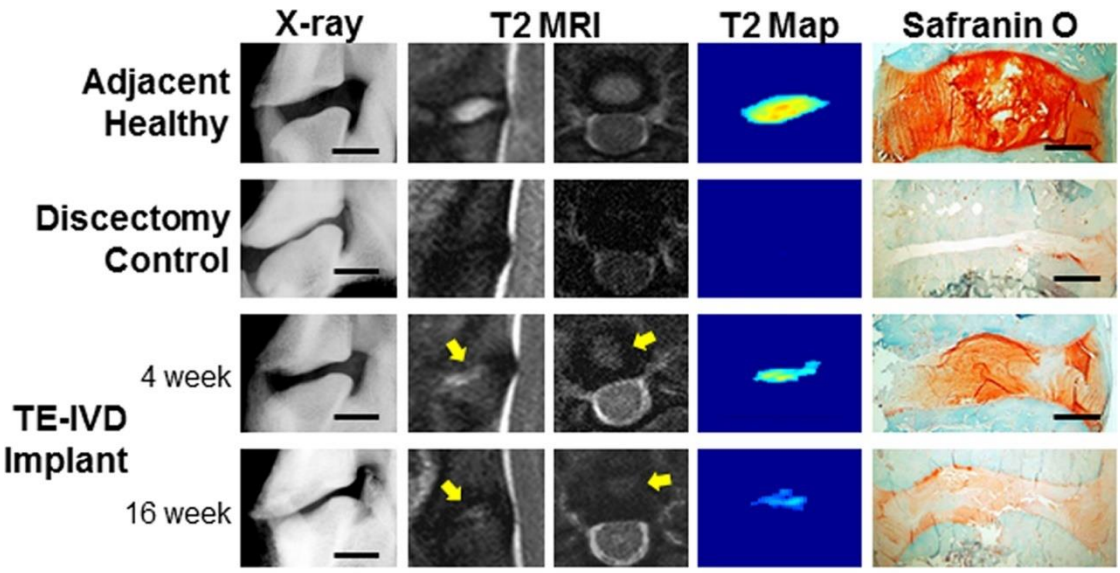

Figure 2.2. X-ray, MRI and histology of adjacent motion segment, discectomy, and TE-IVD at 4 and 16 weeks. Adjacent disc levels showed clear vertebral separation, strong hydration signal in sagittal and axial T2 MRI, highly localized T2 map signal, and abundant staining with Safranin O. Discectomy levels showed no vertebral separation and minimal T2 signal and no soft tissue present between vertebrae. Animals receiving stably transplanted TE-IVD showed clear vertebral separation, with tissue hydration noted in both sagittal and axial T2-weighed MRI (yellow arrows). At both 4 and 16 weeks after transplantation, proteoglycan-rich tissue was observed to be well integrated into the surrounding vertebrae.

Engrafted TE-IVDs produced functional tissue that maintained disc height and tissue hydration

We investigated the ability of TE-IVDs to maintain disc height by measuring the disc height index as described previously.[16] At 4 weeks, the disc height indices of stably implanted TE-IVDs and discectomized discs were 71% and 51% of healthy control discs, respectively. Animals receiving TE-IVDs demonstrated significant decrease in disc height over time ($p<0.001$), with stable implants having larger disc height compared to the discectomy group at both 4 and 16 weeks ($p<0.001$ and $p = 0.012$, respectively) (Fig 2.3). We further assessed the size and hydration of the NP portion in the implanted TE-IVDs following an algorithm based on T2 relaxation time (T2-RT) measurements.[24] After 8 weeks, stable TE-IVDs had significantly higher NP voxel count than discectomy ($p = 0.015$) and demonstrated a significant increase in

NP voxel count from 2 to 8 and 16 weeks (p = 0.009 and 0.020).

Mean NP T2-RT, a value representing NP hydration, was significantly higher for TE-IVDs than discectomy group at 2 and 4 weeks (p<0.001). There was a significant decrease in T2-RT between 2 and 4 weeks in the TE-IVD group, and only this group maintained physiological hydration of the NP of ~60% of adjacent healthy discs. Conversely, the discectomized segments did not show any region of T2 high intensity at 2 and 4 weeks, which confirmed that total discectomy was thoroughly performed. However, a very small amount of T2 high intensity region emerged in the discectomized segment after 8 weeks, probably due to the fluid accumulation induced by a secondary disc degenerative process. This pseudo-NP region observed in one specimen was responsible for paradoxical increase of the mean T2-RT at 8 and 16 weeks.

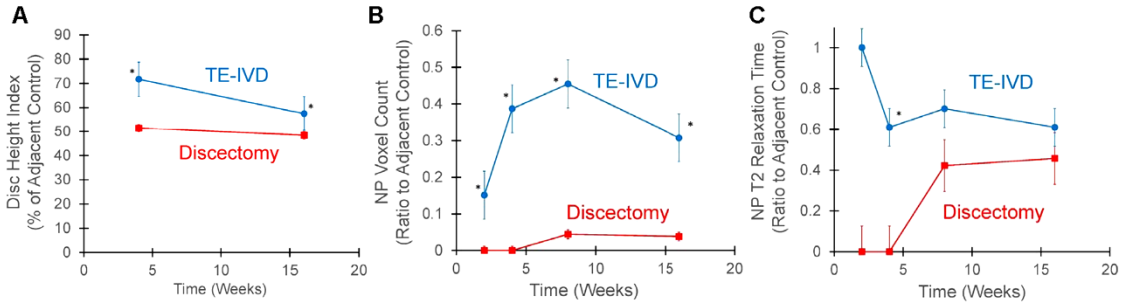

Figure 2.3. Quantitative analysis of disc height index and MRI. A) Stably implanted TE-IVD had significant retention of disc height compared to the discectomy control at 4 and 16 weeks (asterisks, p<0.001 at 4 and p = 0.012 at 16 weeks, respectively). B) TE-IVDs demonstrated significantly higher NP voxel counts than the discectomy controls after 4, 8, and 16 weeks (asterisks denote p<0.02 for all time points) C) TE-IVD had significantly higher T2-relaxation times than the discectomy group at 4 weeks (asterisk, p = 0.007). All data are represented as mean +/- standard error.

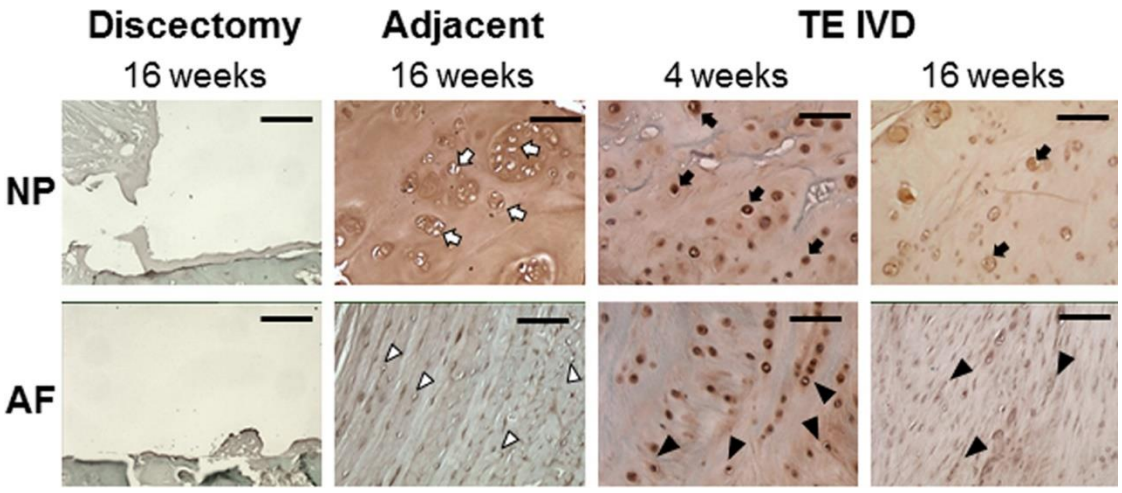

Figure 2.4. Safranin O staining showed an absence of tissue in the intervertebral space of samples in the discectomy group. Healthy tissue in the adjacent motion segment showed strong proteoglycan staining the NP, with numerous clusters of round chondrocytic cells (open arrows) and less staining in the AF, with more elongated fibrochondrocytes arranged in distinct fibrous lamellae (open arrow heads). At 4 weeks, TE-IVD samples had strong proteoglycan staining in both NP and AF, with rounded cells apparent in the NP (filled arrows) and more elongated cells arranged primitive lamellae in the AF. By 16 weeks, staining was more evident in the NP than AF, with some clustering of rounded chondrocytic cells (filled arrows). AF cells were clearly elongated (closed arrow heads) and aligned. All scale bars are 100 μm.

TE-IVDs produced collagen- and proteoglycan-rich extracellular matrix in the AF and NP

A critical benchmark of success for a TE-IVD is the assessment of the biological function of the transplanted tissue as assessed by the ability to form robust extracellular matrix when implanted into the spine. To evaluate this biological function, we performed Safranin O staining for proteoglycans (Fig 2.4) and Picrosirius red staining for fibrillar collagen (Fig 2.5). Both stains demonstrated the successful removal of the IVD and the absence of any robust healing response from the discectomy group. In contrast, TE-IVD implants yielded proteoglycan-rich tissue with distinct morphological features of NP and AF. The morphologies of the NP and AF regions were more similar at 4 weeks, but highly distinct by 16 weeks. The central NP region contained rounded cells and cell clusters characteristic of a chondrocytic phenotype. The morphology of

the NP was similar at 4 and 16 weeks, with the cell clustering that is characteristic of native NP more evident at 16 weeks. AF tissue showed a moderate level of proteoglycan staining at 4 weeks, with staining less pronounced at 16 weeks. At 4 weeks, cells were somewhat elongated, but aligned in nascent lamellae. By 16 weeks, cells were highly elongated, as in the native AF, and aligned into mature lamellae surrounding the NP. Notably, at either 4 or 16 weeks, there was little chronic inflammation or foreign body response to TE IVD implants evident from Safranin O (Fig 2.4), Picrosirius red (Fig 2.5), or Hematoxylin and eosin (supplemental Fig 2.9) stains. At both time points, cells in both the AF and NP regions appeared healthy and there was no sign of implant rejection, despite the implants being seeded with allogenic cells.

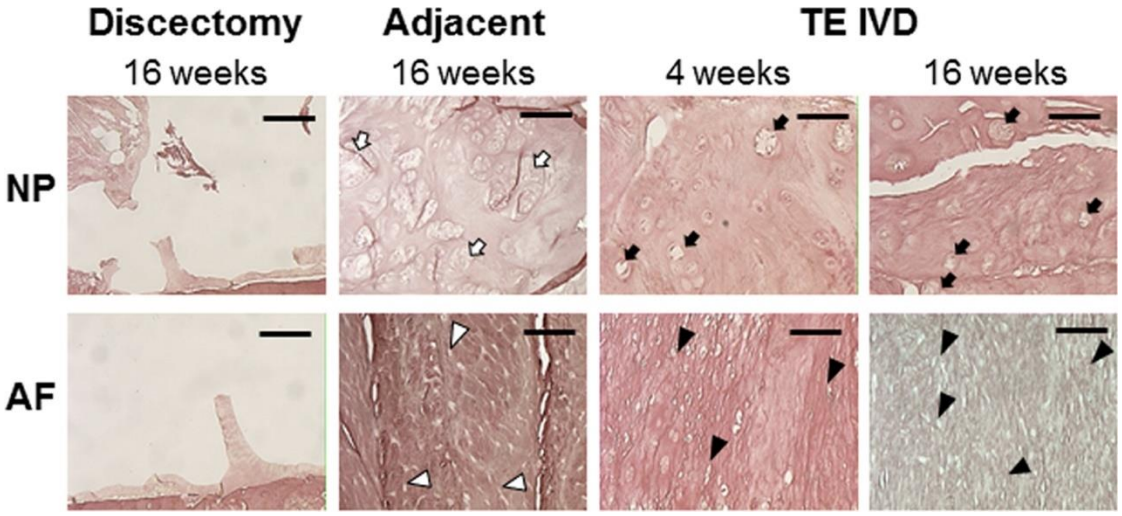

Figure 2.5. Picrosirius red staining showed an absence of tissue in the intervertebral space of samples in the discectomy group. Healthy tissue in the adjacent motion segment showed little staining for collagen in the NP with numerous clusters of round chondrocytic cells (open arrows) and strong staining in the AF, with more elongated fibrochondrocytes arranged in distinct fibrous lamellae (open arrow heads). At 4 weeks, TE-IVD samples had light collagen staining in the NP and stronger staining in the AF, with rounded cells apparent in the NP (filled arrows) and more elongated cells arranged primitive lamellae in the AF. By 16 weeks, staining was present in both NP than AF, with some clustering of rounded chondrocytic cells (filled arrows) in the NP and elongated cells in the AF (closed arrow heads). All scale bars are 100 μm.

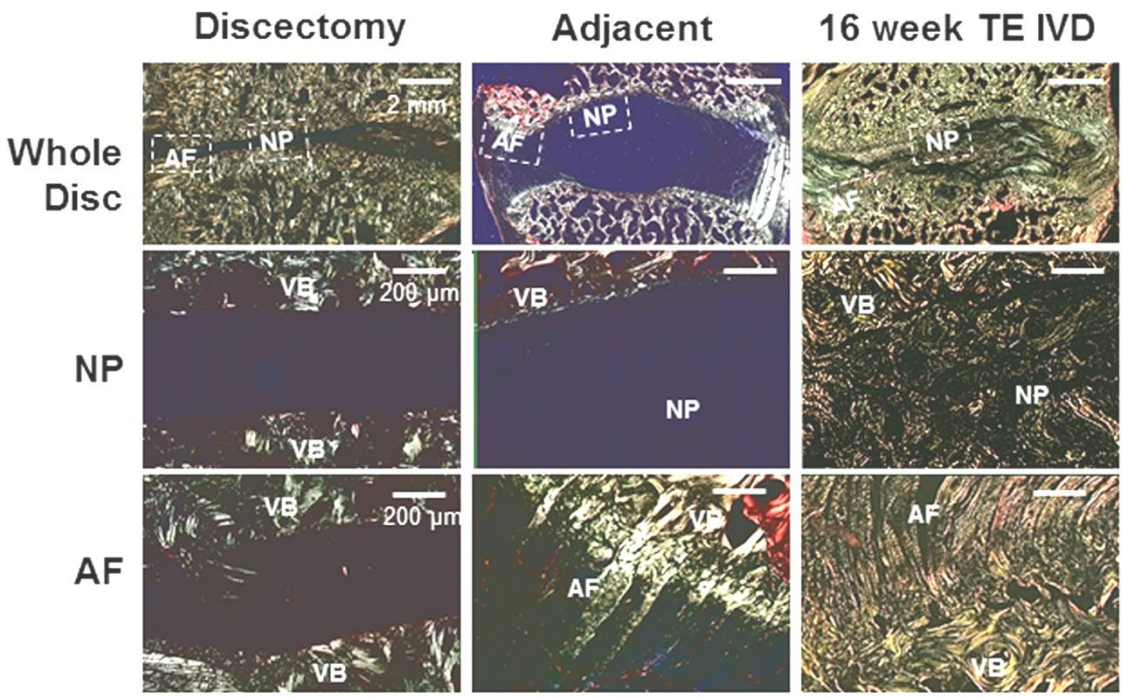

Figure 2.6. Picrosirius red-stained histology under polarized light showed birefringent features associated with collagen fibers. Discectomy samples show collagen organization in vertebrae, with no tissue in the intervertebral space. Adjacent motion segments show the absence of collagen fibers in the NP and large collagen fibers (~50–100 µm) inserting from the AF to the vertebral body (VB). At 16 weeks, TE-IVD samples show the presence of some small, unorganized collagen fibers in the NP, with larger (~20–50 µm) fibers that insert into the vertebral body (VB).

TE-IVDs integrated with neighboring vertebrae and reproduced a native disc shape and composition structure over 16 weeks of implantation

A major challenge in a tissue engineering approach to IVD repair is the integration of a newly grown implant into the surrounding vertebrae. To assess the integration of the implanted TE-IVD, we used polarized light microscopy in conjunction with Picrosirius red staining to evaluate the collagen organization in our implants and its connection to neighboring vertebrae (Fig 2.6). As expected, the adjacent segment showed structures characteristic of the IVD, including highly aligned lamellae in the AF, the absence of fibers in the NP, and insertion of large collagen fibers from the AF into the vertebral body (Fig 2.6 and supplemental Fig 2.7). Discectomized segments showed no tissue in the disc space, with no connection between collagen in the vertebral

body and the intervertebral space (Fig 2.6 and supplemental Fig 2.8). TE-IVD segments showed the presence of tissue throughout the intervertebral space. NP tissue contained some collagen, composed primarily of small, disorganized fibers (Fig 2.6 and supplemental Fig 2.9). AF tissue was composed of large sections of organized collagen fibers that inserted in and connected to the vertebral body.

Discussion

In the present study, we demonstrated the feasibility of total disc replacement using TE-IVDs in the canine cervical spine. Despite the challenging mechanical environment of the beagle spine, the stably implanted TE-IVDs maintained their position, integrated with the host tissue through the reorganization process, and yielded hydrated disc-like tissues over 16 weeks. Although the morphology of TE-IVD implants was distinct from the adjacent healthy IVD, implants contained an NP region with cartilaginous tissue with rounded cells and an AF region with organized fibrous tissue that inserted into the vertebral body. These implants formed organized tissue in the spine that functioned normally throughout the 16 weeks of the study. Reconstructing a discectomized intervertebral segment with *de novo* biological disc implants is an ambitious approach to treating degenerative disc disease of the cervical spine. In 2007, the feasibility of whole allogeneic IVD transplantation was demonstrated in a clinical study with impressive results at 10 years follow up.[7] The potential clinical advantages of allogeneic IVD transplantation are limited by the availability of healthy donor discs, possible adverse immune reaction, and potential disease transmission. *De novo* TE-IVDs, the multi-compartment disc analogs using cells and biomaterials, can potentially overcome these limitations of allogeneic implants and yield favorable outcomes. A variety of *in vitro* studies and *in vivo* studies that employed animal models of nucleotomy or partial IVD resection have indicated the promise of using tissue-engineered constructs for disc replacement,[9,11,13,25-40] however, only three translational

studies have demonstrated the *in vivo* efficacy of biological disc implants in the totally discectomized segment.[11,16]

In the pursuit of a biological construct that can be contained in the interbody cage to reconstruct the segment with non-bony soft tissues, Goldshlager et al. seeded mesenchymal progenitor cells into gelfoam sponges formulated with the chondrogenic agent pentosan polysulfate implanted into fully discectomized sheep lumbar segments in combination with absorbable interbody cages.[41] This study demonstrated the potential of replacing the disc segment with cartilaginous tissues to offer a means of preserving spinal motion, although the reparative tissues were distinct from those of native discs, even accompanied with ossification in some areas or specimens. Xin et al reported the aforementioned allogeneic disc transplantation and demonstrated the feasibility of human telomerase reverse transcription (hTERT) gene-transfected NP to be incorporated with allograft IVD transplantation in the beagle cervical spine.[42] Although their results demonstrated the feasibility of allogeneic disc-based implant to be combined with genetic engineering, use of exogenous genes can hamper the clinical applicability. Previously, we developed *de novo* AF/NP composites derived from component cells to produce TE-IVDs and demonstrated the efficacy of these discs on maintenance of disc height and disc functionality in an *in vivo* rat model.[16] The implanted TE-IVD integrated, with the host vertebrae, histologically restored the disc constitutive structures (i.e. NP and AF), and physiologically maintained NP hydration over 8 months.[19]

To move this approach toward clinical application, larger animals that have a more upright cervical spine were utilized in the present study. Many breeds of small dogs, such as beagles and dachshunds, develop spontaneous cervical disc degeneration as in humans.[23] Further, previous studies have revealed that canine IVDs are exposed to stress conditions similar to or even higher than those of human discs.[21-23,43,44] In

addition, the canine spine shows similar anatomical features and analogous degenerative processes with human discs.[45] Besides showing similar pathological changes, canines are also the only animals diagnosed and treated both medically and surgically as humans for their disc degeneration.[46] As such, canine spinal models have been previously used to investigate disc degeneration and to develop surgical treatments such as spinal fusion[47,48] and regenerative intervention.[38] This is especially true of beagles, which are frequently used for biological approaches aimed at disc regeneration. These canines are classified as chondrodystrophic dogs due to the gradual loss of notochord cells and replacement by chondrocyte-like cells by the stage of skeletal maturity.[49] Notably the absence of such cells at skeletal maturity, which have reparative functions in the intervertebral discs, suggests that such a mechanism is not at play for implanted TE-IVD. In fact, the solely discectomized segments in the present study demonstrated no substantial repair in the disc space.

Moreover, our experiment employing stand-alone TE-IVD implantation under this clinically relevant model gave a fresh insight into development of biological disc treatment. First, mechanical stress causes instability and displacement of the implant. As evidenced by prosthetic TDR,[50] displacement of implant is an arising complication when positioned in a fixation-free fashion, predominantly due to the human spine yielding severe axial loading. However, all the TE-IVDs at the C3/4 segment were stable in our study and maintained disc height up to 70% of adjacent normal discs. Biomechanics are known to be different among different levels of the cervical spine[51] and our findings may suggest biomechanics at this level of the beagle spine are more favorable to the biological disc implantation.

Our data suggested that PLL resection in the experimental segment could enhance the intraoperative stability of biological disc implants. The efficiency of PLL resection in anterior cervical decompression and fusion has been demonstrated.[52]

Resecting the PLL, one of the stabilizer ligaments in the spine unit, may compromise segmental stability of the spine in the motion preserving surgery, however, Yang DL et al demonstrated that removal of the PLL improved clinical outcome of prosthetic total disc replacement via better enlargement of spinal canal without significant effect on spinal imbalance and segmental. The present study also showed that PLL resection did not pronouncedly affect the stability of treated disc segments, and to make matters more favorable, increased the stability of implanted TE-IVDs with close-to-significance.

TE-IVDs that were intraoperatively classified as stable implants, without any evidence of displacement, demonstrated better outcomes over the course of 16 weeks than the discectomy alone group, while the unstably implanted TE-IVDs demonstrated time-dependent degradation after 4 weeks. Notably, implants that were not stable displaced immediately upon removal of distraction, suggesting that additional surgical techniques maybe be needed to ensure that implants remain in place after surgery. Implants that remained in place after surgery were stable until the animals were euthanized.

In addition to the significant mechanical loading of the beagle cervical, a TE-IVD implant is also subject to a milieu with very poor nutritional supply. The indirect blood perfusion of the TE-IVD is via diffusion from blood vessels of the vertebral body through the cartilaginous endplate (EP), but there is no direct conduit of blood perfusion. In fact, the role of nutrition, critical in the long-term durability of implanted biological treatments, has been largely overlooked.[53] This is also corroborated by our finding that the NP portion of TE-IVDs at 16 weeks did not maintain as much disc height, NP hydration, and proteoglycan content as at 2 or 4 weeks. Further, axial distraction using an external fixator can enhance the regenerative capability of cell injection therapy, based on the hypothesis that individually both a distracted segment and cell injection can stimulate disc repair.[54-56]

Chronic immune response to TE-IVD implants composed of allogeneic cells was notably absent in this study. Previous work has shown that transplantation of allogenic mesenchymal stem cells (MSCs) into the rat IVD invoked a minimal immune response,[57] and that allogeneic articular chondrocytes transplanted into the rabbit IVD similarly caused minimal immune response.[58] These studies, combined with total disc transplantation studies conducted in beagles,[42] goats,[59] and humans,[7] and data from the current study, collectively suggest that the disc space has a sufficient level of immunoprivilege to tolerate allogenic cell or tissue transplants. Human disc allograft was first performed in 2007[7] and their results showed the implanted disc engrafted without any rejection, maintained disc space, and improve the patients' symptoms. Combined with other studies, the current study corroborates that allogenic discs and disc spaces have some immune privilege as in cartilage in general. As such, the present study demonstrates that allogenic cell source is not necessary for successful outcomes, as has been noted previously.[42]

Collectively, these data represent the first proof of concept studies demonstrating the regeneration of whole IVD in a large animal model. Implants engrafted successfully and persisted in the spine for up to 16 weeks, with evidence of distinct NP and AF regions. Challenges persist in maintaining function over extended periods of time and in characterizing the mechanical performance of these implants. Specifically, assessing the continued functionality of transplanted discs over long time scales (6–12 months) will be critical for establishing feasibility for human trials. Furthermore, the current study focused on transplantation of TE-IVD into healthy canine spine. The environment of the IVD in the case of degenerative disc will likely be significantly more challenging due to alterations in mechanics and diminished supply of nutrients. Future studies will assess the function of such implants in the degenerative spine to aid in the translation of this technology to clinical practice.

Materials and Methods

Cell preparation

Cell preparation was based on previously described techniques.[16,19] Cervical spines of skeletally mature beagles were purchased (Marshall BioResources) and IVDs were dissected out of the segments. Tissue was washed in PBS (Dulbecco's PBS; Gibco BRL) and then separated into AF and NP regions. To isolate the component cells, tissues were dissected into small pieces and digested in 125 mL of 0.3% wt⁄vol collagenase type II (Worthington Biochemicals) at 37°C for 6 h. Digested tissue was filtered through 100 μm nylon mesh (BD Biosciences) and centrifuged at 936 g for 7 min. Cells were counted and seeded in culture flasks with Ham's F-12 media (Gibco BRL) that contained 10% fetal bovine serum (Gemini Bio Products), penicillin, (100 units/mL), streptomycin (100 μg/mL), amphotericin B (250 ng/mL), and ascorbic acid (25 μg/mL). Cells were cultured at 37°C, 5% CO_2, and normoxia to confluence with media changes twice a week. At confluence, cells were removed from flasks with 0.05% trypsin (Gibco BRL) and counted with a hemocytometer. Cells were then seeded into TE-IVDs (Fig 2.1A).

TE-IVD fabrication

T2-weighted MRI images were obtained of cervical 3/4 and 4/5-disc levels in the beagle (imaging specifics in imaging section). The dorso-ventral and lateral-lateral dimensions of the NP region shown in the MRI were used along with the height of the disc space to model the TE-IVD core as an elliptic cylinder. A model of an injection mold for the NP was created in SolidWorks using the MRI-derived NP dimensions to guide the size of the cavities. The injection mold was then 3D printed of UV-curable watertight acrylic plastic (Shapeways). TE-IVD implant was created using established contracted collagen (AF)/alginate (NP) technique (Fig 2.1B),[14-16] such that the ratio of NP area to the whole contracted disc area matched the 30% ratio observed in the beagle

native disc. Three percent (wt/vol) low viscosity grade alginate (FMC BioPolymer) seeded with 25×10^6 NP cells⁄mL was mixed with 0.02 g/mL $CaSO_4$ (Sigma-Aldrich) to crosslink the alginate and injected into the NP mold (Fig 2.1B). Cell-seeded alginate NP was then removed from molds and placed in the center of a well of a 12-well plate. Collagen type I was obtained from rat-tail tendon (Sprague Dawley, 7–8-wk old) (Pel-Freez Biologicals) using established protocols.[15,60] One and a half milligrams per milliliter collagen gel solution seeded with 1×10^6 AF cells/mL was subsequently poured and gelled around the alginate NP. Constructs were cultured for 2 weeks in previously described media at 37°C, 5% CO_2, and normoxia while collagen gel contracted around alginate NP to the proper AF dimensions.

Total discectomy in canine cervical segments

Skeletally mature male beagles (n = 14) were obtained from Marshall BioResources. The animals were 12 to 18 months old at the time of surgery, with a weight of 15–25 kg. All experimental procedures were reviewed and approved by the Institutional Animal Care and Use Committee at Weill Cornell Medicine. Animals were housed in a facility accredited by the Association for the Assessment and Accreditation of Laboratory Animal Care (AAALAC) in compliance with applicable NY State, and Federal regulations. Initially, the animals underwent endotracheal intubation with administration of IV propofol, followed by a combination of inhaled isoflurane with intravenous fentanyl to maintain anesthesia. Then, the animal was placed in dorsal recumbency with the neck hyperextended and secured to the table with adhesive tape. The surgical site was prepared by clipping hair and scrubbing with chlorhexidine and betadine scrub solution. Animal was preoperatively given a dose of cefazolin 22 mg/kg IV which was repeated every 2–3 hours thereafter during the surgical procedure.

A ventral midline incision was made from the base of the larynx to the sternum. The paired sternocleidomastoideus and sternohyoideus muscles were separated with

blunt dissection, exposing the trachea. Retractors were then positioned to retract the nearest carotid sheath toward the surgeon and the trachea, esophagus, and opposite carotid sheath away from the surgeon. This exposed the paired longus coli muscles, which lie on the ventral surface of the cervical vertebrae. The surgical level was identified by palpation of the prominent transverse process of C6. Small curved hemostats were used to separate the longus coli muscle overlying the ventral annulus.

The subsequent steps were carried out microscopically. After the ventral part of the AF has been incised and resected with a scalpel and a Kerrison rongeur, two self-drilling distraction pins were anteriorly inserted into the adjacent vertebrae and the disc segment was distracted with a Cervical Distractor System. Under segmental dilatation, which is augmented as the disc tissues are resected, the NP was completely extracted using a small tartar scraper, a 4–0 bone curette, and a Kerrison rongeur. The dorsal part of the AF was also resected under careful microscopic observation to expose the posterior longitudinal ligament (PLL) and confirm complete resection of the AF, and in several animals, the PLL.

One segment between C3/4 and C6/7 was totally discectomized in each animal. To determine surgical conditions that promote implant stability in a canine model, we employed different surgical levels as well as binary options between additional PLL resection or not; four of C3/4, four of C4/5, four of C5/6, and two of C6/7 segments were discectomized. Four of the animals underwent PLL resection, while the other did not. All the surgical procedures were performed by two fully-trained spine surgeons.

The neurologic examinations were performed immediately after surgery and periodically throughout the course of the study. These consisted of evaluating the animal’s gait in a straight line and turns to both sides, wheelbarrow on pelvic and thoracic limbs, individual limb hopping, cross extensor reflex and plantar reflex. All

these tests can detect problems with coordination and strength in any of the four limbs, or injury to the spinal cord section at or caudal to the surgery site.

In vivo total disc replacement using tissue-engineered IVDs

TE-IVDs were taken out of culture and kept suspended in aforementioned media inside centrifuge tubes to maintain sterility. Constructs were brought into the operating room and implanted into the 12 segments ranging from C3/4 to C6/7 levels of the beagle spine after complete disc extraction in a single procedure, while the disc space was left untreated in the C5/6 discectomized segments of two animals. TE-IVDs were slipped down on a deliver instrument and inserted into the space. Distraction was slowly released and motion of the implanted TE-IVD was qualitatively evaluated for any motion and overall stability. Implanted TE-IVDs were categorized as displaced or stable, depending on how much of the disc remained within the intervertebral segment following release of retractors; in general, if ¼ of the disc diameter was extruded upon release we considered this displaced. Bipolar cauterization was used for homeostasis and the separated longus coli muscles were sutured to be paired with 5–0 Vicryl sutures. The wound was closed subcutaneously with 5–0 Vicryl and cutaneously with 3–0 polyamide-nylon sutures. Postoperative care was provided by Veterinary Services personnel as per the RARC veterinarian. Sutures was removed 10–14 days postoperatively. Prior to and following implantation, animals were evaluated via physical examination.

Qualitative and quantitative magnetic resonance imaging

All the 14 animals underwent 3 Tesla MRI (Siemens Tim TRIO MRI Scanner, Erlangen, Germany) imaging at 1 month and ten at 3 months postoperatively to qualitatively monitor location and viability of implanted TE-IVDs on sagittal and axial T2-weighted images. For quantitative assessment, the voxel count and average T2 relaxation time in NP were measured according to an algorithm we previously

developed.[24,61,62] We used a sagittal multislice multiecho pulse sequence (TR = 2000 ms, TE = 12 ms, NEX = 2, number of echoes = 12, echo spacing = 12 ms, slice thickness = 1 mm, and matrix size = 320 × 320, resolution: 125 μm × 125 μm × 1 mm) to create a T2 map based on fitting semi log plots of T2 signal intensity versus relaxation time for the 12 acquired echoes. Bruker's proprietary program TopSpin was used for this fitting process. A color map was assigned to the resulting T2 map. Next, a standard region of interest (ROI) measuring approximately 4 mm^2 (comprising 300 voxels) was drawn within the center NP of the healthy disc proximal to the experimental segments. The average T2-relaxation time (T2-RT) of that ROI was measured, and this value minus 3 standard deviations was used to set a subtraction threshold for all voxels in that slice. Voxels with T2 values lower than the threshold were subsequently subtracted. Thus, only voxels with T2 values representing NP tissue remained in the disc space and were then counted. At each time point, the mean voxel count of experimental segments was compared with the mean voxel count of proximal adjacent healthy discs. The mean T2-RT of NP voxels was also calculated

and compared with that of the healthy adjacent control.

Disc height measurements

X-rays were performed at one and four months to measure the disc height of treated segments. Great care was taken to achieve true lateral radiographs of the index segment. The IVD height was expressed as a disc height index, calculated by dividing disc height by adjacent vertebral body height on the basis of the modified method of Lu et al.[63]

Histological assessment

Animals were sacrificed one or four months postoperatively by administering a barbiturate overdose intravenously at a rate of 120 mg/kg. Spines were collected and processed for further *ex vivo* histological assessments. After fixed by 10% neutralized

formalin supplemented with 1% cetylpyridinium chloride (CPC), specimens were decalcified, cut in the mid-sagittal plane, and transferred to 75% ethanol. Segments were embedded in paraffin, then cut to 5-μm thickness, and stained with Alcian Blue, Safranin-O, and Picrosirius Red.

Data analysis and statistics

All the quantitative values from X-rays and MRIs represent the proportion of experimental to adjacent healthy control measurements, and were expressed as mean ± SD. For the analyses for continuous outcomes in disc height index, NP size, and NP hydration, generalized estimating equation (GEE) models were used to assess main effects and interaction factors of disc group and longitudinal assessment of time. Parameter estimates of means and robust standard errors are reported to describe estimated differences in mean changes from baseline controls (discectomy) across stable and displaced implantation groups for the 2, 4, 8 and 16-week time points. Statistical analysis was performed with IBM SPSS Statistics 22 (SPSS, Chicago, IL, USA). P values <0.05 were considered statistically significant.

Supplemental Data

Level				Implant stability: Displaced	Implant stability: Stable
C3/C4	PLL resection	-	Count	0	1
			% within stability	0.0%	16.7%
		+	Count	0	3
			% within stability	0.0%	50.0%
	Total		Count	0	4
			% within stability	0.0%	66.7%
C4/C5	PLL resection	-	Count	3	1
			% within stability	50.0%	16.7%
	Total		Count	3	1
			% within stability		16.7%
C5/C6	PLL resection	-	Count	2	0
			% within stability	33.3%	0.0%
	Total		Count	2	0
			% within stability	33.3%	0.0%
C6/C7	PLL resection	-	Count	1	0
			% within stability	16.7%	0.0%
		+	Count	0	1
			% within stability	0.0%	16.7%
	Total		Count	1	1
			% within stability	16.7%	16.7%
Total	Total		Count	6	6
			% within stability	100.0%	100.0%

Table 2.1. To determine the surgical condition that promotes stable implantation, TE-IVDs were implanted in different spinal levels ranging from C3/4/ to C6/7, and with or without posterior longitudinal ligament (PLL) resection. Based on the implant stability upon distraction release, half of the TE-IVDs remained stable (n = 6), while the other half (n = 6) were considered displaced. Of note, 66.7% of the stable TE-IVDs were the ones implanted at C3/4 although the association between intraoperative implant stability and surgical level was not statistically significant (p = 0.120).

			Implant stability		
			Displaced	Stable	P-value
Level	C3/4	Count	0	4	0.081
		% within Stability	0.0%	66.7%	
	non C3/4	Count	6	2	
		% within Stability	100.0%	33.3%	

Table 2.2. The crosstab demonstrates that the implants at C3/4 had a greater stability with a near significant association compared to the rest of the levels (p = 0.081).

			Implant stability		
			Displaced	Stable	P-value
PLL resection	-	Count	6	2	0.061
		% within Stability	100.0%	33.3%	
	+	Count	0	4	
		% within Stability	0.0%	66.7%	

Table 2.3. The segments with ligament resection all demonstrated that implant stability was nearly significantly higher than the segments with an intact posterior longitudinal ligament (p = 0.061).

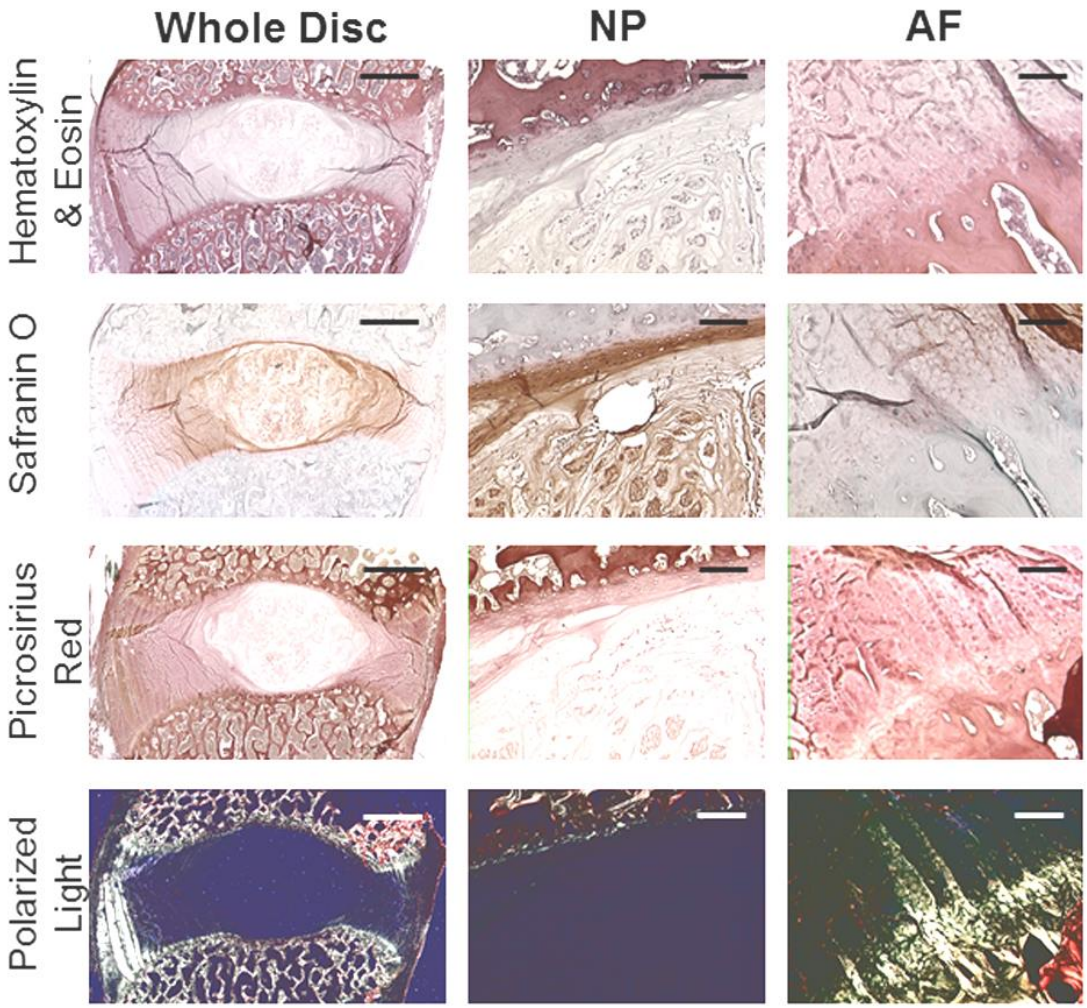

Figure 2.7. Histological assessments at 16 weeks of a healthy adjacent motion segment. Brightfield images are shown for staining with Hematoxylin and eosin, Safranin O, and Picrosirius red, as well as polarized light images of Picrosirius red staining. All scale bars are 200 μm.

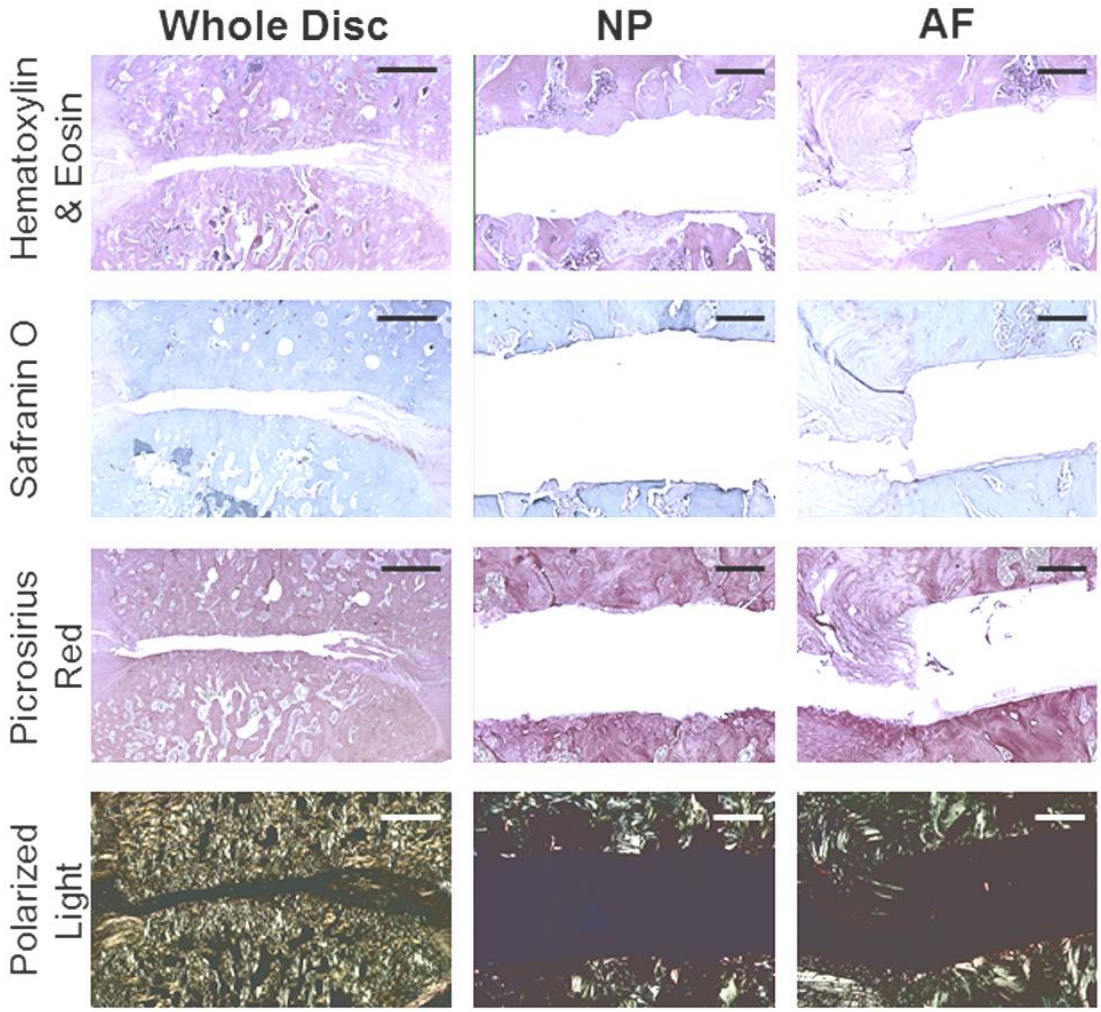

Figure 2.8. Histological assessments at 16 weeks of a motion segment that received a discectomy. Brightfield images are shown for staining with Hematoxylin and eosin, Safranin O, and Picrosirius red, as well as polarized light images of Picrosirius red staining. All scale bars are 200 μm.

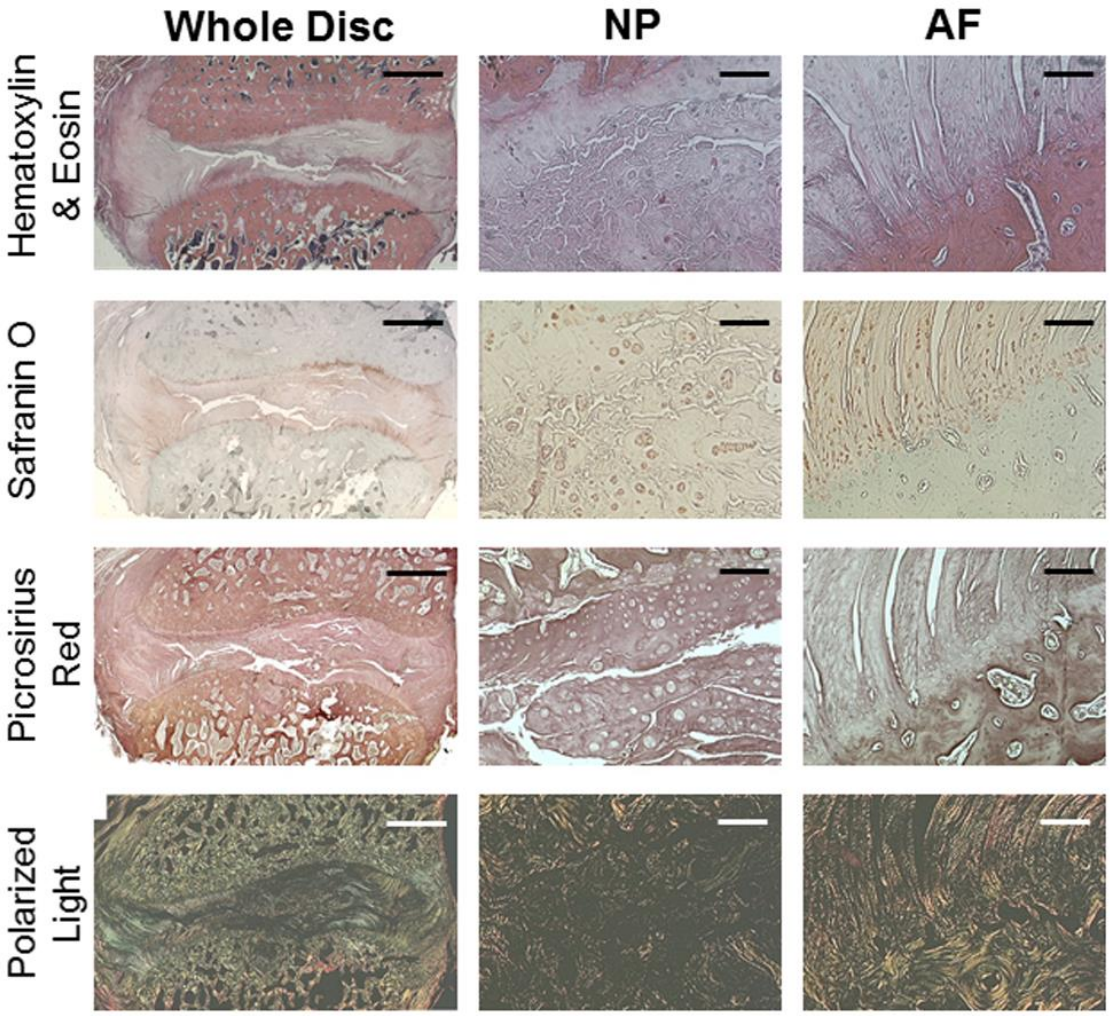

Figure 2.9. Histological assessments at 16 weeks of a motion segment that received a TE-IVD implant. Brightfield images are shown for staining with Hematoxylin and eosin, Safranin O, and Picrosirius red, as well as polarized light images of Picrosirius red staining. All scale bars are 200 μm.

REFERENCES

1. Andersson GB. Epidemiological features of chronic low-back pain. Lancet. 1999; 354(9178):581–5.

2. Brodke DS, Ritter SM. Nonsurgical management of low back pain and lumbar disk degeneration. Instr Course Lect. 2005; 54:279–86.

3. Rajaee SS, Bae HW, Kanim LE, Delamarter RB. Spinal fusion in the United States: analysis of trends from 1998 to 2008. Spine. 2012; 37(1):67–76.

4. Maldonado CV, Paz RD, Martin CB. Adjacent-level degeneration after cervical disc arthroplasty versus fusion. Eur Spine J. 2011;20 Suppl 3:403–7.

5. Sugawara T, Itoh Y, Hirano Y, Higashiyama N, Mizoi K. Long term outcome and adjacent disc degeneration after anterior cervical discectomy and fusion with titanium cylindrical cages. Acta Neurochir (Wien). 2009; 151(4):303–9; discussion 9.

6. Kelly MP, Mok JM, Frisch RF, Tay BK. Adjacent segment motion after anterior cervical discectomy and fusion versus Prodisc-c cervical total disk arthroplasty: analysis from a randomized, controlled trial. Spine. 2011; 36(15):1171–9.

7. Ruan D, He Q, Ding Y, Hou L, Li J, Luk KD. Intervertebral disc transplantation in the treatment of degenerative spine disease: a preliminary study. Lancet. 2007; 369(9566):993–9.

8. Langer R, Vacanti JP. Tissue engineering. Science. 1993; 260(5110):920–6.

9. Mizuno H, Roy AK, Vacanti CA, Kojima K, Ueda M, Bonassar LJ. Tissue-engineered composites of anulus fibrosus and nucleus pulposus for intervertebral disc replacement. Spine. 2004; 29(12):1290–7; discussion 7–8.

10. Mizuno H, Roy AK, Zaporojan V, Vacanti CA, Ueda M, Bonassar LJ. Biomechanical and biochemical characterization of composite tissue-engineered intervertebral discs. Biomaterials. 2006; 27(3):362–70.

11. Zhuang Y, Huang B, Li CQ, Liu LT, Pan Y, Zheng WJ, et al. Construction of tissue-engineered composite intervertebral disc and preliminary morphological and biochemical evaluation. Biochem Biophys Res Commun. 2011; 407(2):327–32.

12. Martin JT, Milby AH, Chiaro JA, Kim DH, Hebela NM, Smith LJ, et al. Translation of an engineered nanofibrous disc-like angle-ply structure for intervertebral disc replacement in a small animal model. Acta Biomater. 2014; 10(6):2473–81.

13. Hamilton DJ, Seguin CA, Wang J, Pilliar RM, Kandel RA. Formation of a nucleus pulposus-cartilage endplate construct in vitro. Biomaterials. 2006; 27(3):397–405.

14. Bowles RD, Williams RM, Zipfel WR, Bonassar LJ. Self-assembly of aligned tissue-engineered annulus fibrosus and intervertebral disc composite via collagen gel contraction. Tissue Eng Part A. 2010; 16 (4):1339–48.

15. Bowles RD, Gebhard HH, Dyke JP, Ballon DJ, Tomasino A, Cunningham ME, et al. Image-based tissue engineering of a total intervertebral disc implant for restoration of function to the rat lumbar spine. NMR Biomed. 2012; 25(3):443–51.

16. Bowles RD, Gebhard HH, Hartl R, Bonassar LJ. Tissue-engineered intervertebral discs produce new matrix, maintain disc height, and restore biomechanical function to the rodent spine. Proc Natl Acad Sci U S A. 2011; 108(32):13106–11.

17. Gebhard H, Bowles R, Dyke J, Saleh T, Doty S, Bonassar L, et al. Total disc replacement using a tissue-engineered intervertebral disc in vivo: new animal model and initial results. Evid Based Spine Care J. 2010; 1(2):62–6.

18. Gebhard H, James AR, Bowles RD, Dyke JP, Saleh T, Doty SP, et al. Biological intervertebral disc replacement: an in vivo model and comparison of two surgical techniques to approach the rat caudal disc. Evid Based Spine Care J. 2011; 2(1):29–35.

19. Grunert P, Gebhard HH, Bowles RD, James AR, Potter HG, Macielak M, et al. Tissue-engineered intervertebral discs: MRI results and histology in the rodent spine. J Neurosurg Spine. 2014; 20(4):443–51.

20. James AR, Bowles RD, Gebhard HH, Bonassar LJ, Hartl R. Tissue-engineered total disc replacement: final outcomes of a murine caudal disc in vivo study. Evid Based Spine Care J. 2011; 2(4):55–6.

21. Lotz JC. Animal models of intervertebral disc degeneration: lessons learned. Spine. 2004; 29 (23):2742–50.

22. O'Connell GD, Vresilovic EJ, Elliott DM. Comparison of animals used in disc research to human lumbar disc geometry. Spine. 2007; 32(3):328–33.

23. Showalter BL, Beckstein JC, Martin JT, Beattie EE, Espinoza Orias AA, Schaer TP, et al. Comparison of animal discs used in disc research to human lumbar disc: torsion mechanics and collagen content. Spine. 2012; 37(15): E900–7.

24. Grunert P, Hudson KD, Macielak MR, Aronowitz E, Borde BH, Alimi M, et al. Assessment of intervertebral disc degeneration based on quantitative magnetic resonance imaging analysis: an in vivo study. Spine. 2014; 39(6): E369–78.

25. Nerurkar NL, Sen S, Huang AH, Elliott DM, Mauck RL. Engineered disc-like angle-ply structures for intervertebral disc replacement. Spine. 2010; 35(8):867–73.

26. Nesti LJ, Li WJ, Shanti RM, Jiang YJ, Jackson W, Freedman BA, et al. Intervertebral disc tissue engineering using a novel hyaluronic acid-nanofibrous scaffold (HANFS) amalgam. Tissue Eng Part A. 2008; 14(9):1527–37.

27. Abbushi A, Endres M, Cabraja M, Kroppenstedt SN, Thomale UW, Sittinger M, et al. Regeneration of intervertebral disc tissue by resorbable cell-free polyglycolic acid-based implants in a rabbit model of disc degeneration. Spine. 2008; 33(14):1527–32.

28. Bendtsen M, Bunger CE, Zou X, Foldager C, Jorgensen HS. Autologous stem cell therapy maintains vertebral blood flow and contrast diffusion through the endplate in experimental intervertebral disc degeneration. Spine. 2011; 36(6):E373–9.

29. Benz K, Stippich C, Fischer L, Mohl K, Weber K, Lang J, et al. Intervertebral disc cell- and hydrogel-supported and spontaneous intervertebral disc repair in nucleotomized sheep. Eur Spine J. 2012; 21 (9):1758–68.

30. Frith JE, Menzies DJ, Cameron AR, Ghosh P, Whitehead DL, Gronthos S, et al. Effects of bound versus soluble pentosan polysulphate in PEG/HA-based hydrogels tailored for intervertebral disc regeneration. Biomaterials. 2014; 35(4):1150–62.

31. Ganey T, Hutton WC, Moseley T, Hedrick M, Meisel HJ. Intervertebral disc repair using adipose tissue derived stem and regenerative cells: experiments in a canine model. Spine. 2009; 34(21):2297–304.

32. Ghosh P, Moore R, Vernon-Roberts B, Goldschlager T, Pascoe D, Zannettino A, et al. Immunoselected STRO-3+ mesenchymal precursor cells and restoration of the extracellular matrix of degenerate intervertebral discs. J Neurosurg Spine. 2012; 16(5):479–88.

33. Huang B, Zhuang Y, Li CQ, Liu LT, Zhou Y. Regeneration of the intervertebral disc with nucleus pulposus cell-seeded collagen II/hyaluronan/chondroitin-6-sulfate tri-copolymer constructs in a rabbit disc degeneration model. Spine. 2011; 36(26):2252–9.

34. Iwashina T, Mochida J, Sakai D, Yamamoto Y, Miyazaki T, Ando K, et al. Feasibility of using a human nucleus pulposus cell line as a cell source in cell transplantation therapy for intervertebral disc degeneration. Spine. 2006; 31(11):1177–86.

35. Leung VY, Aladin DM, Lv F, Tam V, Sun Y, Lau RY, et al. Mesenchymal stem cells reduce intervertebral disc fibrosis and facilitate repair. Stem Cells. 2014; 32(8):2164–77.

36. Li CQ, Huang B, Luo G, Zhang CZ, Zhuang Y, Zhou Y. Construction of collagen II/hyaluronate/chondroitin-6-sulfate tri-copolymer scaffold for nucleus pulposus tissue engineering and preliminary analysis of its physico-chemical properties and biocompatibility. J Mater Sci Mater Med. 2010; 21(2):741–51.

37. Omlor GW, Fischer J, Kleinschmitt K, Benz K, Holschbach J, Brohm K, et al. Short-term follow-up of disc cell therapy in a porcine nucleotomy model with an albumin-hyaluronan hydrogel: in vivo and in vitro results of metabolic disc cell activity and implant distribution. Eur Spine J. 2014; 23(9):1837–47.

38. Revell PA, Damien E, Di Silvio L, Gurav N, Longinotti C, Ambrosio L. Tissue engineered intervertebral disc repair in the pig using injectable polymers. J Mater Sci Mater Med. 2007; 18(2):303–8.

39. Ruan DK, Xin H, Zhang C, Wang C, Xu C, Li C, et al. Experimental intervertebral disc regeneration with tissue-engineered composite in a canine model. Tissue Eng Part A. 2010; 16(7):2381–9.

40. Yang H, Wu J, Liu J, Ebraheim M, Castillo S, Liu X, et al. Transplanted mesenchymal stem cells with pure fibrinous gelatin-transforming growth factor-beta1 decrease rabbit intervertebral disc degeneration. Spine J. 2010; 10(9):802–10.

41. Goldschlager T, Ghosh P, Zannettino A, Gronthos S, Rosenfeld JV, Itescu S, et al. Cervical motion preservation using mesenchymal progenitor cells and pentosan polysulfate, a novel chondrogenic agent: preliminary study in an ovine model. Neurosurg Focus. 2010; 28(6):E4.

42. Xin H, Zhang C, Wang D, Shi Z, Gu T, Wang C, et al. Tissue-engineered allograft intervertebral disc transplantation for the treatment of degenerative disc disease: experimental study in a beagle model. Tissue Eng Part A. 2013; 19(1–2):143–51.

43. Lim TH, Goel VK, Weinstein JN, Kong W. Stress analysis of a canine spinal motion segment using the finite element technique. J Biomech. 1994; 27(10):1259–69.

44. Smit TH. The use of a quadruped as an in vivo model for the study of the spine–biomechanical considerations. Eur Spine J. 2002; 11(2):137–44.

45. Bergknut N, Rutges JP, Kranenburg HJ, Smolders LA, Hagman R, Smidt HJ, et al. The dog as an animal model for intervertebral disc degeneration? Spine (Phila Pa 1976). 2012; 37(5):351–8.

46. Cole TC, Burkhardt D, Ghosh P, Ryan M, Taylor T. Effects of spinal fusion on the proteoglycans of the canine intervertebral disc. J Orthop Res. 1985; 3(3):277–91.

47. Itoh H, Asou Y, Hara Y, Haro H, Shinomiya K, Tagawa M. Enhanced type X collagen expression in the extruded nucleus pulposus of the chondrodystrophoid dog. J Vet Med Sci. 2008: 70(1):37–42.

48. Forterre F, Dickomeit M, Senn D, Gorgas D, Spreng D. Microfenestration using the CUSA Excel ultrasonic aspiration system in chondrodystrophic dogs with thoracolumbar disk extrusion: a descriptive cadaveric and clinical study. Vet Surg. 2011: 40(1):34–39.

49. Hunter CJ, Matyas JR, Duncan NA. Cytomorphology of notochordal and chondrocytic cells from the nucleus pulposus: a species comparison. J Anat. 2004; 205(5):357–62.

50. Ross R, Mirza AH, Norris HE, Khatri M. Survival and clinical outcome of SB Charite III-disc replacement for back pain. The Journal of bone and joint surgery British volume. 2007; 89(6):785–9.

51. Panjabi MM, Crisco JJ, Vasavada A, Oda T, Cholewicki J, Nibu K, et al. Mechanical properties of the human cervical spine as shown by three-dimensional load-displacement curves. Spine (Phila Pa 1976). 2001; 26(24):2692–700.

52. Avila MJ, Skoch J, Sattarov K, Abbasi Fard S, Patel A, Walter CM, et al. Posterior longitudinal ligament resection or preservation in anterior cervical decompression surgery. J Clin Neurosci. 2015; 22 (7):1088–90.

53. Huang YC, Urban JP, Luk KD. Intervertebral disc regeneration: do nutrients lead the way? Nat Rev Rheumatol. 2014; 10(9):561–6.

54. Hee HT, Ismail HD, Lim CT, Goh JC, Wong HK. Effects of implantation of bone marrow mesenchymal stem cells, disc distraction and combined therapy on reversing degeneration of the intervertebral disc. The Journal of bone and joint surgery British volume. 2010; 92(5):726–36

55. Guehring T, Omlor GW, Lorenz H, Engelleiter K, Richter W, Carstens C, et al. Disc distraction shows evidence of regenerative potential in degenerated intervertebral discs as evaluated by protein expression, magnetic resonance imaging, and messenger ribonucleic acid expression analysis. Spine. 2006; 31(15):1658–65.

56. Kuo YW, Hsu YC, Chuang IT, Chao PH, Wang JL. Spinal traction promotes molecular transportation in a simulated degenerative intervertebral disc model. Spine. 2014; 39(9):E550–6.

57. Cunha C, Almeida CR, Almeida MI, Silva AM, Molinos M, Lamas S, et al. Systemic Delivery of Bone Marrow Mesenchymal Stem Cells for In Situ Intervertebral Disc Regeneration. Stem Cells Transl Med. 2016.

58. Zhang Y, Chee A, Shi P, Wang R, Moss I, Chen EY, et al. Allogeneic Articular Chondrocyte Transplantation Downregulates Interleukin 8 Gene Expression in the Degenerating Rabbit Intervertebral Disk In Vivo. Am J Phys Med Rehabil. 2015; 94(7):530–8.

59. Lam SK, Xiao J, Ruan D, Ding Y, Lu WW, Luk KD. The effect of remodeling on the kinematics of the malpositioned disc allograft transplantation. Spine (Phila Pa 1976). 2012; 37(6):E357–66.

60. Elsdale T, Bard J. Collagen substrata for studies on cell behavior. J Cell Biol. 1972; 54(3):626–37.

61. Grunert P, Borde BH, Hudson KD, Macielak MR, Bonassar LJ, Hartl R. Annular repair using high-density collagen gel: a rat-tail in vivo model. Spine. 2014; 39(3):198–206.

62. Grunert P, Borde BH, Towne SB, Moriguchi Y, Hudson KD, Bonassar LJ, et al. Riboflavin crosslinked high-density collagen gel for the repair of annular defects in intervertebral discs: An in vivo study. Acta Biomater. 2015; 26:215–24.

63. Lu DS, Shono Y, Oda I, Abumi K, Kaneda K. Effects of chondroitinase ABC and chymopapain on spinal motion segment biomechanics. An in vivo biomechanical, radiologic, and histologic canine study. Spine (Phila Pa 1976). 1997; 22(16):1828–34; discussion 34–5.

CHAPTER 3

Resorbable plating system stabilizes tissue-engineered intervertebral discs implanted ex-vivo in canine cervical spines[2]

Abstract

Total disc replacement using tissue-engineered intervertebral discs (TE-IVDs) may offer a biological alternative to treat radiculopathy caused by disc degeneration. A composite TE-IVD was previously developed and evaluated in rat tail and beagle cervical spine models in vivo. Although cell viability and tissue integration into host tissue were promising, significant implant displacement occurred at multiple spinal levels. The goal of the present study was to assess the effects of a resorbable plating system on the stiffness of motion segments and stability of tissue-engineered implants subjected to axial compression. Canine motion segments from levels C2/C3 to C5/C6 were assessed as intact (CTRL), after discectomy (Dx), with an implanted TE-IVD only (PLATE-), and with a TE-IVD combined with an attached resorbable plate (PLATE+). Segments under PLATE+ conditions fully restored separation between endplates and showed significantly higher compressive stiffness than segments under PLATE- conditions. Plated segments partially restored more than 25% of the CTRL motion segment stiffness. Plate attachment also prevented implant extrusion from the disc space at 50% compressive strain, and this effect was more significant in segments from levels C3/C4 when compared to segments from level C5/C6. These results suggest that stabilization of motion segments via resorbable plating assists TE-IVD retention in the disc space while allowing the opportunity for implants to fully integrate into the host tissue and achieve optimal restoration of spine biomechanics.

[2] This chapter was recently accepted for publication: Mojica-Santiago JA, Lang GM, Navarro-Ramirez R, Hussain I, Härtl R, Bonassar LJ. (2018) Resorbable plating system stabilizes tissue-engineered intervertebral discs implanted ex-vivo in canine cervical spines. J Orthop Res Spine; *In-press*. DOI: 10.1002/jsp2.1031

Introduction

Intervertebral disc (IVD) degeneration is known to alter the stability and biomechanics of cervical spine motion segments while decreasing the foraminal canal through which nerves stem from the spinal cord, in the most severe cases. Cervical radiculopathy that leads to debilitating or excruciating neck pain in patients (63.5-107.5 per 100,000) is often associated to these changes.[1] First-line treatments include physical therapy and pharmacologic regimens, but surgical intervention is indicated in refractory cases or when the spinal cord is severely compromised. Although standard surgical treatments for cervical radiculopathy and myelopathy involve anterior cervical discectomy and fusion (ACDF) of the diseased motion segment, loss of spine flexibility and reduction of segment range of motion after surgical treatment is suspected to contribute to the onset of adjacent segment disease (ASD).[1-2] Total disc replacement or arthroplasty has also been explored as an alternative treatment to the golden standard to preserve segment stability and motion. However, the efficacy of cervical disc arthroplasty (CDA) in reducing the incidence of symptomatic ASD remains under debate.[3,4] Whereas there may be other factors such as progression of the underlying disc degeneration that influences the occurrence of ASD, the rates of secondary surgical procedures in patients with ACDF is higher than those who received a CDA.[5] Nevertheless, interbody implants and artificial disc replacements[6,7] are subject to wear and generation of debris that may lead to implant dislodgement, osteolysis, and mechanical failure. As such, the importance of restoring segmental motion and native IVD function with minimal risks of implant revisions cannot be overlooked.

Tissue-engineered implants have been investigated in the last decade as biological alternatives to traditional treatments for radiculopathy. Composite tissue-engineered intervertebral discs (TE-IVDs) that mimic the form and function of the native disc have been developed by employing diverse fibrous materials to constitute

the annulus fibrosus (AF) and isotropic gels to recreate the nucleus pulposus (NP).[8-15] We have shown previously a composite TE-IVD that leveraged the cell-driven contraction of collagen type I gels around alginate cores that demonstrated promising results *in vitro* and *in vivo* in the murine caudal spine and the canine cervical spine.[9,15] Our implants restored near native function and tissue integration in rat tails up to 6 months, and stably implanted TE-IVDs maintained cell viability and integration into host tissue in the canine model for 16 weeks. However, retention of TE-IVDs in the disc space remained to be achieved in 50% of the implanted canine segments. Displacement of TE-IVDs during surgery led to destabilization of the motion segment and collapse of the endplates resulting in conditions similar to disc degeneration when implants were displaced through the ventral side.

The benefit of employing a soft engineered implant with a relatively compliant mechanical integrity lies in the ability of the TE-IVD to mature in a dynamically stimulated environment while facilitating integration with surrounding host tissues. The collagen scaffold that constitutes the AF in TE-IVDs undergoes remodeling due to the metabolic activity of embedded cells and the organization of its fibers into a structure that mimics the native disc is enabled by the initial concentration and contractibility of the gel scaffold.[16] Notably, TE-IVDs were shown to increase collagen and proteoglycans content by a factor of 10 over the course of 6 months *in vivo*, during which time the ECM integrated into neighboring vertebrae and provided physiological levels of mechanical function to the motion segment as assessed from static and dynamic aggregate moduli.[9] Furthermore, we observed that all TE-IVDs at the C3/C4 level remained stable in the canine spines *in vivo*, while all TE-IVDs implanted at C5/C6 were displaced likely due to variations in size and angle of the VBs.[15] Based on this previous work, we have identified two main challenges contributing to segment instability after placement of TE-IVDs: 1) mechanical robustness within the motion

segment is limited because the implant needs to be immature to promote integration; 2) vertebral anatomy of motion segments varies by level and is suspected to affect the stability of implantation, which results in implant migration out of the disc space. Axial dynamic distraction using an external fixator alone and in combination with cell therapy have been shown to promote disc repair in rabbit IVDs.[17-19] To achieve IVD implant retention and prevent collapse of the disc space, external fixation of the vertebral bodies (VBs) has also been shown to provide stability in rodent caudal spines.[20-21] Although the disc space height was maintained in these animal models, the implants were not exposed to physiologic loading, which was integral for TE-IVD maturation, integration to host tissue, and restoration of mechanical function. A bio-resorbable fixation system made of 85:15 polylactic-co-glycolic acid (PLGA) plates and screws (Rapidsorb®, Depuy Synthes Co. Johnson & Johnson, West Chester, PA), widely used for cranio-maxillofacial trauma, provides an alternative for temporary and gradually dynamic stabilization of spine motion segments. The PLGA in this commercially available stabilization system has been well characterized for its biocompatibility and resorption kinetics, and is FDA approved for *in vivo* reconstructive procedures.

To address these shortcomings, we asked whether TE-IVD implantation assisted by a resorbable plating system restores motion segment stiffness and prevent implant extrusion under axial compression, thereby improving overall stability of the treated segment. This PLGA system has been rated by the manufacturer to retain 85% of its strength for up to 8 weeks, while its bulk resorption is expected to occur within 12 months. A resorbable plate can enhance short term mechanics and keep the implant in place while the engineered tissues mature; however, the ability of resorbable plates to stabilize motion segments in combination with an engineered implant has not been shown. Our objectives with this study were to evaluate the restoration of the compressive mechanics of motion segments with a combined treatment approach of TE-

IVD implanted with a PLGA fixation system and identify the ability of these resorbable plates to prevent implant extrusion.

Materials and Methods

Cell isolation and TE-IVD fabrication

We adapted the cell preparation methods from previously established protocols.[8-9] Briefly, we harvested cervical IVDs from three skeletally mature canine spines (18-36 months of age, Marshall BioResources, North Rose, NY), washed them in phosphate-buffered saline (Dulbecco's PBS, MediaTech, Manassas, VA) with 1% antibiotic-antimycotic solution (AbAm, 100 µg/mL penicillin, 100 µg/mL streptomycin, and 2.5 µg/mL amphotericin B, MediaTech), and diced the nucleus pulposus (NP) and annulus fibrosus (AF) tissue regions separately. After digesting NP and AF tissues in 0.3% wt./vol. collagenase type II (Worthington Biochemical Corp., Lakewood, NJ) at 37 °C for 12 hours, we filtered the digested tissue solutions through a 100 µm nylon mesh (BD Biosciences, Bedford, MA). Subsequently, we cultured the NP and AF cells separately in Ham's F-12 media (MediaTech) containing 10% fetal bovine serum (Gemini BioProducts, Sacramento, CA), 1% AbAm, and 25 µg/mL ascorbic acid (Sigma-Aldrich, St. Louis, MO) to confluence.

Similarly, we based the TE-IVD fabrication process on established techniques.[9,15] First, we mixed encapsulated canine NP cells (25 x 10^6 cells/mL) in 3% wt./vol. alginate (FMC BioPolymer, Philadelphia, PA) two-to-one with a 0.02 g/mL calcium sulfate (Sigma-Aldrich) solution. Then, we injected the mixture into customized 3D-printed molds with cylindrical cavities made of acrylonitrile butadiene styrene plastic on a Ultimaker 2+ (Ultimaker North America, Cambridge, MA) to produce tissue-engineered NPs. After one hour of immersion in 60 mM calcium chloride (Sigma-Aldrich), we removed and placed the engineered NPs in the center of each well

of a 12-well plate. Next, we mixed an acidic 6 mg/mL collagen stock solution prepared from rat tail tendon fibers (Sprague Dawley, 7-8 weeks old, Pel-Freez Biologicals, Rogers, AR) with a basic solution (10x PBS, 1 N sodium hydroxide, and 1x PBS), in which we seeded canine AF cells (2 x 10^6 cells/mL) to obtain a final concentration of 4 mg/mL. Finally, we created tissue-engineered AF layers by surrounding the engineered NPs with 1.5 mL of the resulting collagen/AF solution and allowing gelation at 37 °C for 30 min. Following gelation, we added 1mL of previously described culture media to each well and cultured the TE-IVDs for 4 weeks with media changes twice a week. TE-IVD implants were made of the same cylindrical shape with an elliptical cross-section for all motion segment levels.

In addition, we also prepared a group of acellular TE-IVDs by adapting the protocol for high density collagen preparation as described previously.[22] Briefly, we prepared and mixed collagen gel stock solutions at 20 mg/mL from collagen type I of the previously described source with the corresponding basic formulation to obtain a final concentration of 10 mg/mL. Then, we poured the resulting neutralized collagen solution into each well of 24-well plates and allowed gelation at 37 °C for 30 min before removing 8-mm biopsy punches to simulate mature TE-IVDs. Thereafter, we maintained these collagen plugs in PBS bath until used for displacement tracking.

Motion segment preparation

To prepare specimens for testing, we obtained eight cervical spines of skeletally mature canines (18-36 months of age, Marshall BioResources) and dissected motion segments from levels C2/C3 through C5/C6 by isolating the IVDs with the vertebral bodies on the adjacent cranial and caudal sides from all nerves, dorsal spinous processes, corresponding ligaments, and other soft tissues surrounding the IVD (Figure 3.1A). We kept the spines frozen after they were harvested from the donor animals and thawed

them at room temperature before isolating the individual motion segments for further testing. We divided the specimens into two cohorts corresponding to the two distinct testing setups to test the biomechanical response of motion segments and to assess the implant retention in the disc space. For the first cohort of motion segments, we allocated four spines and isolated motion segments from levels C2/C4 to C4/C5 (N=3 per spine) through bisection of each VB transversally such that each specimen comprised a native IVD with cranial and caudal endplates intact and half of its corresponding VBs cut (Figure 3.1D). For the second cohort, we isolated motion segments from the levels C3/C4 and C5/C6 of four spines (N = 2 per spine) by removing the adjacent C2/C3 and C4/C5 IVDs such that units of IVD with their corresponding cranial and caudal VBs remained intact. Afterwards, we embedded the VBs of these motion segments in dental molding cement (COE Tray Plastic, GC America, Alsip, IL) maintaining alignment of the long axis of the segment perpendicular to the top and bottom ends of the potting molds (Figure 3.1F).

We tested each specimen in each of the following conditions: (1) as intact (CTRL); (2) after discectomy (DX); and with an implanted TE-IVD (3) without a resorbable plate (PLATE-) or (4) with the plate (PLATE+) (Figure 3.1D). Following initial testing of intact segment, we performed a standard discectomy making a box-like incision through the ventral side and along the IVD/endplate interface followed by AF/NP extraction while preserving the posterior longitudinal ligament. After testing specimens under DX conditions, we inserted 4 mg/mL TE-IVDs into empty disc space of the first cohort and acellular 10 mg/mL TE-IVDs for the second cohort. We prepared fixation plates by cutting longitudinally along the centerline of an 85:15 PLGA plate of 2 x 18 – 2.0 mm holes (Rapidsorb® Rapid Resorbable Strut Plate, Depuy Synthes Co., West Chester, PA) and trimming transversally every two holes into fragments that appropriately matched the distance between endplates on the ventral side of each

segment (Figure 3.1B-C). Since displacement of TE-IVDs occurred ventrally *in vivo*, we aimed to apply the smallest possible plate that minimized the profile on the cervical spine motion segment. Following implantation of TE-IVDs and testing on all specimens, we sanded the cranial and caudal endplates on the ventral side of each segment to fit the resorbable plate closely to the VB. We secured the plate at the ventral midline of each specimen with two 85:15 PLGA screws measuring 2 mm diameter by 6.0 mm long (Rapidsorb® Rapid Resorbable Cortex Screw, Depuy Synthes Co., West Chester, PA), after drilling and tapping holes through the endplates, one in each of the VBs (Figure 3.1D). We chose not to mount wider plates or larger screws, because they would require a more invasive resection of the bony parts of the VBs upon implantation and could interfere with soft tissue structures surrounding the motion segments under *in vivo* conditions.

Biomechanical testing

We implemented two separate testing protocols: (1) multi-step stress relaxation tests to measure the biomechanical response of motion segments under unconfined compression; and (2) continuous compression at constant strain rate to assess the migration of the implanted TE-IVD. First, we took measurements of the VB dimensions, the outer IVD diameter, and disc height with calipers on the CTRL specimens. For the VB, we measured the distance between the contour of the endplate where the AF attaches and the edge of the VB that was cut after isolation from the cervical spine, as well as the major and minor axes of the cranial and caudal VBs. For all experimental conditions, we considered half the average disc space between endplates at the outer AF as the nominal height. Furthermore, we assumed rigid body motion for the VB and endplate, and that the change in IVD area between testing conditions was negligible. As such, all the axial deformations that occurred under each testing condition were assumed to be in the IVD. Subsequently, we reported the average measured height of the outer

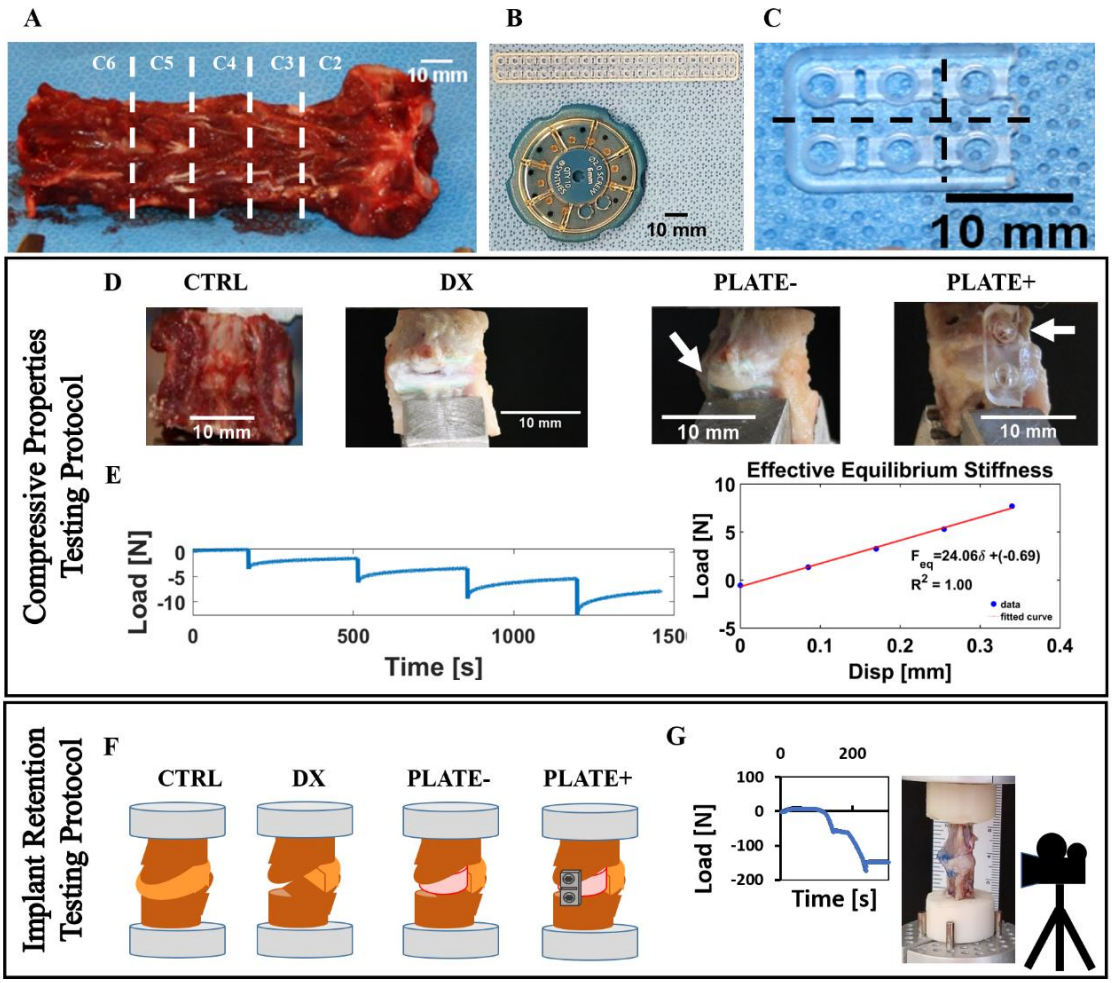

Figure 3.1. A) Preparation of motion segment from levels C2/C3 to C4/C5 (dotted lines indicate vertebrae levels) for mechanical testing. B) Close-up image of PLGA plates and screws as supplied by manufacturer. C) Close-up detail of directions of cuts in PLGA plate (dotted lines) D) Sample images of the motion segments under the examined conditions. E) Testing protocol and setup used to assess the biomechanical response of a motion segment; curves show a sample of loading vs. time for stress relaxation conditions and a sample of the resulting load vs. displacement used to calculate segment stiffness. F) Representation of the motion segments with VBs fixed in dental cement; PLATE- and PLATE+ depict prepared specimens for implant motion tracking. G) Sample of a loading curve resulting from the constant strain rate protocol and setup used to track implant migration in a PLATE- specimen.

AF for DX, PLATE-, and PLATE+ groups as ratios of disc space height to intact segment under each condition.

For the first protocol, we clamped the caudal VB portion of the specimen to the load cell on a mechanical testing system (ELF 3200, EnduraTech, Eden Prairie, MN), while an impermeable plate applied 5% compressive strain steps up to 15% strain on the cranial VB portion (Figure 3.1E).[9,23] During each of the intact and experimental conditions described above, we kept the specimens surrounded by a gauze soaked with PBS (MediaTech) containing protease inhibitors (Roche Diagnostics, Indianapolis, IN). From the resulting load-displacement data, we calculated an effective stiffness for the motion segment in equilibrium, and data from DX, PLATE-, and PLATE+ groups were normalized against their corresponding CTRL segments to calculate ratio of stiffness to intact segments under each condition.

For the second protocol, we clamped the potted VB of the specimen on its caudal end to the testing frame, while an impermeable plate compressed uniaxially at 0.5% strain/sec until segment collapse (Figure 3.1G). To track migration of acellular TE-IVDs in segments, we recorded the uniaxial compression tests at 30 frames per second. We used a video camcorder (Sony CX440 Handycam®, Sony Corp.) fixed on a tripod and controlled exposure settings and frame to focus on the disc space between endplates (Figure 3.3A).

Image analysis and digital image correlation

We matched the frames of the resulting videos to the compression test at constant strain rates and selected the frames corresponding to 5% strain until collapse (Supp. videos S3.1 and S3.2). Then, we used open source digital image correlation software (Ncorr v.1.2)[24] to quantify two-dimensional displacements at the region of interest (ROI) within the disc space corresponding to the TE-IVD and the remaining AF

tissues (Figure 3.3A). From the radial (horizontal) and axial (vertical) displacement maps (Figure 3.3B), we computed average magnitudes of the resultant displacement vectors in the ROI at discrete distances along the segment diameter between the ventral and dorsal sides of the disc space. To discretize the disc space, first we normalized the horizontal values of the ROI to this segment diameter and centered nominal radial locations around the mid-axis of the disc space (x=0). Then, we reported the mean displacements at each nominal radial location as the average of the values from the cranial endplate (y = 0) to the caudal endplate (y = disc space height) while excluding the empty background. We chose to compare the average magnitudes of PLATE- and PLATE+ experimental groups at 50% strain, since these were the maximum allowable strain of the intact motion segments corresponding to these groups (Figure 3.3C-D, Suppl. figures 3.5-3.8).

Statistical analysis

We reported all data as mean ± standard deviation and evaluated data distribution in boxplots. For the biomechanical analysis, we conducted a repeated measures analysis of variance to compare the effect of segment level (C2/C3 to C4/C5) on the ratio of segment stiffness to intact segment in equilibrium over the experimental conditions DX, PLATE-, and PLATE+. We then used Tukey honest-significance difference post-hoc tests to identify significant differences at $p < 0.05$, with the Statistics and Machine Learning Toolbox of MATLAB R2017 (Mathworks, Natick, MA). For the image processing data, we used R (R-Studio, Boston, MA) and the *lme4* function[25] to perform a linear mixed effects analysis of the relationship between vector displacement magnitudes and treatment at discrete radial locations of un-plated and plated segments. As fixed effects, we considered treatment (PLATE- vs. PLATE+), nominal radial location (x = -1 on ventral side to x = 1 on dorsal side), and segment level (C3/C4 vs.

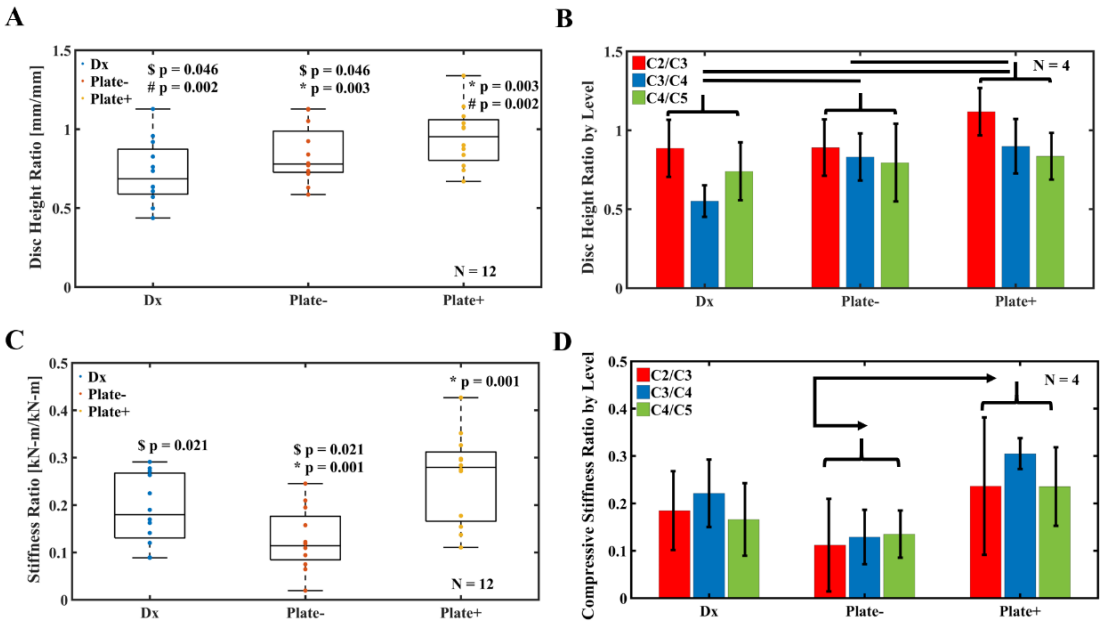

Figure 3.2. A) Disc space height changes under the examined conditions for all motion segments normalized to their corresponding intact CTRL segments; $ $p < 0.05$ between DX and PLATE-, # $p < 0.05$ between DX and PLATE+, and * $p < 0.05$ between PLATE- and PLATE+. B) Disc height ratio for motion segments at each level between C2 and C5 grouped by testing condition (lines correspond to the pairs of conditions with $p < 0.05$). C) Compressive stiffness of all motion segments for each experimental condition normalized to their corresponding intact CTRL segments; $ $p < 0.05$ between DX and PLATE-, and * $p < 0.05$ between PLATE- and PLATE+. D) Compressive stiffness ratio for motion segments at each disc level between C2 and C5 grouped by testing condition (arrows signal the pairs of conditions with $p < 0.05$). Boxplots show the data of all segment levels combined and their distribution through their median and quartiles, while bar graphs data for each level as mean ± standard deviation.

C5/C6) along with the two-factor interaction terms for treatment. As random effects, we accounted for intercepts for spine (N =4) and for the interaction between spine and level. We identified significant differences at $p < 0.05$ using Tukey adjustments for multiple comparisons.

Results

Disc space height restoration

Motion segments with implanted acellular TE-IVDs and resorbable plates attached on the ventral side recovered initial height of the disc space before loading. Motion segments under PLATE+ condition reached significantly higher disc height than either DX ($p = 0.002$) and PLATE- ($p = 0.003$). While there were no marked differences in changes of disc space height between levels C2/C3, C3/C4, and C4/C5 (Figure 3.2B), the disc space height of all motion segments dropped by almost 30% when discectomized compared to the CTRL condition. TE-IVD implantation alone increased the disc space height ratio to 0.84 ± 0.18, while plating in addition to the implant recovered up to 134% of original disc height (Figure 3.2A).

Motion segment stiffness preservation

In equilibrium, plating partially restored segment stiffness to more than 25% of the intact motion segment magnitudes of 60.9 ± 30.9 kN-m. Segments in PLATE+ group showed a significant two-fold increase in stiffness ($p = 0.001$) when compared to the PLATE- group (Figure 3.2C). The stiffness of segments in DX group dropped by more than 80% of their CTRL stiffness and the stiffness ratio of PLATE- group segments to CTRL decreased even further at 0.13 ± 0.07. Segment stiffness ratios in PLATE+ and DX groups were statistically similar, despite the notable increase in disc height and more than 41% difference between their stiffness ratio to CTRL.

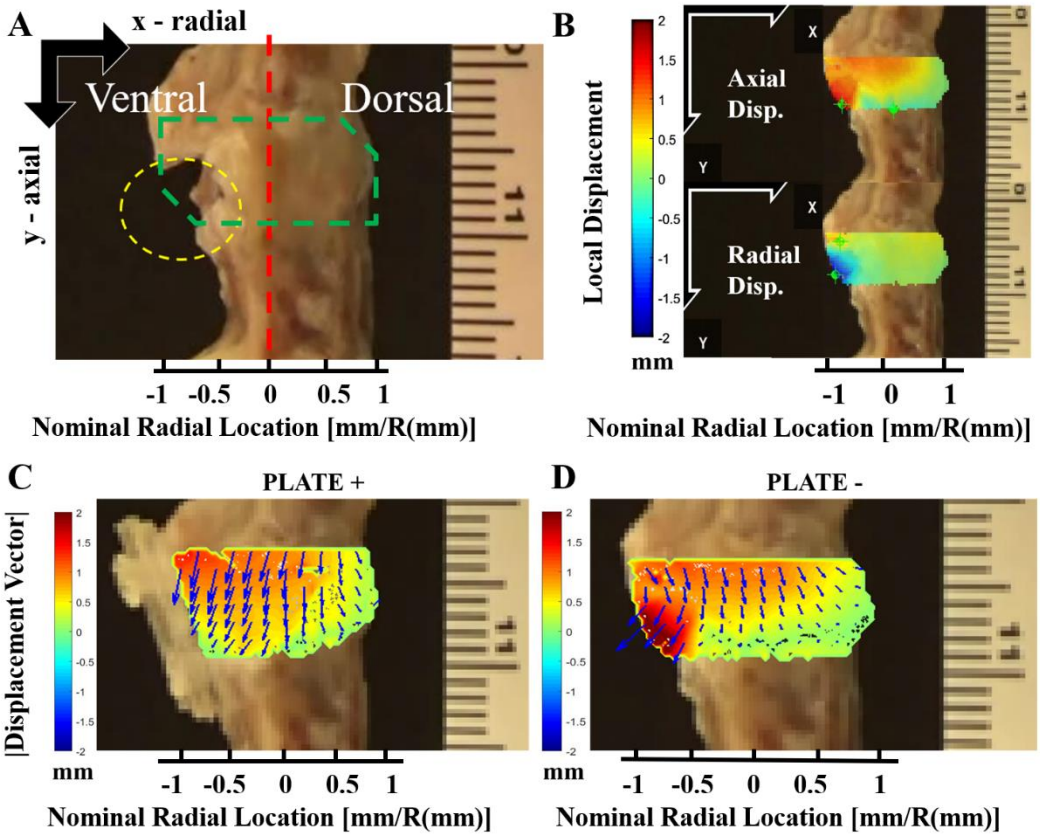

Figure 3.3. A) Representative frame used to track implant migration in a motion segment and reference axes for the positive convention in the radial and axial directions; red dotted line shows central axis used to distinguish ventral and dorsal sides of the frame, green dotted line encloses the ROI within the disc space where displacement was computed, and yellow dotted ellipse encircles the sub-region where TE-IVD was located. B) Samples of 2-D displacement maps for magnitudes in the axial (top) and radial (bottom) orientations; color intensity values represent the local displacements in mm following the positive sign convention displayed by the axes in each of the corresponding orientations. C) Representative plated segment with resultant vectors of displacement (blue arrows) and magnitudes (colormap). D) Representative un-plated segment with resultant vectors of displacement (blue arrows) and magnitudes (colormap). Combined vector fields and colormaps of displacements follow the established signed convention (positive downwards axially and to the right radially).

Differences between stiffness ratio to CTRL were not significant across C2/C3, C3/C4, and C4/C5 levels (Figure 3.2D).

Improved implant retention

Attaching the plate prevented extrusion of the implant through the ventral side of all motion segments at 50% strain. The average magnitudes of vector displacements in the ROI were markedly affected by the nominal location along the radial direction ($p < 2.2 \times 10^{-6}$), by the treatment groups PLATE+ against PLATE- ($p = 6.1 \times 10^{-7}$), and by the combined interactions of treatment with segment level ($p = 1.3 \times 10^{-9}$). Notably, the average displacements in the disc space remained below 0.6 mm in the dorsal side, while the average displacements occurring in the ventral side exceeded 1.1 mm. The specific region located between 30% distance from the center in the ventral side and 100% distance from the center in the dorsal side (dorsal edge) delimited where average displacements were significantly lower across all treatments and levels. The maximum displacements of the acellular TE-IVDs recorded in the PLATE- group were observed consistently at the caudal endplate near the extrusion site (Figure 3.3D, Suppl. figure 3.7), while the maximum displacements in the PLATE+ group were distributed along the cranial endplate (Figure 3.3C, Suppl. figure 3.8).

Plating reduced implant migration between 8-32% (Figure 3.4A) at discrete locations of the disc space. Segments from PLATE+ group had significantly lower average displacement magnitudes than those from PLATE- group at nominal radial locations between 80% and 50% distance from the center on the ventral side, corresponding to the region where the implant was located (Figure 3.3C-D and 3.4B). We observed that implants were partially expelled from the disc space by 5-10% strain and 15-25% strain in PLATE- segments, at C5/C6 and C3/C4 respectively. This trend was consistent with the statistical inference that plating was more effective in reducing

implant migration at C3/C4 segments ($p < 0.0001$), than in C5/C6 segments ($p = 0.41$) (Suppl. table 3.1). Nevertheless, different levels had no significant fixed effects on average displacements at the ROI. There were also no significant random effects observed between spines and combining spines with levels.

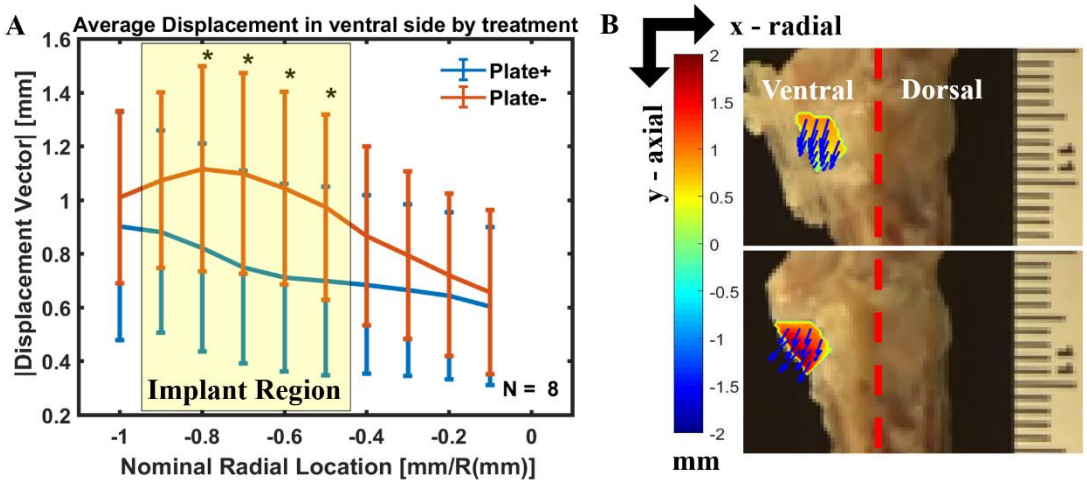

Figure 3.4. A) Processed displacement vector magnitudes measured in the ventral side of the selected ROI in all C3/C4 and C5/C6 motion segments; yellow box corresponds to the region where the TE-IVD was located; * $p < 0.05$ represent significant differences between PLATE- and PLATE+ at the corresponding radial location; data are shown as mean ± standard deviation. B) Representative frames of PLATE+ (top) and PLATE- (bottom) with resulting displacement vector fields and magnitude colormaps specifically corresponding to the implant migration (outlined in yellow).

Discussion

In the present study, we tested the hypothesis that resorbable plating improved stiffness of canine cervical spine motion segments *in vitro* and prevented the extrusion of implanted TE-IVDs from the disc space. We demonstrated that the combination of TE-IVDs implanted with PLGA plates reconditioned motion segment stiffness in compression by restoring the disc space height after discectomy and stabilizing the segment, while retaining the implant in place. Previous efforts of total disc replacement with a combined approach of tissue-engineered implants and external fixation focused

on preventing segment collapse and implant displacement.[20] However, there has been no previous work demonstrating the ability of an implantable bio-resorbable fixation system to restore motion segment stability while preserving disc space height and retention of an engineered implant.

The PLGA temporary stabilization system adequately addresses our findings in the *in vivo* canine model of cervical disc replacement,[15] where some TE-IVDs displaced ventrally. While implanted TE-IVDs alone were able to retain up to 70% of healthy control disc height in motion segments *in vivo* and more than 80% of intact CTRL disc height *in vitro* (Figure 3.2A-B), only with the attachment of the plate we observed complete recovery of disc space height. The relative rigidity of the PLGA plate compared to the hydrogel-based TE-IVDs and the fixation of the PLGA screws through the endplates contributed to the increase in disc height after discectomy. Since attachment of the PLGA screws was performed in an angular fashion from the sanded surface on the ventral side of the caudal and cranial endplates through the VBs, the rigid straight plate was fit closely to the implanted TE-IVD, thus effectively restoring distraction of the VB in the PLATE+ group before loading. In preliminary studies, TE-IVDs demonstrated apparent equilibrium moduli in compression that ranged in the 0.5-5 kPa, which remains orders of magnitude lower than the 0.03-5.96 MPa apparent equilibrium modulus observed in the intact cervical spine segments gathered *ex vivo*. Meanwhile, the PLGA copolymer that constitutes the plates and screws has an initial elastic modulus of 3.1 GPa and an ultimate tensile strength of 66 MPa.[27] The combined approach in PLATE+ segments achieved sufficient mechanical robustness to partially restore intact CTRL segment stiffness (Figure 3.2C-D) when compared to PLATE- segments; therefore, this partial mechanical support allows for continuous load sharing and dynamic mechanical stimulation to the TE-IVD, while transferring loads through the endplates. Furthermore, preliminary tests of cervical spine segments without

resecting the posterior elements and soft tissues revealed that between 60-80% of compressive loads applied onto intact motion segments are shared by these additional tissues. The relative similarity of the intact stiffness ratio between DX and PLATE+ groups likely results from the contact between endplates after DX which confounds the rigidity of an empty disc space with that of a treated segment.

The resorbable plate is expected to provide temporary structural biomechanical support while promoting implant integration in the first 4 to 16 weeks, since the PLGA plate degrades between 4 and 12 months.[26] Faster degradation kinetics *in vitro* than in human maxillofacial bones *in vivo* have been shown previously with PLGA implants; however, the stiffness of intact explants upon isolation from the surrounding fibrous tissue and bone could not be tested.[27] Due to the slower degradation observed clinically in this case, the copolymer implant was expected to retain its bending strength for longer periods than the 75 days tested *in vitro*. It should be noted that the contraindications of the Rapidsorb® fixation system warn against its use in load-bearing applications, unless in conjunction with traditional rigid fixation. In human patients, a combined ACDF approach of a polyether ether ketone (PEEK) spacer with resorbable materials such as poly (L-lactide-co-D, L-lactide) (PDLLA) has been shown to provide similar fusion progress and stability than traditional titanium fixation;[28] however, our intent with this study was to provide temporary stabilization to the implanted TE-IVD instead of promoting rigid fixation of the motion segment. In this context, degradation of the PLGA system is expected to promote a gradual change in load distribution between the TE-IVD and the PLGA plate, unlike the case of existing interbody spinal fusion techniques and external fixation devices previously evaluated in human cadaveric spines.[29-32] Mackiewicz et al. confirmed in a finite element study that introducing highly stiff stabilizing plates into cervical spine motion segments increases stress in the endplate of adjacent segments and that plates that allow greater range of motion show

up to 30% reduction of adjacent plates resulting stress.[33] Matge et al.[34] discussed clinical and radiological observations that suggest dynamic cervical implants as a promising alternative to total disc replacement, anterior cervical discectomy and spinal fusion, and they indicate that preserving motion segment biomechanics reduces stress on facet joints and development of adjacent segment disease. The advantage of our combined approach over existing interbody cage designs and dynamic cervical prosthetics remains in that our TE-IVD has been shown to remodel over time and mature to restore the mechanical function of spine segments to native conditions, when stably implanted and fully engrafted.[9]

The use of video recorded frames during the uniaxial continuous compression protocol and digital image correlation for data processing enabled the quantitative analysis of implant migration within the disc space. Acellular TE-IVDs were retained within the disc space of all segments under PLATE+ conditions, because the PLGA plates served as a physical barrier that prevented complete extrusion of the implants. The distribution of maximum displacements along the cranial endplate in PLATE+ segments (Figure 3.3C) suggests a shift of the implant to accommodate to the endplate shape on the cranial side. As expected, the location of maximum displacements of the PLATE- segments occurred at the implantation site where the space with least resistance remained open (Figure 3.3D), since the inclined shape of the endplate in the ventral side combined with the lack of anchoring for the implant resulted in a wedge-like extrusion. These observations were consistent with the mechanism of extrusion observed in the displaced implants of our *in vivo* canine study.[15] The significant reduction of implant migration in PLATE+ at locations in the ventral side further supports the ability of resorbable plating to retain the TE-IVD inside the disc space (Figure 3.4). Furthermore, the relatively similar displacement profiles observed in all segments outside of the 50% to 80% range of radial distance from central axis suggests that spine flexibility and

overall range of motion around the location of the implant remains unaffected. The quantitative analysis of implant migration also revealed level-dependent differences in the efficacy of our combined treatment approach. Displacements of TE-IVDs were more effectively reduced at C3/C4-level PLATE+ segments than in those of levels C5/C6 (Suppl. table 3.1), likely due to the anatomic differences at the endplates of both segments. These differences were also reflected *in vivo* where 66.67% of the stably implanted TE-IVDs were located in C3/C4-level segments, while 100% of the TE-IVDs implanted in the C5/C6-level segments were displaced.[15] In human cervical spines, marked anatomic differences exist between superior and inferior endplates at upper level and lower level segments.[35-36] These findings provide further insights into the careful considerations that need to be taken when deciding location of implants in cervical motion segments. Whereas the reported measurements of displacement are limited to the resultant sum of local deformations caused by the applied load from those caused by rigid body motion, these parameters provide a quantitative estimate of segment motion under uniaxial compression. Future studies could benefit of differentiating texture to enhance segmentation of the implant and the surrounding tissues within the image and multiple projections to capture a three-dimensional range of motion.

Several limitations in this work warrant important discussion when interpreting our findings within the context of an *ex vivo* model of an *in vivo* scenario. First, this study only assesses the compressive stiffness uniaxially, which does not recapitulate accurately what occurs in the physiological environment *in vivo*. However, our motivation for uniaxial mechanical testing was based on the intraoperative observations where the implants migrated out of the disc space solely from the deformations applied in axial compression upon removal of the distractor pins.[15] Furthermore, with the assistance of the surrounding muscles and ligaments, individual cervical spine segments

in quadrupeds are mainly loaded under axial compression to balance the bending moments from the weight of the head and neck.[45] Challenges remain in characterizing the biomechanical response of motion segments with our proposed treatment under cyclic loading or fatigue, both of which are also relevant in spine biomechanics and help inspect modes of failure in the system. Future work should investigate dynamic testing of motion segments and their biomechanics in the full six degrees of freedom characteristic of the spine. Second, while favorable outcomes in terms of durability and minimal negative inflammatory responses have been shown in cranio-maxillo-facial approaches with several animal models using PLGA plates and screws,[37-38] their load-bearing capacity remains limited.[39] Recent work by Maenz et al.[40] with PLGA-reinforced calcium phosphate cement in ovine VBs suggests a potential use in load-bearing structures given the versatility and manufacturability of PLGA. Third, this study does not include a direct assessment of the degradation kinetics of the resorbable system and its effects on the load distribution across the VBs over time. While *in vitro* assessment of the degradation of the PLGA system could provide estimates on strength retention, the use of this resorbable system in future *in vivo* work is preferable to appropriately assess the efficacy of our proposed combined approach. Fourth, our surgical approach and modifications to the plate require further tuning to minimize the need for sanding the endplate and altering the VB profile. Since the ACDF approach is characterized by minimal invasiveness compared to dorsal or lateral fixation, we recommend exploring the attachment of customized PLGA elements that can adapt to the curvature of the ventral side of the motion segment. Lastly, anatomical differences between human and canine cervical motion segments could also have significant impact on the performance of the resorbable plate examined in this work; furthermore, canine IVDs are exposed to similar or even higher loading compared to humans.[41-47] However, the canine spine shows analogous degenerative processes to those of humans and are

regularly diagnosed and treated for disc degeneration with equivalent surgical approaches.[45-47]

This study provides valuable insights of canine motion segment biomechanics and validates a combined approach of total disc replacement with TE-IVD and an implantable resorbable fixation system. Our findings in the current study present a baseline for further *ex vivo* and *in vivo* animal studies to better discern the long-term biomechanical and integrative properties of cervical TE-IVDs stabilized by resorbable plating. In addition, the method herein described to quantify displacements at specific locations along the radius of endplate offers a tool for estimation of loads occurring at the disc in diverse surgical scenarios. This work demonstrates that the combination of an implanted TE-IVD with a resorbable plate improves implant retention by preventing ventral displacement under uniaxial compression, partially restores the compressive stiffness of intact segments by providing a shared distribution of loads and helps avert the collapse of endplates in the treated disc space.

Supplemental Data

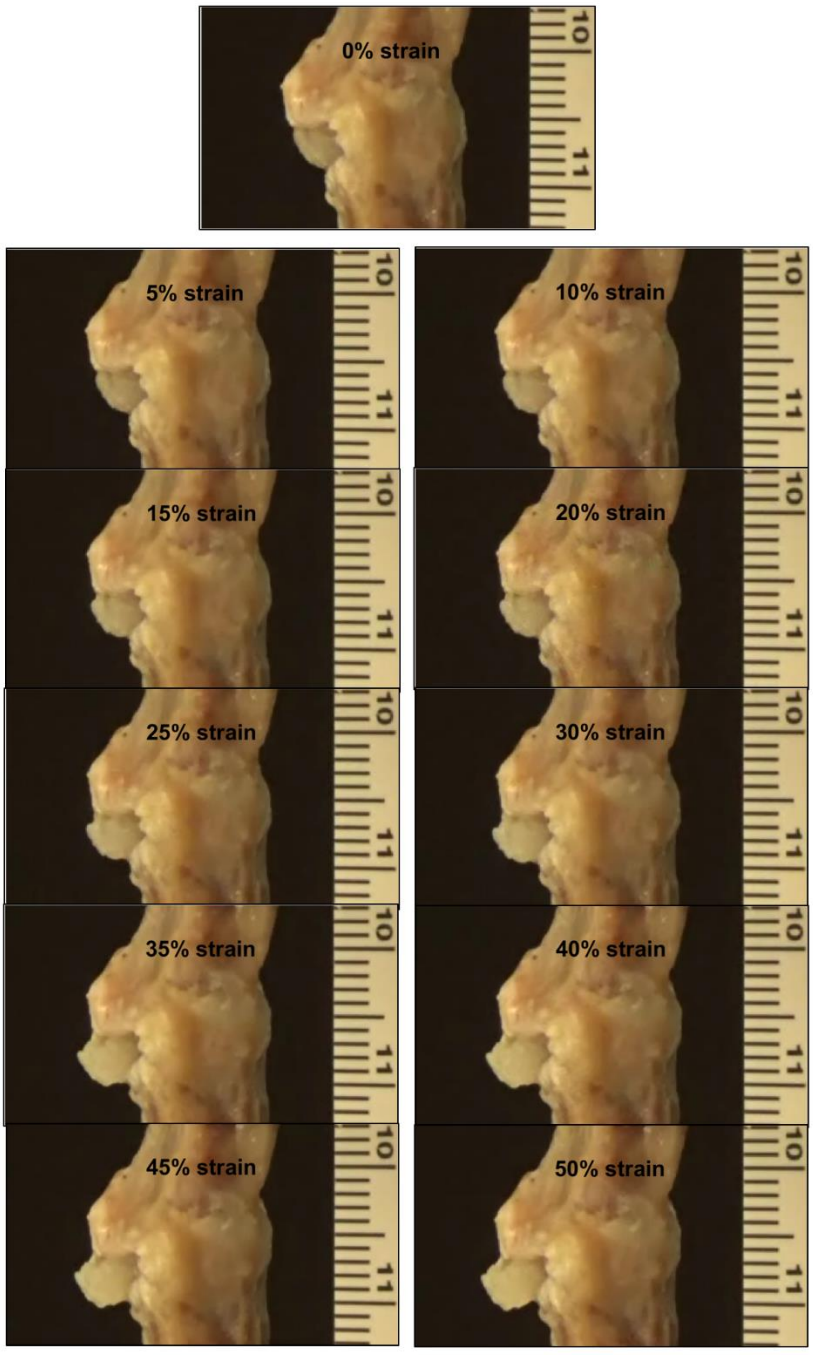

Figure 3.5. Still frames from the supplemental video of a representative PLATE-segment under uniaxial compression at 5% strain intervals up to 50% strain.

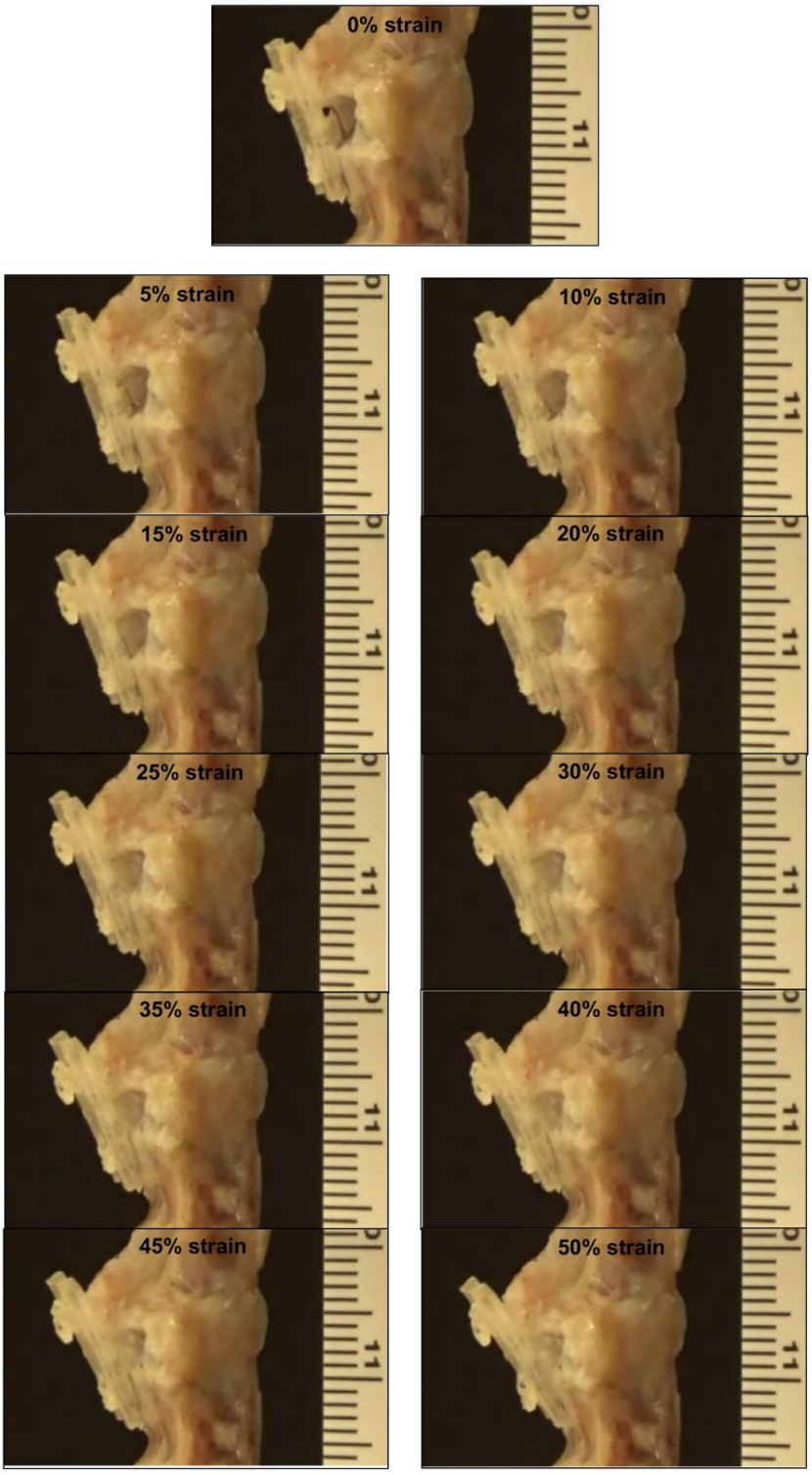

Figure 3.6. Still frames from the supplemental video of a representative PLATE+ segment under uniaxial compression at 5% strain intervals up to 50% strain.

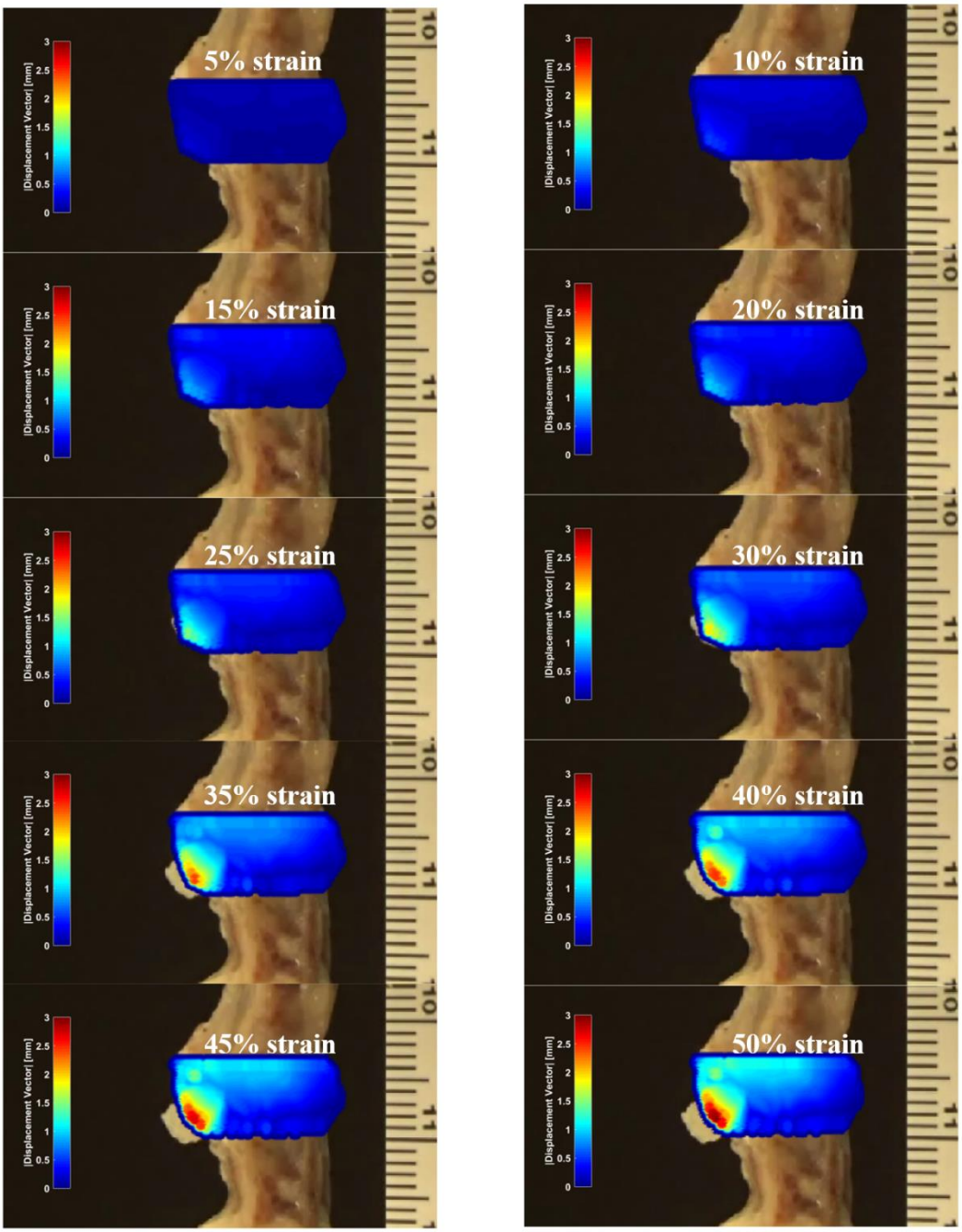

Figure 3.7. Still frames from the supplemental video of the displacement magnitude colormap in a representative PLATE- segment under uniaxial compression at 5% strain intervals up to 50% strain.

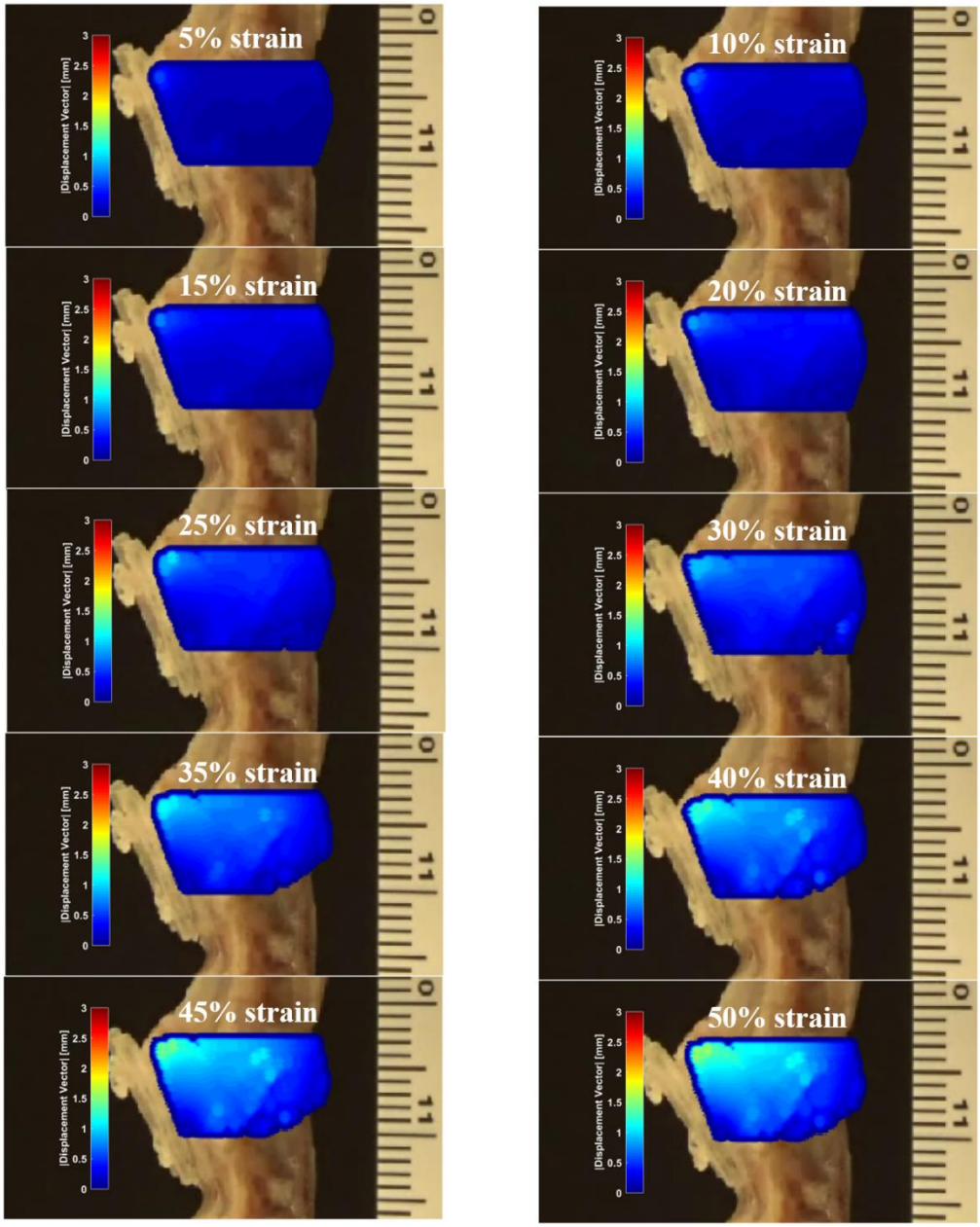

Figure 3.8. Still frames from the supplemental video of the displacement magnitude colormap in a representative PLATE+ segment under uniaxial compression at 5% strain intervals up to 50% strain.

		Treatment	PLATE+	
		Level	C3/C4	C5/C6
Treatment	Level	Avg. Disp.	0.51 mm	0.63 mm
PLATE-	C3/C4	0.78 mm	< 0.0001*	0.36
	C5/C6	0.60 mm	0.51	0.41

Table 3.1. Summary of vector displacement magnitudes averaged over the entire range of nominal radial locations from the ventral side to the dorsal side (x = -1:1 mm/R(mm)) and the resultant p-values from the multiple comparison tests at 0.95 confidence level. Data are grouped by treatment (PLATE- vs. PLATE+, and by level C3/C4 vs. C5/C6); linear mixed model analysis revealed significant differences between treatments at level C3/C4 only (* $p < 0.05$).

REFERENCES

1. Woods BI, Hilibrand AS. 2015. Cervical radiculopathy: epidemiology, etiology, diagnosis, and treatment. J Spinal Disord Tech. 28: E251-9.

2. Hillibrand AS, Robbins M. 2004. Adjacent segment degeneration and adjacent segment disease: the consequences of spinal fusion? Spine J. 4(Suppl. 6): S190-4.

3. Maldonado CV, Paz RD, Martin CB. 2011. Adjacent-level degeneration after cervical disc arthroplasty versus fusion. Eur Spine J. 20(Suppl. 3): S403-7.

4. Jawahar A, Cavanaugh DA, Kerr EJ 3rd, Birdsong EM, Nunley PD. 2010. Total disc arthroplasty does not affect the incidence of adjacent segment degeneration in cervical spine: results of 93 patients in three prospective randomized clinical trials. Spine J. 10(12): 1043-8.

5. Chang KE, Pham MH, Hsieh PC. 2017. Adjacent segment disease requiring reoperation in cervical total disc arthroplasty: A literature review and update. J Clin Neurosci. 37: 20-24.

6. Sugawara T, Itoh Y, Hirano Y, Higashiyama N, Mizoi K. 2009. Long term outcome and adjacent disc degeneration after anterior cervical discectomy and fusion with titanium cylindrical cages. Acta Neurochir (Wien). 151(4): 303-9.

7. Kelly MP, Mok JM, Frisch RF, Tay BK. 2011. Adjacent segment motion after anterior cervical discectomy and fusion versus Prodisc-c cervical total disk arthroplasty: analysis form a randomized, controlled trial. Spine (Phila Pa 1976). 36(15): 1171-9.

8. Mizuno H, Roy AK, Vacanti CA, Kojima K, Ueda M, Bonassar LJ. 2004. Tissue-engineered composites of anulus fibrosus and nucleus pulposus for intervertebral disc replacement. Spine (Phila Pa 1976). 29(12): 1290-7.

9. Bowles RD, Gebhard HH, Hartl R, Bonassar LJ. 2011. Tissue-engineered intervertebral discs produce new matrix, maintain disc height, and restore biomechanical function to the rodent spine. Proc Natl Acad Sci USA. 108(32): 13106-11.

10. Park SH, Gil ES, Cho H, Mandal BB, Tien LW, Min BH, Kaplan DL. 2012. Intervertebral disk tissue engineering using biphasic silk composite scaffolds. Tissue Eng Part A. 18(5-6): 447-58.

11. Nesti LJ, Li WJ, Shanti RM, Jiang YJ, Jackson W, Feedman BA, Kuklo TR, Giuliani JR, Tuan RS. 2008. Intervertebral disc tissue engineering using a novel hyaluronic acid-nanofibrous scaffold (HANFS) amalgam. Tissue Eng Part A. 14(9): 1527-37.

12. Nerurkar NL, Sen S, Huang AH, Elliott DM, Mauck RL. 2010. Engineered disc-like angle-ply structures for intervertebral disc replacement. Spine (Phila Pa 1976). 35(8): 867-73.

13. Lazebnik M, Singh M, Glatt P, Friis LA, Berkland CJ, Detamore MS. 2011. Biomimetic method for combining the nucleus pulposus and annulus fibrosus for intervertebral disc tissue engineering. J Tissue Eng Regen Med. 5(8): e179-87.

14. Zhuang Y, Huang B, Li CQ, Liu LT, Pan Y, Zheng WJ, Luo G, Zhou Y. 2011. Construction of tissue-engineered composite intervertebral disc and preliminary morphological and biochemical evaluation. Biochem Biophys Res Commun. 407(2): 327-32.

15. Moriguchi Y, Mojica-Santiago J, Grunert P, Pennicooke B, Berlin C, Khair T, Navarro-Ramirez R, Ricart Arbona RJ, Nguyen J, Hartl R, Bonassar LJ. 2017. Total disc replacement using tissue-engineered intervertebral discs in the canine cervical spine. PLoS One. 12(10): e0185716.

16. Bowles RD, Williams RM, Zipfel WR, Bonassar LJ. 2010. Self-assembly of aligned tissue-engineered annulus fibrosus and intervertebral disc composite via collagen gel contraction. Tissue Eng Part A. 16(4): 1339-48.

17. Kroeber M, Unglaub F, Guehring T, Nerlich A, Hadi T, Lotz J, Carstens C. 2005. Effects of controlled dynamic disc distraction on degenerated intervertebral discs: an in vivo study on the rabbit lumbar spine model. Spine (Phila Pa 1976). 30(2):181-7.

18. Guehring T, Omlor G, Lorenz H, Engelleiter K, Richter W, Carstens C, Kroeber M. 2006. Disc distraction shows evidence of regenerative potential in degenerated intervertebral discs as evaluated by protein expression, magnetic resonance imaging, and messenger ribonucleic acid expression analysis. Spine (Phila Pa 1976). 31(15): 1658-65.

19. Hee HH, Ismail HD, Lim CT, Goh JCH, Wong HK. 2010. Effects of implantation of bone marrow mesenchymal stem cells, disc distraction and combined therapy on reversing degeneration of the intervertebral disc. J Bone Joint Surg Br. 92(5): 726-36.

20. Martin JT, Milby AH, Chiaro JA, Kim DH, Hebela NM, Smith LJ, Elliott DM, Mauck RL. 2014. Translation of an engineered nanofibrous disc-like angle-ply structure for intervertebral disc replacement in a small animal model. Acta Biomater. 10(6): 2473-81.

21. Iatridis JC, Mente PL, Stokes IA, Aronsson DD, Alini M. 1999. Compression-induced changes in intervertebral disc properties in a rat tail model. Spine (Phila Pa 1976). 24(10): 996-1002.

22. Puetzer JL, Bonassar LJ. 2013. High density type I collagen gels for tissue engineering of whole menisci. Acta Biomater. 9(8): 7787-95.

23. Borde B, Grunert P, Hartl R, Bonassar LJ. 2015. Injectable, high-density collagen gels for annulus fibrosus repair: An in vitro rat tail model. J Biomed Mater Res A. 103(8): 2571-81.

24. Blaber J, Adair B, Antoniou A. 2015. Ncorr: open-source 2D digital image correlation Matlab software. Exp Mech. 55(6): 1105-22.

25. Bates D, Maechler M, Bolker B, Walker S. 2015. Fitting linear mixed-effects models using lme4. J Stat Soft. 67(1): 1-48.

26. Miller RA, Brady JM, Cutright DE. 1977. Degradation rates of oral resorbable implants (polylactates and polyglycolates): rate modification with changes in PLA/PGA copolymer ratios. J Biomed Mater Res. 11(5): 711-9.

27. Landes CA, Ballon A, Roth C. 2006. In-patient versus in vitro degradation of P(L/DL) LA and PLGA. J Biomed Mater Res Part B: Appl Biomater 76B: 403-11.

28. Nabham A, Ishak B, Steimer O, Zimmer A, Pitzen T, Steudel WI, Pape D. 2009. Comparison of bioresorbable and titanium plates in cervical spine fusion – Early radiologic and clinical results. J Spinal Disord Tech. 22: 155-61.

29. Stein MI, Nayak AN, Gaskins RB 3rd, Cabezas AF, Santoni BG, Castellvi AE. 2014. Biomechanics of an integrated interbody device versus ACDF anterior locking plate in a single-level cervical spine fusion construct. Spine J. 14(1): 128-36.

30. Scholz M, Reyes PM, Schleicher P, Sawa AGU, Baek S, Kandziora F, Marciano FF, Crawford NR. 2009. A new stand-alone cervical anterior interbody fusion device: biomechanical comparison with established anterior cervical fixation devices. Spine (Phila Pa 1976). 34(2): 156-60.

31. Majid K, Chinthakunta S, Muzumdar A, Khalil S. 2012. A comparative biomechanical study of a novel integrated plate spacer for stabilization of cervical spine: an in vitro human cadaveric model. Clin Biomech (Bristol Avon). 27(6): 532-6.

32. Wojewnik B, Ghanayem AJ, Tsitsopoulos PP, Voronov LI, Potluri T, Havey RM, Zelenakova J, Patel AA, Carandang G, Patwardhan AG. 2013. Biomechanical evaluation of a low profile, anchored cervical interbody spacer device in the setting of progressive flexion-distraction injury of the cervical spine. Eur Spine J. 22(1): 135-41.

33. Mackiewicz A, Banach M, Denisiewicz A, Bedzinski R. 2015. Comparative studies of cervical spine anterior stabilization systems – finite element analysis. Clin Biomech (Bristol Avon). 32: 72-9.

34. Matge G, Berthold C, Gunness VR, Hana A, Hertel F. 2015. Stabilization with the dynamic cervical implant: a novel treatment approach following cervical discectomy and decompression. J Neurosurg Spine. 22(3): 237-45.

35. Chen H, Zhong J, Tan J, Wu D, Jiang D. 2013. Sagittal geometry of the middle and lower cervical endplates. Eur Spine J. 22(7): 1570-5.

36. Lou J, Liu H, Rong X, Li H, Wang B, Gong Q. 2016. Geometry of inferior endplates of the cervical spine. Clin Neurol Neurosurg. 142: 132-6.

37. Park S, Kim JH, Kim IH, Lee M, Heo S, Kim H, Kim EH, Choy YB, Heo CY. 2013. Evaluation of poly (lactic-co-glycolic acid) plate and screw system for bone fixation. J Craniofac Surg. 24(3): 10231-5.

38. Wiltfang J, Merten HA, Schultze-Mosgau S, Schrell U, Wenzel D, Kessler P. 2000. Biodegradable miniplates (LactoSorb): long-term results in infant minipigs and clinical results. J Craniofac Surg. 11(3): 239-43.

39. Altan A, Damlar I, Sahin O. 2016. Can resorbable fixation screws replace titanium fixation screws? A nano-indentation study. J Oral Maxillofac Surg. 74(7): 1421.e1-5.

40. Maenz S, Brinkmann O, Kunisch E, Horbert V, Gunnella F, Bischoff S, Schubert H, Sachse A, Xin L, Günster J, Illerhaus B, Jandt KD, Bossert J, Kinne RW, Bungartz M. 2017. Enhanced bone formation in sheep vertebral bodies after minimally invasive treatment with a novel, PLGA fiber-reinforced brushite cement. Spine J. 17(5): 709-19.

41. Lotz JC. 2004. Animal models of intervertebral disc degeneration: lessons learned. Spine (Phila Pa 1976). 29(23): 2742-50.

42. O'Connell GD, Vresilovic EJ, Elliott DM. 2007. Comparison of animals used in disc research to human lumbar disc geometry. Spine (Phila Pa 1976). 32(3): 328-33.

43. Showalter BL, Beckstein JC, Martin JT, Beattie EE, Espinoza Orias AA, Schaer TP. 2012. Comparison of animal discs used in disc research to human lumbar disc: torsion mechanics and collagen content. Spine (Phila Pa 1976). 37(15): E900-7.

44. Lim TH, Goel VK, Weinstein JN, Kong W. 1994. Stress analysis of a canine spinal motion segment using the finite element technique. Journal of biomechanics. 27(10): 1259-69.

45. Smit TH. 2002. The use of a quadruped as an in vivo model for the study of the spine - biomechanical considerations. Eur Spine J. 11(2): 137-44.

46. Bergknut N, Rutges JP, Kranenburg HJ, Smolders LA, Hagman R, Smidt HJ. 2012. The dog as an animal model for intervertebral disc degeneration? Spine (Phila Pa 1976). 37(5):351-8.

47. Cole TC, Burkhardt D, Ghosh P, Ryan M, Taylor T. 1985. Effects of spinal fusion on the proteoglycans of the canine intervertebral disc. J Orthop Res. 3(3): 277-91.

CHAPTER 4

Seeding density of human mesenchymal stem cells modulate the structure and composition of tissue-engineered intervertebral discs with high-density collagen annulus fibrosus

Abstract

Tissue-engineered whole intervertebral discs (TE-IVDs) have been previously shown to restore mechanical function in the rodent spine and promote cell viability and integration in the canine spine. However, the *in vitro* development of constructs that reach close-to-native IVD stiffness and composition properties remains an active area of study. In the present work, we assessed the combined effects of high-density collagen (10-20 mg/mL) annulus fibrosus (AF) scaffold and highly-contractile human mesenchymal stem cells (hMSCs) on the structural remodeling and composition of TE-IVDs. Composite TE-IVDs were fabricated, with hMSCs embedded in alginate-based nucleus pulposus as previously established, and high-density collagen (Col) seeded with hMSCs at a range between 2 and 20 million cells/mL for the AF. Structural changes in TE-IVD morphology were assessed by disc contraction measurements and apparent AF densification over 3-4 weeks. After culture, samples were examined histologically and mechanically to identify differences in tissue composition between groups. Significant morphological changes and AF cell-phenotype were observed in 10 mg/mL Col TE-IVDs at increasing seeding density with hMSCs. In 10 mg/mL Col discs, increasing seeding density 5-10 times from the previously reported baseline increased their compressive properties in a dose-dependent manner and their apparent AF density between 1.5-3.5 times their initial Col density. These effects were virtually negligible in 20 mg/mL Col discs. These findings support the potential of employing modulation of hMSCs seeding density in TE-IVDs with dense AF/collagen matrices to achieve a controllable tissue composition and structure of the remodeled AF scaffold.

Introduction

Neck and back pain are among the most debilitating conditions in the industrialized world and intervertebral disc (IVD) degeneration is linked as one of the leading causes of these afflictions.[1-9] Nearly two-thirds of the population are affected by cervical spine-related problems[7-9] and up to $100 billion in costs per year are associated with lower back pain.[10] The IVD has very limited repair capacity due to its avascular nature,[11] and while there are a variety of non-surgical and minimally invasive alternatives to treat disc degeneration, surgical intervention is required for the most severe cases when conservative treatments fail.[12] Among the standard surgical options, partial or total discectomy with spinal fusion of adjacent vertebrae, and total disc replacement with prosthetics remain the most utilized clinically. While these solutions help alleviate the pain, the underlying disc pathology continues to progress and the function of spinal segments as a unit is altered, which can lead to recurrent surgical revisions and further degeneration of the adjacent segments.[13-19]

Growing interest in developing tissue-engineering strategies as biological alternatives to traditional degenerative disc disease therapies have been observed recently. Whereas some efforts focused on separately treating damage in the annulus fibrosus (AF) or nucleus pulposus (NP) regions,[20-27] whole intervertebral disc replacement with tissue-engineered constructs remains an area of continuous improvement.[28-37] We have previously demonstrated promising results *in vitro* and *in vivo* with composite tissue-engineered intervertebral discs (TE-IVDs) that mimic the native IVD structure and employ an engineered NP made of alginate surrounded by a fibrous engineered AF made of low-density collagen type I.[34,37] Notwithstanding that these composite TE-IVDs restored mechanical function in the rodent spine and promoted cell viability and integration in the canine spine, optimum biological and

mechanical benchmarks of IVDs are yet to be developed *in vitro* before human clinical trials might be contemplated with these constructs.[38-39]

A major challenge to overcome for the successful clinical translation of TE-IVDs is to ensure that the implantable construct endures the combined loading present in the demanding mechanical environment of the spine, while maintaining enough compliance to dynamically integrate with the host tissues. The native IVD in humans has region-dependent mechanical properties, as is the case with other animal models of IVD mechanics. The equilibrium modulus ranges between 5 and 65 kPa for the NP[38-40] in unconfined compression and reference aggregate modulus has been described between 25 to 420 kPa for the AF[38,39,41-43] in confined compression. Whereas increasing the mechanical properties of engineered NPs is a logical step in enhancing the stiffness of TE-IVDs *in vitro*, alginate has been shown to achieve sufficient compressive properties to mimic the NP, especially after tissue maturation during culture.[34,40] A key contributor to the mechanical robustness of the IVD lies in the circumferentially-aligned multi-laminated structure of the AF, which possesses regional variations in extracellular matrix composition and cell morphology.[41-46] The AF is also responsible for containing both the tensile stresses that help preserve spinal range of motion and the hydrostatic pressures experienced from NP swelling. Therefore, the interplay between both tissue regions of the composite possesses far more importance in the success of an engineered construct than either one alone. To promote the development of robust TE-IVDs with biomimetic alginate-based NPs, emphasis on the extracellular matrix organization and composition in engineered AF must be critically assessed.

Due to the dominant presence of collagen in native IVDs and the functional anchorage for cells collagen provides, established work employed collagen as the basis for AF scaffolds and relied on cellular contraction and remodeling to produce stiff

composite structures and elicit tissue integration in AF repair.[31,47-50] Whole disc engineering has long benefited from achieving the desired structural organization of oriented collagen fibers at the AF region with low-density (1-4 mg/mL) collagen formulations. In contrast, high-density formulations (10-20+ mg/mL) have been extensively used for other tissue engineering applications, such as meniscus, ear cartilage, and for extracellular matrix studies to understand the behavior of cancer cells.[51-54] High-density collagen has also been shown to present superior stiffness with a well-defined fiber organization and lower hydraulic permeability than low-density gels, especially when remodeling by cell traction was coupled with mechanically relevant boundary conditions.[51] In all of these systems, cellular remodeling and reorganization of collagen were key in achieving appropriate structure and properties.

Due to the deficient vascularity in the IVD and the limited nutrients transport and cell density for both the NP and AF regions, relatively inadequate counts of viable cells can be acquired from native tissues to use in engineering whole discs *in vitro*. Mesenchymal stem cells (MSCs) derived from human bone marrow offer a clinically relevant cell source for IVD tissue engineering. MSCs indeed survive and proliferate within the IVD, and they have been shown to contribute to the regenerative potential of restoring normal structure and function in numerous biological therapies *in vitro*[55-59] and *in vivo*.[60-62] Furthermore, the ability of hMSCs to differentiate into AF-like and NP-like tissue phenotypes has been previously demonstrated with the benefit of exerting greater contractile forces on collagen substrates than AF and NP cell 3D culture systems.[58,63] Currently, MSCs are widely used for whole IVD, NP, and AF tissue engineering in combination with other natural and synthetic biomaterials.[64-66]

As pre-clinical studies with TE-IVDs progress towards large animal models, elucidating the extent to which the coupled interaction of seeding density of cells and

density of the scaffold affect the structural organization and composition of the AF is even more relevant. The initial concentration of cells seeded in a collagen scaffold and the initial density of collagen in an AF scaffold are known to independently affect remodeling of engineered constructs and alter tissue composition and structure. Also, tissue composition and structural organization both have direct effects on the final mechanical and biochemical properties of an engineered construct. Although the combination of high-density collagen and MSCs has been successfully implemented before,[67] a dearth of efforts to recapitulate these effects on functional composite TE-IVDs exists to date.[68] In an effort to understand the interplay between the initial density of a scaffold and its initial cell seeding density, we studied the potential of highly-contractile hMSCs embedded in a dense extracellular matrix to produce organized collagen in engineered AF tissues. Therefore, the objectives of the current study were two-fold: to investigate the potential for dense collagen scaffolds seeded with hMSCs to improve baseline AF properties in TE-IVDs and to assess the effects of seeding density with hMSCs and AF scaffold density on the engineered tissue structural and composition properties.

Materials and Methods

Cell expansion and culture

Cryopreserved human bone marrow-derived MSCs (hMSCs) (MSC-001, RoosterBio Inc., Frederick, MD) were initially expanded to population doubling level (PDL) 6-9 and frozen in optimized freeze media with 10% DMSO (CryoStor® CS10, BioLife Solutions, Inc., Bothell, WA) at $10x10^6$ hMSCs/mL using manufacturer's recommendations. Then, hMSCs were thawed and washed with hBM-MSC High Performance Media containing (KT-001, RoosterBio, Inc.) before seeding them in T-150 and T-500 flasks to allow for high cell yields in constrained incubator space. Cells were cultured at 37 °C, 5% CO_2, and normoxia to PDL 14-15 for 7-10 days in hBM-

MSC High Performance Media (Fig. 4.1A). PDL is used here to measure cellular age rather than the number of passages, as recommended by the manufacturer, because it considers the number of times the cells have doubled since their primary isolation while they retain pluripotency. The media was changed after 5 days if cell expansion appeared delayed upon visual inspection of the culture flasks. Expanded hMSCs were subsequently harvested from T-150 and T-500 flasks with 0.25% trypsin (MediaTech, Manassas, VA).; at which point, cell viability and total cell number were assessed via trypan blue dye and hemocytometer counting standard methods. At least two batches of expanded cells were required to meet the minimum cell count desired.

Collagen solution preparation

Collagen type I was obtained from tendon fibers harvested from rat tails (Sprague Dawley, 7-8 weeks old, Pel-Freez Biologicals, Rogers, AR) as described in previously established work.[54] Briefly, tendons were dissected, submerged in ethanol, and diluted in 0.1% acetic acid at 150 mL/g of dry tendon mass. After collagen from tendons was solubilized for 48 hours at 4 °C, the resultant solution was centrifuged at 9000 rpm for 90 min to separate the heavy residues of fatty and non-solubilized tendon tissues. The clear supernatant collagen solution was collected, let freeze for 24 hours, and lyophilized for at least 48 hours. The lyophilized collagen was then reconstituted in 0.1% acetic acid at 6, 20, and 30 mg/mL stock solutions for storage at 4 °C, until used for TE-IVD fabrication.

Tissue-engineered disc NP fabrication

Composite alginate and collagen TE-IVDs were constructed following previously established techniques using expanded hMSCs.[31] The total count of viable cells was divided into two subsets. The first subset was spun down, and the cell pellet encapsulated in 3% weight per volume alginate (FMC BioPolymer, Philadelphia, PA) dissolved in phosphate-buffered saline (Dulbecco's PBS, MediaTech) at $15\pm5x10^6$

hMSCs/mL, while the second subset was initially suspended in 25-40 mL of the high-performance media in a centrifuge tube and set inside the incubator until use for the collagen/AF portion. The alginate suspension with encapsulated hMSCs was mixed two-to-one with a 0.02 g/mL $CaSO_4$ (Sigma-Aldrich, St. Louis, MO) solution in a three-way syringe stopcock setup (Fig. 4.1C). To produce tissue-engineered NPs, this new mixture was subsequently injection molded into the cavities designed with native canine NPs dimensions of 3D-printed molds (Fig. 4.1B) made of acrylonitrile butadiene styrene plastic on a Ultimaker 2+ (Ultimaker North America, Cambridge, MA). After filled molds were immersed in 60 mM $CaCl_2$ (Sigma-Aldrich) for an hour, the engineered NPs were cut out and centered inside each well of a 24-well plate (Fig. 4.1D and F).

Tissue-engineered AF fabrication and disc culture

To produce engineered AF with high-density collagen gels, we adapted the procedure from previous work[42-44] and used the space between the NP and the boundaries of the wells of a 24-well plate as AF molds (Fig. 4.1E-F). A total of eight groups were created to examine the effects of increasing collagen concentration in AF scaffold and increasing seeding density of hMSCs in TE-IVDs: one baseline 4 mg/mL Col group with $2x10^6$ hMSCs/mL; four groups of 10 mg/mL Col with $2x10^6$, $5x10^6$, $10x10^6$ and $20x10^6$ hMSCs/mL; and three groups of 20 mg/mL Col with $2x10^6$, $10x10^6$, and $20x10^6$ hMSCs/mL. The combination of 10 mg/mL Col with $5x10^6$ hMSCs/mL was explored uniquely to account for the two-to-one ratio of collagen concentration (mg/mL) to cells seeding density (10^6 hMSCs/mL) observed in the baseline group. Stock collagen solutions at 6, 20, and 30 mg/mL were used for fabricating TE-IVDs with final collagen concentrations 4, 10, and 20 mg/mL in the AF, respectively. Several batches of TE-IVDs were cultured given the constraints of incubator space and limited number of hMSCs that could be expanded at a time. However, not all experimental

conditions were assessed simultaneously; therefore, the total count of samples initially fabricated per group ranged between four and eight.

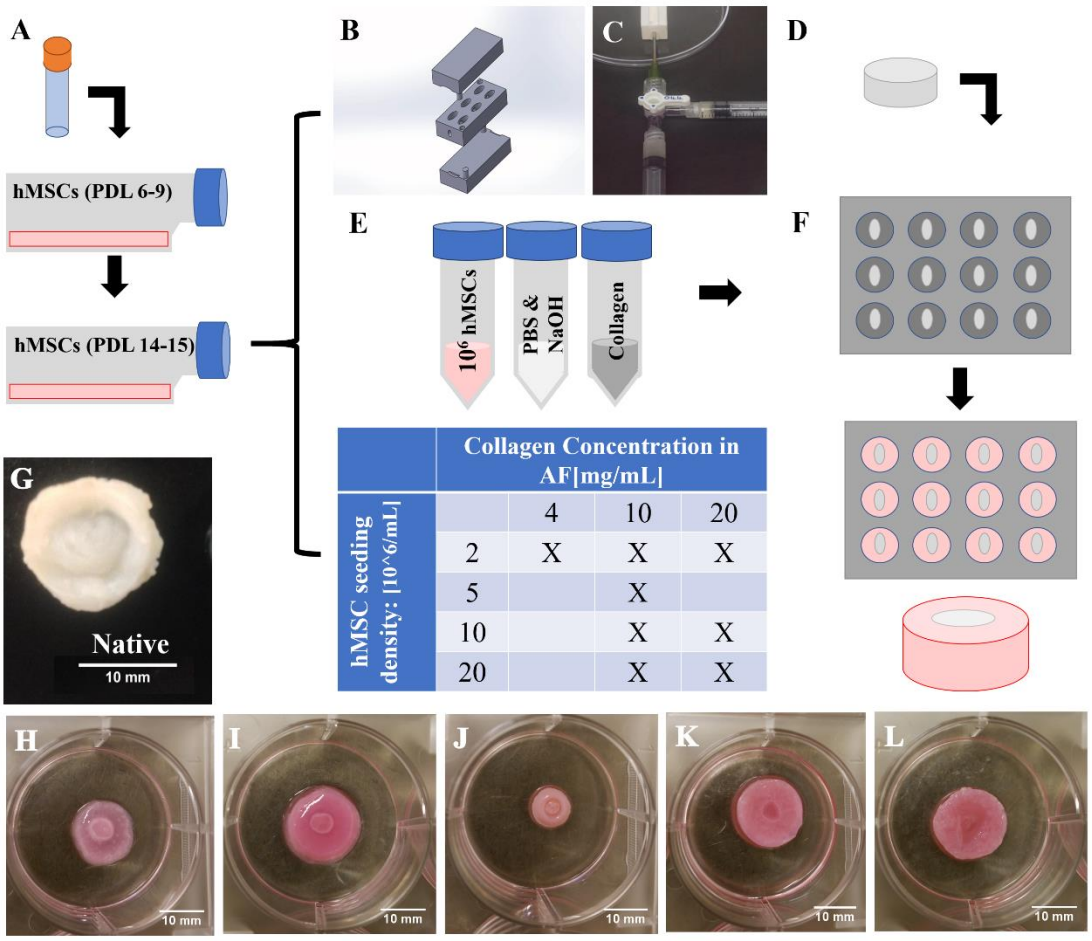

hMSC seeding density: [10^6/mL]	Collagen Concentration in AF[mg/mL]		
	4	10	20
2	X	X	X
5		X	
10		X	X
20		X	X

Figure 4.1. A) Commercially available human MSCs were acquired in highly concentrated frozen vials and expanded to PDL 6-9 first, frozen, and then re-plated to PDL 14-15 expansions. B) 3D-printed molds were designed in CAD software with cylindrical cavities that matched 70% of the ventral-dorsal and lateral-lateral dimensions of native canine NPs. C) Three-way stopcock setup used to combine cell-seeded alginate suspension in one syringe with another syringe containing calcium sulfate immediately before injection molding. D) Schematic of an engineered NP made of crosslinked alginate/hMSCs and modeled as an elliptical cylinder. E) Combinations of hMSCs seeded at various Col concentrations were created by modifying relative ratios of cell-media suspensions, PBS, NaOH, and stock collagen solutions; shown in the table are the experimental groups and baseline control group examined. F) The wells of tissue culture plates were used as molds to surround engineered NPs with hMSCs-seeded Col mixtures and produce TE-IVDs. G) Gross image of a native canine IVD shown to compare TE-IVDs morphology. H-L) Representative TE-IVDs images of the

control 4 mg/mL Col disc group (H), 10 mg/mL Col discs at $10x10^6$ and $20x10^6$ hMSCs/mL (I-J), and 20 mg/mL Col discs at $10x10^6$ and $20x10^6$ hMSCs/mL (K-L).

The preparation of each group in a batch, starting with the groups with the highest cell seeding density to the lowest, proceeded in the following fashion: 1) The concentrated cell suspension prepared from the second subset of hMSCs was spun down and resuspended into the required volume, $Vcells_0$, to meet the highest seeding density desired, $[MSCs]_f$, of the batch as described by equation 1:

$$[MSCs]_f = \frac{[MSCs]_0 \cdot Vcells_0}{Vtotal_f}, \quad (1)$$

where $[MSCs]_0$ denotes the concentration of resuspended cells in stock and $Vtotal_f$ is the total volume of the desired AF solution. 2) Basic diluting solutions that consisted of 10x concentrated PBS, 1x PBS, and 1 N NaOH were kept ice cold and mixed in centrifuge tubes, at the volumetric ratios (equations 2-4) that correspond to the desired total AF volume, $Vtotal_f$:

$$V(10xPBS)_0 = 0.1 \cdot \left(Vtotal_f - Vcells_0\right), \quad (2)$$

$$V(NaOH)_0 = 0.023 \cdot Vcol_0, \quad (3)$$

$$Vtotal_f - Vcol_0 - Vcells_0 = V(1xPBS)_0 + V(10xPBS)_0 + V(NaOH)_0, \quad (4)$$

where $Vcol_0$ is the volume of collagen initially added from the stock, and $V(1xPBS)_0$, $V(10xPBS)_0$, and $V(NaOH)_0$ refer to the volumes of the components of the basic diluting solution described above. 3) Using a three-way syringe stopcock setup, the ice-cold acidic stock solution of collagen required for the final collagen concentration in the AF, $[Col]_f$, (equation 5) was initially mixed with the appropriate volume of basic diluting solution to neutralize pH and maintain 300 mOsm in the collagen:

$$[Col]_f = \frac{[Col]_0 \cdot Vcol_0}{Vtotal_f}, \quad (5)$$

4) Immediately afterwards, the neutralized collagen solution was mixed with the required volume of cell suspension in high-performance media, $V_{cells\ 0}$, using the syringe stopcock setup and extruded through the injection tip around the NPs following a circumferential direction of deposition up to a $V_{total\ f}$ = 750 μL inside each well. 5) Next, steps 2 through 4 were repeated with the different collagen groups under the same high cell seeding density, after which the remaining volume of cell suspension was diluted to the next tier of cell seeding density. The iterative process described above continued with further serial dilutions of the cell suspension until all groups of the lowest cell seeding density of the batch were completed.

Lastly, the collagen in the 24-well plate was allowed to polymerize at 37 °C for 30 min before adding 1mL of culture media that consisted of DMEM without sodium pyruvate (MediaTech), 10% fetal bovine serum (Gemini BioProducts, Sacramento, CA), 1% antibiotic-antimycotic solution (100 μg/ml penicillin, 100 μg/ml streptomycin, 2.5 μg/ml amphotericin B, MediaTech) and 2.5% HEPES buffer (MediaTech) to each well. Within the first 48 hours of culture, the composite units of hMSC-seeded alginate NP and collagen AF that comprised the TE-IVDs were transferred from a 24-well plate to individual 6-well plates grouped by combinations of cell seeding density and collagen concentration in AF scaffold. The TE-IVDs were carefully covered with 2-3 mL of previously described culture media in each well such that the discs did not float in their wells. Discs were subsequently cultured for 3-4 weeks with media changes twice a week.

Morphological analysis

TE-IVDs were allowed to contract over a period of 23-28 days, during which time photographs were taken every 2-4 days coinciding with media changes. The photographs of each TE-IVD (N= 4) were taken at close range such that the bottom of

the well and the TE-IVD contour were at the same focal point (Fig. 4.1H-L). Photos were then uploaded to ImageJ (National Institutes of Health, Bethesda, MD) and scales were set against the bottom of the well with known dimensions. For each timepoint, measurements were taken of the well bottom area (or initial disc area) and the contours corresponding to the whole TE-IVD and the NP region only. Since discs were transferred from 24-well plates to 6-well plates after TE-IVD fabrication, a conversion factor for the ratio of the dimensions was calculated from the measurements provided in the specifications of the manufacturer and considered in the reported values. In a conventional Excel spreadsheet, ImageJ measurements along with their corresponding conversion factors were used to compute whole TE-IVD contraction at each timepoint as a ratio of current area relative to the initial area (or well bottom area). Furthermore, the contour of the NP region at each timepoint was subtracted from the whole disc to account for the relative area corresponding to the AF only. Considering the assumptions that the change in height of the TE-IVD was negligible during culture and that the total collagen remodeling in the AF was such that the deposition of *de novo* collagen balances the loss of scaffold collagen to the culture media, therefore, a relative change in AF area is reported as an apparent change in the initial collagen density of the AF scaffold. This is shown in the following equation:

$$C_t = C_0\left(\frac{A_0 - A_{NP,t}}{A_{IVD,t} - A_{NP,t}}\right), \qquad (6)$$

where A_0 represents the initial whole disc area (or bottom area of the well), $A_{NP,\,t}$ corresponds to the NP contour at the given timepoint, $A_{IVD,\,t}$ is given by the whole TE-IVD contour at the given timepoint, and C_0 and C_t are the initially known collagen density and current timepoint's apparent collagen density in the AF, respectively.

Conventional histological techniques were also applied to the constructs to compare the construct morphology, cell distribution, and deposition of relevant

extracellular matrix in 10 mg/mL and 20 mg/mL TE-IVDs. By the end of the culture period, one or two samples from each group were fixed in 10% phosphate-buffered formalin for 48 hours, followed by at least a 24 hours relocation in 70% ethanol. They were then embedded in paraffin and sectioned at 5 um-thick transversal slices. The sections were stained with Safranin-O to observe GAG content and distinguish NP vs. AF morphology after images were taken by a trained observer with light microscopy.

Mechanical analysis

The effective composite mechanical properties of the TE-IVDs were assessed following previously established protocols for unconfined stress-relaxation tests.[69] Briefly, individual specimens (N= 2-8) were placed in a custom-made smooth impermeable cup mounted on the load cell of a Bose EnduraTech testing frame (ELF 3200, Bose, Inc., Eden Prairie, MN), while an impermeable metallic cap placed at the tip of a displacement actuator applied 5% compressive strain steps up to 50% strain on the top surface of the TE-IVD. The TE-IVDs were kept submerged in PBS (MediaTech) containing protease inhibitors (Roche Diagnostics, Indianapolis, IN) during testing. After mechanical testing, the time-dependent stress response at each strain step was fit to a poro-viscoelastic response curve (equation 7) to obtain effective compressive stresses in equilibrium (Fig. 4.2A).

$$\sigma_{comp} = A\left(1 - e^{-t/\tau}\right) + B, \tag{7}$$

From the resulting compressive stress-strain data, an effective elastic modulus, E_{eq}, for the TE-IVD in equilibrium was calculated (Fig. 4.2B). In addition, to account for the non-linear elasticity observed in TE-IVDs, the effective equilibrium stress vs. stretch data (σ_{eq} vs. λ) were curve-fitted to the hyperelastic Holmes-Mow constitutive law[70]

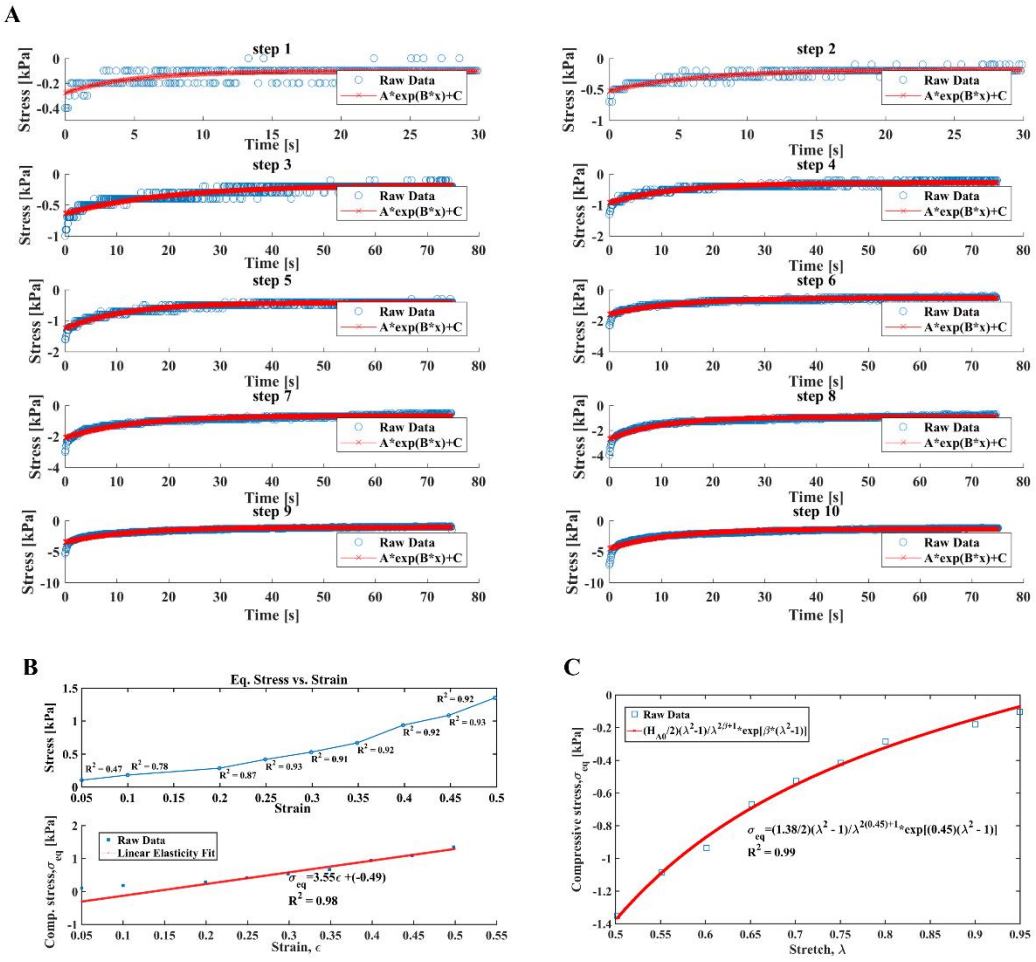

Figure 4.2. A) Representative sample graphs of poro-viscoelastic response to stress-relaxation tests in unconfined compression from 5-50% strain. B) Representative plots of resulting compressive stress-strain in equilibrium and linear fit to calculate effective elastic modulus, E_{eq}. C) Representative plot of effective equilibrium stress vs. stretch data fit to the hyperelastic Holmes-Mow constitutive law for aggregate modulus, H_{A0}, equilibrium stress-stiffening coefficient, β, calculations.

defined by equation 8 following a non-linear least squares regression in MATLAB R2017 (Mathworks, Natick, MA) (Fig. 4.2C):

$$\sigma_{eq} = \frac{1}{2} H_{A0} \left(\frac{\lambda^2 - 1}{\lambda^{2\beta+1}} \right) e^{\beta\left(\lambda^2 - 1\right)}, \qquad (8)$$

where the reference aggregate modulus, H_{A0}, and compressive stress-stiffening coefficient at large strains, β, are the relevant material parameters.

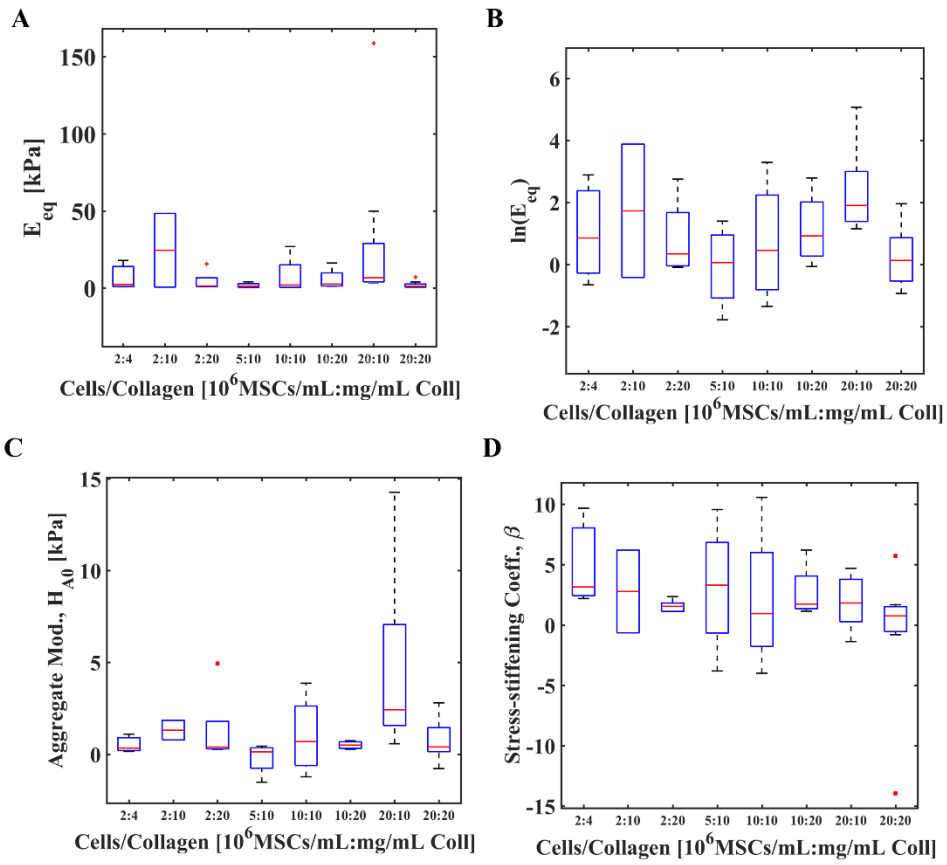

Figure 4.3. A-B) Boxplots of experimental and control E_{eq} data grouped by cells and collagen combinations with marked outliers as red asterisks depicted in standard values and log transformed values. C-D) Boxplots of experimental and control H_{A0} and β data grouped by cells and collagen combinations with red asterisks marking outliers.

The mechanical data corresponding to effective elastic modulus at equilibrium, aggregate modulus, and compressive stress-stiffening coefficient for the 10 mg/mL collagen and 20 mg/mL collagen TE-IVDs were fit to a 4-parameter logistic regression or dose response model (equation 9), where the mechanical response estimates, M = < E_{eq}, H_{A0}, β >, occurred between a minimum response, M_{min} (the value of M at S = 0), and a maximum response, M_{max} (the value of M at S = ∞), as a function of the initial cell seeding density, [x_0], at the AF. This equation was given by:

$$M[x_0] = M_{min} + \frac{(M_{max} - M_{min})}{1 + e^{-b \cdot ([x_0] - EC_{50})}}, \qquad (9)$$

where b represents the Hill's slope of transition to maximum mechanical response and the inflection point, EC_{50}, indicates the initial cell seeding density at which 50% of the maximum mechanical response is observed. Outliers obtained from boxplots of each group of cells and collagen combinations (Fig 4.3A-D) were not included in the sigmoidal curve fits.

Statistical analysis

Measured data for TE-IVD contraction ratio and apparent AF density over time were reported as mean ± standard deviation. For these data, a linear mixed-effects analysis was conducted to inspect the relationship between contraction ratio and two factors, scaffold concentration and cell seeding density, at discrete timepoints. As fixed effects, we considered collagen in scaffold (4 mg/mL, 10 mg/mL, and 20 mg/mL), cell seeding density ($2x10^6$/mL,$10x10^6$/mL, and $20x10^6$/mL), and nominal timepoints in days (t = 0, 2, 4, 7, 10, 14, 18, 21, and 23), along with all the two-factor interaction terms. As random effects, we accounted for intercepts for sample (N= 4). The time-dependent and -independent effects of scaffold concentration and cell seeding density on the apparent AF density were also analyzed with a linear mixed-effects model following similar factors as described with the contraction ratio. In both cases, linear mixed-models were fit using the *lme4* function[71] in R (R-Studio, Boston, MA). For both analyses, significant differences between estimates for each available combination of collagen and cell against other combinations at any given timepoint were identified at $p < 0.05$ using Tukey adjustments for multiple comparisons. The same post hoc tests were performed between said estimates against the previous timepoints within each collagen and cell combination (Fig. 4.4A-B).

Data distribution of the mechanical response parameters E_{eq}, H_{A0}, and β were observed in boxplots to exclude outliers and negative equilibrium or aggregate moduli values from further analysis. A Monte Carlo analysis was conducted for each group of

cell and collagen combination to determine the uncertainty in the curve fit coefficients (M_{max}, M_{min}, b, and EC_{50}).[72] A log transform of the non-negative data was taken to provide a normal distribution for each group and the measured standard deviations were used to generate 100 simulations of data sets with 10 normally distributed random samples each. Each data set was refit to the model curve described in equation 7 by minimizing the RMS error in MATLAB. The coefficients for 10 mg/mL and 20 mg/mL curves were compared with a one-way ANOVA for the collagen factor using R-Studio to identify significant differences at $p < 0.05$. Measured data were shown along the curve fits as mean ± standard error, while the curve fit coefficients compared in bar charts were represented as mean ± standard deviation (Fig. 4.5 and Supplemental Figs. 4.8-4.9).

Lastly, correlation analyses were performed for the mechanical response in equilibrium, E_{eq}, and the IVD ratio to initial area and apparent AF density at the end of culture period as variables dependent upon initial cell and collagen content. The IVD ratio to initial area was expressed as percentage of the original area and the equilibrium modulus was averaged before fitting the data to a plane. Critical correlation values were determined using r-tables with $p< 0.05$ considered significant.

Results

Morphological analysis

Over the 3.5-4 weeks culture period, the collagen AF in the TE-IVDs contracted around the NP reducing the whole disc area relative to the initial area, as shown by the contraction ratio measurements (Figure 4.4A). No significant differences in AF contraction were observed between all 10 mg/mL Col discs and the baseline 4 mg/mL Col discs group at day 2. Conversely, the 20 mg/mL Col discs significantly expanded to 111 ± 6.2% ($p= 0.040$ for 4 mg/mL and $p= 0.049$ for 10 mg/mL) after they were transferred from the 24-well plate to the 6-well plate within the first 2 days. In fact,

through the entire culture period, all 20 mg/mL Col disc groups retained greater area ratios to their initial disc area ($p < 0.01$) than the baseline group and all 10 mg/mL Col discs. By the first week, the 10 mg/mL Col discs with $20x10^6$ hMSCs/mL significantly exceeded the contraction observed on the baseline group by 25.9% ($p= 8x10^{-4}$) and on the other 10 mg/mL Col disc groups with lower seeding densities by 20.1 to 23.4% ($p= 0.004$ and $p= 0.035$ for $2x10^6$ and $10x10^6$ hMSCs/mL, respectively). Only after two weeks, the 10 mg/mL Col discs with $10x10^6$ hMSCs/mL contracted 31.7% past the baseline group ($p< 1x10^{-4}$). Nevertheless, the 10 mg/mL Col discs with $2x10^6$ hMSCs/mL retained similar contraction ratios to the baseline group TE-IVDs at all times.

Significant changes in AF contraction over time for each group were only observed in the TE-IVDs with 4 mg/mL Col and 10 mg/mL Col and at different timepoints. By the fourth day, the control 4 mg/mL group had a significant decrease in area ($p= 0.007$) to 81.3 ± 6.9% from its initial area. Meanwhile, the 10 mg/mL Col discs with $10x10^6$ and $20x10^6$ hMSCs/mL had significant contractions from previous timepoints only after one week, until their second week when they reached 57.9 ± 2.2% ($p= 0.003$) and 36.8 ± 4.0% ($p= 1x10^{-4}$) from their initial areas, respectively. However, the 10 mg/mL Col discs with $2x10^6$ hMSCs/mL exhibited negligible contraction over the culture period similar to the 20 mg/mL Col discs.

In terms of the apparent AF density based on the relative AF area, as the embedded hMSCs pulled on collagen fibers and contracted around the NP, the TE-IVDs experienced changes in collagen AF density ranging between a 3.5-fold increase and a loss of up to 9.4% after 23 days (Fig. 4.4B). As expected for each timepoint, given their initial collagen density, the control 4 mg/mL

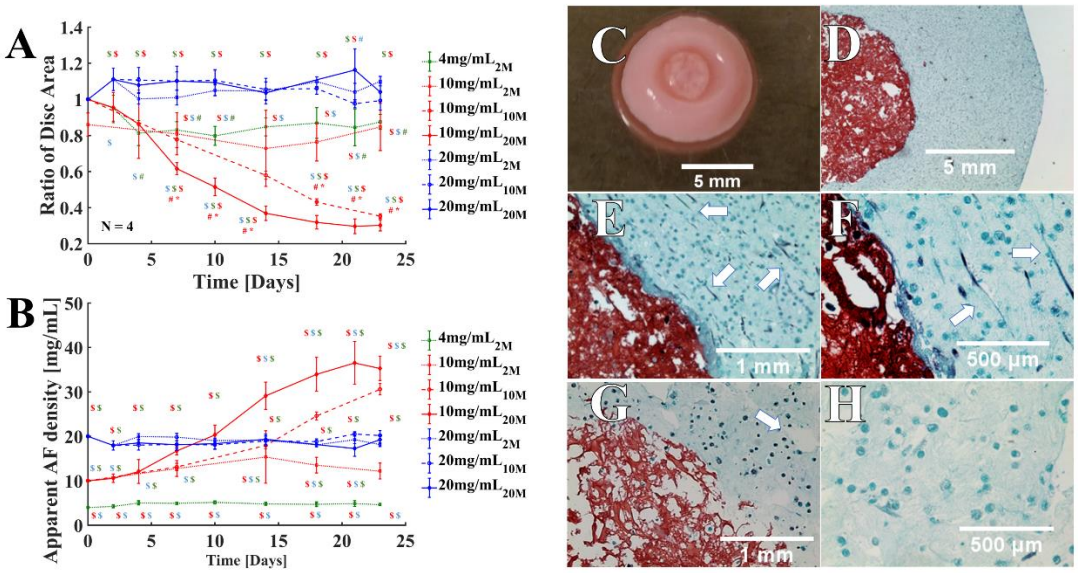

Figure 4.4. A-B) Progression over 23 days of TE-IVD contraction ratios, and apparent AF density based on relative AF area and initial collagen density; $ $p < 0.05$ vs. group color in same timepoint, # $p < 0.05$ vs. same group area ratio at t= 0, * $p < 0.05$ vs. same group area ratio up to at least 3 previous timepoints. C-D) Gross image of a 10 mg/mL Col disc with $20x10^6$ hMSCs/mL and close-up (4x) of its NP/AF interface revealed by Safranin O staining. E-F) White arrows point to the contraction-driven remodeling of collagen fibers around the NP/AF interface in close-up images (20x) and (40x) of the 10 mg/mL Col disc with $20x10^6$ hMSCs/mL. G-H) White arrows point air bubbles trapped in AF scaffold in close-up images (20x) and (40x) of a 20 mg/mL Col disc with $20x10^6$ hMSCs/mL.

Col groups were significantly different from all 10 mg/mL Col discs and all 20 mg/mL Col discs. Interestingly, between days 7 and 10, the 20 mg/mL with $20x10^6$ hMSCs/mL Col discs had statistically similar apparent AF density to the 20 million cells-seeded 10 mg/mL Col TE-IVDs. By the first week, the 10 mg/mL Col discs with $20x10^6$ hMSCs/mL had 27.7% to 31.2% significantly greater apparent density than their 2 million ($p = 0.016$) and 10 million cells-seeded ($p = 0.042$) counterparts, respectively. At day 14, the apparent AF density of 10 mg/mL Col discs with $10x10^6$ hMSCs/mL was no significantly different than the 20 mg/mL Col discs with $10x10^6$ and $20x10^6$ hMSCs/mL; and by day 18, it surpassed their 2 million cells-seeded counterparts by 1.82-fold ($p < 1x10^{-4}$).

Evidently, the most pronounced changes in apparent AF density over time occurred in 10 mg/mL Col TE-IVDs. Since the first week of culture onwards, the 10 mg/mL Col discs with $20x10^6$ hMSCs/mL reached between 1.7- to 3.5-fold increase in apparent AF density ($p< 0.05$) from its initial collagen density. After week 2, the apparent AF density of 2 million cells-seeded 10 mg/mL Col peaked at 1.5 times the initial density ($p= 2x10^{-4}$), while the 10 million cells-seeded cohort reached more than 1.8 times the initial density ($p< 1.1x10^{-3}$) from this timepoint forward. Although the control 4 mg/mL Col discs had an apparent AF density increase by up to 25.7% at day 4, there were no significant differences over time. Similarly, the 20 mg/mL Col discs ranged in apparent AF density between 89.8% and 101%, without significant time-dependent differences in any of the AF scaffolds seeded with $2x10^6$, $10x10^6$, or $20x10^6$ hMSCs/mL.

Histological examination of the tissue structure at the AF of 10 mg/mL and 20 mg/mL TE-IVDs at the end of the culture period uncovered stark differences in collagen remodeling driven by the cell-dependent contraction of the scaffold around the NP (Figure 4.4C-H). Firstly, a tight tissue boundary appeared to form at the NP/AF interface of the 10 mg/mL Col disc, but was absent in the 20 mg/mL Col disc. Although the depicted representative samples were both initially seeded with $20x10^6$ hMSCs/mL, greater cell proliferation was apparent in the 10 mg/mL Col disc than in the 20 mg/mL one. The distribution of cells in the 10 mg/mL AF was also clearer along the circumferentially-aligned collagen fibers than in the 20 mg/mL AF, where they appear scattered and scarce. Additionally, notable gap-holes observed in the AF of the 20 mg/mL Col specimen suggested the presence of air bubbles. Nevertheless, Safranin O staining denoted a proteoglycan-rich extracellular matrix was at the NP region in both specimens with reasonable distinction.

Mechanical analysis

Testing the composite TE-IVDs in unconfined compression provided effective stress responses consistent with biphasic behavior of hydrogels. The goodness of fit for the effective elastic modulus in equilibrium, E_{eq}, given by the coefficient of determination, R^2, varied between 94.8% in average for all 10 mg/mL Col TE-IVDs and 95.0% in average for all 20 mg/mL Col TE-IVDs. A total of 4 outliers and the data corresponding to the baseline 4 mg/mL group were excluded from the 4-parameter dose response curve fit for equilibrium modulus as a function of cell concentration. From the simulated data sets corresponding to the data distribution of equilibrium moduli in 10 mg/mL and 20 mg/mL Col TE-IVDs, the mean RMS error remained between 8.3 and 3.6, and coefficients of variation (CV) of the RMS error between 23.1% and 22.8% for the 10 mg/mL and the 20 mg/mL groups, respectively.

Increase in the initial seeding density of hMSCs had a more pronounced dose-dependent effect in the mean equilibrium modulus of 10 mg/mL Col discs than in 20 mg/mL Col TE-IVDs (Fig. 4.5A). The mean equilibrium modulus remained relatively similar in the 20 mg/mL discs, with a 2.5-fold average increase from the $E_{eq,\ min}$ to $E_{eq,\ max}$, in comparison to the 10 mg/mL discs whose $E_{eq,\ min}$ rose to a nearly 30-fold $E_{eq,\ max}$, with increasing cell content. Surprisingly, the maximum E_{eq} reached by 10 mg/mL discs at 15.1 ± 2.2 kPa was significantly higher ($p< 1x10^{-4}$) than the 4.2 ± 0.7 kPa of 20 mg/mL discs (Fig. 4.5B). Additionally, the EC_{50} was also determined to be significantly higher ($p< 1x10^{-4}$) in discs with a lower collagen density-AF than in those with a higher density-AF, with half-maximum mechanical responses observed at 6.8 ± 1.8 $x10^6$ and 2.6 ± 0.3 $x10^6$ hMSCs/mL, respectively (Fig. 4.5D). Conversely, the 20 mg/mL discs had 3.3-times the minimum E_{eq} ($p< 1x10^{-4}$, Fig. 4.5C) and 4.4-times the Hill's slope of transition to maximum mechanical response ($p< 1x10^{-4}$, Fig. 4.4E) than 10 mg/mL discs.

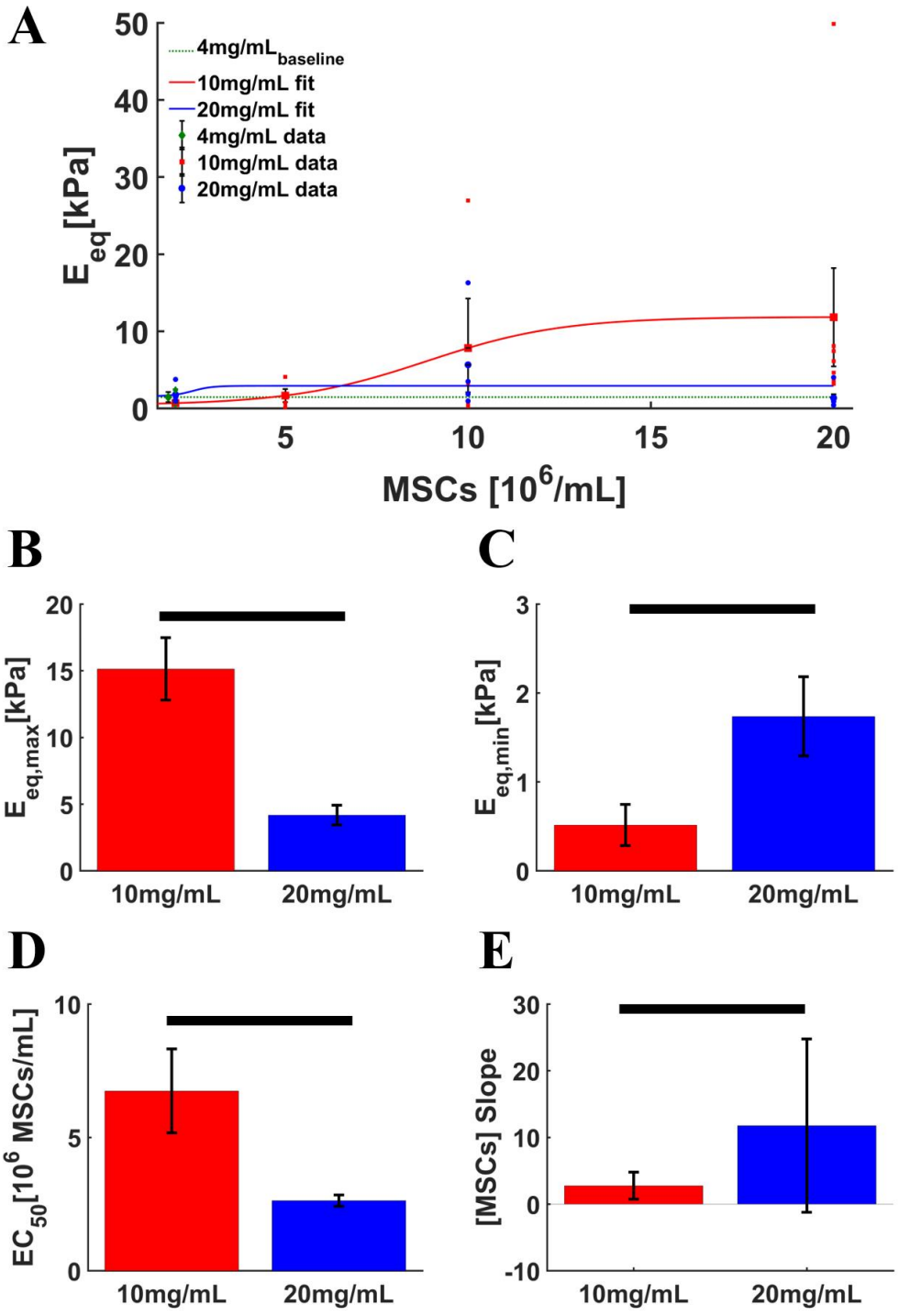

Figure 4.5. A) Curve fit of effective elastic modulus in equilibrium of composite TE-IVDs as a function of hMSCs initial seeding density in AF, grouped by density of collagen/AF scaffold; N = 1-7, mean ± SE. B-E) Coefficients generated from Monte Carlo simulations including maximum and minimum effective elastic moduli, EC_{50} in hMSCs seeding density, and transition slope; N= 100; mean ± SD; bars: $p < 0.05$.

From the Holmes-Mow model analysis, the mean R^2 values of 91.4 ± 21.6% for the 10 mg/mL Col TE-IVDs and 93.3 ± 15.5% for the 20 mg/mL Col TE-IVDs described reasonable curve fits of the nonlinear response of the compressive stresses in equilibrium as a function of stretch (Supplemental Figs. S.8-4.9). However, the dose response analysis for the aggregate modulus, H_{A0}, and stress-stiffening coefficient, β, as a function of increasing cell seeding density resulted in coefficients of variation of the RMS error higher than 25%. For the H_{A0} mechanical response parameter, the mean RMS errors of 13.3 (CV= 52%) and 0.96 (CV= 31.5%) were observed in 10 mg/mL and 20 mg/mL groups, respectively. For the β response parameter, the mean RMS errors of 10 mg/mL discs and 20 mg/mL discs were determined as 6.01 (CV= 49.3%) and 1.27 (CV= 27.9%). Although the data appeared to fit the nonlinear model, the effects of cell seeding density on the aggregate modulus was no different than that of the effective elastic equilibrium modulus. Furthermore, the stress-stiffening coefficient fit was far too poor; thus, the nonlinear model did not provide any additional insights than what the linear elastic model offered.

Global correlation analysis

Three-dimensional multiple correlation analyses identified the effects of the independent variables initial cell seeding density and initial Col concentration in AF scaffolds, on the contraction ratio of TE-IVDs, their apparent AF density, and the average effective equilibrium modulus at the end of culture. All morphological data for the 4 mg/mL baseline, 10 mg/mL, and 20 mg/mL Col discs were plotted together and fit to a plane in the same graph (Fig. 4.6A-B). Final disc size as percentage of original disc area and AF apparent density displayed strong positive correlations ($p< 0.01$ for IVD_{size} and $p< 0.05$ for ρ_{app}) between the initial cell and Col content. As expected, both higher initial hMSCs content and relatively-lower initial Col density had the most TE-IVD contraction determined from the reduced final disc size. This relationship was

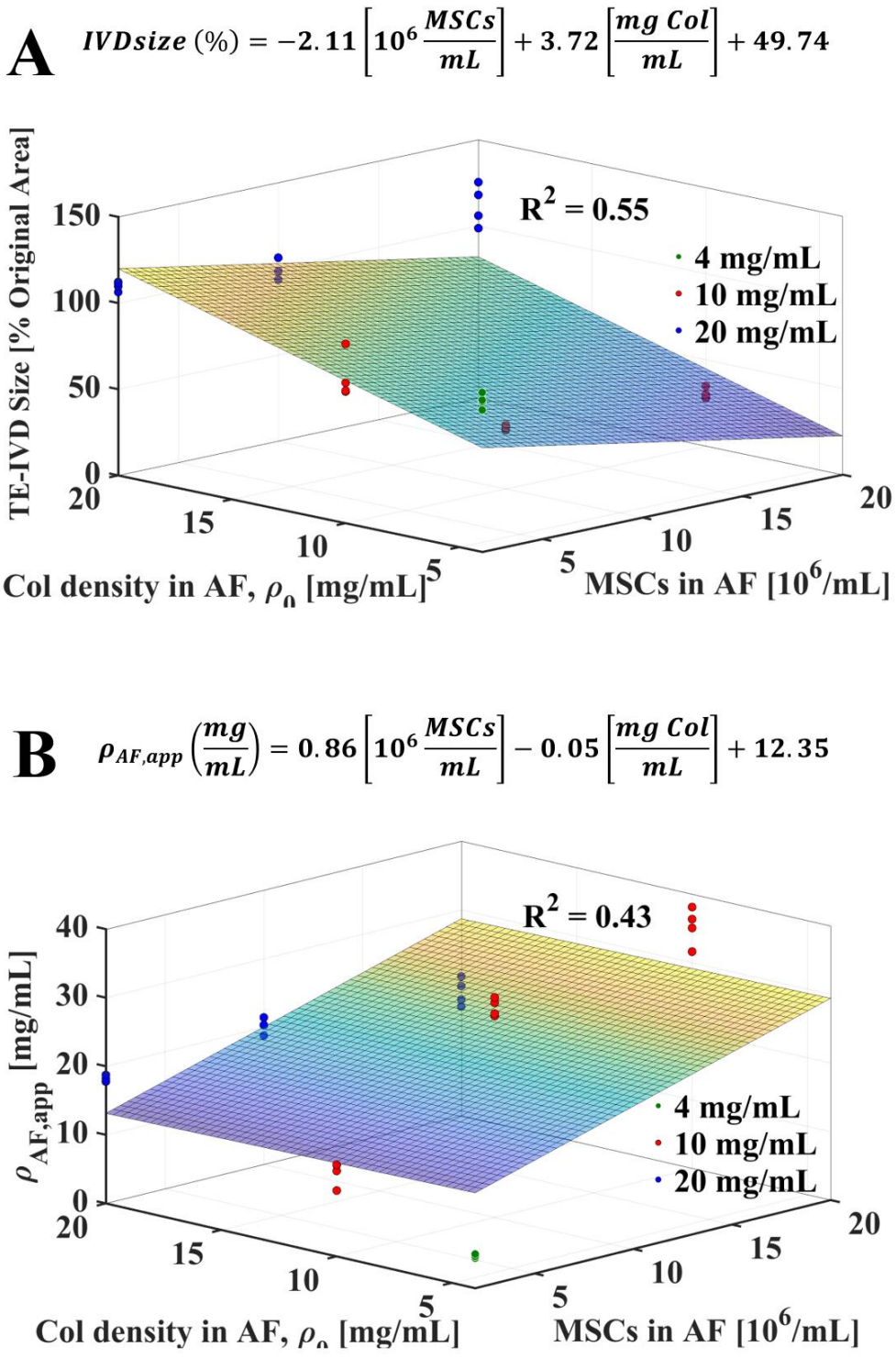

Figure 4.6. Correlation of collagen concentration and initial seeding density at the AF with contraction data as determined from IVD size (A) and apparent AF density (B). Equations describing the correlation factors are shown above each graph; r (26) = 0.479, $p < 0.01$ for IVD_{size} and r (26) = 0.374, $p < 0.05$ for ρ_{app}.

described with the slope for Col as 3.72 (mg Col_0/mL)$^{-1}$ and the slope for hMSCs as -2.11 (million cells/mL)$^{-1}$, appreciated in Fig. 4.6A. Apparent densification of the AF peaked at the highest initial hMSCs content, with initial Col concentration having a weak indirectly proportional effect. From the corresponding equation plane in Fig. 4.6B the cell content slope denotes that an estimated 0.86 mg final Col/hMSC is contributed to the AF density, while the initial collagen content slope seems to slightly diminish the final AF density by 0.05 mg Col_{final} per mg Col_0. For the mechanical data, the average equilibrium moduli of all 4 mg/mL baseline, 10 mg/mL, and 20 mg/mL Col discs were fit to a plane and displayed along with the set of individual data points per group (Fig. 4.7A-B). Although there was no significant positive correlation observed between initial cell and Col content for the mean equilibrium moduli ($r(6)= 0.707 > 0.43$), a prominent positive correlation was found between initial cell density and the final apparent AF density for the same equilibrium statistic ($p< 0.02$). Notably in Fig. 4.7A, the initial Col concentration was a poor predictor for increasing mean equilibrium modulus with a slope of – 0.21 kPa (mg Col_0/mL)$^{-1}$, whereas the expected contribution of the initial content of hMSCs was 0.35 kPa (10^6 MSCs/mL)$^{-1}$. Conversely, Fig. 4.7B shows that increasing final apparent AF density correlated well with increasing mean equilibrium modulus as evident by the 0.37 kPa (mg Col 0/mL)$^{-1}$, but the initial cell density slope appeared negligible at a slope of -0.01 kPa (106 MSCs/mL)$^{-1}$. In this context, the extent to which cells drive the structural remodeling of the available collagen content into a dense matrix served as a better predictor of TE-IVD stiffness than the amount of collagen in the scaffold in the first place.

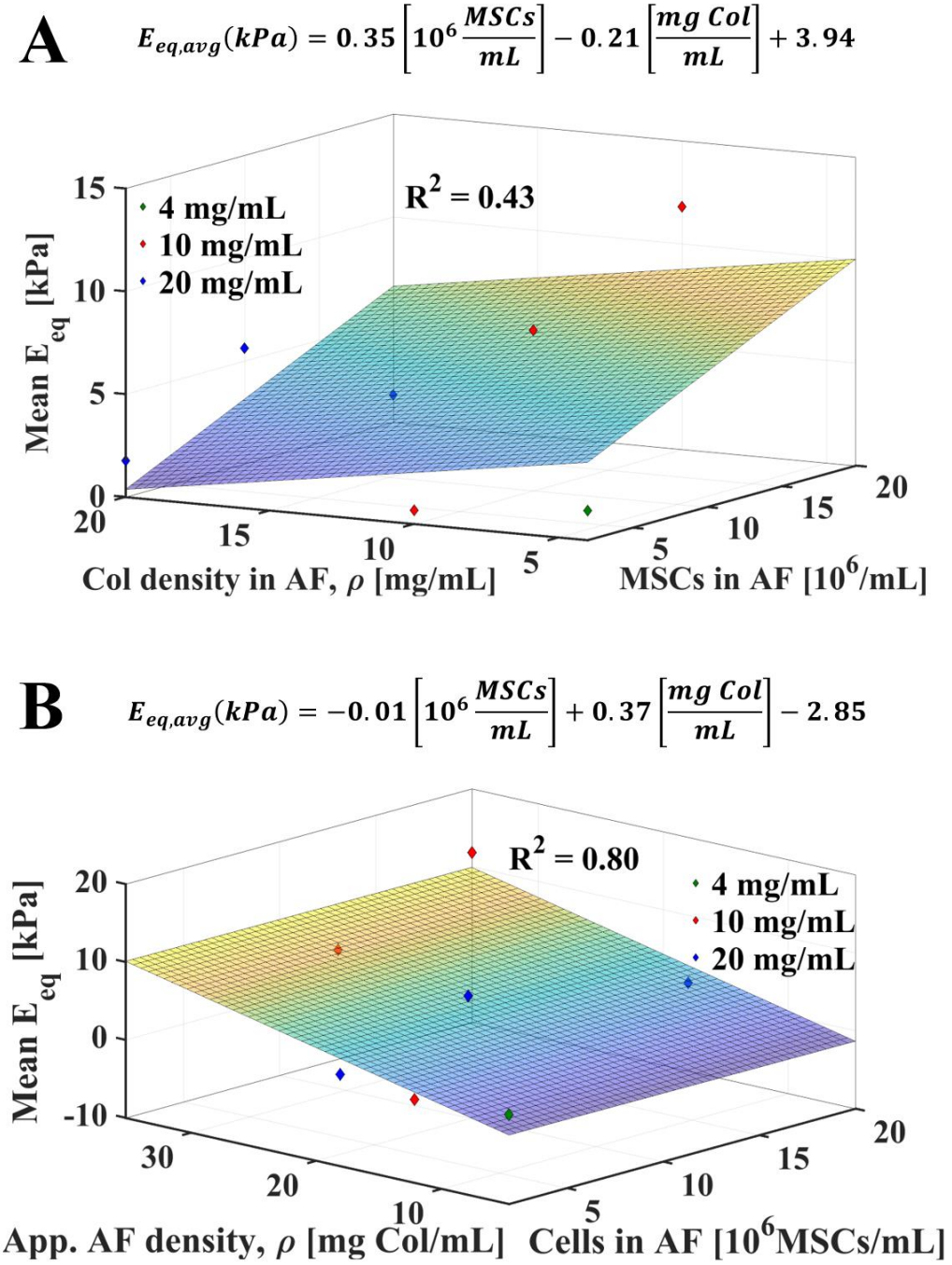

Figure 4.7. A) Correlation of starting collagen concentration and initial seeding density at the AF with mean effective equilibrium data from each combination group. B) Correlation of apparent AF density at the end of culture period and initial seeding density at the AF with mean effective equilibrium data from each combination group. Equations describing quantitatively the correlation factors are shown above each graph; r (6) = .789, $p < 0.02$ for E_{eq} vs. Cells vs. ρ_{app}.

Discussion

The goal of this study was to examine the role of scaffold density as prescribed by the initial collagen concentration and initial cell seeding density on the final composition and structure of TE-IVDs. The current work also served as a proof of concept for the generation of TE-IVD constructs with dense AF matrices. Composite TE-IVDs with AF scaffolds of moderately high initial density (10 mg/mL) contracted significantly over time until they reached and retained their final shape with relevant tissue structure and cell morphology both at the NP and the AF. Composite TE-IVDs with excessively dense AF scaffolds (20 mg/mL) did not contract at all and retained their original morphology without changes in tissue structure and adequate cell shapes. These observations were directly coupled with cell content, suggesting that the initial seeding density of the engineered AF modulates the final tissue composition in concert with AF scaffold density. The compressive properties of the discs were also influenced by the hMSCs initial seeding density in a dose-dependent manner, but the contribution of the initial collagen concentration to the mechanical response was only relevant to the extent that the hMSCs were able to remodel the AF scaffold over the culture period. Moreover, once the final remodeled structure and composition were set, then the stiffness of the TE-IVD were highly correlated with their structure described by an apparent final AF density.

Remodeling of the AF extracellular matrix was dependent on both initial cell density and initial collagen content. In this study, significant morphological changes occurred in 10 mg/mL Col discs, driven by the hMSCs traction on the AF scaffold and the boundary imposed by the alginate NP, that surpassed the changes in baseline and 20 mg/mL Col discs over 3-4 weeks (Fig. 4.4A). This is consistent with the well-known property of cell seeded collagen gels, that contraction decreases with increasing concentrations of collagen.[54,73-75] The AF contraction of 10 mg/mL groups deviated

from that observed in the baseline group within the first week of culture in a seeding density-dependent fashion. At increasing cell densities, this effect was intensified leading to final TE-IVD areas of lower than 40% of their original size. Furthermore, contraction rates observed in 10 mg/mL Col discs with cell seeding densities above the $2x10^6$ cells/mL baseline resulted in AF contraction that was accelerated after the first week and diminished after the second week of culture. This contraction rate change was also observed in the baseline discs, but not on the 20 mg/mL Col discs. Collectively, these findings suggest an inherent potential for hMSCs embedded in collagen matrices to adjust scaffold density until a contraction plateau is reached, which is a desirable trait for tuning the extent of scaffold remodeling *in vitro*.

The quantification of apparent density based on AF ratio to disc provided insights on time-dependent changes of tissue composition during culture that are also influenced by initial concentration of hMSCs. Apparent densification of the high-density collagen gel led 10 mg/mL Col discs to match the initial scaffold density of 20 mg/mL Col discs within one or two weeks (Fig. 4.4B), in response to the contraction observed in the AF. Moreover, this time dependence of apparent AF density of 10 mg/mL Col discs varied as increasing initial cell-seeding concentrations accelerated collagen remodeling. Herein we assumed that hMSCs controlling collagen turnover in AF scaffolds retained a relatively constant total collagen content between timepoints to use the initial collagen density as a relevant parameter. Previous work by Puetzer and Bonassar showed in fact that up to 40% and 60% collagen can be lost to the culture medium in 10 mg/mL and 20 mg/mL Col scaffolds, after 4 weeks.[51] As such, apparent AF density results discussed here should not be confused with true collagen concentration, which could be more accurately approximated by biochemical assays and volumetric information. Rather, apparent AF density provides a measure of structural organization as a function of initial collagen content and tissue composition. In this

context, we demonstrated that moderately-dense collagen scaffolds undergo structural remodeling in a time- and cell content-dependent form.

Limited changes in the apparent AF density and contraction-induced matrix remodeling of the 20 mg/mL and baseline groups indicate that an excessively dense matrix and a low cell-seeding density are both similarly deterrent of remodeling activity and structural organization at the AF. Surprisingly, the baseline group discs did not present AF contraction and remodeling as shown before.[76] This finding could be attributed to relatively low homogeneity in the hMSCs suspensions prepared in series for the AF portion of the several groups in each fabrication batch. Changes in apparent AF density and matrix remodeling, as prominent or limited they appeared, were supported histologically with the highly porous appearance of the AF scaffold in 20 mg/mL contrasting the dense organization of collagen in the AF scaffold of 10 mg/mL discs (Fig. 4.4C-H). While the present study focuses on the effects rather than the mechanism by which cells differentiate into chondrocyte-like and fibrochondrocyte-like phenotypes distinctive of the NP and AF regions in native IVDs, abnormal round-shaped cells were preserved in the AF region of 20 mg/mL possibly indicating poor cell differentiation. However, histological evaluation of the TE-IVDs at 10 mg/mL collagen unveiled elongated cells that were oriented concentrically around the engineered NP and resemble the characteristic phenotype of cells in the AF. In previous work, similar effects were demonstrated with hMSCs in 4 mg/mL baseline constructs in both hypoxic or normoxic culture conditions.[76] Interestingly, the effect of initial seeding density of hMSCs at the AF in 20 mg/mL Col discs was also virtually negligible, likely since the hMSCs were unable to reorganize or circumferentially align the dense scaffold into distinctive fibers. In McCorry et al., high-density collagen constructs seeded with bovine MSCs exhibit abnormally-shaped fiber bundles in comparison with those constructs seeded with fibrochondrocytes or in co-culture of MSCs and

fibrochondrocytes.[77] They also observed that MSCs seeded alone increased GAG and collagen production in high-density collagen, both of which contribute to preferred tissue composition in TE-IVDs as well. This suggests a potential for using AF cells in co-culture with hMSCs in future studies with the interest of providing the desired microenvironment to promote adequate differentiation of hMSCs, extracellular matrix composition, and reorganization of scaffold fibers.

A directly proportional effect was appreciated between initial cell seeding density at the AF and the mechanical response of TE-IVDs in equilibrium. Conversely, increasing initial collagen content had an unexpected negative correlation to the mean effective equilibrium modulus (Fig. 4.7A). Compressive properties of collagen gels are known to be relatively low, especially if cell-seeding effects on remodeling are not appreciated. Although high-density collagen has been shown to achieve superior stiffness with cell-seeded constructs, in the current work, this paradigm is inverted indicating that initial scaffold density alone, without accounting for internal structure remodeling, is a poor predictor for tissue stiffness. Moreover, increasing the initial cell seeding density elicit a dose response to the equilibrium modulus in 10 mg/mL and 20 mg/mL Col discs (Fig. 4.5A). Analysis of the curve-fitting parameters for this dose-dependent behavior revealed that the maximum equilibrium modulus and half-maximum mechanical response was decreased in the TE-IVDs with the highest AF collagen content (Fig. 4.5B-E). The final AF density parameter described from TE-IVD morphology was also weakly correlated to the initial collagen content (Fig.4.6B), thus supporting the idea that an initially dense scaffold is not sufficiently functional without structural remodeling. Nevertheless, the strong correlation between this final AF density parameter with the mean effective equilibrium modulus and initial cell seeding density further highlights the importance of structural organization and matrix remodeling as a strong predictor of composite TE-IVD stiffness. The challenge in remodeling highly

dense matrices into a tightly organized structure can be overcome when combining the appropriate cell content to an adequately formulated dense scaffold.

The current study offered new insights on the interplay between cell seeding and initial scaffold densities on the structural and composition properties of TE-IVDs, however, several limitations in this work should be acknowledged. Sample size for each group of cell content and collagen concentration was limited due to batch culture design for simultaneous testing of several experimental conditions and constraints of incubator space and limited number of hMSCs expanded at a time. It is possible that low statistical power overlooked significant differences between groups of combined formulations; this was relatively apparent after the Monte Carlo simulations supported tightly normalized populations of simulated samples. This low number of samples tested point to the need for a higher number of cell expansions and possibly combining with relevant region-specific NP and AF cells in co-culture with hMSCs. The culture of TE-IVDs seeded with hMSCs without any mechanical conditioning, growth factor and/or chemical stimuli in their media could have implications on their metabolic activity in 3D culture over 3-4 weeks. It should also be noted as a limitation that assays to identify trilineage potential and differentiating markers of hMSCs were not conducted on this population of cells, since we relied on the instructions of the manufacturer that guarantee pluripotency up to the PDL range we used. Nevertheless, extracellular matrix environment and choice of scaffold material have been shown to provide necessary biophysical signals for hMSCs to differentiate into region-specific cells with NP- and AF-like phenotypes.[76] The use of scaffolds as sole indicators of differentiating potential eliminates confounding effects of combining too many factors with an already limited sample availability. Future work should ensure a thorough characterization of the differentiating potential of the hMSCs population used in TE-IVD constructs in addition to assessment of shapes characteristic to the desired phenotype. Another limiting aspect

of this study lies in the assumptions made for mechanical testing, more specifically with utilizing the Holmes-Mow model for unconfined compression measurements without hydraulic permeability data. Also, poor fits of stress-stiffening coefficient relayed that there could be influencing effects missed due to low statistical power or because the strain-dependent behavior is traditionally characterized in a confined compression testing framework. To this end, our inferences focused on the effective mechanical response in equilibrium as described by Kim et al., where a biphasic poroelastic model can be reduced to one or two coefficients.[69] We have not focused on hydraulic permeability data in this context to consolidate the number of variables describing correlating factors and because data analysis yielded poor coefficients of determination arguably due to the significantly different radial boundaries on each group. Computational analyses with simulated hydraulic permeability data could reveal additional effects supporting our findings, but we have considered them beyond the scope of this work.

In the present study, we demonstrated that high-density collagen can be used as an AF scaffold to generate TE-IVDs with enhanced structural organization and tissue composition over previously established baseline formulations. Our findings also supported that remodeling of the AF ECM in TE-IVDs was dependent on both initial cell density and initial collagen content. Such remodeling was observed as cell traction forces pulled on the collagen matrices and recreated circumferentially oriented denser AF. Densification of the AF over time was mostly mediated by initial concentration of hMSCs, where increasing seeding density resulted in higher structural organization in moderately-dense matrices. Therefore, excessively dense matrices and low cell-seeding densities both counteracted the remodeling potential in the TE-IVDs. Higher structural organization was also shown to correlate directly with greater compressive properties in equilibrium, and similarly dependent upon initial cell content more than initial

collagen concentration. This is the first study to our knowledge that employed high-density collagen for AF scaffold in composite IVD replacements. Previous studies on high-density collagen scaffolds for AF engineering have focused on the collagen as a carrier for AF cells or MSCs to fill AF defects.[68,78] Future work should consider co-culture of MSCs with tissue-specific cells to further enhance the structural organization and the conditions for tissue maturation.

Supplemental Data

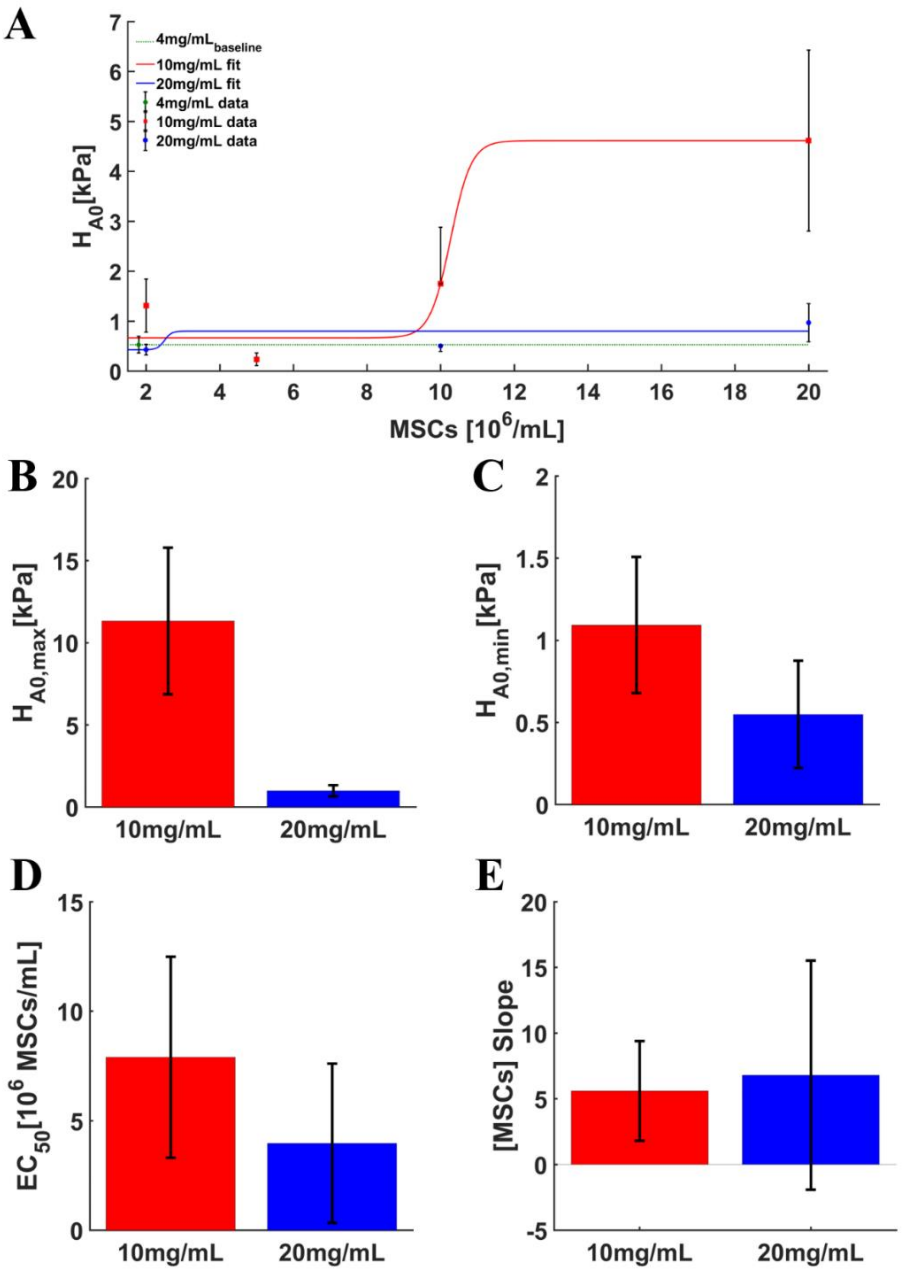

Figure 4.8. A) Curve fit of effective aggregate modulus of composite TE-IVDs as a function of hMSCs initial seeding density in AF, grouped by density of collagen/AF scaffold; N= 1-3; mean ± SE. B-E) Coefficients generated from Monte Carlo simulations including maximum and minimum effective aggregate moduli, EC_{50} in hMSCs seeding density, and transition slope; N= 100; mean ± SD; bars: $p < 0.05$.

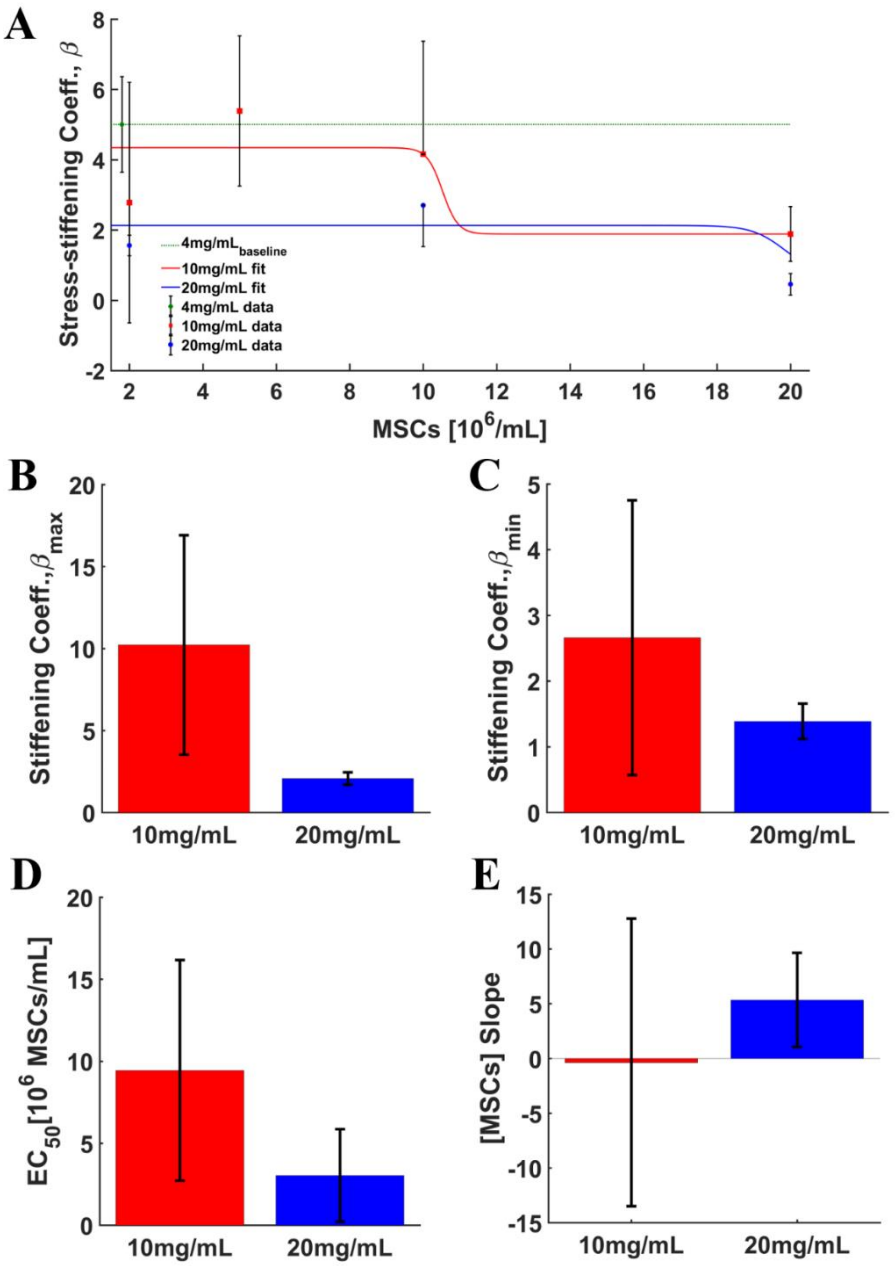

Figure 4.9. A) Curve fit of effective equilibrium stress-stiffening coefficient of composite TE-IVDs as a function of hMSCs initial seeding density in AF, grouped by density of collagen/AF scaffold; N= 1-3; mean ± SE. B-E) Coefficients generated from Monte Carlo simulations including maximum and minimum β coefficient, EC_{50} in hMSCs seeding density, and transition slope; N= 100; mean ± SD; bars: $p < 0.05$.

REFERENCES

1. Menezes Costa LC, Maher CG, Hancock MJ, Herbert RD, Refshauge KM, Henschke N. Prognosis for patients with chronic low back pain: inception cohort study. BMJ 2009; 339: b3829.

2. Luoma K, Riihimaki H, Luukkonen R, Raininko R, Viikari-Juntura E, Lamminen A. Low back pain in relation to lumbar disc degeneration. Spine 2000; 25(4): 487-92.

3. Teraguchi M, Yoshimura N, Hashizume H, Muraki S, Yamada H, Minamide A, Oka H, Ishimoto Y, Nagata K, Kagotani R, Takiguchi N, Akune T, Kawaguchi H, Nakamura K, Yoshida M. Prevalence and distribution of intervertebral disc degeneration over the entire spine in a population-based cohort: the Wakayama Spine Study. Osteoarthritis and Cartilage 2013; 22: 104-110.

4. Sambrook PN, MacGregor AJ, Spector TD. Genetic influences on cervical and lumbar disc degeneration: a magnetic resonance imaging study in twins. Arthritis Rheum 1999; 42: 366-72.

5. Kjaer P, Laboeuf-Yde C, Korsholm L, Sorensen JS, Bendix T. Magnetic resonance imaging and low back pain in adults: a diagnostic imaging study of 40-year-old men and women. Spine 2005; 30: 1173-80.

6. Hassett G, Hart D, Manek N, Doyle DV, Spector TD. Risk factors for progression of lumbar spine disc degeneration: the Chingford Study. Arthritis Rheum 2003; 48: 3112-7.

7. Okada E, Matsumoto M, Ichihara D, Chiba K, Toyama Y, Fujiwara H, et al. Aging of the cervical spine in healthy volunteers: a 10-year longitudinal magnetic resonance imaging study. Spine 2009; 34: 706-12.

8. Arana E, Marti-Bonmatí L, Mollá E, Costa S. Upper thoracic spine disc degeneration in patients with cervical pain. Skeletal Radiol 2004; 33: 29-33.

9. Todd AG. Cervical spine: degenerative conditions. Curr Rev Musculoskelet Med 2011; 4: 168–174.

10. Ehrlich GE. Low back pain. Bull World Health Organ. 2003; 81(9): 671–676.

11. Urban JPG and Roberts S. Degeneration of the intervertebral disc. Arthritis Res Ther 2003; 5(3): 120-130.

12. Masuda K and Lotz JC. New challenges for intervertebral disc treatment using regenerative medicine. Tissue Eng Part B Rev. 2010; 16(1): 147-158.

13. Cowan JA Jr, Dimick JB, Wainess R, Upchurch GR Jr, Chandler WF, La Marca F. 2006. Changes in the utilization of spinal fusion in the United States. Neurosurgery. 59(1): 15-20.

14. Hillibrand AS, Robbins M. 2004. Adjacent segment degeneration and adjacent segment disease: the consequences of spinal fusion? Spine J. 4(Suppl. 6): S190-4.

15. Albert TJ, Eichenbaum MD. 2004. Goals of cervical disc replacement. Spine J. 4(Suppl. 6): S292-3.

16. Maldonado CV, Paz RD, Martin CB. 2011. Adjacent-level degeneration after cervical disc arthroplasty versus fusion. Eur Spine J. 20(Suppl. 3): S403-7.

17. Jawahar A, Cavanaugh DA, Kerr EJ 3rd, Birdsong EM, Nunley PD. 2010. Total disc arthroplasty does not affect the incidence of adjacent segment degeneration in cervical spine: results of 93 patients in three prospective randomized clinical trials. Spine J. 10(12): 1043-8.

18. Sugawara T, Itoh Y, Hirano Y, Higashiyama N, Mizoi K. 2009. Long term outcome and adjacent disc degeneration after anterior cervical discectomy and fusion with titanium cylindrical cages. Acta Neurochir (Wien). 151(4): 303-9.

19. Kelly MP, Mok JM, Frisch RF, Tay BK. 2011. Adjacent segment motion after anterior cervical discectomy and fusion versus Prodisc-c cervical total disk arthroplasty: analysis form a randomized, controlled trial. Spine (Phila Pa 1976). 36(15): 1171-9.

20. Hudson KD, Alimi M, Grunert P, Hartl R, Bonassar LJ. Recent advances in biological therapies for disc degeneration: tissue engineering of the annulus fibrosus, nucleus pulposus and whole intervertebral discs. Curr. Opin. Biotechnol. 2013; 24(5): 872-879.

21. Illien-Jünger S, Sedaghatpour DD, Laudier DM, Hecht AC, Qureshi SA, Iatridis JC. Development of a bovine decellularized extracellular matrix-biomaterial for nucleus pulposus regeneration. J. Orthopaedic Res. 2015;

22. Long RG, Rotman SG, Hom WW, Assael DJ, Grijpma DW, Iatridis JC. In vitro and biomechanical screening of polyethylene glycol and poly (trimethylene

carbonate) block copolymers for annulus fibrosus repair. J. Tissue Eng. Regen. Med. 2016;

23. McGuire R, Borem R, Mercuri J. The fabrication and characterization of a multi-laminate, angle-ply collagen patch for annulus fibrosus repair. J. Tissue Eng. Regen. Med. 2016;

24. Fernandez C, Marionneaux A, Gill S, Mercuri J. Biomimetic nucleus pulposus scaffold created from bovine caudal intervertebral disc tissue utilizing an optimal decellularization procedure. J. Biomed. Mater. Res. Part A. 2016; 104 (12): 3093-3106.

25. Mercuri J, Addington C, Pascal R, Gill S, Simionescu D. Development and initial characterization of a chemically stabilized elastin-glycosaminoglycan-collagen composite shape-memory hydrogel for nucleus pulposus regeneration. J. Biomed. Mater. Res. Part A. 2014; 102(12): 4380-93.

26. Nerurkar NL, Baker BM, Sen S, Wible EE, Elliott DM, Mauck RL. Nanofibrous biologic laminates replicate the form and function of the annulus fibrosus. Nat. Mater. 2009; 8(12): 986-92.

27. Likhitpanichkul M, Dreischarf M, Illien-Junger S, Walter B, Nukaga T, Long R, Sakai D, Hecht A, Iatridis J. Fibrin-genipin adhesive hydrogel for annulus fibrosus repair: performance evaluation with large animal organ culture, in situ biomechanics, and in vivo degradation tests. Eur. Cells Mater. 2014; 28: 25.

28. Mizuno H, Roy AK, Vacanti CA, Kojima K, Ueda M, Bonassar LJ. 2004. Tissue-engineered composites of anulus fibrosus and nucleus pulposus for intervertebral disc replacement. Spine (Phila Pa 1976). 29(12): 1290-7.

29. Nesti LJ, Li WJ, Shanti RM, Jiang YJ, Jackson W, Feedman BA, Kuklo TR, Giuliani JR, Tuan RS. 2008. Intervertebral disc tissue engineering using a novel hyaluronic acid-nanofibrous scaffold (HANFS) amalgam. Tissue Eng Part A. 14(9): 1527-37.

30. Nerurkar NL, Sen S, Huang AH, Elliott DM, Mauck RL. 2010. Engineered disc-like angle-ply structures for intervertebral disc replacement. Spine (Phila Pa 1976). 35(8): 867-73.

31. Bowles RD, Williams RM, Zipfel WR, Bonassar LJ. 2010. Self-assembly of aligned tissue-engineered annulus fibrosus and intervertebral disc composite via collagen gel contraction. Tissue Eng Part A. 16(4): 1339-48.

32. Lazebnik M, Singh M, Glatt P, Friis LA, Berkland CJ, Detamore MS. 2011. Biomimetic method for combining the nucleus pulposus and annulus fibrosus for intervertebral disc tissue engineering. J Tissue Eng Regen Med. 5(8): e179-87.

33. Zhuang Y, Huang B, Li CQ, Liu LT, Pan Y, Zheng WJ, Luo G, Zhou Y. 2011. Construction of tissue-engineered composite intervertebral disc and preliminary morphological and biochemical evaluation. Biochem Biophys Res Commun. 407(2): 327-32.

34. Bowles RD, Gebhard HH, Hartl R, Bonassar LJ. 2011. Tissue-engineered intervertebral discs produce new matrix, maintain disc height, and restore biomechanical function to the rodent spine. Proc Natl Acad Sci USA. 108(32): 13106-11.

35. Park SH, Gil ES, Cho H, Mandal BB, Tien LW, Min BH, Kaplan DL. 2012. Intervertebral disk tissue engineering using biphasic silk composite scaffolds. Tissue Eng Part A. 18(5-6): 447-58.

36. Martin JT, Milby AH, Ikuta K, Poudel S, Pfeifer CG, Elliott DM, Smith HE, Mauck RL. A radiopaque electrospun scaffold for engineering fibrous musculoskeletal tissues: Scaffold characterization and in vivo applications. Acta Biomater. 2015; 26: 97-104.

37. Moriguchi Y, Mojica-Santiago J, Grunert P, Pennicooke B, Berlin C, Khair T, Navarro-Ramirez R, Ricart Arbona RJ, Nguyen J, Hartl R, Bonassar LJ. 2017. Total disc replacement using tissue-engineered intervertebral discs in the canine cervical spine. PLoS One. 12(10): e0185716.

38. Nerurkar NL, Elliott DM, Mauck RL. Mechanical design criteria for intervertebral disc tissue engineering. J Biomech. 2010; 43(6):1017-30.

39. Cortes DH, Jacobs NT, DeLucca JF, Elliott DM. Elastic, permeability and swelling properties of human intervertebral disc tissues: A benchmark for tissue engineering. J Biomech. 2014; 47(9): 2088-94.

40. Cloyd JM, Malhotra NR, Weng L, Chen W, Mauck RL, Elliott DM. Material properties in unconfined compression of human nucleus pulposus, injectable hyaluronic acid-based hydrogels, and tissue engineering scaffolds. Eur Spine J. 2007; 16:1892-8.

41. Best BA, Guilak F, Setton LA, Zhu W, Saed-Nejad F, Ratcliffe A, Weidenbaum M, Mow VC. Compressive mechanical properties of the human anulus fibrosus and their relationship to biochemical composition. Spine. 1994; 19: 212-21.

42. Iatridis JC, Setton LA, Foster RJ, Rawlins BA, Weidenbaum M, Mow VC. Degeneration affects the anisotropic and nonlinear behaviors of human anulus fibrosus in compression. J Biomech. 1998; 31: 535-44.

43. Perie D, Korda D, Iatridis JC. Confined compression experiments on bovine nucleus pulposus and annulus fibrosus: sensitivity of the experiment in determination of compressive modulus and hydraulic permeability. J Biomech. 2005; 38: 2164-71.

44. Cortes DH, Han WM, Smith LJ, Elliott DM. Mechanical properties of the extra-fibrillar matrix of human annulus fibrosus are location and age dependent. J Orthop Res. 2013; 31: 1725-32.

45. Tavakoli J, Elliott DM, Costi JJ. Structure and mechanical function of the inter-lamellar matrix of the annulus fibrosus in the disc. J Orthop. Res. 2016; 34(8): 1307-15.

46. Bruehlmann SB, Rattner JB, Matyas JR, Duncan NA. Regional variations in the cellular matrix of the annulus fibrosus of the intervertebral disc. J Anat. 2002; 201: 159-71.

47. Rong Y, Sugumaran G, Silbert JE, Spector M. Proteoglycans synthesized by canine intervertebral disc cells grown in a type I collagen–glycosaminoglycan matrix. Tissue Eng 2002; 8:1037-47.

48. Saad L, Spector M. Effects of collagen type on the behavior of adult canine annulus fibrosus cells in collagen-glycosaminoglycan scaffolds. J Biomed Mater Res Part A. 2004; 71(2): 233-41.

49. Hudson KD, Mozia RI, Bonassar LJ. Dose-dependent response of tissue-engineered intervertebral discs to dynamic unconfined compressive loading. Tissue Eng Part A. 2015; 21(3-4): 564-72.

50. Borde B, Grunert P, Hartl R, Bonassar LJ. Injectable, high-density collagen gels for annulus fibrosus repair: An in vitro rat tail model. J Biomed Mater Res Part A. 2015; 103A: 2571-81.

51. Puetzer JL, Bonassar LJ. High density type I collagen gels for tissue engineering of whole menisci. Acta Biomaterialia. 2013; 9(8): 7787-95.

52. Bron JL, Mulder HW, Vonk LC, Doulabi BZ, Oudhoff MJ, Smit TH. Migration of intervertebral disc cells into dense collagen scaffolds intended for functional replacement. J Mater Sci: Mater Med. 2012; 23: 813-21.

53. Cohen BP, Hooper RC, Puetzer JL, Nordberg R, Asanbe O, Hernandez KA, Spector JA, Bonassar LJ. Long-term morphological and microarchitectural stability of tissue-engineered, patient-specific auricles in vivo. Tissue Eng Part A. 2016; 22(5-6): 461-8.

54. Cross VL, Zheng Y, Won Choi N, Verbridge SS, Sutermaster BA, Bonassar LJ, Fischbach C, Stroock AD. Dense type I collagen matrices that support cellular remodeling and microfabrication for studies of tumor angiogenesis and vasculogenesis in vitro. Biomaterials. 2010; 31(33): 8596-607.

55. Risbud MV, Albert TJ, Guttapalli A, Vresilovic EJ, Hillibrand AS, Vaccaro AR, Shapiro IM. Differentiation of mesenchymal stem cells towards a nucleus pulposus-like phenotype in vitro: implications for cell-based transplantation therapy. Spine (Phila Pa 1976). 2004; 29(23): 2627-32.

56. Risbud MV, Shapiro IM, Vaccaro AR, et al: Stem cell regeneration of the nucleus pulposus. Spine. 2004; J 4 (Suppl 6):348S–353S.

57. Sakai D, Mochida J, Yamamoto Y, et al: Transplantation of mesenchymal stem cells embedded in Atelocollagen gel to the intervertebral disc: a potential therapeutic model for disc degeneration. Biomaterials. 2003; 24: 3531–41.

58. Hudson KD, Bonassar LJ. Hypoxic expansion of human mesenchymal stem cells enhances three-dimensional maturation of tissue-engineered intervertebral discs. Tissue Eng. Part A. 2017; 23(7-8): 293-300.

59. Watanabe T, Sakai D, Yamamoto Y, Iwashina T, Serigano K, Tamura F, Mochida J. Human nucleus pulposus cells significantly enhanced biological properties in a coculture system with direct cell-to-cell contact with autologous mesenchymal stem cells. J Orthop Res. 2010; 28(5): 623-30.

60. Mochida J, Sakai D, Nakamura Y, Watanabe T, Yamamoto Y, Kato S. Intervertebral disc repair with activated nucleus pulposus cell transplantation: a three-year prospective clinical study of its safety. Eur Cell Mater. 2015; 29: 2012-22.

61. Zhang YG, Guo X, Xu P, Kang LL, Li J. Bone mesenchymal stem cells transplanted into rabbit intervertebral discs can increase proteoglycans. Clin Orthop Relat Res 2005; 430: 219–26.

62. Bendsten M, Bunger CE, Zou X, Foldager C, Jorgensen HS. Autologous stem cell therapy maintains vertebral blood flow and contrast diffusion through the endplate in experimental intervertebral disc degeneration. Spine (Phila Pa 1976). 2011; 36(6): E373-9.

63. Steck E, Bertram H, Abel R, et al: Induction of intervertebral disc-like cells from adult mesenchymal stem cells. Stem Cells. 2005; 23: 403-11.

64. Acosta FL, Lotz J, Ames CP. The potential role of mesenchymal stem cell therapy for intervertebral disc degeneration: a critical overview. Neurosurg Focus. 2005; 19(3): E4.

65. Sakai D. Future perspectives of cell-based therapy for intervertebral disc disease. Eur Spine J. 2008; 17(Suppl 4): S452-S458.

66. Martin JT, Gullbrand SE, Kim DH, Ikuta K, Pfeifer CG, Ashinsky BG, Smith LJ, Elliott DM, Smith HE, Mauck RL. In vitro maturation and in vivo integration and function of an engineered cell-seeded disc-like angle ply structure (DAPS) for total disc arthroplasty. Scientific Reports. 2017; 7: 15765.

67. McCorry MC, Puetzer JL, Bonassar LJ. Characterization of mesenchymal stem cells and fibrochondrocytes in three-dimensional co-culture: analysis of cell shape, matrix production, and mechanical performance. Stem Cell Res Ther. 2016; 7: 39.

68. Guillaume O, Naqvi SM, Lennon K, Buckley CT. Enhancing cell migration in shape-memory alginate-collagen composite scaffolds: in vitro and ex vivo assessment for intervertebral disc repair. J Biomat. Appl. 2014; 29(9): 1230-46.

69. Kim YJ, Bonassar LJ, Grodzinsky AJ. The role of cartilage streaming potential, fluid flow and pressure in the stimulation of chondrocyte biosynthesis during dynamic compression. J Biomech. 1995; 28: 1055-66.

70. Holmes MH and Mow VC. The non-linear characteristics of soft gels and hydrated connective tissues in ultrafiltration. J Biomech. 1990; 23: 1145-56.

71. Bates D, Maechler M, Bolker B, Walker S. Fitting linear mixed-effects models using lme4. J Stat Soft. 2015; 67(1): 1-48.

72. Bonnevie ED, Galesso D, Secchieri C, Cohen I, Bonassar LJ. Elastoviscous transitions of articular cartilage reveal a mechanism of synergy between lubricin and hyaluronic acid. PLoS ONE. 2015; 10(11): e0143415.

73. Elsdale T, Bard J. Collagen substrata for studies on cell behavior. J Cell Biol. 1972; 54(3): 626-37.

74. Bell E, Ivarsson B, Merrill C. Production of a tissue-like structure by contraction of collagen lattices by human fibroblasts of different proliferative potential in vitro. PNAS. 1979; 76(3): 1274-8.

75. Vernon RB, Sage EH. Contraction of fibrillar type I collagen by endothelial cells: a study in vitro. J Cell Biochem. 1996; 60(2): 185-97.

76. Hudson KD, Bonassar LJ. Hypoxic expansion of human mesenchymal stem cells enhances three-dimensional maturation of tissue-engineered intervertebral discs. Tissue Eng Part A. 2017; 23(7-8): 293-300.

77. McCorry MC, Bonassar LJ. Fiber development and matrix production in tissue engineered menisci using bovine mesenchymal stem cells and fibrochondrocytes. Connect Tissue Res. 2017; 58(3-4): 329-41.

78. Pennicooke B, Moriguchi Y, Hussain I, Bonassar LJ, Hartl R. Biological treatment approaches for degenerative disc disease: a review of clinical trials and future directions. Cureus 8(11): e892.

CHAPTER 5

Concluding Remarks

Summary

This dissertation sought to develop canine disc-sized composite TE-IVDs for the *in vivo* evaluation of a pre-clinical canine cervical spine model of total disc replacement (TDR) to support the long-term goal of advancing TE-IVDs closer to translation into humans. In the process of investigating the efficacy of this animal model, not only was the proof of concept objective met successfully, but challenges for achieving a clinically applicable TE-IVD construct related to motion segment stability upon implantation and implant pre-operative composition and structure were also identified (Chapter 2). The stability of canine motion segments was then investigated with a novel treatment approach of a resorbable plating system combined with implanted TE-IVDs, which was found to partially restore the compressive stiffness of segments, provide separation of endplates, and prevent implant migration out of the disc space (Chapter 3). Finally, the effect on TE-IVD structure and composition of initial collagen AF concentration was found to be unexpectedly minimal as compared to the effect that the initial seeding density of human MSCs has in remodeling the AF scaffold into its final apparent AF density (Chapter 4). This chapter discusses the main findings on this dissertation and suggests future directions that can build on this subject.

Canine *in vivo* model for cervical disc replacement

In chapter 2, we demonstrated that fabrication of alginate- and collagen-based TE-IVDs was scalable to produce canine-sized constructs and that stable implantation of these constructs integrate into host tissue and preserves disc hydration and height for up to 16 weeks *in vivo*. In addition, from the testing conditions for surgical intervention, we found that PLL resection failed to prove a differentiating effect overall in stably implanted TE-IVDs. We also discovered that most of the constructs that were retained

in the disc space post-operatively were implanted in level C3/C4. The fact that roughly 50% of all the TE-IVDs were displaced suggests that there is a need to ensure a roster of TE-IVDs of different sizes before the clinicians, since the constructs are designed to hold in the disc space via press fitting. It is also known that motion segments along the spine have different geometries and anatomical dimensions from each other; therefore, morphology of the vertebral endplate arguably plays a greater role of responsibility for the extruded discs than the TE-IVD fabrication process.

The canine cervical spine provides several advantages to study TDR with TE-IVDs. The similarities between human cervical spine and canine cervical spines are more pronounced in the degenerative process that affects IVD ageing and in their kinematic patterns. In rat tails, the highly compressive loading environment with minimal torsional rotation and bending moments was enough to allow the press-fit implantation of TE-IVDs. In the canine model, as it occurs with human spines, the loading environment *in vivo* consisted of coupled bending and torsional loadings; although the higher compressive stresses in the canine neck and the inclined morphology of the cervical endplates aggravated the stability of implanted TE-IVDs. Another aspect that warrants close attention is the increased diffusion length of larger TE-IVDs as the size scaling changes from rat- and canine-sized discs to humans. In preliminary *in vitro* work for this study (Appendix A), 70% smaller TE-IVDs than normal canine IVDs were observed to outperform the size-accurate TE-IVDs. To successfully scale up the TDR of TE-IVDs to human spines, alternative approaches that acknowledge these limitations should be explored; considering anchoring of TE-IVDs to the endplates or employing flexible biomaterials that promote implant stability and guarantees diffusion of metabolites to the disc space in the long term are encouraged.

Combined replacement treatment of TE-IVDs with bioresorbable stabilization

In chapter 3, we proposed a novel combination of treatment employing a bioresorbable fixation plate along with the implanted TE-IVDs. We tested the hypothesis that a combined treatment approach of implanted TE-IVDs with resorbable PLGA plating will improve the stiffness of canine cervical spine motion segments *ex vivo* and prevent the extrusion of TE-IVD constructs from the disc space. This combined treatment was idealized from our findings in the *in vivo* model described in chapter 2; instability of the motion segments after discectomy displaced implanted TE-IVDs out of the disc space ventrally. Our *ex vivo* model captured the mechanism of implant extrusion observed in the canine surgeries upon placement in the disc space without the resorbable plating. Combining resorbable plating with implanted TE-IVDs improved the stability of the motion segments, by increasing the effective stiffness of the segment over the solely implanted treatment and significantly reducing the resultant displacement of TE-IVDs, thereby preventing extrusion of the implants.

Structure and composition of TE-IVDs by cell and collagen densities

In chapter 4, we investigated the interactions between collagen scaffold density and initial cell content in the context of structural remodeling of the AF and resultant tissue composition. We hypothesized that high-density collagen scaffolds seeded with hMSCs will improve baseline AF properties in TE-IVDs in terms of tissue structure and composition. Our findings in this study suggest that the initial seeding density rather than collagen concentration had the most impact in remodeling the AF scaffold, since the structural orientation from which the tissue stiffness rises, and the ECM deposition are directly linked to the metabolic activity of the embedded cells. The extent to which the collagen concentration affects the ECM remodeling is in fact detrimental in that denser matrices require significant more energy expense for cell traction forces to act on them; moreover, excessively stiff hydrogels could lead to deviations of hMSCs from

a predominantly chondrogenic pathway to a mineralized and rigid scaffold while in tissue culture. In the pursuit of scaling up tissue-engineered constructs, material composition, tissue stiffness, and cell viability within regions of larger diffusion distances can all counteract each other. From this work, it is believed that in dense 20 mg/mL matrices, hMSCs were unable to remodel the collagen scaffold simply because they were not obtaining the nutrients required to effect sufficient contractile forces. Conversely, the 10 mg/mL matrices at increasing cell content remodeled the AF scaffold as expected, affecting TE-IVD stiffness in a form dependent on initial cell seeding dose.

Conclusion

Overall, this body of work represents an insightful contribution to the field of intervertebral disc engineering. This work serves as a significant stepping stone in the advancement of clinical translation of total replacement with TE-IVDs. In addition, the methodologies discussed throughout each chapter are applicable to other fields. For example, displacement field analysis of implant motion could provide a tool for estimation of localized strains under various surgical conditions in neurology and with a milieu of potential treatments. Moreover, understanding the interplay between hMSCs and dense collagen scaffolds can help improve on engineered constructs for other fibrous tissues, such as tendons, cardiac muscle, and neural tissues.

Future Directions

The work outlined in this dissertation lays the foundation for a number of future directions. This section includes recommendations for *in vitro* maturation of TE-IVDs to further improve construct properties as well as suggestions for *ex vivo* and *in vivo* studies with the canine cervical spine model of TDR.

Improving TE-IVDs in vitro

The tunability of AF scaffolds and the effects of initial cell seeding on dense matrices can be capitalized to improve designs of composite TE-IVDs at scales closer to human discs. A regional variation of dense AF scaffolds with a moderate collagen concentration at the outer AF and low-density collagen in the inner AF will provide the ideal 3D culture environment for cells to remodel into a native-like IVD structure. Keeping the NP as a highly porous matrix, as with alginate hydrogels, will remain essential for facilitating the diffusion of nutrients within the proposed TE-IVD. As shown in chapter 4, the appropriate combination of cell contents in dense matrices will require further studies to enhance the resulting AF architecture in TE-IVDs with regional variations of remodeling, thereby improving tissue composition and function.

Co-culture of AF and NP cells with bone-marrow derived MSCs has been extensively shown to enhance the maturation of engineered tissues *in vitro*. Future studies of TE-IVDs with hMSCs could employ formulaic combinations of cells derived from partial and/or total discectomies in patients and commercially available hMSCs to effectively obtain a sufficient number of cells to populate human-sized TE-IVDs. The basis for the proposed study has been previously attempted in our group with the isolation of hMSCs from bone marrow aspirate. The advantage in this case would be that AF and NP tissues will help guide the formation of relevant ECM due to cell-cell signaling in concert with the already characterized cell-material interactions.

Hybrids of synthetic fibers embedded in collagen gels represent a potential avenue to develop novel AF scaffold designs. Previous work had employed hybrids of synthetic fibers and hydrogels, such as silk and fibrin gel scaffolds of Park et al., while others have artificially recreated the AF architecture with PGA/PLA or PCL alone without accounting for the developmentally-inspired remodeling observed in collagen-based AF scaffolds. In this context, a hybrid scaffold that employs resorbable fibers

(e.g. PLGA) with an initially laminated architecture and a dense-collagen matrix capable of cell-induced traction constitutes a new generation of composite TE-IVDs. The advantage of such a proposed construct relies on the opportunity to initially guide cell alignment with the resorbable fibers and simultaneously promoting channels for collagen fiber remodeling.

Improving Canine TDR studies

To truly understand the performance of TE-IVDs *in vivo* after TDR, the importance of testing motion segments in torsion and in bending with implanted constructs cannot be overlooked. The range of motion in the cervical spine represents a challenge for the current generation of TE-IVDs that rely entirely on a press-fit implantation as in the rat tail model. Employing the digital correlation displacement mapping technique described in chapter 3 during torsion and bending testing *ex vivo* could help identify mechanisms of failure within motion segments that resemble the complex loading environment in living subjects. In addition, e*x vivo* testing of motion segments under uniaxial dynamic compression is a strongly recommended next step to better assess the long-term effects of unstable implantation of TE-IVDs.

A combined approach of treatment is still recommended for the next phase of *in vivo* testing of TE-IVDs, especially when the geometry of the endplates is considered. While resorbable plating served as a valuable initial step towards combining temporary spinal stabilization with TE-IVD integration, using flexible resorbable materials as physical barrier in lieu of a rigid plate could provide better outcomes in the long term. Lastly, the next phase for *in vivo* studies in canine cervical spines would need to build upon the acquired insights of ideal surgical conditions (i.e. implantation level) and optimized TE-IVD fabrication (e.g. moderately dense matrices with higher degree of AF remodeling).

Given the number of finite element models currently used in the literature to describe spine biomechanics, recreating a clinically relevant simulation of mechanical testing of motion segments would prove beneficial to better understand distribution of loads in the disc space under various treatments such as the ones described in chapter 3. Furthermore, a computational 3D model of the alginate- and collagen- composite TE-IVDs developed in the Bonassar Lab represents an area of interest that remains unexplored, which could be useful in the design of the next generation of composite TE-IVDs. Abundant work has been done in mechanically describing alginate and collagen gels individually, however, little has been done to understand the extent to which these materials contribute to the effective stiffness observed in composite structures such as TE-IVDs. It is recommended here to use a framework based on biochemical constituents similar to that of constitutive modeling of native fibrocartilaginous tissues, especially with further scaling up of constructs towards human-sized TE-IVDs.

The ultimate goal of this research is to clinically translate the state of TE-IVD technology for a biologically-based TDR alternative treatment of DDD. This work demonstrated the feasibility of a clinically-relevant animal model of TDR to further study novel TE-IVD approaches. The basis for *ex vivo* testing of canine motion segments to analyze novel treatments was also proposed. Lastly, the significance of the appropriate content of a clinically relevant cell source in the context of capability to remodel dense AF scaffolds was identified. Altogether, these findings provide new baseline conditions from which to produce the next generation of TE-IVDs.

APPENDICES

Appendix A: Scaling up the fabrication of alginate and collagen tissue-engineered intervertebral discs for a pre-clinical canine model[3]

Introduction

Whole tissue-engineered intervertebral disc (TE-IVD) scaffolds have been produced in the last decade as a biological alternative to treat degenerative disc disease (DDD). Investigators have proposed diverse approaches to construct composite scaffolds with distinct nucleus pulposus (NP) and annulus fibrosus (AF) regions designed for total disc replacement.[1-6] Efforts led to in vivo studies in athymic mice and rats that have yielded promising results, in terms of tissue integration, biochemical composition, and mechanical function.[5,7] However, small animal models limit the composite TE-IVDs to a different biomechanical environment from what occurs in the human spine and have a considerably different anatomy. To date, a larger animal model with comparable loading patterns and anatomical features remain to be studied. Small breeds of dogs develop spontaneous cervical disc degeneration and have been used as animal models for biomechanical studies of disc diseases and surgical procedures.[8-10] The current work seeks to utilize our previously established methods[2] to scale up the manufacture of composite alginate and collagen TE-IVDs for a canine cervical spine model and characterize the mechanical and morphological properties of canine-sized TE-IVDs.

Materials and Methods

Direct measurements of the C2/C3 and C3/C4 IVDs were obtained from three-year old beagles and the dorsoventral, lateral-lateral, and disc height dimensions were used to create customized models of molds with NP-sized cavities in Solid Works. The

[3] Portions of this appendix were published in the Transactions of the Orthopaedic Research Society Annual Meeting in 2014, New Orleans, LA: Jorge A. Mojica-Santiago, Peter Grunert, MD, Roger Hartl, MD, Lawrence J. Bonassar, PhD. Fabrication of canine-sized alginate/collagen tissue-engineered intervertebral discs. http://www.ors.org/Transactions/60/0732.pdf

CAD mold models were fabricated in UV-cured acrylic plastic using 3D printing technology. Four groups of TE-IVDs were produced by varying the size of the disc and the number of AF layers.[2] NP and AF cells were isolated from the lumbar spine of skeletally mature Finn/Dorset cross male sheep and cultured for 3 weeks. NP cells were encapsulated in 3% alginate and injected into the molds to produce NP scaffolds, while AF cells were seeded in 2mg/mL solution of collagen type I gel to create the AF layers. Two groups consisted of double-layered discs - mold cavity dimensions were 1:1 and 3:4 of the CAD model - and a group of single layered discs. The composite discs were cultured for 2-4 weeks and disc size measurements were taken twice a week using ImageJ to measure the annular contraction and the NP/AF ratio. Samples were tested under unconfined axial compression using multi-step stress relaxation methods, and the instantaneous and equilibrium moduli were obtained to assess their viscoelastic response.[11] Statistical significance in all results was determined at a 95% level of confidence with a p-value lower than 0.05, using a single factor analysis of variance followed by a post-hoc Scheffé Test.

Results

The single-layered discs had significantly greater ratios of NP:AF (0.6±0.1 %) than both double-layered groups by the end of the culture period (Fig.1, right). A contraction ranging from 13.8 to 17.9% of the original size was observed in both single-layered and double-layered TE-IVDs by the first week (Fig.1, left). With a mean equilibrium modulus of 1.4±0.6 kPa, the large double-layered discs resulted significantly greater than the 0.3±0.2 kPa of the single-layered group, but there were no significant differences between the mean equilibrium modulus of small double-layered discs (0.7±0.6 kPa) and the other groups (Fig.2, right). Within the double-layered groups, the large discs presented a significantly greater instantaneous modulus (2.1±0.9 kPa) than their 25% smaller counterparts, which yielded mean modulus values of

1.0±0.7 kPa (Fig.2, left). The mean elastic modulus of the single layered discs (0.4±0.1 kPa) resulted significantly different to the large multilamellar disc only.

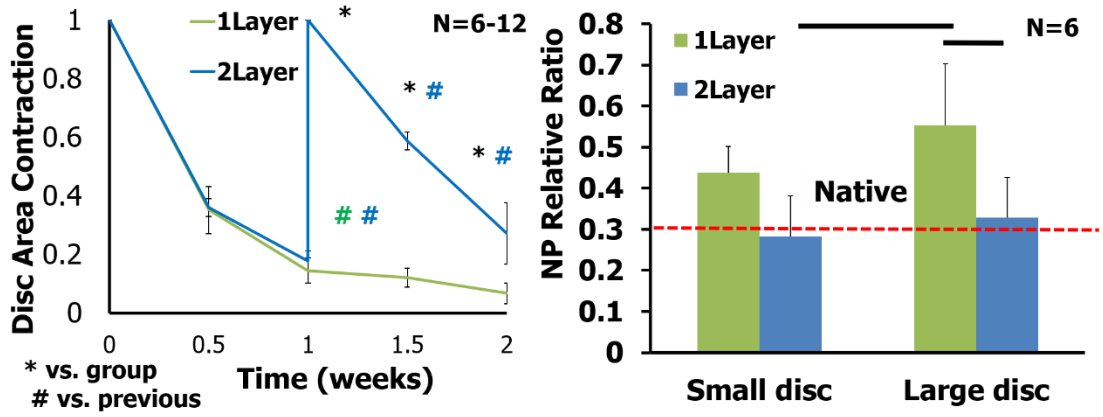

Appendix Figure 1. Disc ratio to the initial area (left) was significantly decreased between time points (#, $p < 0.05$) after 1 week in all groups, and significant differences in contraction (*, $p< 0.05$) were found in 1Layer discs at 1.5 weeks and 2Layer at 2 weeks, when compared to each other. At week 2, NP ratio to the total area (right) was significantly greater in 1Layer large discs than in both double layered discs (bars, $p < 0.05$), but the 2Layer discs were closer to native disc morphology. Data shown as mean ± standard deviation.

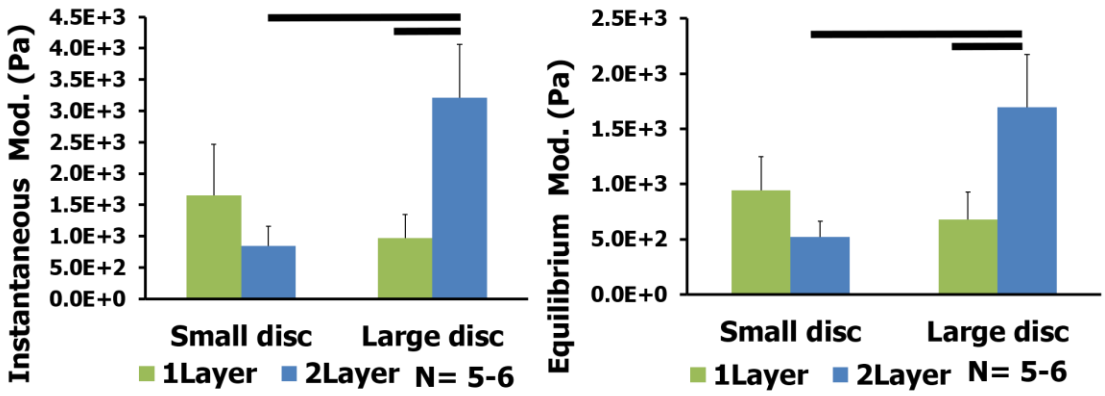

Appendix Figure 2. (Left) 2Layer large discs under uniaxial compression showed significantly higher effective Eq. Mod. and Inst. Mod. (bars, $p < 0.05$) than their single layered counterparts and the 2Layer small discs but showed no significant differences to the 1Layer small discs. Data shown as mean ± standard deviation.

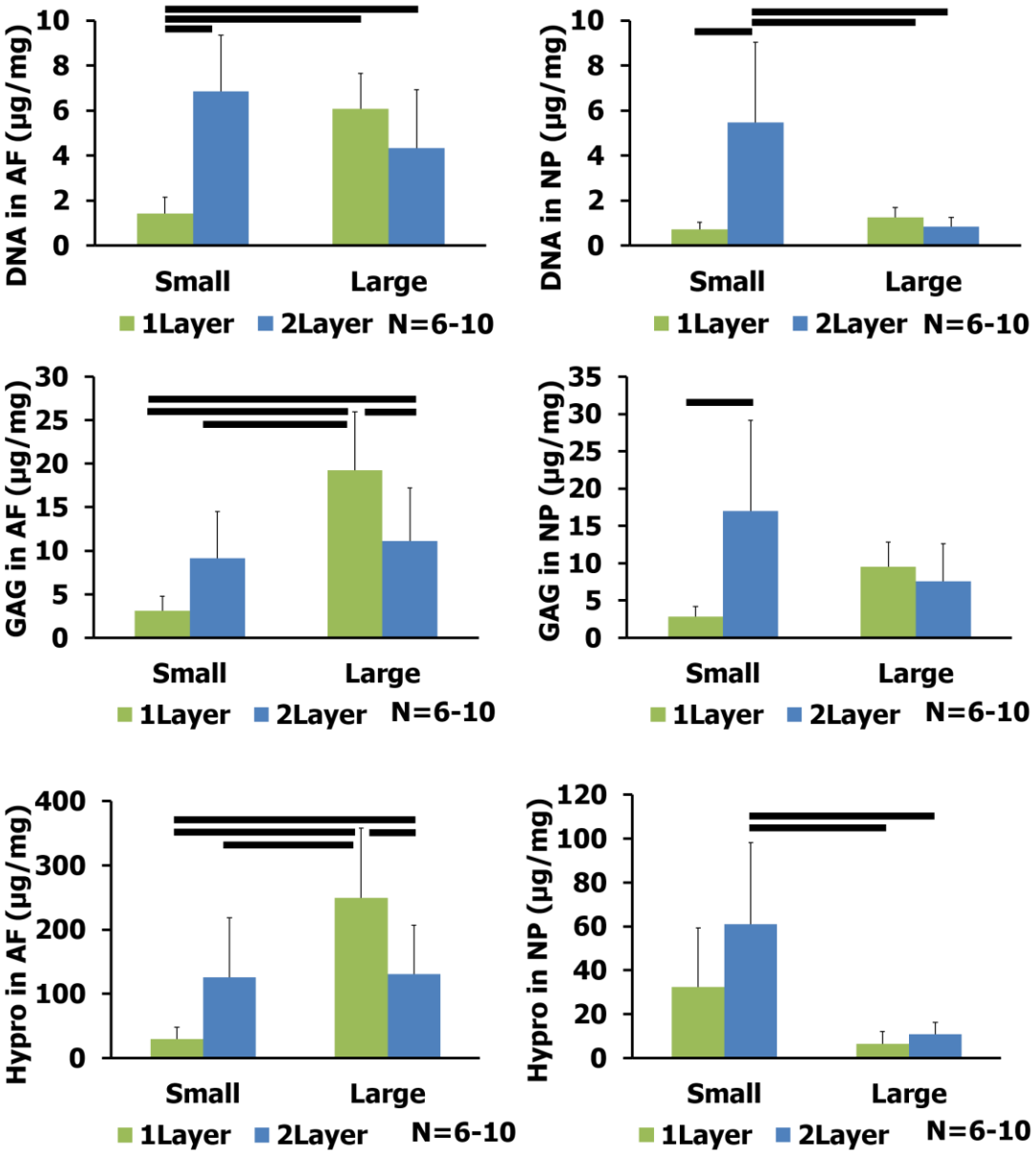

Appendix Figure 3. Biochemical composition of the TE-IVDs changed significantly with the addition of a collagen AF layer. Cell proliferation was generally improved in the NP of smaller discs (top left) as indicated by DNA content, but 1Layer small discs showed significantly less DNA content (bars, $p < 0.05$) than all other groups (top right). Collagen and proteoglycan deposition in the AF of 1Layer large discs surpassed that of all other groups (bars, $p < 0.05$, left side of middle and bottom). Smaller discs with double-AF revealed increased GAGs at the NP (middle right) than their 1Layer counterparts and showed significantly greater collagen content than all large discs (bottom right) (bars, $p < 0.05$). Data shown as mean ± standard deviation.

Discussion

The present studies showed that canine-sized composite TE-IVDs can be successfully produced by the same methods used for our *in vivo* rat TE-IVDs [7]. The implants were based of direct measurements from beagle IVDs and their size and shape were comparable to their native counterparts. Composite discs with double layers showed higher mechanical properties than those with a single layer, but they also exhibit lower NP:AF ratios than their mono-layered counterparts. The addition of collagen-based AF layers coupled with a decrease of the NP:AF ratio accounts for the production of stiffer implants, and thus provided valuable insights with respect to how differences in fabrication parameters have an effect in the compressive properties of the tissue-engineered constructs. Fundamentally, the low relative stiffness of alginate-based NP can reduce the effect of the overall composite stiffness as its relative volume increases. Therefore, in the design and scale up of alginate/collagen composite TE-IVDs, the morphological and composition characteristics allow modifying the construct properties to desired conditions.

This work demonstrates the use of established fabrication methods of composite alginate/collagen TE-IVDs, which have proven successful in rat in vivo models, as a scalable process to construct canine-sized cervical TE-IVDs. Such a large animal model with comparable morphology and biomechanical environment to human spine is required to translate this technology to clinical use as an alternative to total disc replacement with synthetic prosthetics.

		Small		Large	
		1Layer	2Layer	1Layer	2Layer
NP Relative Area (Native = 0.3)		0.4 ± 0.1	0.3 ± 0.1	0.6 ± 0.1	0.3 ± 0.1
Instantaneous Modulus (kPa)		1.7 ± 0.8	0.8 ± 0.1	1.0 ± 0.2	3.4 ± 0.9
Equilibrium Modulus (kPa)		0.9 ± 0.3	0.5 ± 0.1	0.7 ± 0.1	1.7 ± 0.5
DNA Cont (µg/mg DW)	NP	0.7 ± 0.3	5.5 ± 3.6*	1.3 ± 0.4	0.8 ± 0.4
	AF	1.4 ± 0.7	6.9 ± 2.5	6.1 ± 1.6	4.3 ± 2.6
Hypro Cont (µg/mg DW)	NP	32.4 ± 26.8	61.0 ± 37.2	6.5 ± 5.5	10.8 ± 5.4
	AF	30.2 ± 17.8	125.5 ± 92.6	249.1 ± 109.1	131.1 ± 75.5
GAG Cont (µg/mg DW)	NP	2.8 ± 1.4	17.0 ± 12.2	9.5 ± 3.3	7.6 ± 5.1
	AF	3.1 ±1.7	9.1 ± 5.3	19.3 ± 6.7	11.1 ± 6.1

Appendix Table 1. Summary of NP area ration, mechanical properties and biochemical composition measurements in two distinct sizes of TE-IVDs with 1 and 2 AF layers. The dotted box highlights the group corresponding to the design conditions selected for the subsequent *in vivo* study, particularly due to the highest cell content achieved. Data statistics shown as mean ± standard deviation.

References

1. Nesti+ Tiss Eng Pt A 2008;
2. Bowles+ Tiss Eng Pt A 2010;
3. Nerurkar+ Spine 2010;
4. Lazebnik+ J Tiss Eng Regen Med 2011;
5. Zhuang+ Biochem Biophys Res Commun 2011;
6. Park+ Tiss Eng Pt A 2012;
7. Bowles+ PNAS 2011;
8. Shores+ Comp Cont Educ Pract Vet 1982;
9. Smith+ Eur Spine J 2002;
10. Forterre+ Vet Surg 2010;
11. Kim+ J Biomech 1995.

Appendix B: Riboflavin crosslinking and high-density collagen enhance mechanical and biochemical properties of tissue-engineered intervertebral discs[4]

Introduction

Composite tissue-engineered intervertebral disc (TE-IVD) scaffolds with distinct nucleus pulposus (NP) and annulus fibrosus (AF) regions have been produced in the last decade as a proposed biological alternative to total disc replacement with synthetic implants.[1-6] TE-IVDs that have been tested *in vivo* with murine models provided promising outcomes;[5,7] however, these small animal models differ from the human spine in loading patterns and anatomical features. Current efforts have focused on evaluating the TEIVDs in a canine cervical spine model; thus, a scaled-up approach of fabricating composite alginate and collagen TE-IVDs has been characterized.[8] In order to restore the biomechanical function of the spinal motion segment, the stiffness of the TE-IVDs must be increased to withstand significantly high compressive loads in vivo. Riboflavin has been shown to effectively crosslink collagen gels[9] and increase gel stiffness without affecting cell viability. High density collagen gels have also been shown to help mechanically repair annular defects *in vivo* and *vitro*.[10] This work seeks to examine the effect of scaffold density and crosslinking on the mechanical and biochemical properties of TE-IVDs.

Materials and Methods

NP and AF cells were isolated from the cervical spine of skeletally mature beagles and cultured for 2 weeks. NP cells were encapsulated in 3% alginate and injected into the molds to produce NP scaffolds, while AF cells were seeded in 2mg/mL solution of collagen type I gel to create the AF layers. Two groups of TE-IVDs were

[4] Portions of this appendix were published in the Transactions of the Orthopaedic Research Society Annual Meeting in 2015, Las Vegas, NV: Jorge A. Mojica-Santiago, Yu Moriguchi, MD-PhD, Peter Grunert, MD, Roger Hartl, MD, Lawrence J. Bonassar, PhD. Effect of Scaffold Density and Crosslinking on Alginate and Collagen Tissue-Engineered Intervertebral Discs.
https://www.ors.org/Transactions/61/1588.pdf

produced using previously shown methods[2] by varying the size of disc and four subgroups were fabricated: double AF layer low density collagen (LDC) at 2 mg/mL, riboflavin-crosslinked LDC discs (LDC+Ribo) at 0.5 mM, double AF layer high density collagen (HDC) at 4 mg/mL, and riboflavin-crosslinked HDC discs (HDC+Ribo) at 0.5mM. All groups were cultured for 2 weeks and tested using multi-step stress relaxation tests with unconfined axial compression to determine instantaneous (IM) and equilibrium moduli (EM).[11] NP and AF scaffold regions were individually examined for DNA, proteoglycan (GAG), and collagen (Hypro) composition using conventional biochemical assays.[12-14] Statistical significance in all results was determined at a 95% level of confidence with a p-value lower than 0.05, using a single factor analysis of variance followed by a post-hoc Scheffé Test.

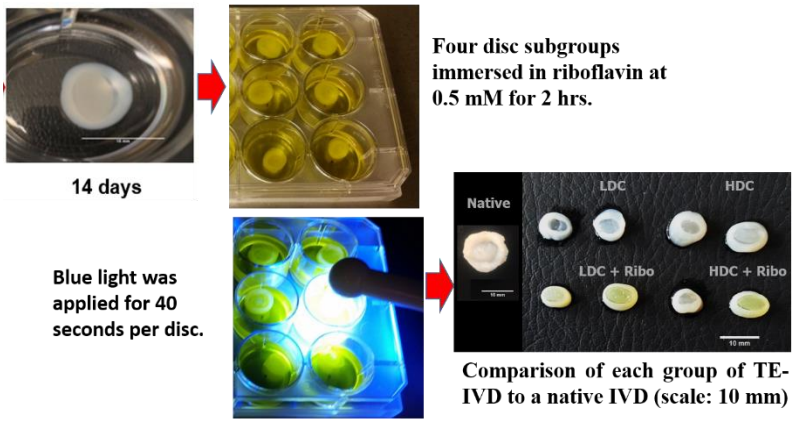

NP size & crosslinking		Collagen Density
Small	Ribo at 0.5mM	2 mg/mL (LDC)
		4 mg/mL (HDC)
	No Ribo	2 mg/mL (LDC)
		4 mg/mL (HDC)
Large	Ribo at 0.5 mM	2 mg/mL (LDC)
		4 mg/mL (HDC)
	No Ribo	2 mg/mL (LDC)
		4 mg/mL (HDC)

Appendix Figure 4. To examine the effect of scaffold density and crosslinking with riboflavin on the mechanical and biochemical properties of canine TE-IVDs, a total of eight groups were examined after 2 weeks of culture. The diagram (left) shows the steps followed to induce collagen crosslinking in TE-IVDs, whereas the table (right) shows the experimental design layout to summarize varied conditions.

Results

The LDC subgroup of large discs had nearly three times the equilibrium modulus (EM) (1.7±0.5 kPa) of their smaller counterparts with similar density and showed higher EM than large discs with HDC [Figure 5, top right]. No significant differences were observed between all other subgroups of small discs and large discs and in the

instantaneous modulus (IM) of all groups [Figure 5, top left]. Smaller discs with only LDC favored cell proliferation at NP region greater than in all other groups [Figure 5, bottom right]; however, the AF showed significantly greater DNA content in small discs with HDC + Ribo than in all but the small discs LDC group [Figure 5, bottom left]. Production of GAG and collagen in the AF was not statistically different across all groups. [Figure 6, left side in top and bottom rows]. Nevertheless, GAG production increased significantly in the NP of large discs with un-crosslinked highly dense AF scaffolds (HDC + Ribo) [Figure 6, top right]. Collagen production was notably decreased in the NP of all groups except in the baseline LDC smaller discs [Figure 6, bottom right].

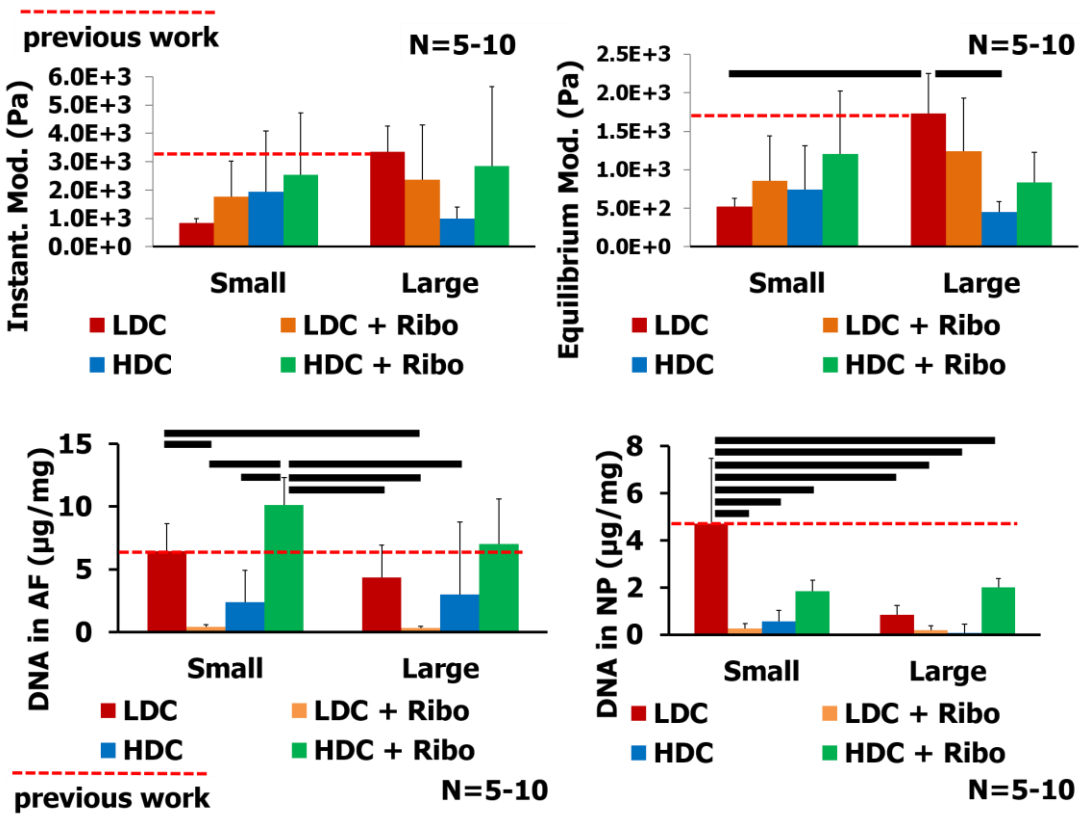

Appendix Figure 5. Effective compressive properties (top row) of whole discs and cell proliferation metrics (bottom) at the NP and AF regions of the TE-IVDs. Dotted line refers to properties measured in previous work for comparison purposes. Bars indicate statistically significant differences between group pairs at both ends of the bar. Data shown as mean ± standard deviation.

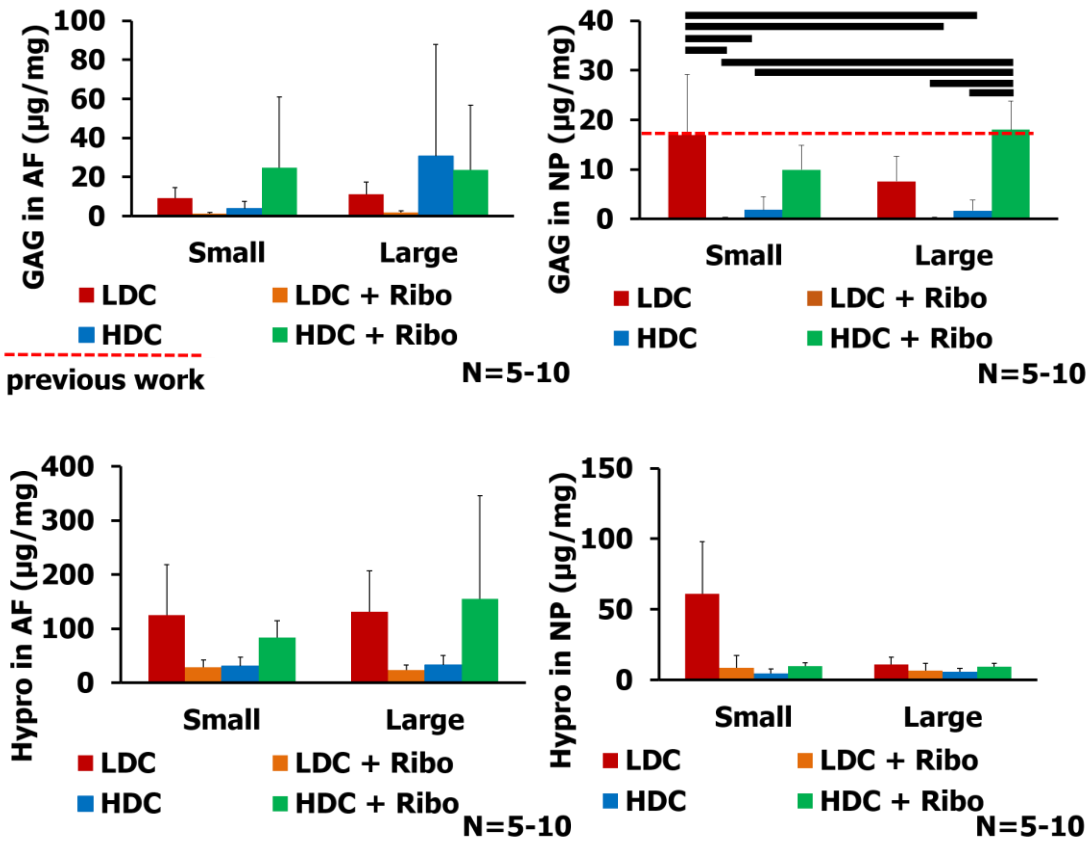

Appendix Figure 6. Biochemical composition of the ECM in TE-IVDs assessed by proteoglycan content (GAG, top row) and collagen content (Hypro, bottom row) separated by NP and AF regions. Bars indicate statistically significant differences between group pairs at both ends of the bar. Data shown as mean ± standard deviation.

Discussion

The present studies showed that the GAG composition in the NP of canine-sized composite TE-IVDs can be successfully improved by riboflavin-crosslinking and high-density collagen approaches. In equilibrium, size of the composite disc was shown to have the most effect on effective compressive stiffness than other variables. Notably, crosslinking of a collagen scaffold with double AF density increased the compressive properties in most small discs to that of large discs. This contrasts with previous studies, where bi-layered large discs showed greater effective stiffness than bi-layered small discs. The combination of high density collagen with riboflavin also increased cell

density at the AF of small discs, although the decreased matrix deposition in the NP of all other groups suggests that localized effects occur from these treatments. Likely, a denser crosslinked scaffold effectively reduces diffusion of metabolites through the AF thereby affecting cell proliferation and subsequent matrix production at the NP.

Utilizing chemically-driven crosslinking and denser scaffolds appear to have greater effect on biochemical properties of the TE-IVDs. This work demonstrates the use of established methods to evaluate crosslinking and scaffold density changes on a composite alginate and collagen TE-IVD, which have proven successful in rat *in vivo* models. Characterizing the effects of these approaches in canine-sized constructs helps to further develop a pre-clinical cervical spine model.

References

1. Nesti+ Tiss Eng Pt A 2008;
2. Bowles+ Tiss Eng Pt A 2010;
3. Nerurkar+ Spine 2010;
4. Lazebnik+ J Tiss Eng Regen Med 2011;
5. Zhuang+ Biochem Biophys Res Commun 2011;
6. Park+ Tiss Eng Pt A 2012;
7. Bowles+ PNAS 2011;
8. Mojica-Santiago+ ORS 2014
9. Ibusuki+ Tiss Eng 2007
10. Grunert+ Spine 2014;
11. Kim+ J Biomech 1995;
12. Kim+ Anal Biochem 1988;
13. Enobakhare+ Anal Biochem 1996;
14. Neuman+ J Biol Chem 1950.

Appendix C: MATLAB codes for data analysis and figure plots

Viscoelasticfit.m for motion segment analysis

```
%Input Initialization
%Enter filename,thickness,diameter,steps, and
initial guess:
clc
clear all
filename = '8-24-16S1C34TEIVD+'
%filename = '10mg0M_01-22-18_4'
string = sprintf('%s Model Fit
Summary.txt',filename);
diary(string)
fprintf('Initialized data: \n')
rawdata =
importdata(sprintf('%s.txt',filename));
time = rawdata.data(:,2);
% disp = rawdata.data(:,3);
% load = rawdata.data(:,4);
disp = rawdata.data(:,4);
load = rawdata.data(:,5);
% thickness = 1.74
% diameter = [8.51;9.61]
% offset = 0
% %don't use less than 5 steps:
% steps = offset-
thickness*[.05,.1,.15,.2,.35,.45]'
% start = [-1;10;-.005]
thickness = 1.7;
diameter = [11.69;14.66];
steps = -1*[0,.085,.17,.255,.34]';
offset = 0;
start = [-10;100;-5];
%-----------------------------------------------------
-------------------%
%Raw Data Visualization
figure
subplot(length(steps)-
2,2,1),plot(time,disp),xlabel('time
[s]'),ylabel('disp [mm]');
subplot(length(steps)-
2,2,2),plot(time,load,'LineWidth',3),
xlabel('time
[s]','FontSize',14,'FontWeight','bold'),ylabel('lo
ad [N]','FontSize',14,'FontWeight','bold');
%-----------------------------------------------------
-------------------%
%Model Fitting
fprintf('Estimated coefficients for each step:
\n')
modelFun = @(b,time) (b(1)*exp(-
time/b(2)))+b(3);
%
%%fo =
fitoptions('Method','NonlinearLeastSquares','St
artPoint',start);
%modelfit =
fittype(modelFun,'independent','time','depende
nt','load','options',fo);
%%modelfit = fittype('a - exp(-time/tau) +
b','dependent',{'load'},'independent',{'time'},'co
efficients',{'a','b','tau'},'options',fo);
for j = 1:length(steps)
   stepload{1,j} =
load(ismembertol(disp,steps(j)));
   steptime{1,j} =
time(ismembertol(disp,steps(j)))-
min(time(ismembertol(disp,steps(j))));
   %stepload{1,j} = load(disp == steps(j));
   %steptime{1,j} = time(disp == steps(j))-
min(time(disp == steps(j)));
   %[loadfit,gof{k},output{k}] =
fit(steptime{1,k},stepload{1,k},modelfit)

%subplot(4,2,k+2),plot(modelfit,steptime{1,k}
,stepload{1,k}),legend('Location','southeast'),le
gend('boxoff');
   %loadcoeffs(:,k) = loadfit.Coefficients;
   loadfit =
fitnlm(steptime{1,j},stepload{1,j},modelFun,st
art)
   subplot(length(steps)-
2,2,j+2),scatter(steptime{1,j},stepload{1,j},10,'
filled','DisplayName','data');
   hold on

plot(steptime{1,j},predict(loadfit,steptime{1,j}
),'LineWidth',2,'DisplayName','fit');
   xlabel('time [s]'),ylabel('load [N]');

legend('Location','southeast'),legend('boxoff');
   hold off
   loadcoeffs(:,j) =
loadfit.Coefficients.Estimate;
end
%-----------------------------------------------------
-------------------%
```

```
%Visualization of Stress vs. Strain & Load vs. Displacement Curves
strain = (steps-offset)/thickness;
instress = (loadcoeffs(1,:)' + loadcoeffs(3,:)')/(.25*mean(diameter)^2);
eqstress = (loadcoeffs(3,:)')/(.25*mean(diameter)^2);
subplot(length(steps)-2,2,length(steps)+3),
plot(strain,eqstress,'-o','DisplayName','Eq. stress')
hold on
plot(strain,instress,'-o','DisplayName','Inst. stress')
xlabel('strain'),ylabel('stress [MPa]');
legend('Location','northwest'),legend('boxoff');
hold off
subplot(length(steps)-2,2,length(steps)+4),
plot(steps,loadcoeffs(3,:)','-o','DisplayName','Eq. load')
hold on
plot(steps,(loadcoeffs(1,:)' + loadcoeffs(3,:)'),'-o','DisplayName','Inst. load')
xlabel('disp [mm]'),ylabel('load [N]');
legend('Location','northwest'),legend('boxoff');
hold off
% fID = fopen('Data Analysis Summary.txt','w');
% fprintf(fID,'
savefig(sprintf('%s Model Fitting.fig',filename));
diary off
```

Mechanova2.m for repeated measures ANOVA of motion segment mechanics

```
%These are some of the linear and mixed effects models attempted at first,
%but given the lack of significance of added effects and similar
%significance from the repeated measures model, the former weren't used.
% m1 = fitlm(mechanics,'Interactions','ResponseVar','EqMod','PredictorVars',{'Condition','Level'},'CategoricalVar',{'Condition','Level'});
% m2 = fitlme(mechanics,'EqMod~Condition+Level+Condition:Level+(1|Spine)');
% m3 = fitlme(mechanics,'EqMod~Condition+(1|Level)');
% m4 = fitlme(mechanics,'EqMod~Condition+Condition*Level');

%This model was adapted from the Longitudinal Data Ranova Example:
%The raw data is entered as a table into matlab and the desired response
%is selected from the column. In this case, the eq. stiffness ratio is
%registered for 12 specimens measured at 3 consecutive experimental
%conditions (Dx,Plate-,Plate+). Experimental conditions are considered as
%repeated measures (within subjects), and specimens are grouped into
%3 categories (C2/3 to C4/5) each sourced from 4 independent spines.

mechanics = readtable('Matlab Mechanics.xlsx');
EqStiffRatio = mechanics.ES_CTRL;
x1 = [EqStiffRatio(1:3);EqStiffRatio(13:15);EqStiffRatio(25:27);EqStiffRatio(37:39)];
x2 = [EqStiffRatio(4:6);EqStiffRatio(16:18);EqStiffRatio(28:30);EqStiffRatio(40:42)];
x3 = [EqStiffRatio(7:9);EqStiffRatio(19:21);EqStiffRatio(31:33);EqStiffRatio(43:45)];
x4 = [EqStiffRatio(10:12);EqStiffRatio(22:24);EqStiffRatio(34:36);EqStiffRatio(46:48)];
EqStiffRatiomatrix = [x2,x3,x4];
level = {'C23';'C34';'C45';'C23';'C34';'C45';'C23';'C34';'C45';'C23';'C34';'C45'};
EqStiffRatiormtable = table(level,EqStiffRatiomatrix(:,1),EqStiffRatiomatrix(:,2),EqStiffRatiomatrix(:,3),'VariableNames',{'level','cond1','cond2','cond3'});
ExpCond = dataset({'Dx' 'Plate-' 'Plate+'},'VarNames',{'ExpCond'});
EqStiffRatiorm = fitrm(EqStiffRatiormtable,'cond1-cond3 ~ level','WithinDesign',ExpCond)
ranovatbl1 = ranova(EqStiffRatiorm)
```

```
pairwisecond =
multcompare(EqStiffRatiorm,'ExpCond')
pairwiselevel =
multcompare(EqStiffRatiorm,'level')
%Graph boxplots of the data with relevant p-
values. Requires to look at the
%pairwise comparisons first before deciding
where to add the significant
%p-values to their corresponding groups.
figure
boxplot(EqStiffRatiomatrix,'Labels',{'Dx','Plate
-','Plate+'},'Colors','k','Whisker',2)
hold on
scatter(ones(12,1),EqStiffRatiomatrix(:,1),'fille
d','LineWidth',10)
scatter(ones(12,1).*2,EqStiffRatiomatrix(:,2),'f
illed','LineWidth',10)
scatter(ones(12,1).*3,EqStiffRatiomatrix(:,3),'f
illed','LineWidth',10)
title('Ratio of stiffness relative to intact
segment by experimental
condition','FontSize',14),
ylabel('\bf Stiffness Ratio [kN-m/kN-
m]','FontSize',14),ylim([0 0.5])
ax = gca; ax.XAxis.LineWidth = 2.5;
ax.YAxis.LineWidth = 2.5;
ax.XAxis.Label.FontSize = 14;
ax.YAxis.Label.FontSize = 14;
ax.XAxis.FontSize = 14; ax.YAxis.FontSize =
14;
ax.XAxis.FontWeight = 'bold';
ax.YAxis.FontWeight = 'bold';
p = pairwisecond.pValue;
str1 = {sprintf(' $ p = %.3f ',p(2)),sprintf(' $ p =
%.3f \n * p = %.3f ',p(2),p(4)),sprintf(' * p =
%.3f ',p(4))};
str2 = {sprintf(' N = %2.0f
',length(EqStiffRatiomatrix))};
locx = [1,2,3];
locy = [max(EqStiffRatiomatrix)];
text(locx,locy +
0.025,str1,'FontWeight','bold','FontSize',14);
annotation('textbox',[.75 .1 .2
.1],'String',str2,'FitBoxToText','on','FontWeight
','bold','FontSize',14);
legend({'Dx','Plate-
','Plate+'},'Location','northwest','FontWeight','b
old','FontSize',14),
legend('boxoff')
hold off
```

AllMechTable.m for mechanical analysis of TE-IVD mechanics

```
%Viscoelastic & Holmes-Mow fits for unconf
comp multistep stress relaxdata%
filename = '20mgMechData.xlsx';
rawdata = importdata(filename);          %load
raw data spreadsheet into
                                %structure of
matrix arrays
size(rawdata.data);
ncols = size(rawdata.data,2);
nrows = size(rawdata.data,1);
SpecMat = rawdata.data(:,1:6:ncols);
CollMat = rawdata.data(:,2:6:ncols);
CellMat = rawdata.data(:,3:6:ncols);
Time = rawdata.data(:,4:6:ncols);
Pos = rawdata.data(:,5:6:ncols);
Load = rawdata.data(:,6:6:ncols);
%dxMat = diff(Pos);                  %height
change row(i+1)-row(i)
%dtMat = diff(Time);                  %time
change row(i+1)-row(i)
%Rate = dxMat./dtMat;
%calculate strain rate per elm
%initialize values of height and two diameters
in mm
%these values correspond to 4mg/ml samples
% height = [1.74,1.21,1.6];
% dMat = [11.56,14.36,11.25];
% dMat(2,:) = [12.98,9.08,15.64];
%these values correspond to 10mg/ml samples
% height =
[2.24,1.5,2.48,1.74,1.68,1.3,1.26,1.92,1.78,2.2,
1.83,1.24,...
%    1.18,1.82,3,2,2,1.97,1.34,2.24,2.72,1.78];
% dMat =
[8.8,8.4,8.19,9.61,11.45,5.42,12.08,9.54,12.49,
13.17,11.34,...
%
9.23,11.16,11.52,7,6.5,6.3,5.26,8.13,6.65,5.77,
4.53];
% dMat(2,:) =
[8.8,8.4,9.67,8.51,12.68,10,9.33,13.14,8.47,9.8
4,11.2,...
```

```
%
11.39,11.56,10.76,7,7.4,6.8,5.09,10.19,6.29,5.4
6,4.93];
%these values correspond to 20mg/ml samples
% height =
[2.4,2.1,1.66,2.5,1,2.01,2.7,2.29,2.3,1.3,1.62,2.
56,2,1,1,3,...
%     2.8,2.8,2.06,1.5,1.92];
% dMat =
[7.8,8.54,7.94,8.8,14,13.73,12.4,14.58,12.74,1
3.35,13.43,13.8,...
%
11.56,13.75,13.75,8,7.5,8,11.72,16.01,12.74];
% dMat(2,:) =
[7.8,8.54,7.94,8.8,13,12.38,15.01,15.23,14.69,
13.25,14.24,...
%
13.65,12.37,13.75,13.75,10,9,9,13.51,13.29,15.
06];
%these values correspond to 60mg/ml samples
(actual native IVDs)
% height = [4,5,5,5];
% dMat = [14,14.6,14.6,13.34];
% dMat(2,:) = [12,13,14.3,12.6];

hMat = repmat(height,nrows,1);
Pos0 = (Pos-Pos(1,:));
StrainMat = (Pos-Pos(1,:))./hMat;
Davg = mean(dMat);
AMat =
repmat(.25*pi*power(Davg,2),nrows,1);
%matrix of ref. config. area
PMat = (Load-Load(1,:))./AMat;
%1stP-K stress matrix in MPa
steps = [.05,.1,.15,.2,.25,.3,.35,.4,.45,.5];
nsteps = length(steps);
% TimeSteps = cell(length(steps),no_samples);
% StrainSteps =
cell(length(steps),no_samples);
% LoadSteps = cell(length(steps),no_samples);
% PSteps = cell(length(steps),no_samples);
% coeff = cell(size(TimeSteps));
% R2 = cell(size(TimeSteps));
% instress = cell(1,no_samples);tau =
cell(1,no_samples);
% eqstress = cell(1,no_samples);plotR2 =
cell(1,no_samples);
% strain = cell(1,no_samples);stretch =
cell(1,no_samples);
% A = cell(size(TimeSteps));
% B = cell(size(TimeSteps));
% C = cell(size(TimeSteps));
% EMcoeff = cell(1,no_samples);
% EMR2 = cell(1,no_samples);
% permstress = cell(1,no_samples);Ha =
cell(1,no_samples);
% perm = cell(1,no_samples);
% Kcoeff = cell(1,no_samples);
% KR2 = cell(1,no_samples);

%data parsing and rearranged until here, next
comes the splitting into the
%individual steps for each one of the tested
samples
%no_samples = size(PMat,2);
%total no. of samples or last sample of interest
from the spreadsheet
%you may start the counter j with whichever
sample graph you want to see,or
%enter 1 if you are plotting all samples
(requires high processing power)
sample1 = inputdlg('Enter no. of the first
sample to plot');
sample1 = str2double(sample1);
no_samples = inputdlg('Enter no. of last
sample in the range of interest');
no_samples = str2double(no_samples);
for j = sample1:no_samples
   for i = 1:nsteps
      TimeSteps{i,j} = Time(ismembertol(-
StrainMat(:,j),steps(i),1e-2,'DataScale',1),j);
      TimeSteps{i,j} = TimeSteps{i,j} -
min(TimeSteps{i,j});
      StrainSteps{i,j} =
StrainMat(ismembertol(-
StrainMat(:,j),steps(i),1e-2,'DataScale',1),j);
      LoadSteps{i,j} = Load(ismembertol(-
StrainMat(:,j),steps(i),1e-2,'DataScale',1),j);
      PSteps{i,j} = (1e3)*PMat(ismembertol(-
StrainMat(:,j),steps(i),1e-2,'DataScale',1),j);
   end
end
for j = sample1:no_samples
   figure('Name',sprintf('Load vs. time for
e/step in sample %d',j)),
   fig = gcf;fig.OuterPosition = [-
5.5,34.5,1381,885];hold on
   for i = 1:nsteps

subplot(ceil(nsteps/2),2,i),scatter(TimeSteps{i,j
},LoadSteps{i,j})
      xlabel('Time [s]'),ylabel('Load
[N]'),title(sprintf('step %d',i));
   end
   hold off

savefig(sprintf('Load_time_plots_sample%d.fi
g',j));
end
```

```
%questdlg('Would you like to continue to
perform poroviscoelastic step fits?');
w = warndlg('Continue to perform individual
steps model fits.', 'Continue?');
drawnow                          % Necessary to
print the message
waitfor(w);

%proceed to perform the individual fits using
the poroviscoelastic model
%Aj*exp(Bj*x)+Cj similar to A(1-exp(-
t/tau)+B, where Aj=-A (lastpt-1stpt),
%B=-1/tau (random guess- alginate has
tau~=3-6), C=A+B (~=last pt of curve)
poroviscFun = 'A*exp(B*x)+C';
poroviscfit =
fittype(poroviscFun,'coefficients',{'A','B','C'});
for j = sample1:no_samples
   figure('Name',sprintf('Stress vs. time model
fits for e/step sample %d',j)),
   fig = gcf;fig.OuterPosition = [-
5.5,34.5,1381,885];  %shows full screen
   for i = 1:nsteps
      guessA = -PSteps{i,j}(size(PSteps{i,j},1)-
5)+PSteps{i,j}(1);
      guessB = -.05;
      guessC = PSteps{i,j}(size(PSteps{i,j},1)-
5);
      [f1,good1] =
fit(TimeSteps{i,j},PSteps{i,j},poroviscfit,'Start
Point',[guessA,guessB,guessC]);
      coeff{i,j} = coeffvalues(f1);
      R2{i,j} = good1.rsquare;

subplot(ceil(nsteps/2),2,i),scatter(TimeSteps{i,j
},PSteps{i,j});
      hold
on,plot(TimeSteps{i,j},f1(TimeSteps{i,j}),'rx-
');
      xlabel('Time [s]'),ylabel('Stress
[kPa]'),title(sprintf('step %d',i));
      legend('Raw Data','A*exp(B*x)+C')
   end
   hold off

savefig(sprintf('Porovisc_steps_fits_sample%d.
fig',j));
end
w = warndlg('Continue to stress-strain and
perm-strain plots.', 'Continue?');
drawnow
waitfor(w);

%plot the eq.stress, inst. stress and perm. as a
function of strain
for j = sample1:no_samples
   figure('Name',sprintf('Stress vs. strain for
sample %d',j)),
   fig = gcf;fig.OuterPosition = [-
5.5,34.5,1381,885];
   for i = 1:nsteps
      A{i,j} = coeff{i,j}(1);
      B{i,j} = coeff{i,j}(2);
      C{i,j} = coeff{i,j}(3);
   end
   instress{:,j} =
cellfun(@minus,C(1:nsteps,j),A(1:nsteps,j));
   tau{:,j} = cellfun(@rdivide,num2cell(-
ones(nsteps,1)),B(1:nsteps,j));
   eqstress{:,j} =
cellfun(@minus,num2cell(zeros(nsteps,1)),C(1
:nsteps,j));
   strain{:,j} = -
cellfun(@mean,StrainSteps(1:nsteps,j));
   stretch{:,j} = 1-strain{:,j};
   plotR2{:,j} = [R2{:,j}];


subplot(3,1,1),plot([strain{:,j}],[eqstress{:,j}],'
o-')
   xlabel('Strain'),ylabel('Stress [kPa]'),title('Eq.
Stress vs. Strain');
   for i = 1:length(strain{:,j})

text(strain{:,j}(i),eqstress{:,j}(i),sprintf('\nR^2
= %1.2f',plotR2{:,j}(i)))
   end

subplot(3,1,2),plot([strain{:,j}],[instress{:,j}],'x
-')
   xlabel('Strain'),ylabel('Stress
[kPa]'),title('Inst. Stress vs. Strain');
   subplot(3,1,3),plot([strain{:,j}],[tau{:,j}],'+-
')
   xlabel('Strain'),ylabel('Tau [sec]'),title('Tau
vs. Strain');

   %checkpoint asking if the figs. and pts. are
adequate and reasonable
   check1 = questdlg('Do you want to exclude
any step points?','Check plots');
   while strcmp(check1,'Yes') == 1
      prompt1 = (['Enter the step points you
want to exclude' newline...
         '(in column vector if more than one
point [#;#;#])']);
      dlg_title1 = 'Exclude steps';
      ans1 = inputdlg(prompt1,dlg_title1);
      ans1 = str2num(ans1{:});
      if isempty(ans1) == 1
```

```
            return;
        elseif any(ans1) < 1
            error('You entered a step point that does
not exist, please try again');
            return;
        elseif any(ans1) > nsteps
            error('You entered a step point that does
not exist, please try again');
            return;
        else
            instress{:,j}(ans1) = [];
            tau{:,j}(ans1) = [];
            eqstress{:,j}(ans1) = [];
            strain{:,j}(ans1) = [];
            stretch{:,j}(ans1) = [];
            plotR2{:,j}(ans1) = [];

            fig;

subplot(3,1,1),plot([strain{:,j}],[eqstress{:,j}],'
o-')
            xlabel('Strain'),ylabel('Stress
[kPa]'),title('Eq. Stress vs. Strain');
            for i = 1:length(strain{:,j})

text(strain{:,j}(i),eqstress{:,j}(i),sprintf('\nR^2
= %1.2f',plotR2{:,j}(i)))
            end

subplot(3,1,2),plot([strain{:,j}],[instress{:,j}],'x
-')
            xlabel('Strain'),ylabel('Stress
[kPa]'),title('Inst. Stress vs. Strain');

subplot(3,1,3),plot([strain{:,j}],[tau{:,j}],'+-')
            xlabel('Strain'),ylabel('Tau
[sec]'),title('Tau vs. Strain');

            check1 = questdlg('Do you want to
exclude any step points?','Check Plots');
        end
    end

savefig(sprintf('Stress_strain_perm_sample%d.
fig',j));
end
w = warndlg('Continue to choose linear region
for elastic mod.', 'Continue?');
drawnow
waitfor(w);

%Choose the linear region for modulus
calculations inst. and in eq.
for j = sample1:no_samples
    figure('Name',sprintf('Linear stress-strain for
sample %d',j)),
    fig = gcf;fig.OuterPosition = [-
5.5,34.5,1381,885];
    check2 = 'Yes';
    while strcmp(check2,'Yes') == 1

subplot(2,1,1),plot([strain{:,j}],[eqstress{:,j}],'
o-')
        xlabel('Strain'),ylabel('Stress
[kPa]'),title('Eq. Stress vs. Strain');
        for i = 1:length(strain{:,j})

text(strain{:,j}(i),eqstress{:,j}(i),sprintf('\nR^2
= %1.2f',plotR2{:,j}(i)))
        end
        prompt2 = {sprintf('Enter lower bound of
the linear region for sample %d',j),...
            sprintf('Enter upper bound of the linear
region for sample %d',j)};
        dlg_title2 = 'Choose linear region';
        num_lines = 1;def_ans =
{'1',num2str(length(strain{:,j}))};
        ans2 =
inputdlg(prompt2,dlg_title2,num_lines,def_ans
);
        lims = str2double(ans2);
        if lims(1) > lims(2)
            error('You have entered a step point
that does not exist, please try again');
            return
        elseif lims(2) >
cellfun(@str2num,def_ans(2))
            error('You have entered a step point
that does not exist, please try again');
            return
        end
        [f2,good2] =
fit(strain{:,j}(lims(1):lims(2)),eqstress{:,j}(lim
s(1):lims(2)),'poly1');
        EMcoeff{:,j} = coeffvalues(f2);
        EMR2{:,j} = good2.rsquare;

fig;subplot(2,1,2),scatter(strain{:,j},eqstress{:,j
},'Filled'),hold on
        plot(f2,'rx-'),hold off
        str1 = [newline,newline,'\sigma_{eq}='];
        str2 = sprintf('%3.2f',EMcoeff{:,j}(1));
        str3 = '\epsilon +';
        str4 = sprintf('(%2.2f)',EMcoeff{:,j}(2));
        str5 = sprintf('\nR^2 = %1.2f',EMR2{:,j});

text(median(strain{:,j}),median(eqstress{:,j}),..
.
```

```
strcat(str1,str2,str3,str4,str5),'FontSize',14);
        xlabel('Strain,
\epsilon'),ylabel('Compressive
stress,\sigma_{eq} [kPa]');
        legend('Raw Data','Linear Elasticity Fit')
        check2 = questdlg('Do you want to
redefine the linear region?','Check fit');
    end
    savefig(sprintf('Linear_stress-
strain_sample%d.fig',j));
end
w = warndlg('Continue to fit Holmes-Mow
permeability model.', 'Continue?');
drawnow
waitfor(w);

%Use Holmes-Mow hydr. permeability
equation to fit raw time constants
PermFun = 'K0*(((x-
0.2)/0.8)^alpha)*exp(0.5*M*((x^2)-1))';
Permfit =
fittype(PermFun,'coefficients',{'K0','alpha','M'}
);
for j = sample1:no_samples
    permstress{:,j} = eqstress{:,j}-
EMcoeff{:,j}(2);
    Ha{:,j} = 1e3*permstress{:,j}./strain{:,j};
    perm{:,j} = (.25*power(Davg(:,j)*1e-
3,2))./(pi^2*Ha{:,j}.*tau{:,j});
    [f3,good3] =
fit(stretch{:,j},perm{:,j},Permfit);
    Kcoeff{:,j} = coeffvalues(f3);
    KR2{:,j} = good3.rsquare;
    figure('Name',sprintf('Permeability vs.
stretch for sample %d',j)),
    fig=gcf;fig.OuterPosition = [-
5.5,34.5,1381,885];
    scatter(stretch{:,j},perm{:,j},'v','Filled'),hold
on
    plot(f3,'rx-');
    str1 = [newline,newline,'K ='];
    str2 = sprintf('(%1.2e)',Kcoeff{:,j}(1));
    str3 = '((\lambda-0.2)/0.8)';
    str4 = sprintf('^{%2.2f}',Kcoeff{:,j}(2));
    str5 = '*exp[0.5';
    str6 = sprintf('(%2.2f)',Kcoeff{:,j}(3));
    str7 = '(\lambda^2-1)]';
    str8 = sprintf('\nR^2 = %1.2f',KR2{:,j});

text(median(stretch{:,j}),f3(median(stretch{:,j}
)),...

strcat(str1,str2,str3,str4,str5,str6,str7,str8),'Font
Size',14);
    xlabel('Stretch, \lambda'),ylabel('Hydr.
Perm.,K [m^4/N-s]');
    legend('Raw Data','(K_0)((\lambda-
0.2)/0.8)^{\alpha}*exp[0.5*M*(\lambda^2-
1)]')
    legend('Location','southwest')
    hold off

savefig(sprintf('HM_perm_sample%d.fig',j));
end
w = warndlg('Continue to fit Holmes-Mow
modulus stiffening model.', 'Continue?');
drawnow
waitfor(w);

%Use Holmes-Mow model to calculate
stiffening coeff. and initial agg. mod.
% HMcoeff = cell(1,no_samples);HMR2 =
cell(1,no_samples);
HMFun = '0.5*Ha0*(((x^2)-
1)/(x^(2*beta+1)))*exp(beta*((x^2)-1))';
HMfit =
fittype(HMFun,'coefficients',{'Ha0','beta'});
for j = sample1:no_samples
    [f4,good4] = fit(stretch{:,j},-
eqstress{:,j},HMfit);
    HMcoeff{:,j} = coeffvalues(f4);
    HMR2{:,j} = good4.rsquare;
    figure('Name',sprintf('Stress-stretch for
sample %d',j)),
    fig = gcf;fig.OuterPosition = [-
5.5,34.5,1381,885];
    plot(f4,'rx-',stretch{:,j},-eqstress{:,j},'o');
    str1 =
[newline,newline,newline,'\sigma_{eq}='];
    str2 = sprintf('(%3.2f/2)',HMcoeff{:,j}(1));
    str3 = '(\lambda^2 - 1)';
    str4 = '/\lambda';
    str5 =
sprintf('^{2(%2.2f)+1}',HMcoeff{:,j}(2));
    str6 =
sprintf('*exp[(%2.2f)',HMcoeff{:,j}(2));
    str7 = sprintf('\nR^2 = %1.2f',HMR2{:,j});
    text(median(stretch{:,j}),-
median(eqstress{:,j}),...

strcat(str1,str2,str3,str4,str5,str6,str3,']',str7),'Fo
ntSize',14);
    xlabel('Stretch,
\lambda'),ylabel('Compressive
stress,\sigma_{eq} [kPa]');
    legend('Raw Data','(H_{A0}/2)(\lambda^2-
1)/\lambda^{2\beta+1}*exp[\beta*(\lambda^2-
1)]')
```

```
    savefig(sprintf('Holmes-
Mow_stress_fits_sample%d.fig',j));
end
% for filenames ending in .xlsx use the
following code to save analyzed data
save(strcat(filename(1:(end-
5)),'.mat'),'A','AMat','B','C','CellMat',...

'coeff','CollMat','Davg','dMat','EMcoeff','EMR
2','eqstress','Ha',...

'height','hMat','HMcoeff','HMR2','instress','Kco
eff','KR2','Load',...

'LoadSteps','no_samples','nsteps','perm','permst
ress','plotR2','PMat',...

'Pos','Pos0','PSteps','R2','sample1','SpecMat','st
eps','strain',...

'StrainMat','StrainSteps','stretch','tau','Time','Ti
meSteps');
w = warndlg('Continue to create longform table
arrays for R-Studio', 'Continue?');
drawnow
waitfor(w);

%Set up longform table for statistical analysis
in R-Studio
%Consolidate sample columns into rows with
the column designations as shown
%below, use string format for all non-numeric
data representations.

dates = ["01-22-18","08-07-17","11-06-
17","10-16-17","12-17-18"];
Date04 = [repmat(dates(3),3,1)];
Date10 =
[repmat(dates(1),4,1);repmat(dates(3),2,1);rep
mat(dates(5),4,1);...

repmat(dates(5),4,1);repmat(dates(3),3,1);repm
at(dates(5),5,1)];
Date20 =
[repmat(dates(1),4,1);dates(2);repmat(dates(3),
4,1);dates(2);...

repmat(dates(3),3,1);repmat(dates(2),2,1);repm
at(dates(4),3,1);...
    repmat(dates(3),3,1)];
DateNat = [repmat(dates(2),4,1)];

load('4mgMechData.mat');
for j = sample1:no_samples
    EqMod(j,:) = EMcoeff{:,j}(1);
    EMgof(j,:) = EMR2{:,j};
    HM0(j,:) = HMcoeff{:,j}(1);
    Beta(j,:) = HMcoeff{:,j}(2);
    HMgof(j,:) = HMR2{:,j};
end
M04 = zeros(no_samples,5);
M04 =
[EqMod,EMgof,HM0,Beta,HMgof];T04 =
table;
T04.Collagen = string(CollMat(1,:)');T04.Cells
= string(CellMat(1,:)');
T04.Date = Date04;T04.EqMod =
M04(:,1);T04.EMgof = M04(:,2);
T04.HM0 = M04(:,3);T04.Beta =
M04(:,4);T04.HMgof = M04(:,5);
figure,boxplot(M04(:,1),T04.Cells);hold on

scatter([ones(3,1)],M04(:,1),'filled','LineWidth'
,5);hold off
    title('Eq.Mod. of 4mg/mL TE-
IVDs','FontSize',14),
    ylabel(' E_{eq} [kPa]'),xlabel('Cells,
[M/mL]'),ax = gca;
    ax.XAxis.LineWidth =
2.5;ax.YAxis.LineWidth = 2.5;
    ax.XAxis.Label.FontSize = 14;
ax.YAxis.Label.FontSize = 14;
    ax.XAxis.FontSize = 14; ax.YAxis.FontSize
= 14;
    ax.XAxis.FontWeight = 'bold';
ax.YAxis.FontWeight = 'bold';
figure,boxplot(M04(:,2),T04.Cells);hold on

scatter([ones(3,1)],M04(:,2),'filled','LineWidth'
,5);hold off
    title('Fits of E_{eq} for 4mg/mL TE-
IVDs','FontSize',14),
    ylabel('R^2'),xlabel('Cells, [M/mL]'),ax =
gca;
    ax.XAxis.LineWidth =
2.5;ax.YAxis.LineWidth = 2.5;
    ax.XAxis.Label.FontSize = 14;
ax.YAxis.Label.FontSize = 14;
    ax.XAxis.FontSize = 14; ax.YAxis.FontSize
= 14;
    ax.XAxis.FontWeight = 'bold';
ax.YAxis.FontWeight = 'bold';
figure,boxplot(M04(:,3),T04.Cells);hold on

scatter([ones(3,1)],M04(:,3),'filled','LineWidth'
,5);hold off
    title('Holmes-Mow Mod. of 4mg/mL TE-
IVDs','FontSize',14),
    ylabel(' H_{A0} [kPa]'),xlabel('Cells,
[M/mL]'),ax = gca;
```

```
    ax.XAxis.LineWidth =
2.5;ax.YAxis.LineWidth = 2.5;
    ax.XAxis.Label.FontSize = 14;
ax.YAxis.Label.FontSize = 14;
    ax.XAxis.FontSize = 14; ax.YAxis.FontSize
= 14;
    ax.XAxis.FontWeight = 'bold';
ax.YAxis.FontWeight = 'bold';
figure,boxplot(M04(:,4),T04.Cells);hold on

scatter([ones(3,1)],M04(:,4),'filled','LineWidth'
,5);hold off
    title('Stress-stiffening coeff. of 4mg/mL TE-
IVDs','FontSize',14),
    ylabel('\bf \beta','FontSize',14),ax = gca;
    ax.XAxis.LineWidth = 2.5;
ax.YAxis.LineWidth = 2.5;
    ax.XAxis.Label.FontSize = 14;
ax.YAxis.Label.FontSize = 14;
    ax.XAxis.FontSize = 14; ax.YAxis.FontSize
= 14;
    ax.XAxis.FontWeight = 'bold';
ax.YAxis.FontWeight = 'bold';
figure,boxplot(M04(:,5),T04.Cells);hold on

scatter([ones(3,1)],M04(:,5),'filled','LineWidth'
,5);hold off
    title('Fits of Holmes-Mow for 4mg/mL TE-
IVDs','FontSize',14),
    ylabel('R^2'),xlabel('Cells, [M/mL]'),ax =
gca;
    ax.XAxis.LineWidth =
2.5;ax.YAxis.LineWidth = 2.5;
    ax.XAxis.Label.FontSize = 14;
ax.YAxis.Label.FontSize = 14;
    ax.XAxis.FontSize = 14; ax.YAxis.FontSize
= 14;
    ax.XAxis.FontWeight = 'bold';
ax.YAxis.FontWeight = 'bold';

load('10mgMechData.mat');
for j = sample1:no_samples
    EqMod(j,:) = EMcoeff{:,j}(1);
    EMgof(j,:) = EMR2{:,j};
    HM0(j,:) = HMcoeff{:,j}(1);
    Beta(j,:) = HMcoeff{:,j}(2);
    HMgof(j,:) = HMR2{:,j};
end
M10 = zeros(no_samples,5);
M10 =
[EqMod,EMgof,HM0,Beta,HMgof];T10 =
table;
T10.Collagen = string(CollMat(1,:)');T10.Cells
= string(CellMat(1,:)');
T10.Date = Date10;T10.EqMod =
M10(:,1);T10.EMgof = M10(:,2);
T10.HM0 = M10(:,3);T10.Beta =
M10(:,4);T10.HMgof = M10(:,5);
figure,boxplot(M10(:,1),T10.Cells);hold on

scatter([ones(4,1);ones(2,1)*2;ones(4,1)*3;one
s(4,1)*4;ones(8,1)*5],...
      M10(:,1),'filled','LineWidth',5);hold off
    title('Eq.Mod. of 10mg/mL TE-
IVDs','FontSize',14),
    ylabel(' E_{eq} [kPa]'),xlabel('Cells,
[M/mL]'),ax = gca;
    ax.XAxis.LineWidth =
2.5;ax.YAxis.LineWidth = 2.5;
    ax.XAxis.Label.FontSize = 14;
ax.YAxis.Label.FontSize = 14;
    ax.XAxis.FontSize = 14; ax.YAxis.FontSize
= 14;
    ax.XAxis.FontWeight = 'bold';
ax.YAxis.FontWeight = 'bold';
figure,boxplot(M10(:,2),T10.Cells);hold on

scatter([ones(4,1);ones(2,1)*2;ones(4,1)*3;one
s(4,1)*4;ones(8,1)*5],...
      M10(:,2),'filled','LineWidth',5);hold off
    title('Fits of E_{eq} for 10mg/mL TE-
IVDs','FontSize',14),
    ylabel('R^2'),xlabel('Cells, [M/mL]'),ax =
gca;
    ax.XAxis.LineWidth =
2.5;ax.YAxis.LineWidth = 2.5;
    ax.XAxis.Label.FontSize = 14;
ax.YAxis.Label.FontSize = 14;
    ax.XAxis.FontSize = 14; ax.YAxis.FontSize
= 14;
    ax.XAxis.FontWeight = 'bold';
ax.YAxis.FontWeight = 'bold';
figure,boxplot(M10(:,3),T10.Cells);hold on

scatter([ones(4,1);ones(2,1)*2;ones(4,1)*3;one
s(4,1)*4;ones(8,1)*5],...
      M10(:,3),'filled','LineWidth',5);hold off
    title('Holmes-Mow Mod. of 10mg/mL TE-
IVDs','FontSize',14),
    ylabel(' H_{A0} [kPa]'),xlabel('Cells,
[M/mL]'),ax = gca;
    ax.XAxis.LineWidth =
2.5;ax.YAxis.LineWidth = 2.5;
    ax.XAxis.Label.FontSize = 14;
ax.YAxis.Label.FontSize = 14;
    ax.XAxis.FontSize = 14; ax.YAxis.FontSize
= 14;
    ax.XAxis.FontWeight = 'bold';
ax.YAxis.FontWeight = 'bold';
```

```
figure,boxplot(M10(:,4),T10.Cells);hold on

scatter([ones(4,1);ones(2,1)*2;ones(4,1)*3;ones(4,1)*4;ones(8,1)*5],...
      M10(:,4),'filled','LineWidth',5);hold off
   title('Stress-stiffening coeff. of 10mg/mL TE-IVDs','FontSize',14),
   ylabel('\bf \beta','FontSize',14),ax = gca;
   ax.XAxis.LineWidth = 2.5;
ax.YAxis.LineWidth = 2.5;
   ax.XAxis.Label.FontSize = 14;
ax.YAxis.Label.FontSize = 14;
   ax.XAxis.FontSize = 14; ax.YAxis.FontSize = 14;
   ax.XAxis.FontWeight = 'bold';
ax.YAxis.FontWeight = 'bold';
figure,boxplot(M10(:,5),T10.Cells);hold on

scatter([ones(4,1);ones(2,1)*2;ones(4,1)*3;ones(4,1)*4;ones(8,1)*5],...
      M10(:,5),'filled','LineWidth',5);hold off
   title('Fits of Holmes-Mow for 10mg/mL TE-IVDs','FontSize',14),
   ylabel('R^2'),xlabel('Cells, [M/mL]'),ax = gca;
   ax.XAxis.LineWidth = 2.5;ax.YAxis.LineWidth = 2.5;
   ax.XAxis.Label.FontSize = 14;
ax.YAxis.Label.FontSize = 14;
   ax.XAxis.FontSize = 14; ax.YAxis.FontSize = 14;
   ax.XAxis.FontWeight = 'bold';
ax.YAxis.FontWeight = 'bold';

load('20mgMechData.mat');
for j = sample1:no_samples
   EqMod(j,:) = EMcoeff{:,j}(1);
   EMgof(j,:) = EMR2{:,j};
   HM0(j,:) = HMcoeff{:,j}(1);
   Beta(j,:) = HMcoeff{:,j}(2);
   HMgof(j,:) = HMR2{:,j};
end
M20 = zeros(no_samples,5);
M20 = [EqMod,EMgof,HM0,Beta,HMgof];T20 = table;
T20.Collagen = string(CollMat(1,:)');T20.Cells = string(CellMat(1,:)');
T20.Date = Date20;T20.EqMod = M20(:,1);T20.EMgof = M20(:,2);
T20.HM0 = M20(:,3);T20.Beta = M20(:,4);T20.HMgof = M20(:,5);
figure,boxplot(M20(:,1),T20.Cells);hold on

scatter([ones(4,1);ones(5,1)*2;ones(4,1)*3;ones(8,1)*4],M20(:,1),...
      'filled','LineWidth',5);hold off
   title('Eq.Mod. of 20mg/mL TE-IVDs','FontSize',14),
   ylabel(' E_{eq} [kPa]'),xlabel('Cells, [M/mL]'),ax = gca;
   ax.XAxis.LineWidth = 2.5;ax.YAxis.LineWidth = 2.5;
   ax.XAxis.Label.FontSize = 14;
ax.YAxis.Label.FontSize = 14;
   ax.XAxis.FontSize = 14; ax.YAxis.FontSize = 14;
   ax.XAxis.FontWeight = 'bold';
ax.YAxis.FontWeight = 'bold';
figure,boxplot(M20(:,2),T20.Cells);hold on

scatter([ones(4,1);ones(5,1)*2;ones(4,1)*3;ones(8,1)*4],M20(:,2),...
      'filled','LineWidth',5);hold off
   title('Fits of E_{eq} for 20mg/mL TE-IVDs','FontSize',14),
   ylabel('R^2'),xlabel('Cells, [M/mL]'),ax = gca;
   ax.XAxis.LineWidth = 2.5;ax.YAxis.LineWidth = 2.5;
   ax.XAxis.Label.FontSize = 14;
ax.YAxis.Label.FontSize = 14;
   ax.XAxis.FontSize = 14; ax.YAxis.FontSize = 14;
   ax.XAxis.FontWeight = 'bold';
ax.YAxis.FontWeight = 'bold';
figure,boxplot(M20(:,3),T20.Cells);hold on

scatter([ones(4,1);ones(5,1)*2;ones(4,1)*3;ones(8,1)*4],M20(:,3),...
      'filled','LineWidth',5);hold off
   title('Holmes-Mow Mod. of 20mg/mL TE-IVDs','FontSize',14),
   ylabel(' H_{A0} [kPa]'),xlabel('Cells, [M/mL]'),ax = gca;
   ax.XAxis.LineWidth = 2.5;ax.YAxis.LineWidth = 2.5;
   ax.XAxis.Label.FontSize = 14;
ax.YAxis.Label.FontSize = 14;
   ax.XAxis.FontSize = 14; ax.YAxis.FontSize = 14;
   ax.XAxis.FontWeight = 'bold';
ax.YAxis.FontWeight = 'bold';
figure,boxplot(M20(:,4),T20.Cells);hold on

scatter([ones(4,1);ones(5,1)*2;ones(4,1)*3;ones(8,1)*4],M20(:,4),...
      'filled','LineWidth',5);hold off
```

```
   title('Stress-stiffening coeff. of 20mg/mL TE-IVDs','FontSize',14),
   ylabel('\bf \beta','FontSize',14),ax = gca;
   ax.XAxis.LineWidth = 2.5; ax.YAxis.LineWidth = 2.5;
   ax.XAxis.Label.FontSize = 14; ax.YAxis.LineWidth = 2.5;
   ax.XAxis.FontSize = 14; ax.YAxis.FontSize = 14;
   ax.XAxis.FontWeight = 'bold'; ax.YAxis.FontWeight = 'bold';
figure,boxplot(M20(:,5),T20.Cells);hold on

scatter([ones(4,1);ones(5,1)*2;ones(4,1)*3;ones(8,1)*4],M20(:,5),...
      'filled','LineWidth',5);hold off
   title('Fits of Holmes-Mow for 20mg/mL TE-IVDs','FontSize',14),
   ylabel('R^2'),xlabel('Cells, [M/mL]'),ax = gca;
   ax.XAxis.LineWidth = 2.5;ax.YAxis.LineWidth = 2.5;
   ax.XAxis.Label.FontSize = 14; ax.YAxis.LineWidth = 14;
   ax.XAxis.FontSize = 14; ax.YAxis.FontSize = 14;
   ax.XAxis.FontWeight = 'bold'; ax.YAxis.FontWeight = 'bold';

C04 = table2cell(T04);C10 = table2cell(T10);C20 = table2cell(T20);
TCell = cat(1,C04,C10,C20);T = cell2table(TCell,'VariableNames',...

{'Collagen','Cells','Date','EM','EMgof','HM0','Beta','HMgof'});
writetable(T,'MechDataLong.csv');
save('MechDataTable.mat','dates','Date04','Date10','Date20','DateNat',...

'M04','M10','M20','T04','T10','T20','C04','C10','C20','TCell','T');
Mech = readtable('MechDataLong.xlsx');
%%%
```

```
 NP10_20 =
Cont.NPratio(Cont.Collagen==10&Cont.Cells
==20);
 AF10_20 =
Cont.AFrho(Cont.Collagen==10&Cont.Cells=
=20);
 Day10_20 =
Cont.Day(Cont.Collagen==10&Cont.Cells==2
0);
IVD20_2 =
Cont.IVDratio(Cont.Collagen==20&Cont.Cell
s==2);
 NP20_2 =
Cont.NPratio(Cont.Collagen==20&Cont.Cells
==2);
 AF20_2 =
Cont.AFrho(Cont.Collagen==20&Cont.Cells=
=2);
 Day20_2 =
Cont.Day(Cont.Collagen==20&Cont.Cells==2
);
IVD20_10 =
Cont.IVDratio(Cont.Collagen==20&Cont.Cell
s==10);
 NP20_10 =
Cont.NPratio(Cont.Collagen==20&Cont.Cells
==10);
 AF20_10 =
Cont.AFrho(Cont.Collagen==20&Cont.Cells=
=10);
 Day20_10 =
Cont.Day(Cont.Collagen==20&Cont.Cells==1
0);
IVD20_20 =
Cont.IVDratio(Cont.Collagen==20&Cont.Cell
s==20);
 NP20_20 =
Cont.NPratio(Cont.Collagen==20&Cont.Cells
==20);
 AF20_20 =
Cont.AFrho(Cont.Collagen==20&Cont.Cells=
=20);
 Day20_20 =
Cont.Day(Cont.Collagen==20&Cont.Cells==2
0);
%
IVD04_2mat =
[IVD04_2(1:4),IVD04_2(5:8),IVD04_2(9:12),I
VD04_2(13:16),...

IVD04_2(17:20),IVD04_2(21:24),IVD04_2(25
:28),IVD04_2(29:32),...
   IVD04_2(33:36)];

NP04_2mat =
[NP04_2(1:4),NP04_2(5:8),NP04_2(9:12),NP0
4_2(13:16),...

NP04_2(17:20),NP04_2(21:24),NP04_2(25:28
),NP04_2(29:32),...
   NP04_2(33:36)];
AF04_2mat =
[AF04_2(1:4),AF04_2(5:8),AF04_2(9:12),AF0
4_2(13:16),...

AF04_2(17:20),AF04_2(21:24),AF04_2(25:28
),AF04_2(29:32),...
   AF04_2(33:36)];
IVD10_2mat =
[IVD10_2(1:4),IVD10_2(5:8),IVD10_2(9:12),I
VD10_2(13:16),...
   IVD10_2(17:20)];
NP10_2mat =
[NP10_2(1:4),NP10_2(5:8),NP10_2(9:12),NP1
0_2(13:16),...
   NP10_2(17:20)];
AF10_2mat =
[AF10_2(1:4),AF10_2(5:8),AF10_2(9:12),AF1
0_2(13:16),...
   AF10_2(17:20)];
IVD10_10mat =
[IVD10_10(1:4),IVD10_10(5:8),IVD10_10(9:
12),...
   IVD10_10(13:16),IVD10_10(17:20)];
NP10_10mat =
[NP10_10(1:4),NP10_10(5:8),NP10_10(9:12),.
..
   NP10_10(13:16),NP10_10(17:20)];
AF10_10mat =
[AF10_10(1:4),AF10_10(5:8),AF10_10(9:12),.
..
   AF10_10(13:16),AF10_10(17:20)];
IVD10_20mat =
[IVD10_20(1:4),IVD10_20(5:8),IVD10_20(9:
12),...

IVD10_20(13:16),IVD10_20(17:20),IVD10_2
0(21:24),IVD10_20(25:28),...
   IVD10_20(29:32),IVD10_20(33:36)];
NP10_20mat =
[NP10_20(1:4),NP10_20(5:8),NP10_20(9:12),.
..

NP10_20(13:16),NP10_20(17:20),NP10_20(21
:24),NP10_20(25:28),...
   NP10_20(29:32),NP10_20(33:36)];
AF10_20mat =
[AF10_20(1:4),AF10_20(5:8),AF10_20(9:12),.
..
```

```
AF10_20(13:16),AF10_20(17:20),AF10_20(21
:24),AF10_20(25:28),...
    AF10_20(29:32),AF10_20(33:36)];
IVD20_2mat =
[IVD20_2(1:4),IVD20_2(5:8),IVD20_2(9:12),I
VD20_2(13:16),...

IVD20_2(17:20),IVD20_2(21:24),IVD20_2(25
:28),...
    IVD20_2(29:32),IVD20_2(33:36)];
NP20_2mat =
[NP20_2(1:4),NP20_2(5:8),NP20_2(9:12),NP2
0_2(13:16),...

NP20_2(17:20),NP20_2(21:24),NP20_2(25:28
),...
    NP20_2(29:32),NP20_2(33:36)];
AF20_2mat =
[AF20_2(1:4),AF20_2(5:8),AF20_2(9:12),AF2
0_2(13:16),...

AF20_2(17:20),AF20_2(21:24),AF20_2(25:28
),...
    AF20_2(29:32),AF20_2(33:36)];
IVD20_10mat =
[IVD20_10(1:4),IVD20_10(5:8),IVD20_10(9:
12),...

IVD20_10(13:16),IVD20_10(17:20),IVD20_1
0(21:24),IVD20_10(25:28),...
    IVD20_10(29:32),IVD20_10(33:36)];
NP20_10mat =
[NP20_10(1:4),NP20_10(5:8),NP20_10(9:12),
NP20_10(13:16),...

NP20_10(17:20),NP20_10(21:24),NP20_10(25
:28),...
    NP20_10(29:32),NP20_10(33:36)];
AF20_10mat =
[AF20_10(1:4),AF20_10(5:8),AF20_10(9:12),
AF20_10(13:16),...

AF20_10(17:20),AF20_10(21:24),AF20_10(25
:28),...
    AF20_10(29:32),AF20_10(33:36)];
IVD20_20mat =
[IVD20_20(1:4),IVD20_20(5:8),IVD20_20(9:
12),...

IVD20_20(13:16),IVD20_20(17:20),IVD20_2
0(21:24),IVD20_20(25:28),...
    IVD20_2(29:32)];
NP20_20mat =
[NP20_20(1:4),NP20_20(5:8),NP20_20(9:12),.
..

NP20_20(13:16),NP20_20(17:20),NP20_20(21
:24),NP20_20(25:28),...
    NP20_2(29:32)];
AF20_20mat =
[AF20_20(1:4),AF20_20(5:8),AF20_20(9:12),.
..

AF20_20(13:16),AF20_20(17:20),AF20_20(21
:24),AF20_20(25:28),...
    AF20_2(29:32)];
%
figure,hold on;
errorbar([0,2,4,7,10,14,18,21,23],mean(IVD04
_2mat),std(IVD04_2mat),':s','LineWidth',2,'Col
or',[0 0.5 0]),
errorbar([0,7,14,18,23],mean(IVD10_2mat),std
(IVD10_2mat),':sr','LineWidth',2),
errorbar([0,7,14,18,23],mean(IVD10_10mat),st
d(IVD10_10mat),'--or','LineWidth',2),
errorbar([0,2,4,7,10,14,18,21,23],mean(IVD10
_20mat),std(IVD10_20mat),'-
dr','LineWidth',2),
errorbar([0,2,4,7,10,14,18,21,23],mean(IVD20
_2mat),std(IVD20_2mat),':sb','LineWidth',2),
errorbar([0,2,4,7,10,14,18,21,23],mean(IVD20
_10mat),std(IVD20_10mat),'--
ob','LineWidth',2),
errorbar([0,2,4,7,10,14,21,23],mean(IVD20_20
mat),std(IVD20_20mat),'-db','LineWidth',2),
hold off;
legend({'4mg/mL_{2M}','10mg/mL_{2M}','10
mg/mL_{10M}','10mg/mL_{20M}',...

'20mg/mL_{2M}','20mg/mL_{10M}','20mg/m
L_{20M}'},'Location',...

'southoutside','Orientation','horizontal','FontSiz
e',16,...
    'FontWeight','bold');legend('boxoff')
ylabel('Ratio of Disc Area'),xlabel('Time
[Days]'),ax = gca;
    ax.XAxis.LineWidth =
2.5;ax.YAxis.LineWidth = 2.5;
    ax.XAxis.Label.FontSize = 20;
ax.YAxis.Label.FontSize = 20;
    ax.XAxis.FontSize = 20; ax.YAxis.FontSize
= 20;
    ax.XAxis.FontWeight = 'bold';
ax.YAxis.FontWeight = 'bold';
%
figure,hold on;
```

```
errorbar([0,2,4,7,10,14,18,21,23],mean(NP04_
2mat),std(NP04_2mat),':s','LineWidth',2,'Color'
,[0 0.5 0]),
errorbar([0,7,14,18,23],mean(NP10_2mat),std(
NP10_2mat),':sr','LineWidth',2),
errorbar([0,7,14,18,23],mean(NP10_10mat),std
(NP10_10mat),'--or','LineWidth',2),
errorbar([0,2,4,7,10,14,18,21,23],mean(NP10_
20mat),std(NP10_20mat),'-dr','LineWidth',2),
errorbar([0,2,4,7,10,14,18,21,23],mean(NP20_
2mat),std(NP20_2mat),':sb','LineWidth',2),
errorbar([0,2,4,7,10,14,18,21,23],mean(NP20_
10mat),std(NP20_10mat),'--ob','LineWidth',2),
errorbar([0,2,4,7,10,14,21,23],mean(NP20_20
mat),std(NP20_20mat),'-db','LineWidth',2),
hold off;
legend({'4mg/mL_{2M}','10mg/mL_{2M}','10
mg/mL_{10M}','10mg/mL_{20M}',...

'20mg/mL_{2M}','20mg/mL_{10M}','20mg/m
L_{20M}'},'Location',...

'southoutside','Orientation','horizontal','FontSiz
e',16,...
   'FontWeight','bold');legend('boxoff')
ylabel('NP Area in Disc [%]'),xlabel('Time
[Days]'),ax = gca;
   ax.XAxis.LineWidth =
2.5;ax.YAxis.LineWidth = 2.5;
   ax.XAxis.Label.FontSize = 20;
ax.YAxis.Label.FontSize = 20;
   ax.XAxis.FontSize = 20; ax.YAxis.FontSize
= 20;
   ax.XAxis.FontWeight = 'bold';
ax.YAxis.FontWeight = 'bold';
%
figure,hold on;
errorbar([0,2,4,7,10,14,18,21,23],mean(AF04_
2mat),std(AF04_2mat),':s','LineWidth',2,'Color'
,[0 0.5 0]),
errorbar([0,7,14,18,23],mean(AF10_2mat),std(
AF10_2mat),':sr','LineWidth',2),
errorbar([0,7,14,18,23],mean(AF10_10mat),std
(AF10_10mat),'--or','LineWidth',2),
errorbar([0,2,4,7,10,14,18,21,23],mean(AF10_
20mat),std(AF10_20mat),'-dr','LineWidth',2),
errorbar([0,2,4,7,10,14,18,21,23],mean(AF20_
2mat),std(AF20_2mat),':sb','LineWidth',2),
errorbar([0,2,4,7,10,14,18,21,23],mean(AF20_
10mat),std(AF20_10mat),'--ob','LineWidth',2),
errorbar([0,2,4,7,10,14,21,23],mean(AF20_20
mat),std(AF20_20mat),'-db','LineWidth',2),
hold off;
legend({'4mg/mL_{2M}','10mg/mL_{2M}','10
mg/mL_{10M}','10mg/mL_{20M}',...

'20mg/mL_{2M}','20mg/mL_{10M}','20mg/m
L_{20M}'},'Location',...

'southoutside','Orientation','horizontal','FontSiz
e',16,...
   'FontWeight','bold');legend('boxoff')
ylabel('Apparent AF density
[mg/mL]'),xlabel('Time [Days]'),ax = gca;
   ax.XAxis.LineWidth =
2.5;ax.YAxis.LineWidth = 2.5;
   ax.XAxis.Label.FontSize = 20;
ax.YAxis.Label.FontSize = 20;
   ax.XAxis.FontSize = 20; ax.YAxis.FontSize
= 20;
   ax.XAxis.FontWeight = 'bold';
ax.YAxis.FontWeight = 'bold';
%
% tbl=Cont;
% tbl.Collagen=categorical(tbl.Collagen);
% tbl.Cells=categorical(tbl.Cells);
% % mdl =
fitlm(tbl,'IVDratio~Collagen*Cells*Day')
% % anova(mdl)
% [~,~,stats] =
anovan(tbl.IVDratio,{tbl.Collagen tbl.Cells
tbl.Day},...
%
'model','interaction','varnames',{'Collagen','Cell
s','Day'})
% [results,means] =
multcompare(stats,'Dimension',[1 2])
% [results,means] =
multcompare(stats,'Dimension',[1 3])
% [results,means] =
multcompare(stats,'Dimension',[2 3])
% [results,means] =
multcompare(stats,'Dimension',[1 2 3]); %3240
multiple
% %comparisons because
9days*3cellconc*3collconcs.
% sigdif = results(results(:,6)<0.05,[1:2,6]);
% % %repeated measures cannot work due to
unbalanced design (some days have
% % more specimens than others) consider
mixed-effects model instead, since
% % three-way anova is also not useful (time
measures are not independent)
% tblrm = tbl;
% tblrm(tblrm.Collagen=='4',:)=[];
% tblrm(tblrm.Day==2,:)=[];
% tblrm(tblrm.Day==4,:)=[];
% tblrm(tblrm.Day==10,:)=[];
% tblrm(tblrm.Day==18,:)=[];
% tblrm(tblrm.Day==21,:)=[];
```

```
% VarNames =
{'Collagen','Cells','day0','day7','day14','day23'}
;
%
rmtable=table(tblrm.Collagen(tblrm.Day==0),t
blrm.Cells(tblrm.Day==0),...
%
tblrm.IVDratio(tblrm.Day==0),tblrm.IVDratio(
tblrm.Day==7),...
%
tblrm.IVDratio(tblrm.Day==14),tblrm.IVDrati
o(tblrm.Day==23),...
%     'VariableNames',VarNames);
%
Days=dataset({'0','7','14','23'}','VarNames',{'Da
ys'});
% rmdl = fitrm(rmtable,'day0-
day23~Collagen*Cells','WithinDesign',Days);
```

datadistplots.m for boxplots and surface graphs of global correlation analysis

```
% Eq Mod vs. Cells & Collagen Data
Distribution Plot
figure,boxplot(Mech.EM,[Mech.Cells,Mech.C
ollagen]);
ylabel('E_{eq} [kPa]','FontSize',20);
xlabel('Cells/Collagen [10^6MSCs/mL:mg/mL
Coll]','FontSize',20),ax=gca;
ax.XAxis.LineWidth=2.5;ax.YAxis.LineWidth
=2.5;
a = get(get(gca,'children'),'children');   % Get
the handles of all the objects
t = get(a,'tag');   % List the names of all the
objects
idx=strcmpi(t,'box');  % Find Box objects
boxes=a(idx);          % Get the children you
need
set(boxes,'linewidth',2); % Set width
set(a(strcmpi(t,'median')),'linewidth',2); % Set
width
set(a(strcmpi(t,'outliers')),'linewidth',5); % Set
width
set(a(strcmpi(t,'upper adjacent
value')),'linewidth',2); % Set width
set(a(strcmpi(t,'upper whisker')),'linewidth',2);
% Set width
set(a(strcmpi(t,'')),'fontsize',0.1); % Set boxplot
fontsize
set(a(strcmpi(t,'')),'color',[1 1 1]);
ax.FontName = 'Times New Roman';
ax.XAxis.LineWidth =
2.5;ax.YAxis.LineWidth = 2.5;
   ax.XAxis.FontSize = 20; ax.YAxis.FontSize
= 32;
   ax.XAxis.Label.FontSize = 32;
ax.YAxis.Label.FontSize = 32;
   ax.XAxis.FontWeight = 'bold';
ax.YAxis.FontWeight = 'bold';
xticks(ax,[1,2,3,4,5,6,7,8]);xticklabels(ax,{'2:4'
,'2:10','2:20',...
   '5:10','10:10','10:20','20:10','20:20'});
%
% Log-normalized Eq Mod vs. Cells &
Collagen Data Distribution Plot
figure,boxplot(log(Mech.EM),[Mech.Cells,Me
ch.Collagen]);
ylabel('ln(E_{eq})','FontSize',20);
xlabel('Cells/Collagen [10^6MSCs/mL:mg/mL
Coll]','FontSize',20),ax=gca;
ax.XAxis.LineWidth=2.5;ax.YAxis.LineWidth
=2.5;
a = get(get(gca,'children'),'children');   % Get
the handles of all the objects
t = get(a,'tag');   % List the names of all the
objects
idx=strcmpi(t,'box');  % Find Box objects
boxes=a(idx);          % Get the children you
need
set(boxes,'linewidth',2); % Set width
set(a(strcmpi(t,'median')),'linewidth',2); % Set
width
set(a(strcmpi(t,'outliers')),'linewidth',5); % Set
width
set(a(strcmpi(t,'upper adjacent
value')),'linewidth',2); % Set width
set(a(strcmpi(t,'upper whisker')),'linewidth',2);
% Set width
set(a(strcmpi(t,'lower adjacent
value')),'linewidth',2); % Set width
set(a(strcmpi(t,'lower whisker')),'linewidth',2);
% Set width
set(a(strcmpi(t,'')),'fontsize',0.1); % Set boxplot
fontsize
set(a(strcmpi(t,'')),'color',[1 1 1]);
ax.FontName = 'Times New Roman';
ax.XAxis.LineWidth =
2.5;ax.YAxis.LineWidth = 2.5;
   ax.XAxis.FontSize = 20; ax.YAxis.FontSize
= 32;
   ax.XAxis.Label.FontSize = 32;
ax.YAxis.Label.FontSize = 32;
```

```
    ax.XAxis.FontWeight = 'bold';
ax.YAxis.FontWeight = 'bold';
xticks(ax,[1,2,3,4,5,6,7,8]);xticklabels(ax,{'2:4'
,'2:10','2:20',...
    '5:10','10:10','10:20','20:10','20:20'});
%
% Holmes-Mow Agg. Mod vs. Cells &
Collagen Data Distribution Plot
figure,boxplot(Mech.HM0,[Mech.Cells,Mech.
Collagen]);
ylabel('Aggregate Mod., H_{A0}
[kPa]','FontSize',20);
xlabel('Cells/Collagen [10^6MSCs/mL:mg/mL
Coll]','FontSize',20),ax=gca;
ax.XAxis.LineWidth=2.5;ax.YAxis.LineWidth
=2.5;
a = get(get(gca,'children'),'children');   % Get
the handles of all the objects
t = get(a,'tag');   % List the names of all the
objects
idx=strcmpi(t,'box');  % Find Box objects
boxes=a(idx);          % Get the children you
need
set(boxes,'linewidth',2); % Set width
set(a(strcmpi(t,'median')),'linewidth',2); % Set
width
set(a(strcmpi(t,'outliers')),'linewidth',5); % Set
width
set(a(strcmpi(t,'upper adjacent
value')),'linewidth',2); % Set width
set(a(strcmpi(t,'upper whisker')),'linewidth',2);
% Set width
set(a(strcmpi(t,'lower adjacent
value')),'linewidth',2); % Set width
set(a(strcmpi(t,'lower whisker')),'linewidth',2);
% Set width
set(a(strcmpi(t,'')),'fontsize',0.1); % Set boxplot
fontsize
set(a(strcmpi(t,'')),'color',[1 1 1]);
ax.FontName = 'Times New Roman';
ax.XAxis.LineWidth =
2.5;ax.YAxis.LineWidth = 2.5;
    ax.XAxis.FontSize = 20; ax.YAxis.FontSize
= 32;
    ax.XAxis.Label.FontSize = 32;
ax.YAxis.Label.FontSize = 32;
    ax.XAxis.FontWeight = 'bold';
ax.YAxis.FontWeight = 'bold';
xticks(ax,[1,2,3,4,5,6,7,8]);xticklabels(ax,{'2:4'
,'2:10','2:20',...
    '5:10','10:10','10:20','20:10','20:20'});
%
% Holmes-Mow Stiffening Beta vs. Cells &
Collagen Data Distribution Plot
figure,boxplot(Mech.Beta,[Mech.Cells,Mech.C
ollagen]);
ylabel('Stress-stiffening Coeff.,
\beta','FontSize',20);
xlabel('Cells/Collagen [10^6MSCs/mL:mg/mL
Coll]','FontSize',20),ax=gca;
ax.XAxis.LineWidth=2.5;ax.YAxis.LineWidth
=2.5;
a = get(get(gca,'children'),'children');   % Get
the handles of all the objects
t = get(a,'tag');   % List the names of all the
objects
idx=strcmpi(t,'box');  % Find Box objects
boxes=a(idx);          % Get the children you
need
set(boxes,'linewidth',2); % Set width
set(a(strcmpi(t,'median')),'linewidth',2); % Set
width
set(a(strcmpi(t,'outliers')),'linewidth',5); % Set
width
set(a(strcmpi(t,'upper adjacent
value')),'linewidth',2); % Set width
set(a(strcmpi(t,'upper whisker')),'linewidth',2);
% Set width
set(a(strcmpi(t,'lower adjacent
value')),'linewidth',2); % Set width
set(a(strcmpi(t,'lower whisker')),'linewidth',2);
% Set width
set(a(strcmpi(t,'')),'fontsize',0.1); % Set boxplot
fontsize
set(a(strcmpi(t,'')),'color',[1 1 1]);
ax.FontName = 'Times New Roman';
ax.XAxis.LineWidth =
2.5;ax.YAxis.LineWidth = 2.5;
    ax.XAxis.FontSize = 20; ax.YAxis.FontSize
= 32;
    ax.XAxis.Label.FontSize = 32;
ax.YAxis.Label.FontSize = 32;
    ax.XAxis.FontWeight = 'bold';
ax.YAxis.FontWeight = 'bold';
xticks(ax,[1,2,3,4,5,6,7,8]);xticklabels(ax,{'2:4'
,'2:10','2:20',...
    '5:10','10:10','10:20','20:10','20:20'});
%
%
% Import ContractionLong.xlsx using import
tool
Cont = ContractionLong;
rhoAF = Cont.AFrho(Cont.Day==23);rhoAF =
flip(rhoAF);
contAF =
Cont.IVDratio(Cont.Day==23);contAF =
flip(contAF);
cellsAF = Cont.Cells(Cont.Day==23);cellsAF
= flip(cellsAF);
```

```
collAF =
Cont.Collagen(Cont.Day==23);collAF =
flip(collAF);
avgCells = [2,2,10,20,2,10,20];

cells04 =
MechData.Cells(MechData.Collagen==4);
col04 = cells04;
cells10 =
Mech.Cells(Mech.Collagen==10&Mech.Cells
~=5); col10 = cells10;
cells20 = Mech.Cells(Mech.Collagen==20);
col20 = cells20;
vecEM04 =
Mech.EM(MechData.Collagen==4);
vecEM10 =
Mech.EM(Mech.Collagen==10&Mech.Cells~
=5);
vecEM20 = Mech.EM(Mech.Collagen==20);

avgrhoAF =
[mean(rhoAF(1:4)),mean(rhoAF(5:8)),mean(rh
oAF(9:12)),...

mean(rhoAF(13:16)),mean(rhoAF(17:20)),mea
n(rhoAF(21:24)),...
   mean(rhoAF(25:28))];

col04(col04==2) = avgrhoAF(1);
col10(col10==2) = avgrhoAF(2);
col10(col10==10) = avgrhoAF(3);
col10(col10==20) = avgrhoAF(4);
col20(col20==2) = avgrhoAF(5);
col20(col20==10) = avgrhoAF(6);
col20(col20==20) = avgrhoAF(7);

avgEM =
[mean(EM04_2),avgEM10(1),avgEM10(3:end
),avgEM20];
avgCol = [4,10,10,10,20,20,20];
%
% Import MechDataLong.xlsx using import
tool
MechData = MechDataLong1;
[sf1 gosf1] =
fit([MechData.Cells,MechData.Collagen],Mec
hData.EM,...
   'poly11','Exclude',[4:7,9,21,26:29,30,41])
MechData([9,21,30,41],:) = [];
figure,plot(sf1),hold on,
scatter3(MechData.Cells(MechData.Collagen=
=4&MechData.Cells~=0),...

MechData.Collagen(MechData.Collagen==4&
MechData.Cells~=0),...,

MechData.EM(MechData.Collagen==4&Mech
Data.Cells~=0),50,...
   'MarkerEdgeColor','k','MarkerFaceColor',[0
0.5 0])
scatter3(MechData.Cells(MechData.Collagen=
=10&MechData.Cells~=0),...

MechData.Collagen(MechData.Collagen==10
&MechData.Cells~=0),...,

MechData.EM(MechData.Collagen==10&Mec
hData.Cells~=0),50,...
   'MarkerEdgeColor','k','MarkerFaceColor','r')
scatter3(MechData.Cells(MechData.Collagen=
=20&MechData.Cells~=0),...

MechData.Collagen(MechData.Collagen==20
&MechData.Cells~=0),...,

MechData.EM(MechData.Collagen==20&Mec
hData.Cells~=0),50,...

'MarkerEdgeColor','k','MarkerFaceColor','b'),h
old off;
zlabel('E_{eq} [kPa]','FontSize',20);
ylabel('Collagen in AF
[mg/mL]','FontSize',20);
xlabel('MSCs in AF
[10^6/mL]','FontSize',20),ax=gca;
ax.FontName = 'Times New Roman';
ax.XAxis.LineWidth =
2.5;ax.YAxis.LineWidth =
2.5;ax.ZAxis.LineWidth = 2.5;
ax.XAxis.FontSize = 30; ax.YAxis.FontSize =
30;ax.ZAxis.FontSize = 30;
ax.XAxis.Label.FontSize =
32;ax.YAxis.Label.FontSize =
32;ax.ZAxis.Label.FontSize = 32;
ax.XAxis.FontWeight =
'bold';ax.YAxis.FontWeight =
'bold';ax.ZAxis.FontWeight = 'bold';
lg = legend('4 mg/mL baseline','10 mg/mL','20
mg/mL');legend('boxoff');
lg.FontWeight = 'bold';lg.FontSize =
20;lg.Location = 'West';
str = sprintf('R^2 = %.2f',gosf1.rsquare);
a = annotation('textbox',[.5 .5 .3
.3],'String',str,'FitBoxToText','on');
a.LineStyle = 'none'; a.FontSize = 20;
a.FontWeight = 'bold';
a.FontName = 'Times New Roman';

% Mech = MechDataLong1;
% Mech([9,21,30,41],:) = [];
```

```
[sf2 gosf2] =
fit([Mech.Cells,Mech.Collagen],Mech.EM,'poly11')
figure,plot(sf2),hold on,
%
scatter3(MechData.Cells(MechData.Collagen==4&MechData.Cells~=0),...
%
MechData.Collagen(MechData.Collagen==4&MechData.Cells~=0),...,
%
MechData.EM(MechData.Collagen==4&MechData.Cells~=0),50,...
%
'MarkerEdgeColor','k','MarkerFaceColor',[0 0.5 0])
scatter3(Mech.Cells(Mech.Collagen==10&Mech.Cells~=0),...

Mech.Collagen(Mech.Collagen==10&Mech.Cells~=0),...,

Mech.EM(Mech.Collagen==10&Mech.Cells~=0),50,...
    'MarkerEdgeColor','k','MarkerFaceColor','r')
scatter3(Mech.Cells(Mech.Collagen==20&Mech.Cells~=0),...

Mech.Collagen(Mech.Collagen==20&Mech.Cells~=0),...,

Mech.EM(Mech.Collagen==20&Mech.Cells~=0),50,...

'MarkerEdgeColor','k','MarkerFaceColor','b'),hold off;
zlabel('E_{eq} [kPa]','FontSize',20);
ylabel('Col density in AF, \rho [mg/mL]','FontSize',20);
xlabel('MSCs in AF [10^6/mL]','FontSize',20),ax=gca;
ax.FontName = 'Times New Roman';
ax.XAxis.LineWidth = 2.5;ax.YAxis.LineWidth = 2.5;ax.ZAxis.LineWidth = 2.5;
ax.XAxis.FontSize = 30; ax.YAxis.FontSize = 30;ax.ZAxis.FontSize = 30;
ax.XAxis.Label.FontSize = 32;ax.YAxis.Label.FontSize = 32;ax.ZAxis.Label.FontSize = 32;
ax.XAxis.FontWeight = 'bold';ax.YAxis.FontWeight = 'bold';ax.ZAxis.FontWeight = 'bold';
lg = legend('10 mg/mL','20 mg/mL');legend('boxoff');
lg.FontWeight = 'bold';lg.FontSize = 20;lg.Location = 'West';
str = sprintf('R^2 = %.2f',gosf2.rsquare);
a = annotation('textbox',[.5 .5 .3 .3],'String',str,'FitBoxToText','on');
a.LineStyle = 'none'; a.FontSize = 20;
a.FontWeight = 'bold';
a.FontName = 'Times New Roman';
%
%%This is the one:
[sf3 gosf3] =
fit([avgCells',avgCol'],avgEM','poly11')
figure,s1 = plot(sf3),hold on
scatter3(MechData.Cells(MechData.Collagen==4&MechData.Cells~=0),...

MechData.Collagen(MechData.Collagen==4&MechData.Cells~=0),...,

MechData.EM(MechData.Collagen==4&MechData.Cells~=0),80,...
    'MarkerEdgeColor','k','MarkerFaceColor',[0 0.5 0])
scatter3(Mech.Cells(Mech.Collagen==10&Mech.Cells~=0),...

Mech.Collagen(Mech.Collagen==10&Mech.Cells~=0),...,

Mech.EM(Mech.Collagen==10&Mech.Cells~=0),80,...
    'MarkerEdgeColor','k','MarkerFaceColor','r')
scatter3(Mech.Cells(Mech.Collagen==20&Mech.Cells~=0),...

Mech.Collagen(Mech.Collagen==20&Mech.Cells~=0),...,

Mech.EM(Mech.Collagen==20&Mech.Cells~=0),80,...

'MarkerEdgeColor','k','MarkerFaceColor','b'),hold off;
s1.FaceAlpha = 0.5;
zlabel('E_{eq} [kPa]','FontSize',36);
ylabel('Col density in AF, \rho [mg/mL]','FontSize',36);
xlabel('MSCs in AF [10^6/mL]','FontSize',36),ax=gca;
ax.FontName = 'Times New Roman';
ax.XAxis.LineWidth = 2.5;ax.YAxis.LineWidth = 2.5;ax.ZAxis.LineWidth = 2.5;
ax.XAxis.FontSize = 36; ax.YAxis.FontSize = 36;ax.ZAxis.FontSize = 36;
```

```
ax.XAxis.Label.FontSize =
36;ax.YAxis.Label.FontSize =
36;ax.ZAxis.Label.FontSize = 36;
ax.XAxis.FontWeight =
'bold';ax.YAxis.FontWeight =
'bold';ax.ZAxis.FontWeight = 'bold';
lg = legend('4 mg/mL','10 mg/mL','20
mg/mL');legend('boxoff');
lg.FontWeight = 'bold';lg.FontSize =
36;lg.Location = 'West';
str = sprintf('R^2 = %.2f',gosf3.rsquare);
a = annotation('textbox',[.5 .5 .3
.3],'String',str,'FitBoxToText','on');
a.LineStyle = 'none'; a.FontSize = 36;
a.FontWeight = 'bold';
a.FontName = 'Times New Roman';

[sf4 gosf4]=
fit([avgCells',avgrhoAF'],avgEM','poly11')
figure,s2 = plot(sf4);hold on,
scatter3(cells04,col04,vecEM04,50,...
   'MarkerEdgeColor','k','MarkerFaceColor',[0
0.5 0])
scatter3(cells10,col10,vecEM10,50,...
   'MarkerEdgeColor','k','MarkerFaceColor','r')
scatter3(cells20,col20,vecEM20,50,...

'MarkerEdgeColor','k','MarkerFaceColor','b'),h
old off;
s2.FaceAlpha = 0.5;
zlabel('E_{eq} [kPa]','FontSize',20);
ylabel('App. AF density, \rho [mg
Col/mL]','FontSize',20);
xlabel('Cells in AF
[10^6MSCs/mL]','FontSize',20),ax=gca;
ax.FontName = 'Times New Roman';
ax.XAxis.LineWidth =
2.5;ax.YAxis.LineWidth =
2.5;ax.ZAxis.LineWidth = 2.5;
ax.XAxis.FontSize = 36; ax.YAxis.FontSize =
36;ax.ZAxis.FontSize = 36;
ax.XAxis.Label.FontSize =
36;ax.YAxis.Label.FontSize =
36;ax.ZAxis.Label.FontSize = 36;
ax.XAxis.FontWeight =
'bold';ax.YAxis.FontWeight =
'bold';ax.ZAxis.FontWeight = 'bold';
lg = legend('4 mg/mL','10 mg/mL','20
mg/mL');legend('boxoff');
lg.FontWeight = 'bold';lg.FontSize =
36;lg.Location = 'East';
str = {sprintf('R^2 = %.2f',gosf4.rsquare),'Fit to
E_{eq,avg}'};
a = annotation('textbox',[.5 .5 .3
.3],'String',str,'FitBoxToText','on');
a.LineStyle = 'none'; a.FontSize = 36;
a.FontWeight = 'bold';
a.FontName = 'Times New Roman';

[sf5 gosf5]=
fit([cellsAF,collAF],rhoAF,'poly11')
figure,s3 = plot(sf5),hold on,
scatter3(cellsAF(1:4),collAF(1:4),rhoAF(1:4),8
0,...
   'MarkerEdgeColor','w','MarkerFaceColor',[0
0.5 0])
scatter3(cellsAF(5:16),collAF(5:16),rhoAF(5:1
6),80,...
   'MarkerEdgeColor','k','MarkerFaceColor','r')
scatter3(cellsAF(17:28),collAF(17:28),rhoAF(
17:28),80,...

'MarkerEdgeColor','k','MarkerFaceColor','b'),h
old off;
s3.FaceAlpha = 0.5;
zlabel('\rho_{AF,app} [mg/mL]','FontSize',36);
ylabel('Collagen in AF
[mg/mL]','FontSize',36);
xlabel('MSCs
[10^6/mL]','FontSize',36),ax=gca;
ax.FontName = 'Times New Roman';
ax.XAxis.LineWidth =
2.5;ax.YAxis.LineWidth =
2.5;ax.ZAxis.LineWidth = 2.5;
ax.XAxis.FontSize = 36; ax.YAxis.FontSize =
36;ax.ZAxis.FontSize = 36;
ax.XAxis.Label.FontSize =
36;ax.YAxis.Label.FontSize =
36;ax.ZAxis.Label.FontSize = 36;
ax.XAxis.FontWeight =
'bold';ax.YAxis.FontWeight =
'bold';ax.ZAxis.FontWeight = 'bold';
lg = legend('4 mg/mL','10 mg/mL','20
mg/mL');legend('boxoff');
lg.FontWeight = 'bold';lg.FontSize =
36;lg.Location = 'East';
str = {sprintf('R^2 = %.2f',gosf5.rsquare)};
a = annotation('textbox',[.5 .5 .3
.3],'String',str,'FitBoxToText','on');
a.LineStyle = 'none'; a.FontSize = 36;
a.FontWeight = 'bold';
a.FontName = 'Times New Roman';

contAF = 100*contAF;
[sf6 gosf6]=
fit([cellsAF,collAF],contAF,'poly11')
figure,s4 = plot(sf6),hold on,
scatter3(cellsAF(1:4),collAF(1:4),contAF(1:4),
80,...
```

```
    'MarkerEdgeColor','w','MarkerFaceColor',[0
0.5 0])
scatter3(cellsAF(5:16),collAF(5:16),contAF(5:
16),80,...
    'MarkerEdgeColor','k','MarkerFaceColor','r')
scatter3(cellsAF(17:28),collAF(17:28),contAF(
17:28),80,...

'MarkerEdgeColor','k','MarkerFaceColor','b'),h
old off;
s4.FaceAlpha = 0.5;
zlabel('TE-IVD Size [% Original
Area]','FontSize',36);
ylabel('Collagen in AF
[mg/mL]','FontSize',36);
xlabel('MSCs
[10^6/mL]','FontSize',36),ax=gca;
ax.FontName = 'Times New Roman';
ax.XAxis.LineWidth =
2.5;ax.YAxis.LineWidth =
2.5;ax.ZAxis.LineWidth = 2.5;
ax.XAxis.FontSize = 36; ax.YAxis.FontSize =
36;ax.ZAxis.FontSize = 36;
ax.XAxis.Label.FontSize =
36;ax.YAxis.Label.FontSize =
36;ax.ZAxis.Label.FontSize = 36;
ax.XAxis.FontWeight =
'bold';ax.YAxis.FontWeight =
'bold';ax.ZAxis.FontWeight = 'bold';
lg = legend('4 mg/mL','10 mg/mL','20
mg/mL');legend('boxoff');
lg.FontWeight = 'bold';lg.FontSize =
36;lg.Location = 'East';
str = {sprintf('R^2 = %.2f',gosf6.rsquare)};
a = annotation('textbox',[.5 .5 .3
.3],'String',str,'FitBoxToText','on');
a.LineStyle = 'none'; a.FontSize = 36;
a.FontWeight = 'bold';
a.FontName = 'Times New Roman';
```